Neutral Particle Transport in the Plasma Edge and Divertor Region

A Thesis
Presented to The Academic Faculty

by

Roberto Rubilar

In Partial Fulfillment
of the Requirements for the Degree of
Doctor of Philosophy in
Nuclear and Radiological Engineering
in the School of Mechanical Engineering

Georgia Institute of Technology
June 2000

Neutral Particle Transport in the Plasma Edge and Divertor Region

Approved:

Weston M. Stacey, Chair

John Mandrekas

Farzad Rahnema

Edward W. Thomas

J. Narl Davidson

Robert K. Feeney

Date Approved   June 2, 2000

To my loved ones, who made it possible
To them my gratitude

ACKNOWLEDGMENTS

I would like to take a moment to thank all those who in one way or another guided, helped, and supported me during the completion of this thesis. I am grateful to my research advisor, Dr. Weston M. Stacey, Jr., for his continual guidance and useful discussions during the course of this work. I am also grateful to Dr. John Mandrekas for always being willing to help me understand and clarify the many intricate aspects of the theory used in this work. I am appreciative of the members of my reading committee, Drs. Farzad Rahnema, Edward W. Thomas, J. Narl Davidson, and Roberto K. Feeney for taking the time to read this work and make useful comments. My sincere thanks to Dr. Darren Stotler at Princeton Plasma Physics Laboratory for his willingness to explain and clarify the use of the Monte Carlo codes DEGAS and DEGAS 2. My thanks to Dr. Marvin E. Rensink at Lawrence Livermore National Laboratory for helping me with the information needed in one of the divertor models used in this study, and to Dr. Larry W. Owen at Oak Ridge National Laboratory for his help in describing the DIII-D experiment and results.

I also wish to express my appreciation to my wife, Lisa, for her patience, understanding, and moral support throughout this endeavor.

TABLE OF CONTENTS

LIST OF TABLES

LIST OF FIGURES

SUMMARY

The transport of neutral atoms and molecules at the edge of a magnetically confined plasma plays an important role in the overall plasma performance. This transport problem is characterized by geometrical complexity, widely varying mean free paths, and sharp particle density variations. Most of the methods used to study neutral particles in plasmas are limited either by excessive computational time (Monte Carlo), inability to treat complex geometries, failure to treat widely varying mean free paths (diffusion theory, discrete ordinates) or lack of accuracy in some regimes (diffusion theory).

Two related computational methods for neutral particle transport in the outer regions of a diverted tokamak plasma have been recently introduced. These methods subdivide the computational domain into a number of relatively large regions, calculate transmission and escape probabilities for these regions using first flight integral transport methods, and then balance the partial currents or fluxes across the surfaces bounding these regions. While implementing these methods, a number of approximations were made in order to simplify the treatment of the angular distribution of particles and to characterize the transport probabilities. This work reports on the evaluation of the accuracy of these various approximations. This evaluation was based on a detailed comparison with Monte Carlo. In addition, a number of correction factors were introduced to improve accuracy. When dealing with the transport of a single species of monoenergetic neutrals, this model was shown to be capable of achieving accuracies comparable to Monte Carlo calculations at a fraction of the computational time. A further purpose of this work is to report the comparison of these methods and Monte Carlo calculations and experimental results for neutral densities in the DIII-D edge plasma.

CHAPTER I

INTRODUCTION

1.1 The Importance of Neutrals in the Plasma Edge

The transport of neutral atoms and molecules (particles that are unaffected by magnetic fields) at the edge of a magnetically confined plasma plays an important role in determining the overall plasma performance. Impurities in the plasma can dilute the fuel (i.e., D-T) and give rise to radiation losses. In order to restrict their entry into the plasma two techniques are used; the first is to make use of a material limiter to define an outer plasma boundary; the second modifies the magnetic field to produce a magnetic divertor to keep particles away from the vacuum vessel [1]. These techniques are shown in figure 1.1 from Wesson [1].
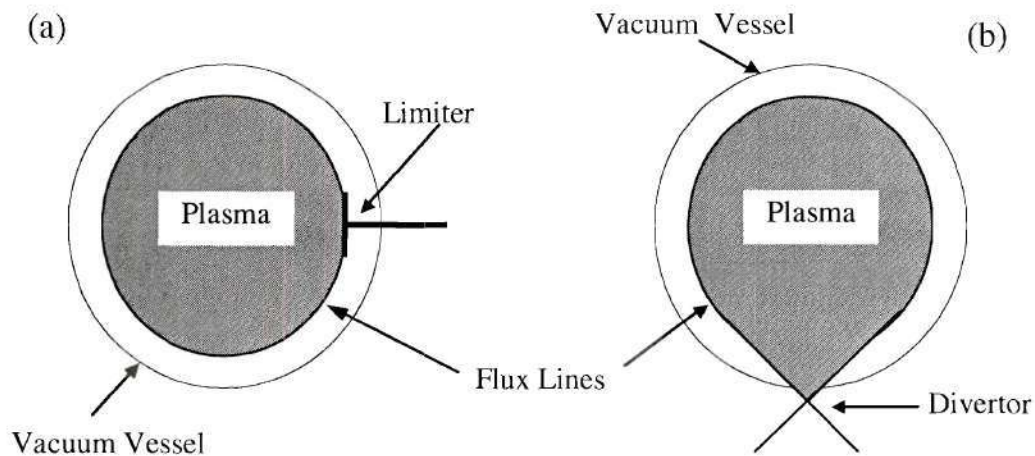
Figure 1.1. Separation of plasma from vacuum vessel by limiter (a) and divertor (b) (from reference 1).

1

In 1961 Sakharov [2, 3] first pointed out that neutral hydrogen could travel deep into a hot plasma by repeated charge exchange. The same is true for neutrals of other species. There is strong evidence that suggests a link between neutral particles and the overall plasma power and particle balances, temperature and density profiles, plasma confinement, particle and energy fluxes to the wall of the device, erosion of the first wall, performance of the pumping systems, etc. [2, 4, 5, 6]. For instance, Tendler [2] points out that neutral particles refuel the plasma as they become ionized, causing a net increase in the total momentum and energy of the plasma. He also states that limiters cannot shield the first wall from being struck by energetic neutrals emerging from the inner core after recombination and charge-exchange with neutral beams has occurred. Thus, sputtering by charge-exchange neutrals can constitute both a major source of impurities to the plasma and a major damage mechanism to the wall of the plasma chamber. Furthermore, in order to sustain long-pulse operation in reactors such as the International Thermonuclear Experimental Reactor (ITER), impurities have to be pumped. The efficiency of the pumping system depends on the amount and the type of impurities generated [5]. In order to avoid the extreme heat and particle loads to the divertor plate and first wall, a condition known as "detached plasma" is highly desirable. Detachment gives rise to radiative cooling by introducing impurities in the plasma edge. This reduces the temperature in the divertor region to a level low enough (~ 1 eV) to trigger the increase of neutrals by recombination of ions and electrons [7, 8]. Niemczewski [9] indicates that there are strong indications that the onset of detachment is influenced by the neutral population in the divertor region. More recently, Tsuchiya et al. [10] have reported that edge neutrals have an important

influence on the condition of the H-mode transition in JT-60U. Stacey et al. [11] have also reported that in DIII-D continuous gas puff fueled high-power shots, the Multifaceted Asymmetric Radiation from the edge (MARFE) onset was coincident with the sharp increase in neutral density in the plasma edge. Therefore, neutral particle transport is by no means a trivial problem, and a better understanding of the behavior of neutral particles is of great relevance to the further advance of fusion plasma physics.

1.2 Characteristics of Neutral Particle Transport in the Plasma Edge

In contrast with the physical phenomena found in the plasma core, where the relative neutral hydrogen density (i.e., the ratio of neutral hydrogen to the total particle density) is on the order of 10^{-5} or less and temperatures reach 10^4 eV, the typical values for the neutral particle density and the temperature at the plasma edge are on the order of 10^{20}-10^{21} m^{-3} (near the divertor) and 5-20 eV respectively. As particle and energy fluxes emerging from the plasma core increase, the amount of recycled neutral gas also increases. The inelastic collisions of plasma particles with cold recycling gas (whose temperature is determined primarily by the energy of dissociated Franck-Condon atoms, which is about 3-5 eV) are responsible for the temperature decline at the plasma edge [12, 13].

It is also important to mention that neutral particle density at the plasma edge may reach values close to 10% of the total particle density, and more importantly, that the neutral density near the divertor can exceed that of the ions. Indeed, according to Janev et al. [12] most of the particles found near the wall are neutral hydrogen with a density that approximates 50% of total charged particles found near the wall. Figure 1.2 from

McCracken [14] illustrates the typical temperature and plasma profiles found in the edge of a tokamak plasma.
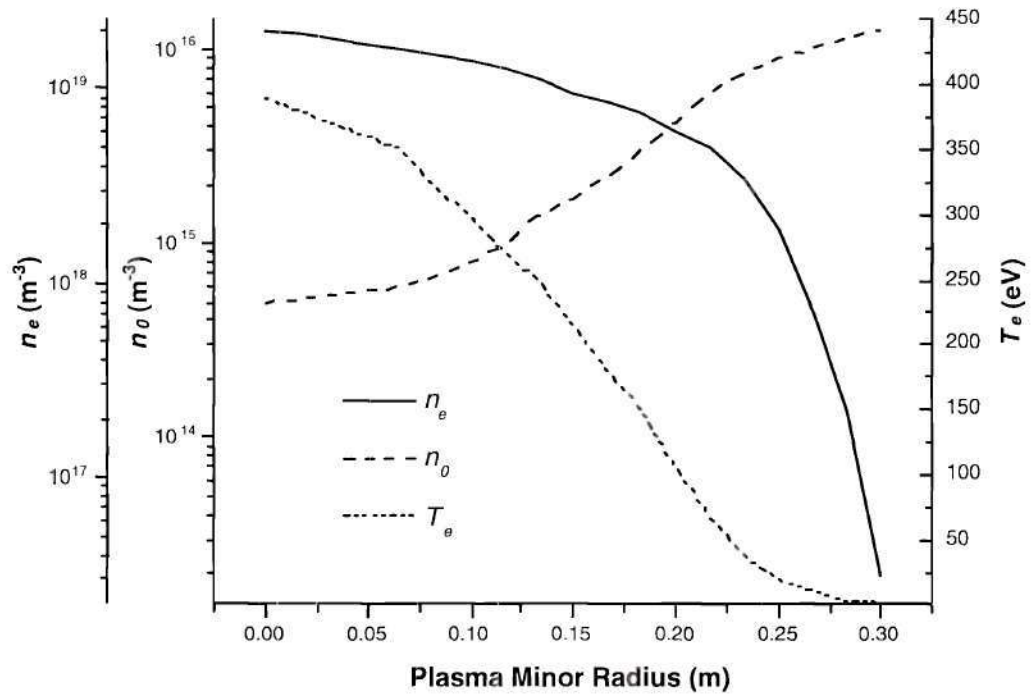
Figure 1.2. Typical temperature and density profiles in tokamak plasmas (from ref. 14).

1.3 Methods for Solving for the Neutral Flux Distribution

1.3.1 Introduction

The equation that determines the density profiles of the neutrals is the Boltzmann equation, in which all the relevant atomic processes are contained in the collision terms. The three-dimensional and time independent Boltzmann equation is

$$v(E)\hat{\Omega}\cdot\nabla n(\vec{r},\hat{\Omega},E)+\Sigma_t(\vec{r},E)v(E)n(\vec{r},\hat{\Omega},E)=S(\vec{r},\hat{\Omega},E) \quad +$$

$$\int_{4\pi}d\hat{\Omega}'\int_0^\infty dE'\,v(E')n(\vec{r},\hat{\Omega}',E')\Sigma_s(\vec{r}:\hat{\Omega}',E'\to\hat{\Omega},E)$$

(1.1)

where v is the velocity of the neutral particle; n is the neutral particle density distribution; Σ_t is the total cross section for all the interactions between electrons/neutrals or ions/neutrals (ionization, charge-exchange, elastic scattering, etc.); S represents all the external neutral sources or internal creation processes such as recombination; and Σ_s is the cross section for all the events that change the energy and direction of the neutral particle, such as charge-exchange or scattering.

A successful treatment of geometric complexities and widely varying mean free paths in present diverted tokamak plasmas is very challenging. Over the years many methods that were first applied to neutron transport have been adapted for neutral particle transport in the plasma edge. The most popular methods for solving for the neutral flux distribution are the spherical harmonics or P_n method (including the lowest order diffusion theory approximation), the discrete ordinates or S_n method (both P_n and S_n are approximations to

5

the above integrodifferential transport equation), the Monte Carlo method, and integral transport methods. The discrete ordinates and Monte Carlo methods are the ones most used today to analyze neutron transport in reactors.

1.3.2 Spherical Harmonics or P_n Method

The spherical harmonics method is the oldest method, with references dating back to 1926 [15]. Even though this method is not widely used today, it is considered the theoretical basis for the diffusion theory, which is widely used. Nevertheless, the spherical harmonics method is still an important tool for transport analysis. The procedure for finding a solution to the one-dimensional transport equation is as follows. If ψ, the neutral flux distribution, is defined as $\psi = nv$ and μ as the cosine of the angle made by the velocity vector v of the neutral particle and the x-axis; then the one-dimensional and time independent Boltzmann equation is

$$\mu \frac{\partial \psi(x,\mu,E)}{\partial x} + \Sigma_t(x,E)\psi(x,\mu,E) = S(x,\mu,E) \; + $$
$$\frac{1}{2}\int_0^\infty dE' \int_{-1}^1 d\mu' \Sigma_s\left(x:\mu',E' \to \mu,E\right) \tag{1.2}$$

The idea is to write the unknown ψ (x, μ, E) as an expansion of a finite number of known functions of angle, and since the integration over μ ranges from 1 to -1, the most convenient expansion functions are the Legendre Polynomials. With this in mind

6

$$\psi(x,\mu,E) = \sum_{n=0}^{N} \left(\tfrac{2n+1}{2}\right) \psi_n(x,E) P_n(\mu) \qquad (1.3)$$

The scattering term (i.e., Σ_s (x:μ', $E' \to \mu$, E) usually depends only on the scattering angle, in other words only on the relative direction of travel not on the absolute direction of travel. Thus this term can be written as

$$\Sigma_s(x,\mu_0,E' \to E) = \sum_{n=0}^{N} \left(\tfrac{2n+1}{2}\right) \Sigma_{sl}(x,E' \to E) P_l(\mu_0) \qquad (1.4)$$

where $\mu_0 = \cos\theta = \mu' \cdot \mu$ represents the scattering angle.

Now these expressions can be placed in the original transport equation, equation 2, then multiplied by Legendre polynomials of various orders, namely, P_l, $l = 1, 2, ...N$, and integrated over the angular variable. At this point the orthogonality, recurrence relations, and additive properties of the spherical harmonics [15-22] can be used to obtain the expressions:

$$\frac{d\psi_1(x,E)}{dx} + \Sigma_t(x,E)\psi_0(x,E) = S(x,E) + \int_0^\infty dE' \Sigma_{s0}(x:E' \to E) \qquad (1.5)$$

for $l = 0$, and

$$\frac{(l+1)}{(2l+1)} \frac{\partial \psi_{l+1}}{\partial x} + \frac{l}{(2l+1)} \frac{\partial \psi_{l-1}}{\partial x} \Sigma_t(x,E)\psi_l(x,E) = \int_0^\infty dE' \Sigma_{sl}(x,E' \to E)\psi_l(x,E') \quad (1.6)$$

for $l = 1, 2, 3, ...$

The angular components of the differential scattering cross section are defined as

$$\Sigma_{sl}(x, E' \rightarrow E) = \int_{-1}^{1} d\mu_0 \, \Sigma_s(x, E' \rightarrow E, \mu_0) P_l(\mu_0) \qquad (1.7)$$

The boundary conditions, which cannot be imposed exactly due to previous approximations, can still be approximated by Marshak-type boundary conditions. For instance a vacuum condition, which otherwise can be represented as $\psi(a, \mu, E) = 0$, can be represented as

$$\sum_{n=0}^{N} \left(\tfrac{2n+1}{2}\right) \psi_l(a, E) \int_0^1 P_l(\mu) P_n(\mu) d\mu = 0 \qquad (1.8)$$

for $l = 1, 3, \dots N$. Similar expressions can be found for reflective, incident flux, and other boundary conditions.

In order to force closure of the equations, and thus obtain the P_n approximation, the last term ψ_{N+1} is dropped and what is left is a set of $N + 1$ coupled integrodifferential equations in space and energy. These equations can now be solved numerically by approximating the spatial derivatives with finite difference schemes, and the energy dependence can be implemented with multigroup techniques.

It is very important to mention that the P_1 approximation leads to the well known and widely used diffusion theory. The P_1 expansion (ignoring energy dependence for the purpose of illustration) yields

8

$$\frac{d\psi_1(x)}{dx} + (\Sigma_t - \Sigma_{s0})\psi_0(x) = S \tag{1.9}$$

$$\frac{1}{3}\frac{d\psi_0(x)}{dx} + (\Sigma_t - \Sigma_{s1})\psi_1(x) = 0 \tag{1.10}$$

solving for ψ_1 in (1.9) then substituting it in (1.10)

$$-\frac{d}{dx}\left(D\frac{d\psi_0(x)}{dx}\right) + (\Sigma_t - \Sigma_{s0})\psi_0(x) = S \tag{1.11}$$

where $D = [3\Sigma_{tr}]^{-1}$, and $\Sigma_{tr} = \Sigma_t - \Sigma_{s1}$. The multidimension extension of this equation is

$$-\nabla \cdot D \nabla \psi_0(x) + (\Sigma_t - \Sigma_{s0})\psi_0(x) = S \tag{1.12}$$

This is the well known diffusion equation.

When the spherical harmonics method is applied to two and three dimensions, the expansion terms become extremely complicated. However, Stacey et al. [23] have shown the possibility of reformulating the spherical harmonics equations as an extended diffusion theory and then extending it to multidimensions as above. Other methods are preferable when dealing with problems of higher dimension. One such method is the discrete ordinates or S_n method. The spherical harmonics method has been studied in great detail by many authors and on some occasions it has been applied to neutral particle transport in fusion plasmas [24]; references 15-22 are a good starting point for the reader interested in the subject.

1.3.3 Discrete Ordinates Method

The discrete ordinates method had its origin in radiation transport calculations in stellar atmospheres. Since then, the method has evolved and is now used extensively in reactor analysis calculations in situations where the diffusion theory has proved to be inadequate [17]. It has therefore become the dominant method for obtaining numerical solutions to the integrodifferential form of the transport equation. To put it simply, this method consists of evaluating the angular distribution of the neutral flux at discrete angular directions or ordinates. This is the prime characteristic that differentiates this method from the spherical harmonics method, in which the angular variable is treated as continuous. In principle, the solution of the transport equation can be found to a high degree of accuracy simply by taking enough discrete ordinates. Although the method is conceptually simple, it requires careful tracking in order to preserve particles. If every step is done correctly, the method leads to computer algorithms of high efficiency [17].

In the most general case, the total angular dependence of $\psi(r, \mu, E)$ is eliminated by taking a discrete number of directions, i.e., μ_v (n = 1, 2, 3,..., N) where $\mu_v = i\mu_{xn} + j\mu_{yn} + k\mu_{zn}$ where i, j, k represent the unit vectors in the x, y, and z direction. Therefore, the unknown function becomes $\psi(r, \mu_n, E)$. In this way the integral over μ is now represented by a summation

$$\int_{-1}^{1} d\mu\, \psi(r, \mu', E') \cong \sum_{n=1}^{N} w_n\, \psi(r, \mu, E) \tag{1.13}$$

where the w_n are quadrature weights for the particular numerical integration scheme used to handle the angular integrals. Since the values of the μ_{in} are not unique, the main factors that determine the choice of directions are the physical insights of the problem and the experience. For the one-dimensional and the time independent transport equation, this treatment leads to

$$\mu_{xn} \frac{\partial \psi(x, \mu_n, E)}{\partial x} + \Sigma_t(x, E)\psi(x, \mu_n, E) = S(x, \mu_n, E) +$$
$$\frac{1}{2} \sum_{n'=1}^{N} \int_0^\infty dE'\, w_n\, \Sigma_s(x, \mu_{n'} \to \mu_n, E' \to E)\psi(x, \mu_{n'}, E') \tag{1.14}$$

This forms a set of N-coupled differential equations which, with the corresponding boundary conditions, can be solved by replacing the energy variable with a sum over a finite number of energy groups, and by making use of finite difference approximations to approximate the spatial derivatives. The implementation of the method is rather long, but the N-coupled differential equations can be solved on almost any computer.

The selection of the quadrature weights, w_n, and of the directions cosines, μ_v, are important when assessing the accuracy of the solutions of these equations. It is customary to obey the following requirements when selecting these quantities [19]:

1) w_n is always positive. This requirement arises from the intrinsic nature of the integral term in equation (1.2); i.e. its value is always positive.

2) Since particle flow is equally important in both positive and negative directions, then it is the norm to make a symmetric choice of quadrature weights and of directions about $\mu = 0$. Thus

$$\mu_n = -\mu_{N+1-n} \qquad \text{and} \qquad w_n = w_{N+1-n}$$

If N is even, then at a reflective boundary, (e.g. at $x = 0$, $\psi_n(0) = \psi_{N+1-n}(0)$ for $n = 1$, 2, ... N/2) and at a vacuum boundary (e.g. at $x = a$, $\psi_n(a) = 0$, for $n = N/2 + 1$, $N/2 + 2$, ... N). Therefore, an even value for N will automatically provide the correct number of boundary conditions for the set of N-coupled differential equations. If N is odd then the direction cosine, $\mu = 0$, would be perpendicular to the x axis, which implies that the derivative term vanishes.

In closing, it is important to mention that it is possible to establish a relationship between discrete ordinates and spherical harmonics. Unfortunately this equivalence breaks down when treating complex multidimensional configurations. This method, though powerful, has been applied to a limited number of geometries (slabs, cylinders, and spheres). Unfortunately, plasma edge and divertor regions are geometrically complex, thus it is doubtful that the discrete ordinates method will be useful. This particular method has been studied in great detail [15-22], and has been used in geometrically simple neutral transport calculations in the past [25-28], but is not presently used in neutral calculations in the more complex divertor geometries. It is also important to mention that differential transport methods in general (i.e., discrete ordinates, spherical harmonics, etc.) have two shortcomings in treating plasma edge problems; 1) in order to achieve accuracy and

numerical stability it is required that the mesh spacing be smaller than the mean free path. This is a serious limitation in regions such as near the divertor plate where the mean free path can be a few millimeters, 2) they are not well suited for treating regions with a long mean free path (e.g., private flux regions, near-vacuum regions near the walls of a tokamak).

In the treatment of the S_n and P_n computational methods, the errors are systematic. For instance there are uncertainties in the cross section data, and there are errors associated with the discretization of the angle-space-time-energy of the phase space, not to mention that with rare exceptions these methods do not allow the full representation of three dimensional geometries. Thus, much effort in these methods is spent on improving the computational time and accuracy, and less on trying to represent the complexity of three dimensional configurations [16].

1.3.4 Monte Carlo Method

An alternative approach to solving the Boltzmann equation is to use the Monte Carlo Method. This method, first applied to neutron transport studies, found its way into the analysis of the problem of neutral particle transport after several modifications of techniques employed in neutron transport were made. The Monte Carlo method, unlike the previous methods, is capable of representing in a straightforward way very complex geometries (such as plasma and divertor chambers). Also, aside from uncertainties in the cross section data, the errors in Monte Carlo calculations take the form of stochastic uncertainties. The Monte Carlo method is, in a basic sense, the simulation of a large but

finite number of particle histories (in this case neutral particles) created by the use of a random number generator. For each history created, one or more random numbers are used to sample the appropriate probabilities distributions for energy, angles, path length, reaction types (charge-exchange, ionization, recombination, etc.), and so on. In fact, there is no need to make use of the transport equation for the most basic operations; the only thing needed is a complete (or even sufficiently accurate) mathematical description of the probability distributions that govern the stochastic variables in the problem in question. The final accuracy of the results attained with this method can be thought of as a function of the inadequacies of the physical model used, the uncertainties of the cross section data, and the inherent statistical nature of the method. Since the magnitude of the statistical error is inversely proportional to the square root of the number of particle histories generated, increasing the number of histories reduces the uncertainty in the final solution. This imposes a computational penalty on the time necessary for the analysis of the problem of interest. Nevertheless, this method has been used considerably in the computation of neutral particle transport, including the outer regions of a diverted tokamak plasma.

Today's most powerful and extensively used Monte Carlo neutral codes in edge plasma calculations are DEGAS, EIRENE, and NIMBUS. The DEGAS code (the latest version is DEGAS2) was originally developed in 1982 by Princeton Plasma Physics Laboratory (PPPL); it has three-dimensional capabilities and enables the treatment of multiple hydrogen, H_2, helium and hydrocarbons [2, 5]. The EIRENE code, used mainly in Europe, is capable of treating, in three dimensions, multiple hydrogen and H_2 [2]. NIMBUS was

introduced in 1983 by Cupini et al. from NET and is capable of handling the three-dimensional treatment of D-T and H_2 [2, 29].

In closing, it is important to remember that the Monte Carlo method also provides a way to explore new parameters, as well as a means for validating the S_n and P_n methods or any other numerical or analytical method. Monte Carlo has proved to be a useful, highly accurate tool. It is the most widely used tool for the analysis of neutral particle transport in complex configurations when analytical solutions are almost impossible and numerical schemes are extremely time-consuming, and where the computational time is not a restriction. Unfortunately, because of its statistical nature, the iterative treatment of plasma/neutral reactions, often found when a Monte Carlo neutral code is coupled to an edge fluid code, is difficult. Calculations can take anywhere from several hours to several days to complete. References 15-22, 29-31 are a good starting point for the study of this subject.

1.3.5 Integral Transport Methods

The integral transport method (first used in the calculation of periodic flux distributions within the fuel-moderator-coolant cells of infinite reactor lattices) is quite different from the discrete ordinates technique already discussed. Instead of discretizing the angular dependence, the integral methods are based on integrating out the angular dependence of the transport equations. By eliminating the angular dependence, the angular variable can in principle be treated with perfect accuracy. In other words, the level of accuracy is determined by a willingness to evaluate numerically the expressions resulting from the

15

angular integration [17]. Thus, equation (1.2) can be integrated making use of an integrating factor

$$\frac{\partial\left(\psi\, e^{\int_0^l \Sigma_t\, dl}\right)}{\partial l} = e^{\int_0^l \Sigma_t\, dl}\, \bar{S}(x, E, \mu) \tag{1.15}$$

where S represents the scattering term and the external source term. Integration leads to

$$\psi(l, E, \mu) = \int_0^l dl'\, e^{-\int_{l'}^l \Sigma_t\, dl}\, \bar{S}(l', E, \mu) \ + \ e^{-\int_0^l \Sigma_t\, dl}\, \psi(0, E, \mu) \tag{1.16}$$

From this point on the solution is an iterative procedure such that

$$\psi = \sum_{n=1}^{\infty} \psi_n(l, E, \mu) \tag{1.17}$$

where

$$\psi_n(l, E, \mu) = \int_0^l dl'\, e^{-\int_{l'}^l \Sigma_t\, dl}\, \bar{S}(l', E, \mu) + S_{sc}(\psi_{n-1}) \tag{1.18}$$

in which S_{sc}, the secondary source, is the n-1 iteration solution.

Particles of a given source going in a particular direction are exponentially attenuated as the integral of the inverse mean free path along the direction of flight. For a fixed source, the solution to the flux distribution is simply dependent on the geometry of the problem. Unfortunately, if one of the processes by which the neutrals are attenuated (such as charge-exchange or recombination) gives rise to another neutral with a different energy and direction, the process is in itself a secondary neutral source which is uniquely

16

distributed in space. The same is true for processes that become tertiary, and quatertiary, neutral sources. Thus, the solution to the flux distribution becomes an iterative process for which the next iteration step uses an approximate evaluation of the distributed source plus the exact solution of the particle transport from the approximate source. The iteration process becomes time-consuming because couplings exist among all spatial points (something that is inherent to the integral transport formulation). In order to speed up the iteration process, it has become customary to solve for the flux distribution of fixed sources (such as reflection from the wall) and to neglect all secondary sources. This procedure is good in just a few cases, in particular when the ionization rate is greater than the charge-exchange rate. The method becomes impractical for complex geometries and when the rate of processes that result in secondary sources becomes large (such as charge exchange near the wall and divertor plates) [16, 17, 19, 32]. Despite this limitation, the integral transport method has been applied in the edge region of fusion plasmas for simple one-dimensional problems [33].

1.3.6 TEP/ICB Method

The Interface Current method has been used extensively in fission reactor calculations [17, 22]. Recently the one-dimensional Interface Current Balance (ICB) and its two-dimensional extension, the Transmission/Escape Probability (TEP) formulations of integral transport theory, were introduced for the purpose of studying neutral particle transport in the outer regions of diverted tokamaks [32, 34]. The methods were implemented in one-dimensional and two-dimensional monoenergetic neutral transport codes, namely, ICB and

17

GTNEUT. The methods are based on the balancing of particle fluxes/currents across surfaces and internal sources and are capable of treating complex geometries (GTNEUT) including regions of very long as well as short mean free paths. They have the advantage of coupling among contiguous regions in the spatial domain of the problem. This near-neighbor coupling is the main benefit over the typical integral transport formulation where an all-regions coupling exists.

Early studies showed that the TEP/ICB methods can provide an accurate and computationally economical solution of neutral particle transport in diverted tokamak plasmas.

1.4 Conclusions and Objectives

Neutral particle transport is an important issue in the outer region of a diverted tokamak. At this point in time there are no methods that can treat neutral transport in the plasma edge and divertor region with both computational economy and accuracy.

Monte Carlo codes such as DEGAS2, EIRENE, and NIMBUS are the best currently available, and their use yields very accurate results –provided that computational time is not a pressing issue. Other methods (S_n, P_n, etc.) are limited by their inability to treat the complex geometrical configurations and widely varying mean free paths found in the plasma edge and divertor region.

The recently introduced TEP method is promising in its ability to provide both accuracy and speed in treating problems with complex geometry and widely varying mean free paths. The ability of the method to handle neutral transport in complex configurations,

along with its versatility while treating long and short mean free path regions (a characteristic that no other method has), makes it very attractive. Moreover, the results obtained with a preliminary version TEP-based code, GTNEUT, are in good agreement with those obtained with DEGAS, and they were generated at a fraction of the computation time. Thus, this method has the two potential qualities –time economy and accuracy— that no other methods have been able to attain.

A major purpose of this thesis is to investigate the validity of the basic transport assumptions of the TEP/ICB methodology. The accuracy of a number of approximations made in the implementation of the methodology are evaluated by comparing them with Monte Carlo. The thesis also presents correction factors which improve the accuracy of the method. In addition, this work compares the TEP-based code GTNEUT with Monte Carlo calculations for a number of diverted tokamak plasma models in order to evaluate the adequacy of the TEP method in its current state of development, for realistic neutral particle transport calculations in the edge and divertor plasma regions in tokamaks. Finally, it compares the TEP calculation with Monte Carlo and experimental results for neutral densities in the DIII-D tokamak.

CHAPTER II

ICB/TEP TRANSPORT METHODOLOGY

2.1 Introduction

Commonly used in reactor core calculations [17, 22, 37-40], integral transport methods have been used for the calculation of neutral particle transport in the edge regions of fusion plasmas [33]. The purpose of this chapter is to review the Interface Current Balance (ICB) [34] formulation of integral transport theory and to demonstrate that when extended to multidimensions, the method is equivalent to the Transmission and Escape Probability (TEP) method [32].

2.2 Interface Current Balance: 1D Transport Methodology

The purpose of this section is to describe the one-dimensional Interface Current Balance and the two-dimensional Transmission/Escape Probabilities formulations of integral transport theory [33, 41].

Let $J^{+/-}$ represent the partial currents going forward and backward in a slab region bounded by surfaces i and $i+1$ as shown in figure 2.1. In addition, let μ be the cosine of the angle that the particle makes with the direction of travel (i.e., along the x axis). Furthermore, assume that 1) the region Δ_i can be characterized by a uniform total cross section Σ_{ti}; 2) the incident angular fluxes at surfaces i and $i + 1$ are isotropically distributed in half space (i.e. double P_0 approximation); 3) both charge-exchange and scattering of neutrals result in an isotropic directional distribution, and that 4) the distribution of first-

collided, second-collided, or n-collided particle sources is uniform over the region.
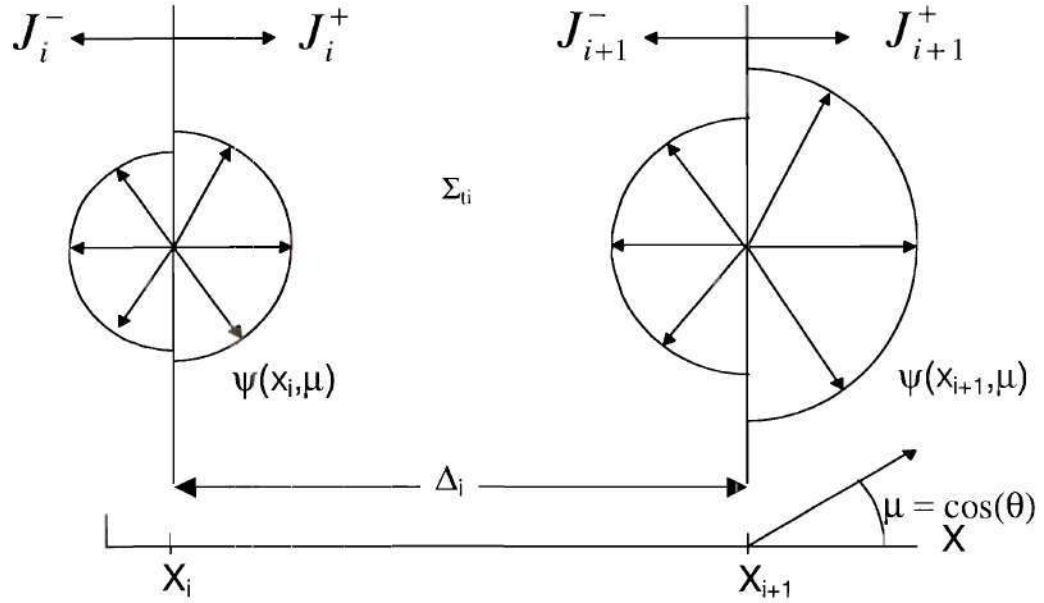
Figure 2.1. Interface current model schematic in 1D slab geometry.

The emerging partial currents through surfaces i and $i+1$ can be expressed as the sum of incident partial currents and of any internal sources present in the region. Thus, the interface current balance over the interval Δ_i can be expressed as

$$J_{i+1}^+ = T_i J_i^+ + R_i J_{i+1}^- + \frac{1}{2} s_i P_i + \left(s_i^+ - \frac{1}{2} s_i \right) P_{oi}$$

$$J_i^- = T_i J_{i+1}^- + R_i J_i^+ + \frac{1}{2} s_i P_i + \left(s_i^- - \frac{1}{2} s_i \right) P_{oi}$$

(2.1)

where T_i represents the total transmission probability which can be written as the sum of

the first flight or uncollided transmission probability T_{oi}, and the total reflection probability R_i

$$T_i = T_{0i} + R_i \tag{2.2}$$

With reference to figure 2.1, the first flight transmission probability T_{oi} can be defined as the ratio of the uncollided partial current at x_{i+1} over the total incident current at x_i,

$$T_{0i} = \frac{J^+_{unc}(x_{i+1})}{J^+_{total}(x_i)} = \frac{J^+_{unc}(x_{i+1})}{J^+_i} \tag{2.3}$$

It can be shown that if the neutral particle distribution function at x_i varies as $f(x_i, \mu) \sim \mu^n$, then

$$T_{0i} = (n+2)E_{n+3}(\Delta_i \Sigma_{ti}) \tag{2.4}$$

where E_n represents the exponential integral function of the nth order[17], namely

$$E_n(z) \equiv \int_0^1 \mu^{n-2} e^{-z/\mu} d\mu \tag{2.5}$$

Thus, for a uniform distribution function (i.e., for an isotropic incident flux) $f(x_i, \mu) \sim \mu^0$, $T_{oi} = 2E_3$. For a cosine distribution function (i.e., cosine distributed incident flux), $f(x_i, \mu) \sim \mu^1$, $T_{oi} = 3E_4$, etc. If there is an isotropic surface source at x_i, then $f(x_i, \mu) \sim \mu^{-1}$ and the transmission probability is $T_{oi} = E_2(\Delta_i \Sigma_{ti})$.

The total reflection probability R_i, in equation 2.2, is defined as

$$R_i = \tfrac{1}{2} c_i P_i \left(1 - 2E_3 \left(\Delta_i \Sigma_{ti} \right) \right) \tag{2.6}$$

The quantity P_i in equation (2.6) represents the total escape probability (i.e., includes all the generations of charge-exchange and elastic scattering), which is a function of the first flight escape probability P_{0i} (for the case of an isotropic collision rate distribution within the slab region) and of the fraction c_i of the collision rate that is due to scattering and/or charge-exchange (i.e., to events which do not remove the particle). This fraction of particles forms a source of once-collided particles, and it is assumed to have a uniform as well as an isotropic distribution (isotropic in this case means half the particles exit to the right and half exit to the left). Thus,

$$P_i \equiv P_{0i} \sum_{n=0}^{\infty} \left[c_i \left(1 - P_{0i} \right) \right]^n = \frac{P_{0i}}{1 - c_i \left(1 - P_{0i} \right)} \tag{2.7}$$

where the first flight escape probability P_{0i} in a slab can be defined as [42]

$$P_{0i} = \frac{1}{\Delta_i \Sigma_{ti}} \left[\frac{1}{2} - E_3 \left(\Delta_i \Sigma_{ti} \right) \right] \tag{2.8}$$

and the charge-exchange and scattering fraction c_i is (in the absence of neutral-neutral scattering and ion impact ionization) equal to

$$c_i = \frac{\langle \sigma v \rangle_{cx} + \langle \sigma v \rangle_{el}}{\langle \sigma v \rangle_{cx} + \langle \sigma v \rangle_{el} + \frac{n_e}{n_i} \langle \sigma v \rangle_{ion}} \tag{2.9}$$

23

where the $\langle \sigma v \rangle_{xx}$ represent the reaction rates, averaged over the Maxwellian distributions of both ions and neutrals, for the processes of charge-exchange, cx, elastic scattering, $el.$, and over the electron distribution for the ionization process, ion.

Solving for J_i^+ in the first of equation of (2.1) and substituting the result into the second equation leads to a matrix relation between the partial currents at adjacent surfaces

$$\begin{bmatrix} J_i^+ \\ J_i^- \end{bmatrix} = \begin{bmatrix} \left(T_i^{-1}\right) & \left(-T_i^{-1}R_i\right) \\ \left(R_iT_i^{-1}\right) & \left(T_i - R_iT_i^{-1}R_i\right) \end{bmatrix}\begin{bmatrix} J_{i+1}^+ \\ J_{i+1}^- \end{bmatrix} + \frac{1}{2}s_i\left\{ P_i\begin{bmatrix} -T_i^{-1} \\ 1 - R_iT_i^{-1} \end{bmatrix} + P_{oi}\begin{bmatrix} -T_i^{-1}\left(s_i^+ - \frac{1}{2}s_i\right) \\ \left(s_i^- - \frac{1}{2}s_i\right) - R_iT_i^{-1}\left(s_i^+ - \frac{1}{2}s_i\right) \end{bmatrix} \right\} \tag{2.10}$$

This representation has the form of the response matrix formalism [17, 22] of neutron transport theory. The solution for this representation is obtained by simply sweeping from one boundary of the problem to the other in an iterative fashion.

The ionization rate can be calculated by balancing the currents over the interval Δ_i, thus

$$I_i = \frac{(1 - c_i)\left(\left(J_i^+ + J_{i+1}^-\right)(1 - T_{0i}) + S_i(1 - P_{0i})\right)}{\left(1 - c_i(1 - P_{0i})\right)} \tag{2.11}$$

The main advantage of the ICB formulation over integral transport methods lies in its discretization scheme, which results in coupling between next neighboring regions rather

24

than, the coupling all regions of the problem.

2.2.1 Boundary Conditions in Slab Geometry

There are three easily identifiable boundary conditions that can be imposed on the left most surface of figure 2.1 (i.e., x = 0, $i = 0$). These are: 1) $J_0^+ = \Gamma_{in}$ if a known current of particles Γ_{in} is incident from the left; 2) the incident current $J_0^+ = 0$ if a vacuum or a nonscattering medium exists for x < 0; and 3) when a source-free scattering medium exists for x < 0, the boundary condition can be adequately expressed as an albedo condition of the form $J_0^+ = \alpha \, \Gamma_0^-$ where α represents the albedo and Γ_0^- the current across the left surface.

2.2.2 Generalization of 1D Methodology

Extending the ICB methodology to higher dimensions is straightforward. Let $J_i^+ = J_i^{in}$, $J_i^- = J_i^{out}$, $J_{i+1}^+ = J_{i+1}^{out}$, and $J_{i+1}^- = J_{i+1}^{in}$. Let also

$$
\begin{aligned}
\Lambda_{i+1}^s s_i P_i &= \tfrac{1}{2} s_i P_i + \left(s_i^+ - \tfrac{1}{2} s_i\right) P_{oi} \\
\Lambda_i^s s_i P_i &= \tfrac{1}{2} s_i P_i + \left(s_i^- - \tfrac{1}{2} s_i\right) P_{oi}
\end{aligned}
\tag{2.12}
$$

where Λ_i^s represents the fraction of escaped particles exiting through surface i and Λ_{i+1}^s represents the fraction of particles exiting through surface $i + 1$. With the help of equations (2.2), (2.4), and (2.6-2.8), it is possible to cast equation (2.1) into

$$J_{i+1}^{out} = T_{oi}J_i^{in} + (1 - T_{oi})(J_i^{in} + J_{i+1}^{in})c_iP_i\Lambda_{i+1} + \Lambda_{i+1}^s s_iP_i$$
$$J_i^{out} = T_{oi}J_{i+1}^{in} + (1 - T_{oi})(J_i^{in} + J_{i+1}^{in})c_iP_i\Lambda_i + \Lambda_i^s s_iP_i$$

$$(2.13)$$

It is now clear that the exiting current across surface i or $i + 1$ is made up of three quantities: 1) the inward current across the surface in question times the probability T_{0i} that the particle traversed the region uncollided and exited through this surface; 2) the inward current across the bounding surfaces of the region times the collision probability $(1 - T_{0i})$ times the probability c_i that the first collision was a scattering event times the total escape probability P_i from region i times the directional probability Λ that the escaping particle moves across the given surface; 3) any internal source of particles s_i within the region times the total escape probability P_i from region i, times the directional probability Λ^s that the escaping particle crosses the surface in question.

2.3 Two-Dimensional Extension of the Interface Current Balance Method

In the two-dimensional configuration shown in figure 2.2, the generalization of equation (2.13) to two dimensions is done simply by writing the partial current from region k into i as J_{k-i}. The uncollided probability for particles going from region k to j through region i can be denoted by T_{0i}^{kj}. Finally, Λ_{ij} can represent the probability that a particle born or scattered in region i can go into region j. Thus, the partial current from region i into region j, J_{i-j} can be obtained by summing over all regions k adjacent to region i, namely

26

$$J_{i-j} = \sum_k^i T_{oi}^{kj} J_{ki} + \sum_k^i \left(1 - \sum_l^i T_{oi}^{kl}\right) J_{ki} c_i P_i \Lambda_{ij} + \Lambda_{ij}^s s_i P_i \qquad (2.14)$$

$$J_{ki} T_{0i}^{kj} \qquad\qquad c_i P_i \Lambda_{ij} J_{ki} \left(1 - \sum_l^i T_{0i}^{kl}\right)$$
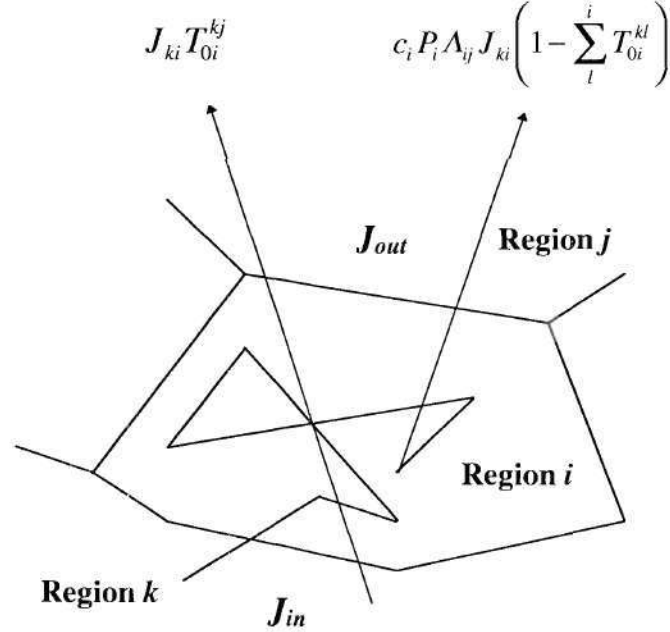
Fig. 2.2. Interface current model nomenclature in 2D slab geometry.

Once again, the three terms in the equation above represent:

1) the sum of the currents entering region i from all adjacent regions times the probability that the particle will exit region i into region j without a collision;

2) the sum of the currents entering region i from all contiguous regions times the total escape probability P_i that the particles escape region i after one or more scattering (including charge-exchange) collision times the probability c_i that the first collision was a scattering event, times the probability Λ_{ij} that the scattered particle escaping from region i goes into region j;

3) any internal source of particles in region i (e.g. recombination), times the escape

27

probability P_i, that the particle in region i escapes into region j times the probability Λ^s_{ij} that the escaping source particle will enter region j.

Equation (2.14) is nothing more than a balance of currents over k regions, and in order to solve it, the first flight transmission and first flight escape probabilities must be calculated. For this reason, the higher dimensionality of the ICB formulation is commonly referred to as the transmission and escape probability method (TEP).

The ionization rate in each region can be calculated by taking into account the ionization of any external neutral sources and of the collided fraction of neutrals flowing into the region of interest from all adjacent regions [32]. Thus

$$I_i = \frac{\left[S_i \left(1 - P_{0i} \right) + \sum_k^i J_{k-i} \left(1 - \sum_l^i T_{0i}^{ki} \right) \right] \left[1 - c_i \right]}{\left(1 - c_i \left(1 - P_{0i} \right) \right)} \qquad (2.15)$$

The neutral particle balance in region i can be obtained from the balance of fluxes and of internal sources, thus

$$N_i = \frac{\left[S_i - \sum_k^i \left(J_{k-i} - J_{i-k} \right) \right]}{N_{ion} \langle \sigma v \rangle_{ion}^i} \qquad (2.16)$$

28

2.4 Transmission Probabilities in Two-Dimensional Geometries [41]

Consider a region with volume V_i with a plane cross section (x-y) as the one shown in figure 2.3, in which the z direction is normal to it. Let also figure 2.4 represent the three-dimensional and vertical projections of figure 2.3. The location ξ_1 in figure 2.3 can be identified as the projection onto the horizontal plane of the vertical axis shown in figure 2.4. The corresponding differential solid angle in this coordinate system is given by

$$d\Omega = \frac{1}{4\pi} \sin\theta' \, d\theta' \, d\phi = -\frac{1}{4\pi} \cos\theta \, d\theta \, d\phi \qquad (2.17)$$
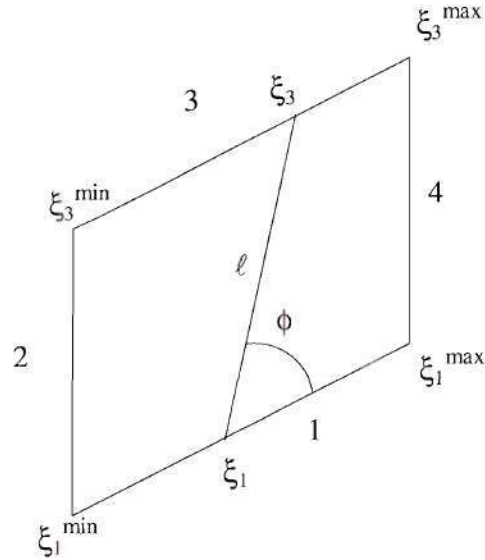
Figure 2.3 Planar projection of geometry for the calculation of the transmission probability in 2D.
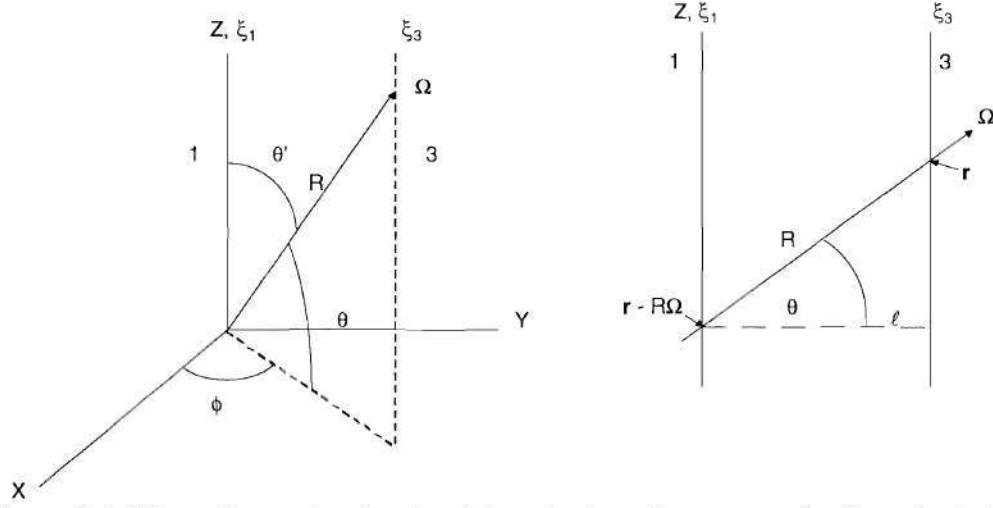
Figure 2.4 Three-dimensional and axial projection of geometry for the calculation of the transmission probability in 2D.

The incident directional flux $\psi(\mathbf{r} - R\Omega,\Omega)$ out of volume V_1 at location ξ_1 is attenuated

when it traverses the distance R to reach the location ξ_2 before going into volume V_3

$$\psi\left(\mathrm{r},\Omega\right) = \psi\left(\mathrm{r} - R\Omega,\ \Omega\right) e^{-\Sigma R} \tag{2.18}$$

The incident partial current density (#/cm^2-s) out of volume V_1 at location ξ_1 is given by

$$
\begin{aligned}
j_{in}\left(\xi_1\right) &= \int_{n_{in}\cdot\Omega>0} d\Omega\ \left(\mathrm{n}_{in}\cdot\Omega\right)\ \psi\left(\mathrm{r}-R\Omega\right) \\
&= -\frac{1}{4\pi}\int_0^\pi d\phi \int_{-\pi/2}^{\pi/2} d\theta\ \cos^2\theta\ \sin\phi\ \psi\left(\mathrm{r}-R\Omega\right)
\end{aligned}
\tag{2.19}
$$

where $\mathbf{n}_{in}\cdot\Omega = \cos\theta\sin\phi$ was used. If the incident flux is isotropic in the incident hemisphere

(double-P_0 approximation), equation (2.19) reduces to

$$j_{in}^{iso}(\xi_1) = \frac{1}{4}\psi(\mathbf{r} \cdot R\Omega) \tag{2.20}$$

By multiplying equation (2.19) by the (arbitrary) axial dimension H and integrating over $\xi_1^{min} \leq \xi_1 \leq \xi_1^{max}$, the incident partial current (#/s) is obtained, namely

$$J_{in} = H \int_{\xi_1^{min}}^{\xi_1^{max}} d\xi_1 \, j_{in}(\xi_1) \tag{2.21}$$

The contribution to the current into volume V_3 from incident neutrals from volume V_1 which entered volume V_i at location ξ_1 within the solid angle subtended by volume V_3, and traversed volume V_i uncollided to entered volume V_3 is given by

$$\begin{aligned}
J_{out} &= H \int_{\xi_1^{min}}^{\xi_1^{max}} d\xi_1 \int_{\substack{(\Omega \cdot \vec{n}_{out}))0 \\ \phi(\xi_1) \ni 3}} d\Omega \, (\Omega \cdot n_{out}) \, \psi(r - R\Omega, \Omega) \, e^{-\Sigma R} \\
&= \int_{\xi_1^{min}}^{\xi_1^{max}} d\xi_1 \int_{\phi_{min}(\xi_1)}^{\phi_{max}(\xi_1)} d\phi \int_{-\pi/2}^{\pi/2} d\theta \, \cos^2\theta \, \sin\phi \, e^{-\frac{\Sigma l(\phi(\xi_1))}{\cos\theta}} \psi(r - R\Omega, \Omega)
\end{aligned} \tag{2.22}$$

where $\mathbf{n}_{out} \cdot \Omega = cos\theta sin\phi_{out}$ (note that if the interfaces of volume V_i with volumes V_1 and V_3 are not parallel, $\mathbf{n}_{out} \cdot \Omega$ is not necessarily equal to $\mathbf{n}_{in} \cdot \Omega = cos\theta sin\phi$) and $\phi(\xi_1) \ni 3$ indicates angles ϕ from a point ξ_1 which intersect the interface with region 3. If the incident flux out of volume V_1 is isotropic in the incident directional hemisphere, equation 2.22 reduces to

$$J_{out}^{iso} = \frac{H}{2\pi} \int_{\xi_1^{min}}^{\xi_1^{max}} d\xi_1 \int_{\phi_{min}(\xi_1)}^{\phi_{max}(\xi_1)} d\phi \int d\phi \, \sin\phi_{out} \, Ki_3\left(\Sigma l(\phi(\xi_i))\right) \psi(r - R\Omega) \tag{2.23}$$

31

Therefore, the transmission probability for an isotropic incident flux distribution out of volume V_1, uniformly distributed over $\xi_1^{min} \leq \xi_1 \leq \xi_1^{max}$, can be expressed as the ratio of the incident partial current out of volume V_i over the incident partial current entering volume V_i.

$$T_{0i}^{13} \equiv \frac{J_{out}^{iso}}{J_{in}^{iso}} = \frac{2}{\pi} \frac{\int_{\xi_1^{min}}^{\xi_1^{max}} d\xi_1 \int_{\phi_{min}(\xi_1)}^{\phi_{max}(\xi_1)} d\phi \, \sin\phi_{out} \, Ki_3\left(\Sigma l\left(\phi(\xi_i)\right)\right)}{\left(\xi_1^{max} - \xi_1^{min}\right)} \tag{2.24}$$

where Ki_n represents the Bickley function of the nth order [17, 43, 44], namely

$$Ki_n(\tau) = \int_0^{\pi/2} d\theta (\sin\theta)^{n-1} e^{\left(\frac{-\tau}{\sin\theta}\right)} \tag{2.25}$$

2.5 Escape Probabilities in Two-Dimensional Geometries

The flux per unit surface area dA normal to the direction of flight at a distance R away from an isotropic point source is $\exp(-\Sigma R)/4\pi R^2$. As shown in figure 2.4, the surface area normal to the direction Ω of neutral travel is $dA = Rd\theta l d\phi = l^2 d\theta d\phi/\cos\theta$. Consequently, in regard to figure 2.5, the outward current of uncollided neutrals over the surface labeled ξ_2 into volume V_3 that is produced by an isotropic source of unit strength per axial length located at $\mathbf{r}_i$ within volume V_i is

$$J_{out}^3(r_i) = \int_{A \supset S_3} (n_{out} \cdot \Omega) \frac{e^{-\Sigma R} dA}{4\pi R^2}$$

$$= \int_{A \supset S_3} d\phi \int_{-\pi/2}^{\pi/2} d\theta \, (\cos\theta \sin\phi_{out}) \frac{e^{\frac{-\Sigma l(\phi)}{\cos\theta}} \left(\frac{l^2}{\cos\theta} \right)}{4\pi \left(\frac{l}{\cos\theta} \right)^2}$$

$$= \int_{A \supset S_3} d\phi \, \sin\phi_{out} \frac{1}{2\pi} \int_0^{\pi/2} d\theta \, \cos^2\theta \, e^{\frac{-\Sigma l(\phi)}{\cos\theta}}$$

$$= \int_{A \supset S_3} d\phi \, \sin\phi_{out} \frac{Ki_3(\Sigma l(\phi))}{2\pi}$$

(2.26)

where $\phi \supset S_3$ indicates the range of $\phi_{min} < \phi < \phi_{max}$ subtended by side S_3 at location $\mathbf{r}_i$ within volume V_i.
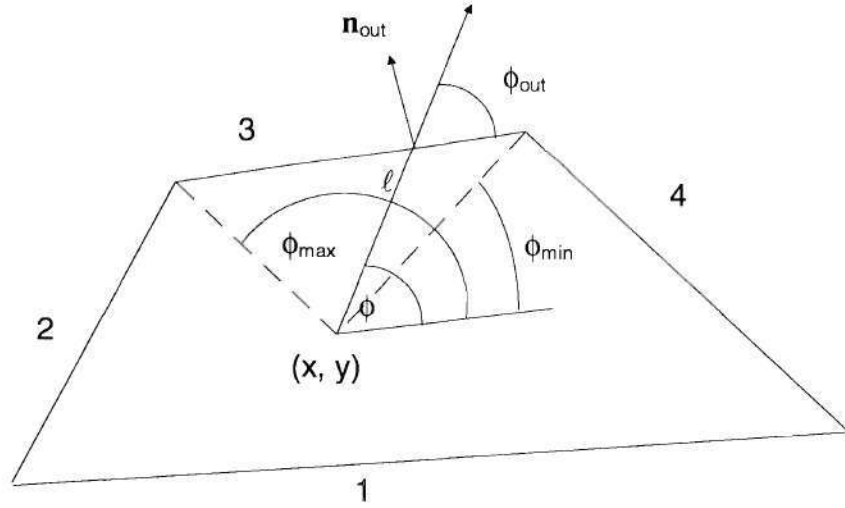
Figure 2.5 Planar projection of geometry for the calculation of the escape probability in 2D.

The probability that an isotropic, uniform neutral source s_i will produce an uncollided current $s_i \Lambda^s_{i3} P_{oi}$ from volume V_i into volume V_3 is the same as the average value of $J^3_{out}(x,y)$ over the planar 2D area A_i of volume V_i

$$
\begin{aligned}
\Lambda_{i3} P_{0i} &= \frac{1}{A_i} \int_{A_i} dx\, dy\, J^3_{out}(x,y) \\
&= \frac{1}{A_i} \int_{A_i} dx\, dy \int_{\phi \supset S_3} d\phi\, \sin\phi_{out} \frac{Ki_3\big(\Sigma l(\phi)\big)}{2\pi}
\end{aligned}
\tag{2.27}
$$

The correct value of $\mathbf{n}_{out}$ is the outward normal to the surface in question, and ϕ_{out} is measured against the orientation of that surface. In contrast ϕ may be measured with respect to a fixed coordinate system. This means that usually $\phi_{out} \neq \phi$, although it simplifies matters to orient the coordinate system so that $\phi_{out} = \phi$.

The total uncollided escape probability, or first flight escape probability, is obtained by adding the contributions from equation (2.27) for all volumes V_k that are adjacent to volume V_i

$$
P_{0i} = \sum_k \Lambda_{ik} P_{0i}
\tag{2.28}
$$

and the directional escape fractions can be calculated from

$$
\Lambda_{ij} = \frac{\Lambda_{ij} P_{0i}}{P_{0i}} = \frac{\Lambda_{ij} P_{0i}}{\sum_k \Lambda_{ik} P_{0i}}
\tag{2.29}
$$

2.5.1 Approximations for the First Flight Escape Probability

A more general expression for the probability that a neutral particle born uniformly and isotropically in a convex body B (shown in figure 2.6) will escape uncollided (i.e., equation 2.27) is given by [19, 42, 45]

$$P_o = \frac{\lambda}{\bar{l}_s} \int \left(1 - e^{l_s/\lambda}\right)\phi(l_s)dl_s = \frac{\lambda}{\bar{l}_s} - \int e^{-l_s/\lambda}\phi(l_s)dl_s$$

(2.30)
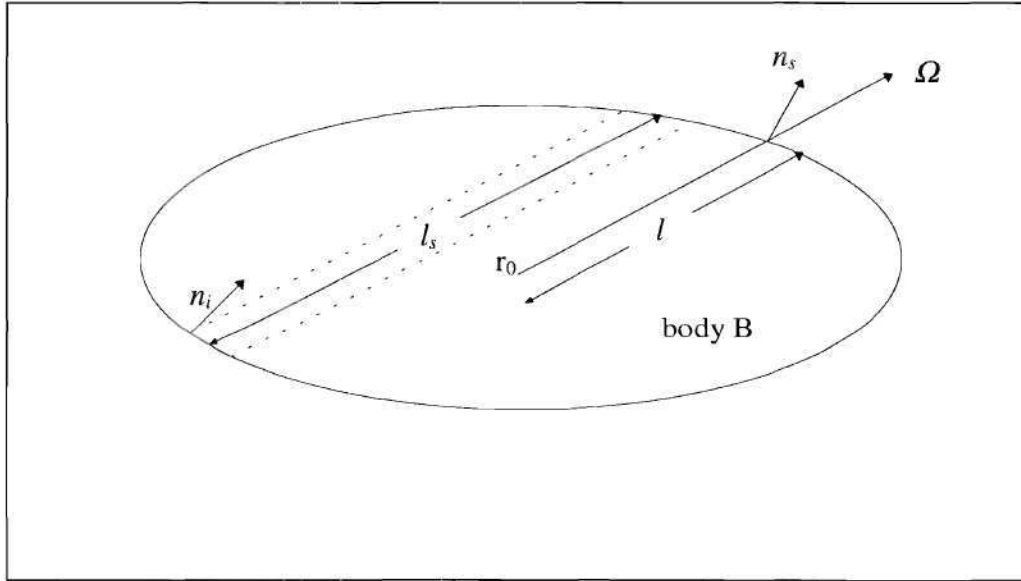
Figure 2.6. Escape probability from a convex body.

where $\phi(l_s)$ denotes the chord distribution function of the body in question and $\bar{l}_s$ is equal to the mean chord length. The main problem in computing (2.30) lies in the fact that it is very difficult to find an exact expression for the chord distribution function. These are

known only for a handful of basic geometries such as slabs, spheres, and cylinders. Thus, it is practically impossible to evaluate this integral analytically. Many approximations to the first flight escape probability have been made using series expansions, treating the integral in its corresponding limits, polynomials expansions, numerical tabulations for different geometries, etc. The first approximation to equation (2.30) was based on physical considerations. For instance, if the dimensions of the body are smaller than the mean free path, the exponential term inside the integral can be expanded. Subsequently, equation (2.30) reduces to

$$P_0 \cong 1 - \frac{1}{2} \frac{\overline{\left(l_s^2 \right)}}{\overline{l_s} \lambda} \approx 1 \qquad (2.31)$$

The physical interpretation of this expression means that all particles will tend to escape from the body. Conversely, if the dimensions of the body are greater than the mean free path, the exponential term inside the integral vanishes, meaning that physically all particles will have a very small chance of escaping the body. Thus, equation (2.30) reduces to

$$P_0 \cong \frac{\lambda}{\overline{l_s}} = \frac{\lambda S}{4V} \qquad (2.32)$$

These observations lead Wigner et al. [46] to introduce a simple approximation to equation (2.30), namely, a rational approximation

36

$$P_0 = \frac{1}{1 + \dfrac{\bar{l}_s}{\lambda}} = \frac{1}{1 + \dfrac{4V}{\lambda S}} = \frac{1}{\left(\dfrac{4V}{\lambda S}\right)} \left(1 - \frac{1}{1 + \dfrac{4V}{\lambda S}}\right) \tag{2.33}$$

where V and S represent the volume and surface area of the body respectively.

It is evident that the rational approximation does not depend on the $\phi(l_s)$, but only on the mean chord length, which in general is $\bar{l} = 4V/S$. Unfortunately, the rational approximation gives errors of up to 18% for intermediate values of $\bar{l}/\lambda = \Sigma\bar{l}$ for the case of a circular cylinder [19, 47-50]. In 1963, Sauer proposed an approach based on the method of chord theory [47]. His approach consisted of deriving from a carefully chosen, one parametric chord distribution function which has the same general properties as the exact chord distribution in the body of interest. A geometric index for the case of a circular cylinder was determined by requiring that the logarithm moment of the exact as well as the approximate chord distribution function be the same. Thus, the Sauer approximation to the first flight escape probability is

$$P_0^{Sauer} = \frac{1}{\Sigma\bar{l}} \left[1 - \frac{1}{\left(1 + \dfrac{\Sigma\bar{l}}{(n+1)}\right)^{n+1}} \right] \tag{2.34}$$

where the parameter n, the geometric index, is equal to 3.58 for the case of an infinite cylinder. Once again, for large $\Sigma\bar{l}$ (i.e., $\lambda \to 0$), Sauer approximation reduces to

37

$$P_0^{Sauer} = \frac{1}{\Sigma \bar{l}} \qquad (2.35)$$

For small $\Sigma \bar{l}$ (i.e., $\lambda \to \infty$), Equation (2.34) can be expanded:

$$P_0^{Sauer} = \frac{1}{\Sigma \bar{l}} \left[1 - \left\{ 1 - \left(\frac{\Sigma \bar{l}}{c} \right) c + \frac{c(c-1)}{2} \left(\frac{\Sigma \bar{l}}{c} \right)^2 + ... \right\} \right]$$
$$= 1 - \frac{(c-1)}{2c} \Sigma \bar{l} \qquad (2.36)$$

It is evident from equation (2.34) that for $n = 0$, Sauer approximation reduces to the original Wigner rational approximation (i.e., equation 2.33).

There are some more recent approximations of the first flight escape probability [47-51]. These involve an expansion of some kind which require the use of a number of constant coefficients. Although these behave similarly to the rational and Sauer approximations for both large and small values of $\Sigma \bar{l}$, they do not show the simplicity and mathematical elegance of the Sauer approximation.

2.6 Total Escape Probability

Once again P_0 represents the probability that a particle can escape from a region without a collision. However, it is also possible that the particle or its progeny can escape after one, two, or n-collisions. For instance, $(1 - P_0)c_i P_0$ represents the probability that a particle escapes after one collision. The particle can escape after two collisions with probability $(1 - P_0)^2 c_i^2 P_0$ and so on. Thus, the total escape probability can be

38

mathematically expressed as

$$P = P_0 \sum_{n=0}^{\infty} \left(c_i \left(1 - P_0 \right) \right)^n = \frac{P_0}{1 - c_i \left(1 - P_0 \right)} \tag{2.37}$$

where $c_i = \dfrac{\langle \sigma v \rangle_{cx} + \langle \sigma v \rangle_{el}}{\langle \sigma v \rangle_{cx} + \langle \sigma v \rangle_{el} + \dfrac{n_e}{n_i} \langle \sigma v \rangle_{ion}}$ represents the fraction of neutrals that have had a

charge-exchange or scattering event.

CHAPTER III

ACCURACY OF FIRST FLIGHT TRANSMISSION

AND ESCAPE PROBABILITIES

3.1 Introduction

The first flight transmission and escape probabilities can, in principle, be calculated exactly. However, several approximations were made in the practical implementation of the TEP/ICB methodology in the interest of computational efficiency. The purposes of this chapter are to evaluate the errors introduced by such approximations and to develop improved approximations or correction factors where needed.

3.2 Accuracy of the First Flight Transmission Probability

3.2.1 First Flight Transmission Probability in a Uniform Region [35, 36]

The expression that defined the first flight transmission probability (i.e., equation 2.24) was derived assuming that the region was represented by uniform temperature and density distributions (i.e., uniform mean free paths). The purpose of this section is to evaluate, by comparison with Monte Carlo codes DEGAS and MCNP4B [5, 52], the accuracy of the algorithm used to calculate T_0. This was evaluated for a variety of regions with a totally ionizing medium, uniform plasma conditions (temperature equal to 10 eVs and density equal to 1.0×10^{19} m^{-3}), vacuum boundary conditions, no internal sources and a cosine distributed source on one of the surfaces. The results that compare the T_0 predicted by TEP-algorithm with Monte Carlo are shown in figure 3.1. The agreement between the

Figure 3.1. First flight transmission probability comparison.
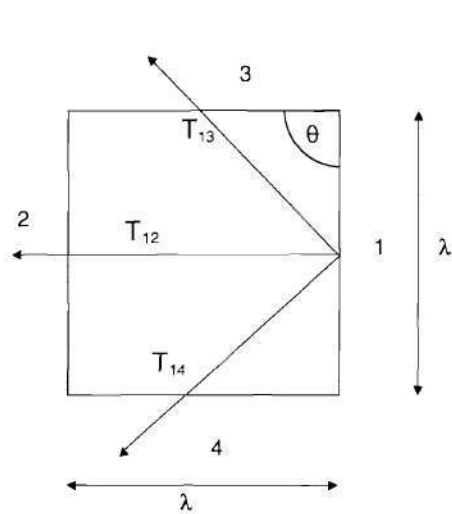
	GTNEUT	Monte Carlo
T_{12}	0.126	0.126
T_{13}	0.161	0.161
T_{14}	0.161	0.159
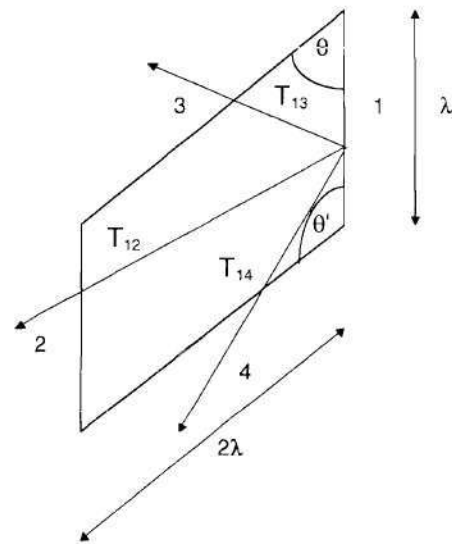
	GTNEUT	Monte Carlo
T_{12}	0.00571	0.00577
T_{13}	0.647	0.647
T_{14}	0.0140	0.0141
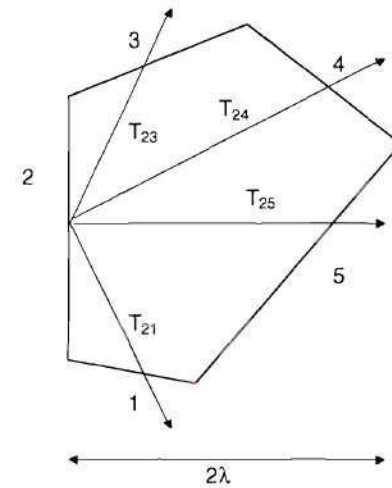
	GTNEUT	Monte Carlo
T_{21}	0.06633	0.0667
T_{23}	0.05086	0.05137
T_{24}	0.02165	0.02154
T_{25}	0.06412	0.06491

two was remarkably good, with an error of less than 1.5%. These validated the reduction of the analytical expression (i.e., equation 2.24) to computational algorithms and coding.

3.2.2 First Flight Transmission Probability in a Nonuniform Region

The expression (2.24) was later evaluated using a mean free path, λ_{av}, calculated at the average plasma parameters to characterize nonuniformities (i.e., temperature or density) in a region. In general

$$T_0 = \frac{2}{\pi} \frac{\int_{\xi_1^{min}}^{\xi_1^{max}} d\xi_1 \int_{\phi_{min}(\xi_1)}^{\phi_{max}(\xi_1)} d\phi \sin\phi \, Ki_3\left(\alpha(\phi,\xi_i)\right)}{\left(\xi_1^{max} - \xi_1^{min}\right)}$$

$$\alpha(\phi,\xi_i) = \int_0^l \frac{dl'}{\lambda(\phi,\xi_i)} \tag{3.1}$$

where $\alpha(\phi, \xi_i)$ represents the optical thickness of the region. It is evident that T_0 is a function of the optical thickness along the total path traveled. It is possible, at least in principle, to calculate the actual optical thickness of the region exactly. Unfortunately, in nonuniform regions this can become a computationally-intensive task. Thus, it was computationally advantageous to approximate $\alpha(\phi, \xi_i)$ by means of an "average" mean free path, λ_{av}. The simplest way to accomplish this was by using a linear average, namely

$$\lambda_{av} = \lambda\left(\frac{x_1+x_2}{2}\right) \tag{3.2}$$

where x represents the quantity being averaged (i.e., temperature or density) and the subscripts 1 and 2 represent the boundaries of the region.

42

The evaluation was done for media with several optical thicknesses. This calculation was done on a square region for a case of a nonuniform temperature but uniform density, and for a case with uniform temperature but nonuniform density. The situations are illustrated in figure 3.2.

In the first case, the temperature was allowed to vary linearly from the value at one boundary to the value at the opposite boundary, while the density remained constant at 5×10^{18} m^{-3}. It is important to mention that linear temperature or density profiles are not typical in the divertor region. However, if the computational regions are small, any nonuniformities can be approximated by a linear function. In this limit the present evaluation should be valid. The results of this study can be seen in table 3.1.

Table 3.1; T_0 (λ_{av}) for a Region with Linear Temperature Variation, Uniform Density

T (eV) =	100 - 50	100 - 10	100 - 1	10 - 1
Optical thickness	2.130	2.252	2.240	2.164
T_0 **exact**	0.09062	0.08584	0.08751	0.09070
T_0 (λ_{av})	0.09355	0.08836	0.08719	0.09503
Error %	3.23	2.94	-0.37	**4.78**

T (eV) =	100 - 50	100 - 10	100 - 1	10 – 1
Optical thickness	0.213	0.225	0.224	0.216
T_0 **exact**	0.25058	0.24818	0.24863	0.25043
T_0 (λ_{av})	0.25138	0.24878	0.24816	0.25208
Error %	0.32	0.24	-0.19	0.66
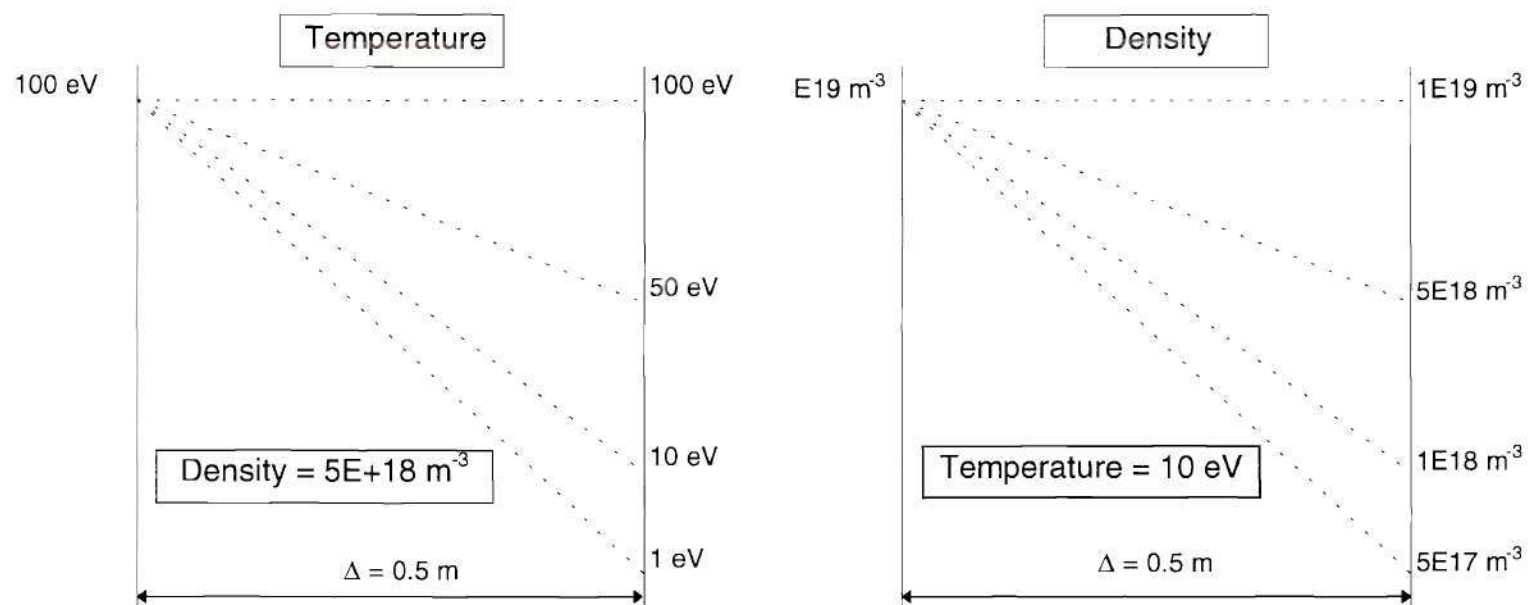
Figure 3.2. Temperature and density distributions for a nonuniform region model.

For optically thick regions, with a temperature range of 1 - 100 eVs, the error was less than 5%. Over the same temperature range, but for an optically thin region, the error was not greater than 1%.

In the second case the density was allowed to vary linearly while the temperature remained fixed at 10 eVs. The results agreed precisely with the exact solution. This was because the mean free path is directly proportional to the particle density ($\lambda^{-1} = \Sigma = n\sigma(T)$) and because the TEP-based code GTNEUT does not include density-dependent cross section data. The results of this evaluation for optically thick regions are shown in table 3.2.

Table 3.2; T_0 (λ_{av}) for a Region with Linear Density Variation, Uniform Temperature

n (m^{-3}) =	1E19 - 5E18	1E19 - 1E18	1E19 - 5E17
Optical thickness	3.354	2.460	2.348
T_0 **exact**	0.007656	0.02119	0.02409
T_0 (λ_{av})	0.007656	0.02119	0.02409
Error %	0.0	0.0	0.0

Based on these results, the error that was introduced in calculating the uncollided fraction, T_0, of incident particles transmitted through a medium with a nonuniform temperature distribution was small enough to justify the use of an "average" mean free path. The same was true for regions with a linear density distribution.

3.3 Accuracy of the First Flight Escape Probability

In chapter II, the proper expression for the first flight escape probability, i.e., equation 2.27, was introduced. This can be calculated exactly for any geometry of interest provided the proper chord distribution function is known. Although exact, this calculation would be very time consuming and would negatively affect the computational economy of the method. Section 2.5.1 in the previous chapter mentioned that to avoid this penalty, it was more practical and computationally efficient to calculate the first flight escape probability using some other simple approximations. One of these approximations was the rational approximation (equation 2.33) first introduced by Wigner in 1955 [46] and later re-examined by Sauer in 1963 [47].

3.3.1 First Flight Escape Probability Test in a Uniform Region [35]
3.3.1.a Parametric Dependence of P_0

The purpose of this section is to discuss the rational approximations suggested by Wigner and Sauer for the calculation of the first flight escape probability, rather than using the more complex expression previously defined (i.e., equation 2.27). To avoid the evaluation of this difficult expression, Wigner suggested the expression, introduced as equation 2.33 in chapter II,

$$P_0 = \frac{1}{1+X} \tag{3.3}$$

A more general expression for cylindrical regions was later introduced by Sauer (i.e., equation 2.34)

$$P_0 = \frac{1}{X}\left(1 - \frac{1}{\left(1 + \frac{X}{n}\right)^n}\right)$$

(3.4)

where $n = 4.58$ and the parameter $X \equiv 4V/\lambda S$ is defined in terms of the volume, V, the surface area, S, and the mean free path, λ.

The first step in this test was to calculate P_0 using the Monte Carlo code MCNP4B in order to test whether the parametric dependence of P_0 can be characterized by a single parameter, namely X. A variety of simple geometric figures (square, rectangle, triangle, circle and trapezoid) with different volume-to-surface ratios were used for this purpose. In order to calculate P_0, each region contained a uniform plasma with $<\sigma v>_{cx} = <\sigma v>_{el} = 0$ (i.e., only ionization processes were allowed), so that only the uncollided particles escaped. Each model also had a uniformly distributed neutral source and vacuum boundary conditions. Thus, P_0 was equal to the ratio of the leakage to the total source, i.e., $P_0 = L/S_{tot}$. The calculated P_0's predicted by MCNP4B are plotted versus the parameter X in figure 3.3. It is clear that P_0 is well characterized as a function of the single parameter X and does not otherwise depend strongly on the mean chord length or geometry.

3.3.1.b Accuracy of the Rational Approximations

As mentioned, it is desirable for the sake of computational efficiency to use a rational approximation for P_0, rather than to calculate P_0 from equation 2.34. Thus, the next test
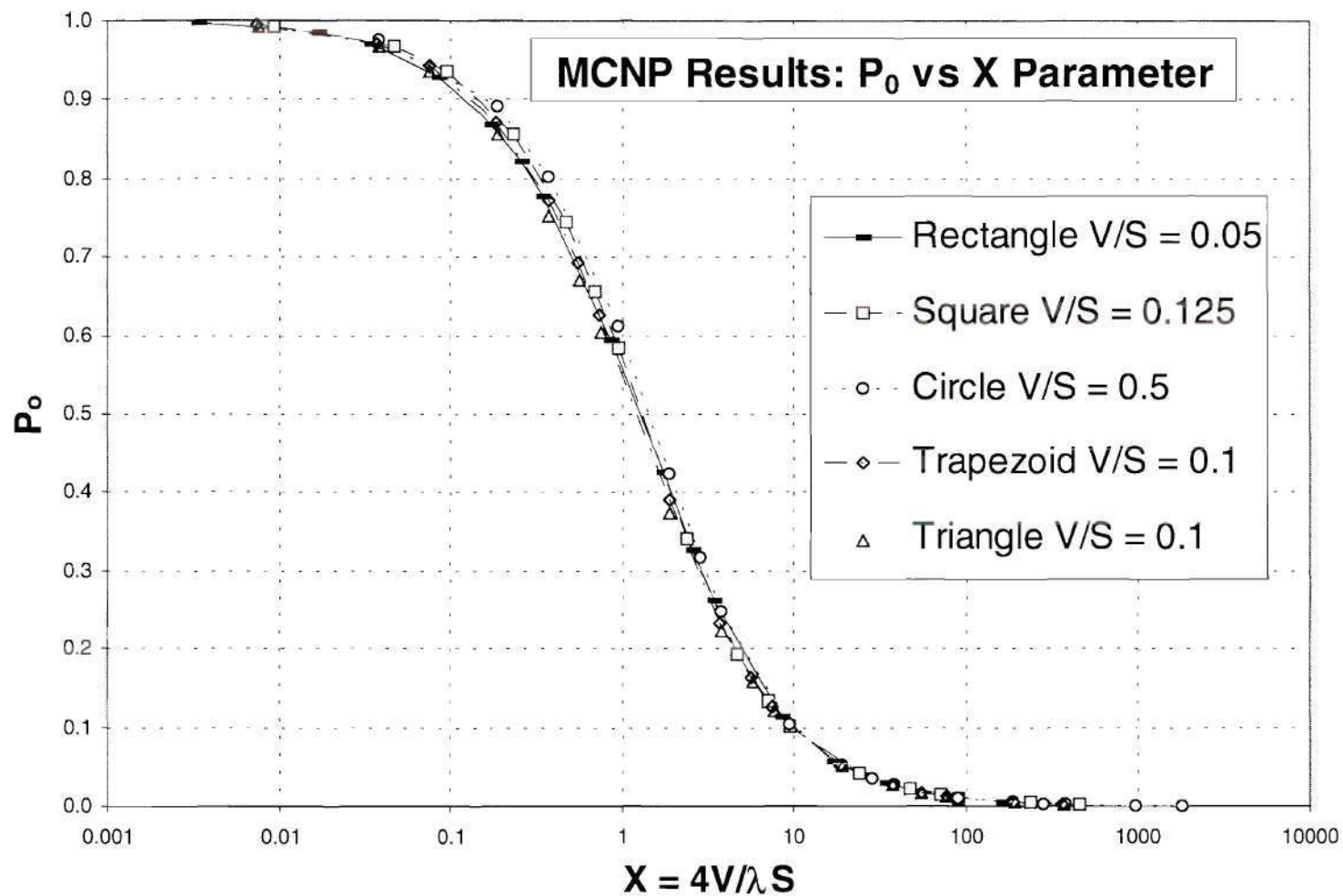
Figure 3.3. First flight escape probability as calculated by Monte Carlo for various geometries and surface-to-volume ratios plotted versus the parameter $X = 4V/\lambda S$.

was the calculation of P_0 using Wigner's and Sauer's rational approximations for comparison with P_0 predicted with MCNP4B for a variety of geometries and surface-to-volume ratios. Although Sauer's approximation strictly applies only to cylindrical geometry, it was also evaluated for the other geometries considered. This comparison is shown in figures 3.4 for trapezoidal geometry. Based on these results, it was concluded that both Wigner's and Sauer's rational approximations approached the analytical limit 1/X as the parameter X becomes large. It can be readily seen that Wigner's rational approximation underpredicted P_0 for an intermediate range of X (0.1 ~ 20), a well known result from neutron transport [47-50]. On the other hand, Sauer's rational approximation overpredicted P_0 over the same interval. It is worth mentioning at this point that all the detailed divertor models studied in chapter VII (ITER-EDA, DIII-D, and C-Mod) fell in the region where X is 0.01 ~ 100). In the limit as the parameter X becomes small, both Wigner's and Sauer's rational approximations approached the analytical limit of 1. Similar behavior was observed in all the geometries tested.

To reduce the errors seen with Wigner's and Sauer's rational approximations, a new rational approximation is introduced with a form similar to that of Sauer's. This was done using all the values of P_0 predicted by MCNP for all geometries tested (see figure 3.3). The value of n that best fit all the geometries was 2.09. By way of example, figure 3.5 shows P_0 as calculated by Wigner's, Sauer's, and the new (n = 2.09) rational approximations compared with the predicted Monte Carlo results as a function of the X parameter, for the trapezoid model. Clearly, the new rational approximation showed an improvement in the intermediate range 0.1 ~ 20 of X and still preserved the analytical

49
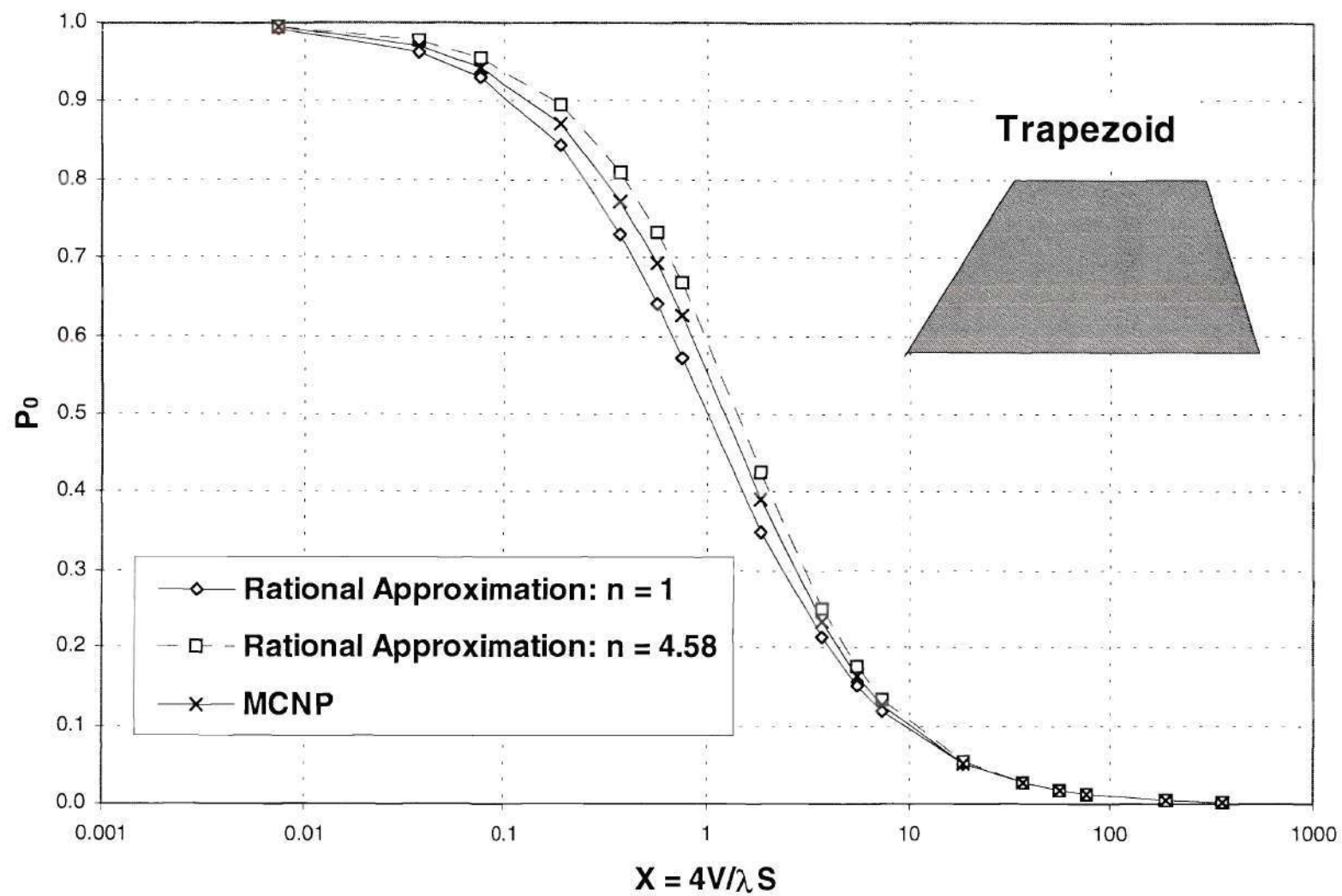
Figure 3.4. Rational approximation comparison for first flight escape probability.
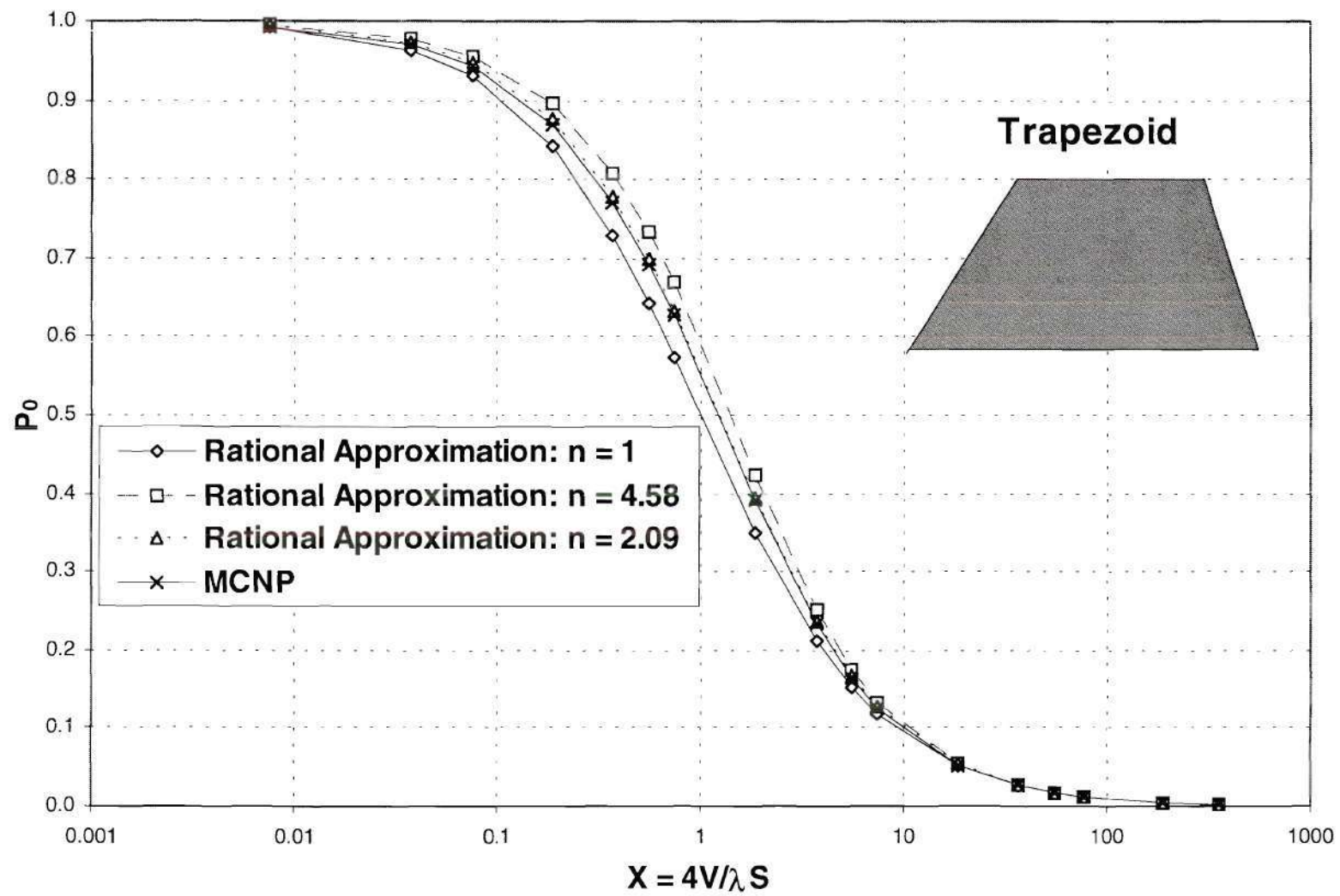
Figure 3.5. New rational approximation comparison for the first flight escape probability.

limits of Wigner's and Sauer's rational approximations. A comparison of the rational approximations for other geometries are shown in figures 3.6 – 3.10. These figures show the percent error with respect to Monte Carlo for each of the geometries tested. Figure 3.11 summarizes the error for the new rational approximation ($n = 2.09$) compared with Monte Carlo results for all the geometries tested. It is clear that the maximum relative error of the new rational approximation was about 5% for all geometries, with the exception of the cylindrical (circle), where the error could be as large as 12%. It is also clear that the new rational approximation is more accurate than the Wigner or Sauer approximation for all geometries except cylindrical (circle), for which the Sauer approximation was superior since it was explicitly defined for an infinite cylinder.

3.4 Total Escape Probability

P_0 represents the probability that a particle can escape from a region without a collision. It is also possible that the particle or its progeny can escape after one, two, or n-collisions. For example, $(1 - P_0)c_iP_0$ represents the probability that a particle escapes after one collision. The probability that a particle can escape after two collisions is $(1 - P_0)^2 c_i^2 P_0$ and so on. Consequently, the total escape probability can be mathematically expressed as

$$P = P_0 \sum_{n=0}^{\infty} \left(c_i \left(1 - P_0 \right) \right)^n = \frac{P_0}{1 - c_i \left(1 - P_0 \right)} \tag{3.5}$$
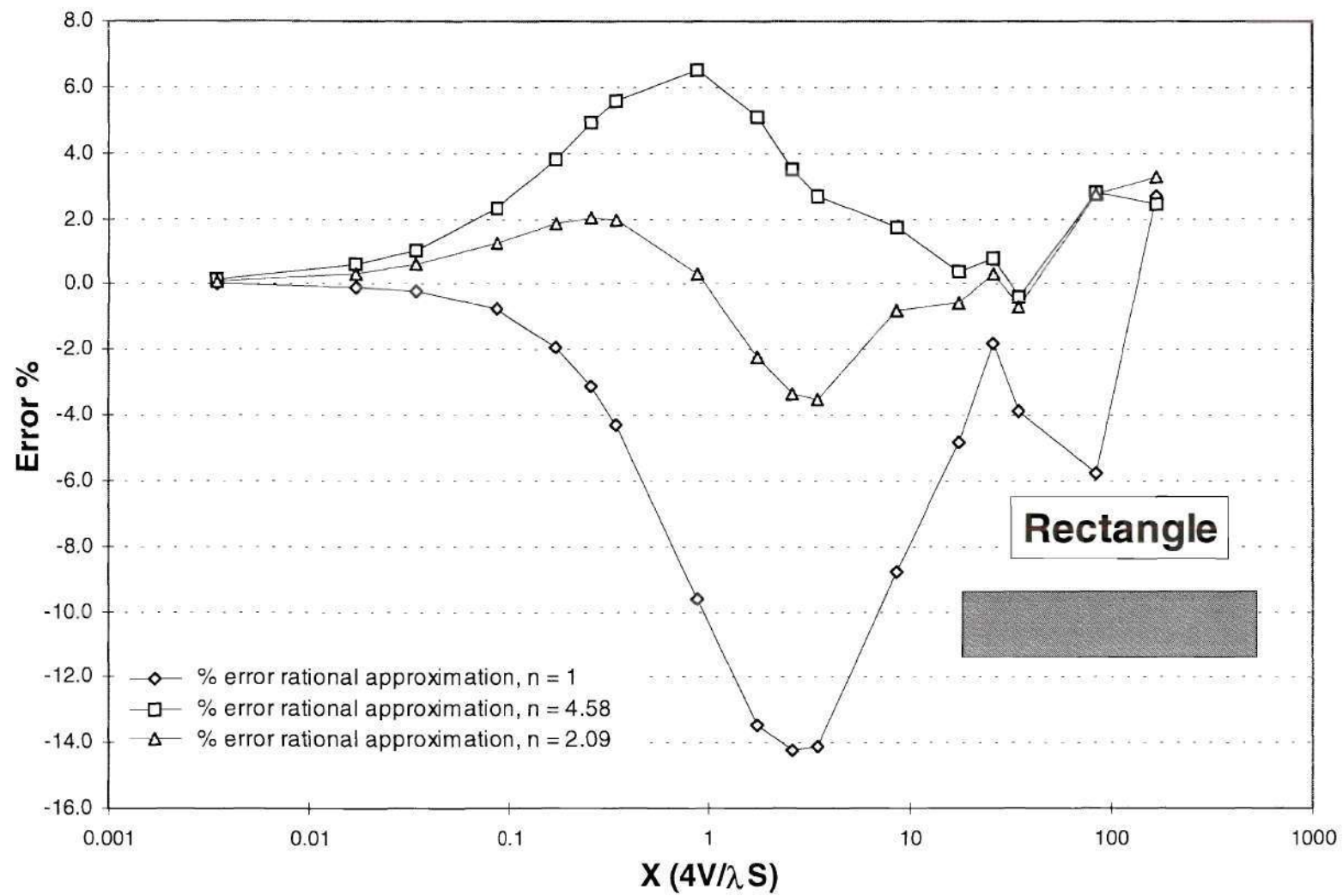
Figure 3.6. Error comparison for the three rational approximations for the rectangular geometry.
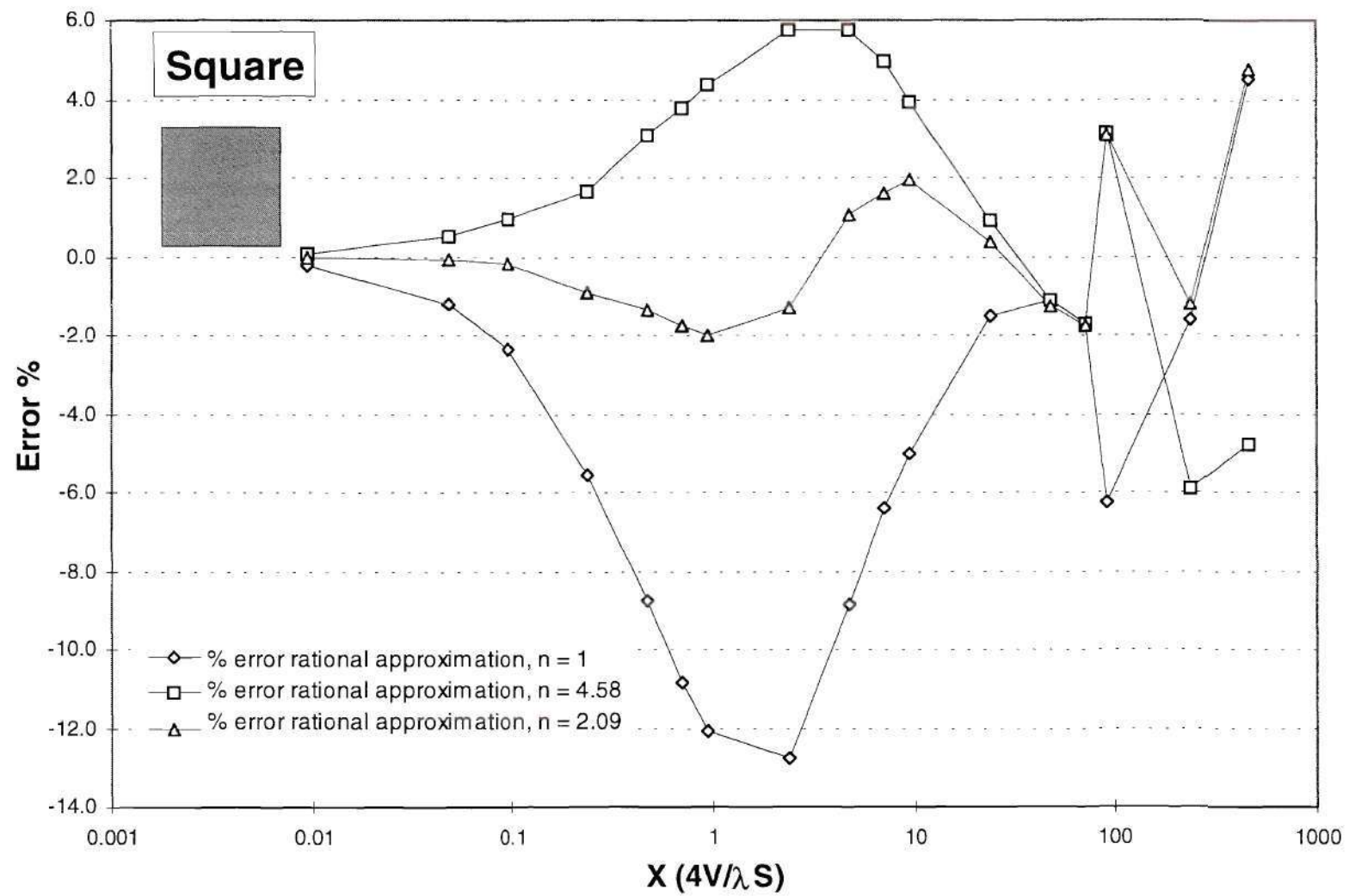
Figure 3.7. Error comparison for the three rational approximations for the square geometry.
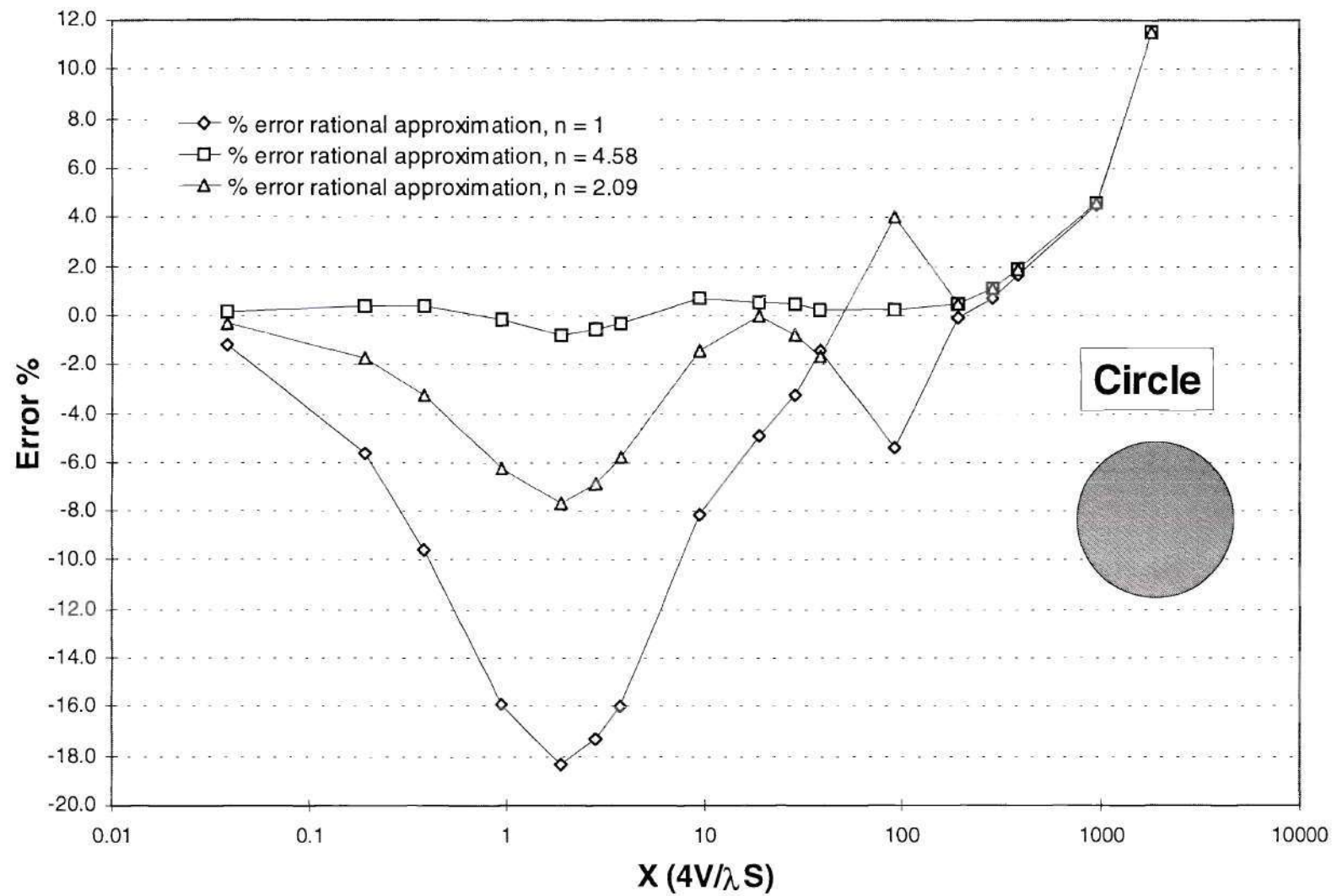
Figure 3.8. Error comparison for the three rational approximations for the circular geometry.
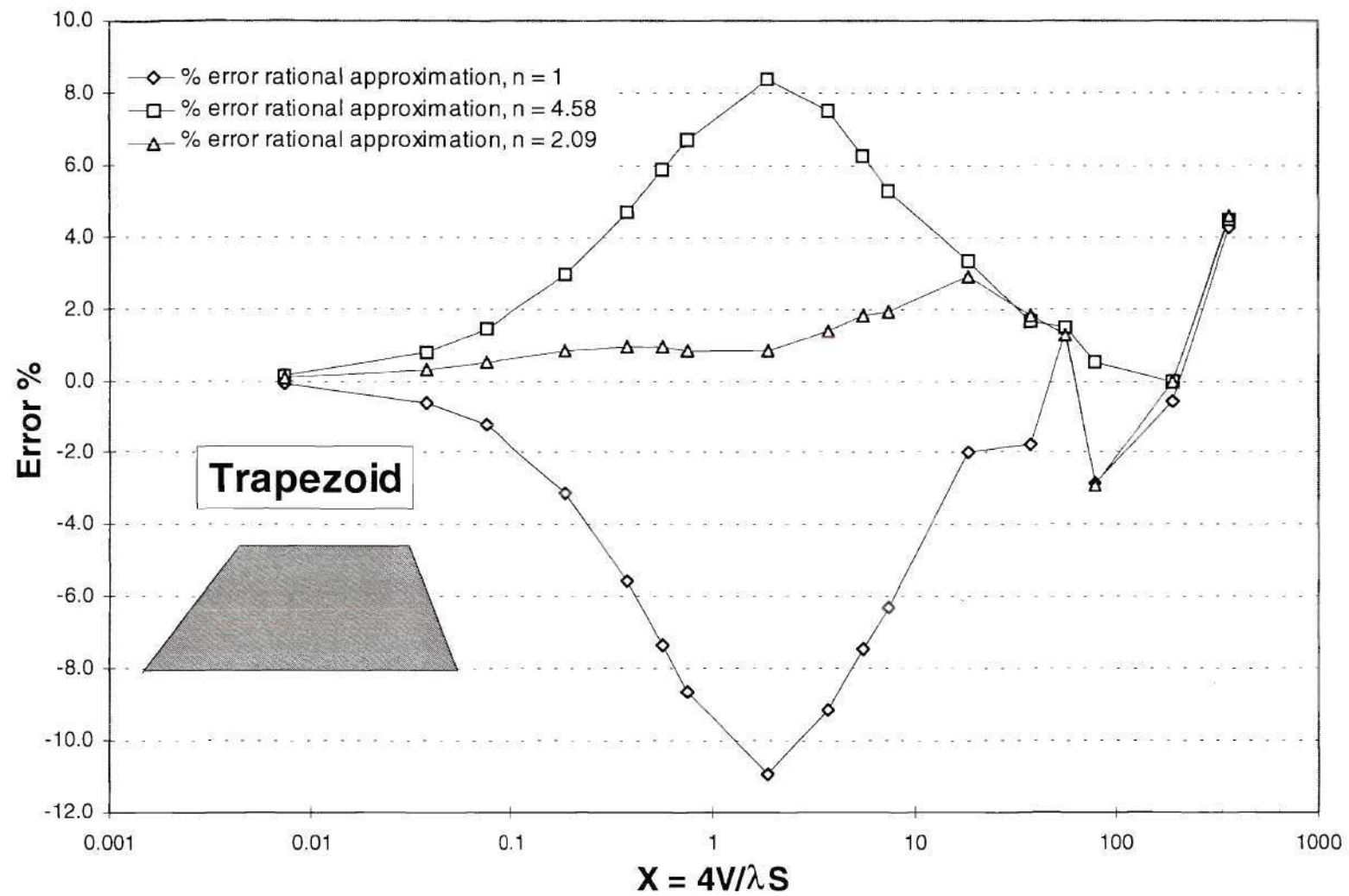
Figure 3.9. Error comparison for the three rational approximations for the trapezoidal geometry.
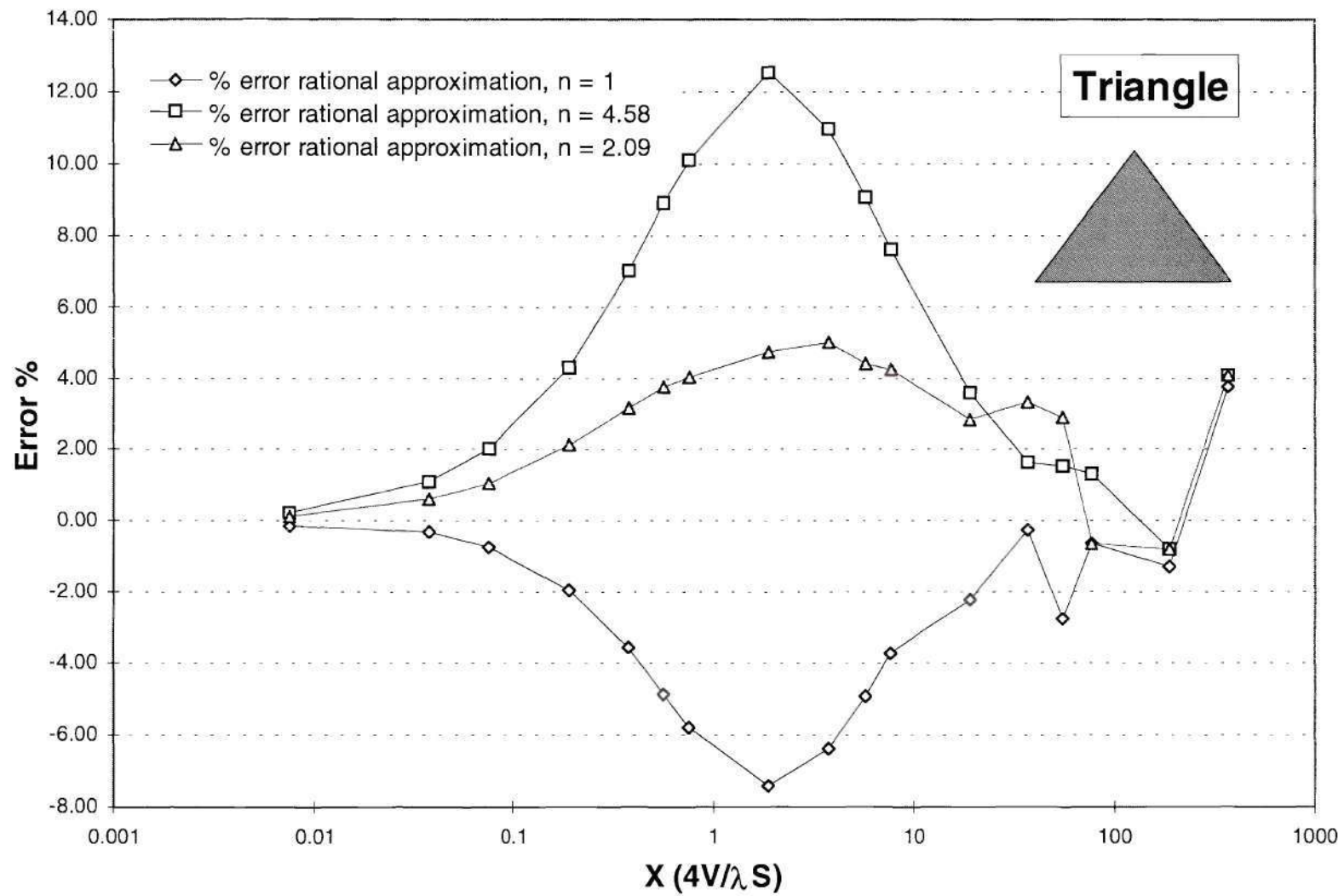
Figure 3.10. Error comparison for the three rational approximations for the triangular geometry.
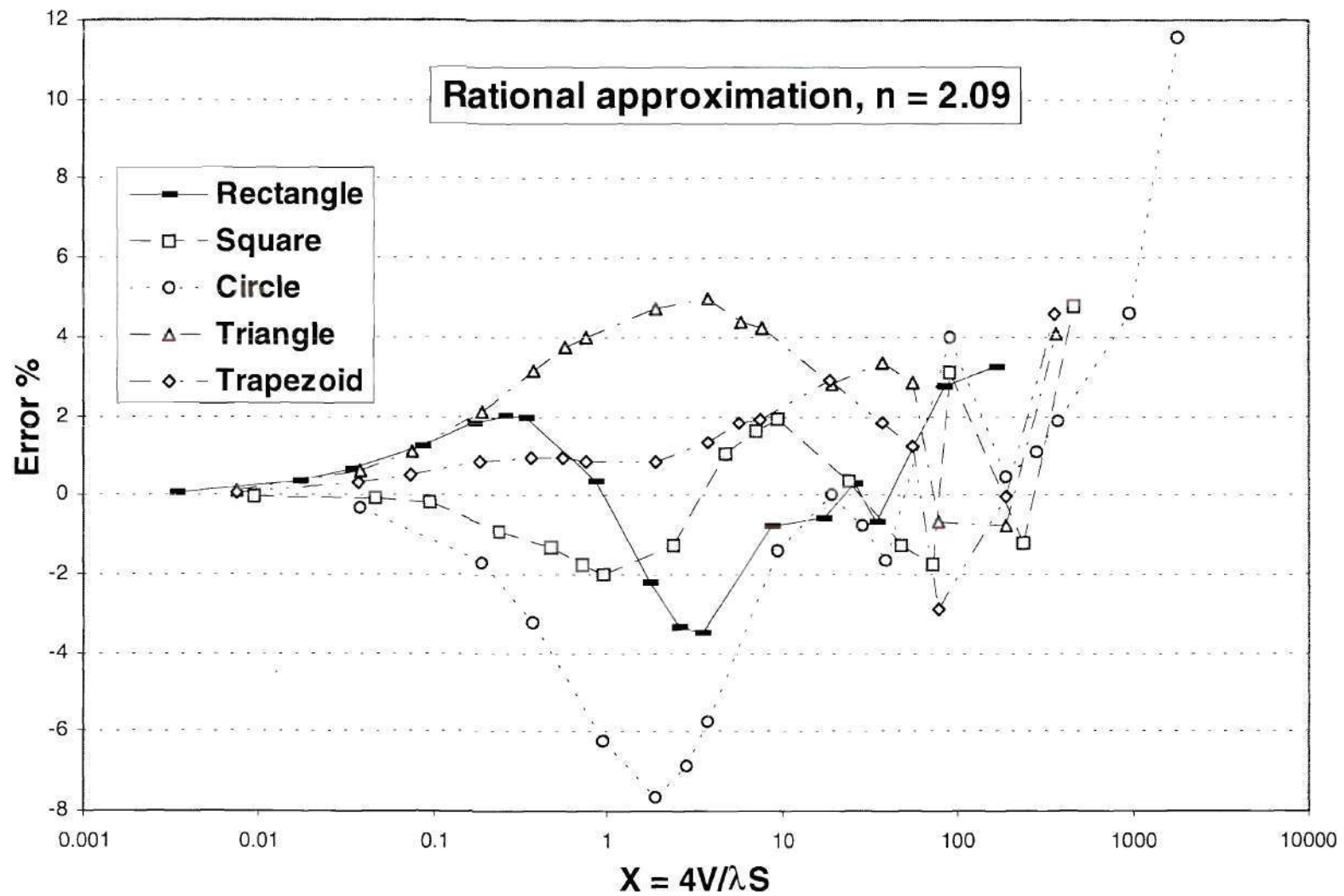
Figure 3.11. Error in the new rational approximation (n = 2.09) for a variety of geometries.

Let $\varepsilon = \Delta P/P$ and $\varepsilon_0 = \Delta P_0/P_0$ define the fractional error in the total escape probability and the fractional error in the first flight escape probability respectively. The two errors are related by

$$\varepsilon \equiv \frac{\Delta P}{P} = \frac{\Delta P_0}{P_0}\left[1 - \frac{c_i P_0}{1 - c_i P_0}\right] \equiv \varepsilon_0\left[1 - \frac{c_i P_0}{1 - c_i P_0}\right] \tag{3.6}$$

It is clearly seen in equation (3.6) that ε is less than ε_0. This fact is illustrated in figure 3.12. For example, if $P_0 = 0.5$ and $c_i = 0.8$, then for a value $\varepsilon_0 = 0.06$, the fractional error in the total escape probability, ε, is approximately 0.2%. Thus, the relative error in the total escape probability, which is the quantity that enters the TEP calculation, will be less than the error in the first flight escape probability discussed in the previous sections.

3.4.1 Escape Probability in a Uniform Medium with a Nonuniform Source Distribution

Implicit in the development of the rational approximation and in the relationship between the first flight (P_0) and total (P) escape probabilities are the assumptions that the escape probability is the same at every point within the region and that the collision source is uniformly distributed over the region. These assumptions are questionable for situations in which the primary source of particles in a region with dimensions greater than the mean free path result from collisions of particles incident across a bounding surface. For example, in the region in front of the divertor plate, there is a highly directional flux of particles recycling from the plate, and the first collision source within the region is highly peaked towards the divertor plate, rather than uniformly distributed (the second and later
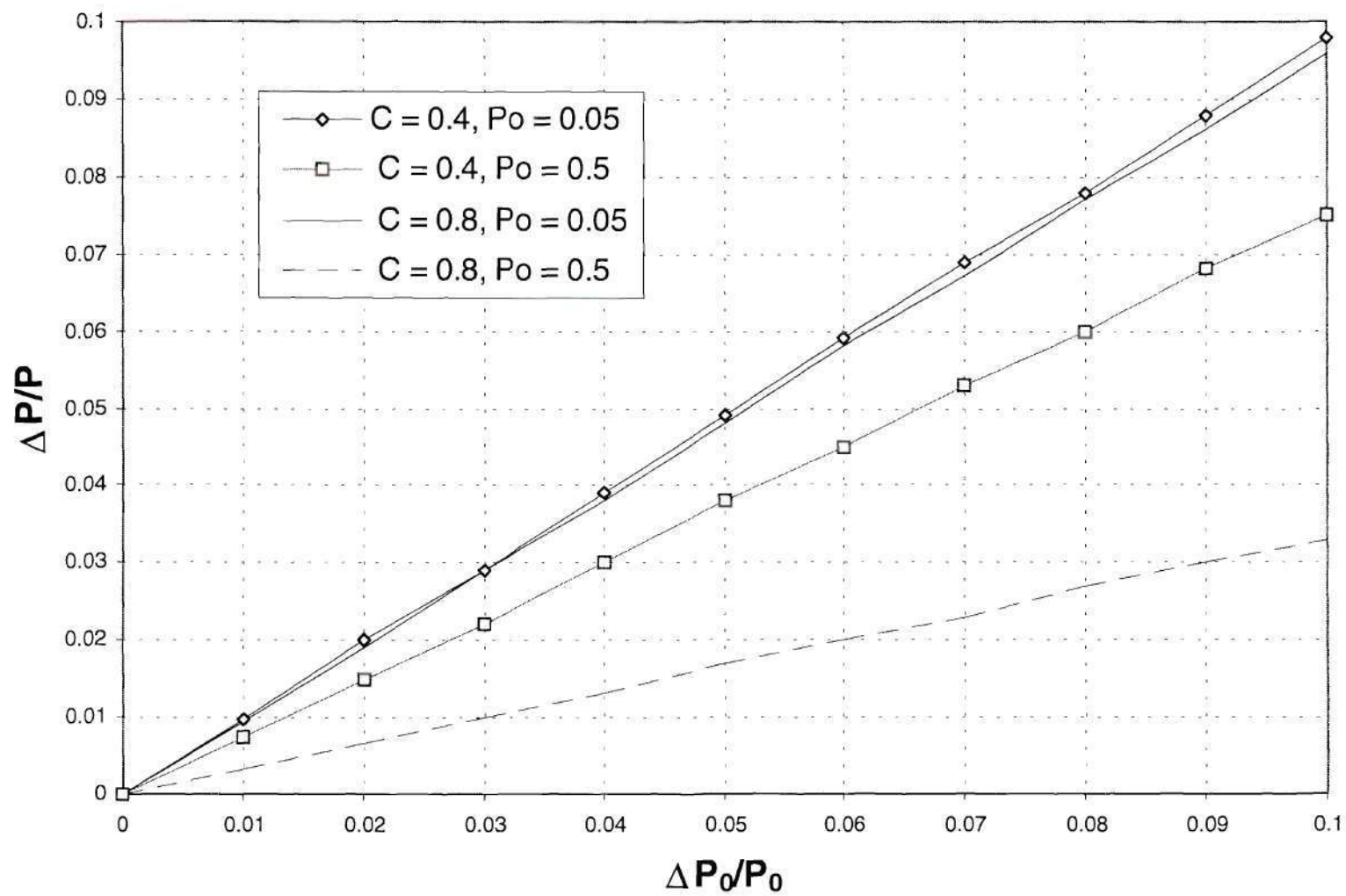
Figure 3.12. Total escape probability error as a function of change in the first flight escape probability.

collision sources would be more nearly uniformly distributed).

The purpose of this section [36] is to evaluate the accuracy of using the first flight (P_0) and total escape (P) probabilities using the rational approximation with $n = 2.09$ in a region with a nonuniform source distribution. The evaluation was carried out in a simple square region (i.e., $l = 0.5$ m) using a linear source distribution within the region, a uniform plasma background, and vacuum boundary conditions. (The source distribution in front of the divertor plate is not linear, but more like an exponential or power-like distribution. However, if the computational space is small, the source distribution can present linear characteristics. In these terms, this evaluation should be appropriate). The model is shown in figure 3.13.

The correct first flight and total escape probability were determined by using MCNP4B and compared to the predicted values obtained with equations 3.4 and 3.5. The evaluation was carried out for different values of c_i, the average number of secondary collisions, and for various values of the mean free path. The results shown in table 3.3 revealed that the rational approximation predicted the first flight escape probability to within an error of 5% for problems in which the dimension of the region was greater than the mean free path. However, unlike the case with a uniform source, for which the error in the total escape probability was always less than the error in the first flight escape probability, the error for the total escape probability in a region with a nonuniform source distribution was about 7% for regions in which the dimensions were significantly greater than the mean free path. For regions with dimensions equal to or smaller than the mean free path, the error in the total escape probability was smaller than the error in the first flight escape probability.

61
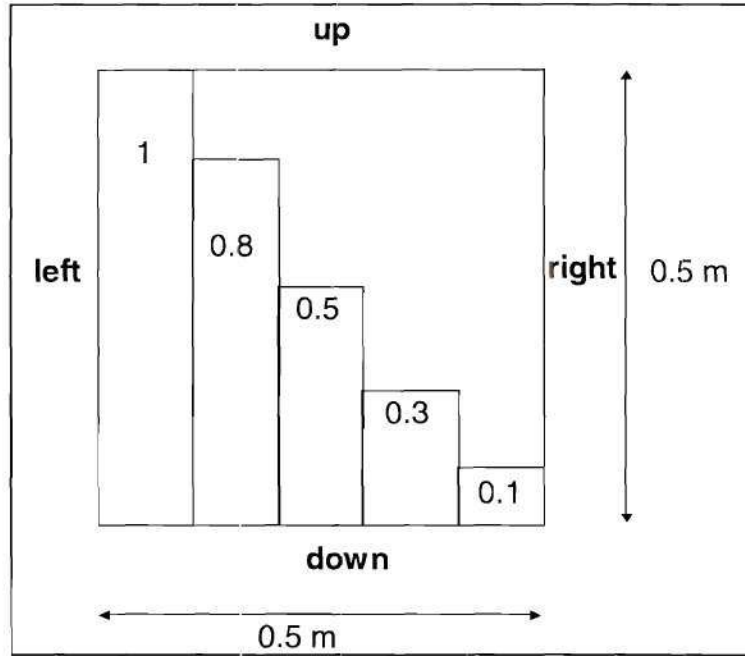
Figure 3.13. Model for the escape probability study for uniform square region with a nonuniform source distribution.

Table 3.3. Escape Probabilities for Uniform Square Region
with a Nonuniform Source Distribution

Pure Ionizing Medium; $c_i = 0.0$			
mfp(m) $\rightarrow$	0.11	0.53	5.3
Monte Carlo P_0	0.194	0.587	0.938
Rational Approximation	0.203	0.573	0.934
Error % ($\Delta P_0/P_0$)	4.63	-2.39	-0.43

Scattering Medium ; $c_i = 0.80$			
mfp(m) $\rightarrow$	0.11	0.53	5.3
Monte Carlo P	0.512	0.869	0.987
Total Escape Prob. P	0.548	0.865	0.985
Error % ($\Delta P/P$)	7.03	-0.46	-0.20

3.4.2 Escape Probability in a Nonuniform Medium

In general, the plasma temperature and density distributions within a region will be nonuniform. In order to make use of the rational approximation for P_0, it is necessary to define an effective mean free path based on average plasma parameters for the region.

The purpose of this section is to evaluate the first flight and total escape probabilities in a square region (l = 0.5 m) with a nonuniform temperature and density, but a uniformly distributed source. A pictorial description of the nonuniformities in temperature and density is shown in figures 3.14 - 3.15. The Monte Carlo simulation explicitly represented these nonuniformities and source distribution. An average mean free path, based on a simple linear average of the temperate and density (just as in section 3.2.2), was used to characterize the nonuniformities in the region (i.e., $\lambda_{av} = \lambda(x_1 + x_2)/2$ where x represents the quantity being averaged). These λ_{av} were then used to evaluate the expressions for the escape probabilities.

There were two cases of particular interest for the problem of a nonuniform density: 1) A purely ionizing medium (no elastic scattering or charge-exchange); and 2) a medium with finite elastic scattering and charge-exchange. The results of this test are shown in table 3.4.
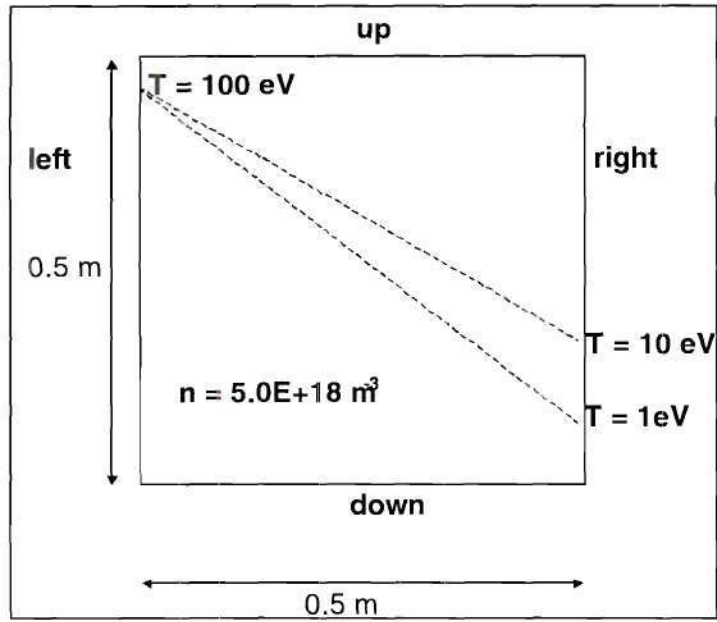
Figure 3.14; Escape probability model for a square region with a nonuniform
temperature distribution, uniform density and uniform source.
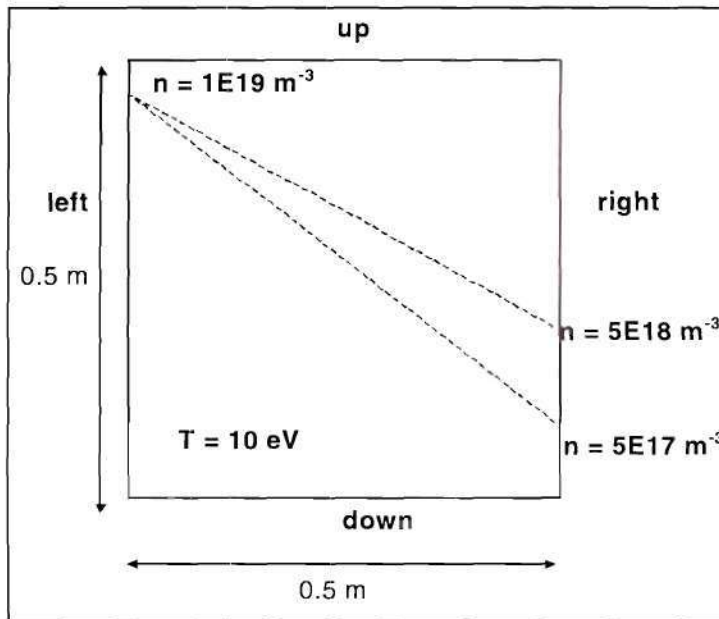
Figure 3.15; Escape probability model for a square region with a nonuniform
density distribution, uniform temperature and uniform source.

Table 3.4. Escape Probabilities in a Nonuniform Medium

	T(eV)		n(m^{-3})	
	100 – 10	10 – 1	1E19 – 5E18	1E19 – 5E17
	$c_i = 0.0$, n = 5E18 m^{-3}		$c_i = 0.0$, T = 10 eV	
Optical Thickness	0.903	0.174	0.706	0.494
Monte Carlo P_0	0.596	0.894	0.659	0.743
Rat. Approx. P_0	0.567	0.904	0.645	0.725
Error % ($\Delta P_0/P_0$)	-4.88	1.15	-2.09	-2.44
	$c_i = 0.55 - 0.78$, n = 5E18 m^{-3}		$c_i = 0.80$, T = 10 eV	
Optical Thickness	2.252	2.164	3.354	2.348
Monte Carlo P	0.567	0.875	0.602	0.712
Escape Prob. P	0.553	0.895	0.623	0.708
Error % ($\Delta P/P$)	-2.52	2.25	3.49	-0.53

The results indicated that using λ_{av} is adequate for evaluating the first flight and total escape probability in a nonuniform medium to within 5%, even when very large nonuniformities were present.

3.4.3 Directional Escape Fractions [35, 36]

With reference to equation 2.14, Λ_{ij} represents the probability that a neutral particle escaping from region i goes into region j. The current version of the TEP method used in the GTNEUT code assumes that there is no preferential direction for the collided escape probability, but that the escape fraction across a given surface is proportional to the fractional surface area of that surface. Thus, the escape fraction going across each surface of a square region with a uniform source and a uniform plasma background is simply 0.25.

It seems necessary to examine the effect of nonuniformities (i.e., source, plasma density or temperature) on the fraction of neutrals escaping across each surface. A pictorial description of the nonuniformities studied are shown in figures 3.13 - 3.15. The Monte

Carlo results for the case of a nonuniform source distribution are shown in table 3.5. It is evident that the escape is preferentially across the surface where the source is largest and reduced across the opposite surface nearest the region of reduced source (i.e., the escape probability is greater than 0.25 across the left surface and less than 0.25 across the right surface of the square). It is important to note that the extent of this directionality effect is inversely proportional to the mean free path within the region.

The Monte Carlo results for the cases with nonuniform temperature and density distributions, but with a uniformly distributed source, are shown in table 3.6 and 3.7 respectively. It is evident from table 3.6 that for regimes with small and large optical thicknesses, the directionality of the escape fraction from a region with a nonuniform temperature and uniform source and density distributions is not very significant. However, the directionality of the escape fraction for a region with a nonuniform density and uniform source and temperature distributions could be quite significant. Table 3.7 shows that the directionality effect becomes more pronounced in situations where the density varies by more than one order of magnitude (i.e., a factor of between $10 - 20$). These results suggested that when treating a physical region that has a large density gradient, it should be modeled with 2-3 computational regions in order to reduce the directional escape effects.

Table 3.5. Directional Escape Fractions for a Square Region
with a Nonuniform Source and a Uniform Plasma Background

Pure Ionizing Medium; $c_i = 0.0$			
mfp(m) $\rightarrow$	0.11	0.53	5.3
Λ_{right}	0.0725	0.1537	0.1948
Λ_{left}	0.4307	0.3479	0.3068
Λ_{up}	0.2470	0.2498	0.2485
Λ_{down}	0.2498	0.2486	0.2499

Scattering Medium ; $c_i = 0.80$			
Λ_{right}	0.1093	0.1684	0.1963
Λ_{left}	0.3930	0.3318	0.3052
Λ_{up}	0.2479	0.2493	0.2485
Λ_{down}	0.2498	0.2504	0.2499

Table 3.6. Directional Escape Fractions for a Square Region with
Nonuniform Temperature and Uniform Source and Density

	T(eV)	
	100 – 10	10 – 1
	$c_i = 0.0$, n = 5E18 m^{-3}	
Optical Thickness	0.903	0.174
Λ_{right}	0.2540	0.2658
Λ_{left}	0.2518	0.2312
Λ_{up}	0.2490	0.2506
Λ_{down}	0.2452	0.2524
	$c_i = 0.55 - 0.78$, n = 5E18 m^{-3}	
Optical Thickness	2.252	2.164
Λ_{right}	0.2471	0.2633
Λ_{left}	0.2559	0.2335
Λ_{up}	0.2448	0.2513
Λ_{down}	0.2486	0.2518

Table 3.7. Directional Escape Fractions for a Square Region with
Nonuniform Density and Uniform Source and Temperature

	$n(m^{-3})$	
	1E19 – 5E18	1E19 – 5E17
	$c_i = 0.0$, T = 10 eV	
Optical Thickness	**0.706**	**0.494**
Λ_{right}	0.2660	0.2799
Λ_{left}	0.2352	0.2205
Λ_{up}	0.2348	0.2483
Λ_{down}	0.2509	0.2513
	$c_i = 0.80$, T = 10 eV	
Optical Thickness	**3.354**	**2.348**
Λ_{right}	0.2803	0.3132
Λ_{left}	0.2227	0.1952
Λ_{up}	0.2480	0.2437
Λ_{down}	0.2489	0.2479

3.5 First Flight Source Distribution Correction [35, 36]

In regions next to the divertor plate, highly directional incident recycling fluxes would be expected to create a strong nonuniform first collision source distribution, similar to an exponential or power distribution. Thus, significant directional escape probability effects would be expected, with preferential escape back towards the divertor plate. In order to correct for this directionality effect, a correction factor was determined from a number of Monte Carlo calculations of uniform regions with both isotropic and cosine distributed sources incident on one surface. The computational domain for the study was a square region with a characteristic dimension Δx and vacuum boundary conditions. The sources were incident on the left surface of the square region. The computational model is shown in figure 3.16. The study was done for a variety of Δx and λ. For example, Table 3.8

shows the results for the directional escape fractions in a square region with a variety of Δx, mean free paths, $c_i = 0.8$, and for an isotropic plane source incident from the left. It is clear that the first collision source distribution of an incident isotropic flux distribution was quite nonuniform. There was a substantial preferential escape across the incident surface. An escape directionality factor was defined from the ratio of escaping forward to backward neutrals, $\Lambda_{forward}/\Lambda_{backward}$ (i.e., neutrals escaping across the right surface, $J_{forward}$ over the neutrals escaping across the left surface, $J_{backward}$). This ratio is plotted and fitted (see figure 3.17) as a function of the parameter Σx, where x is given by $x = 4V/S$ for the square.
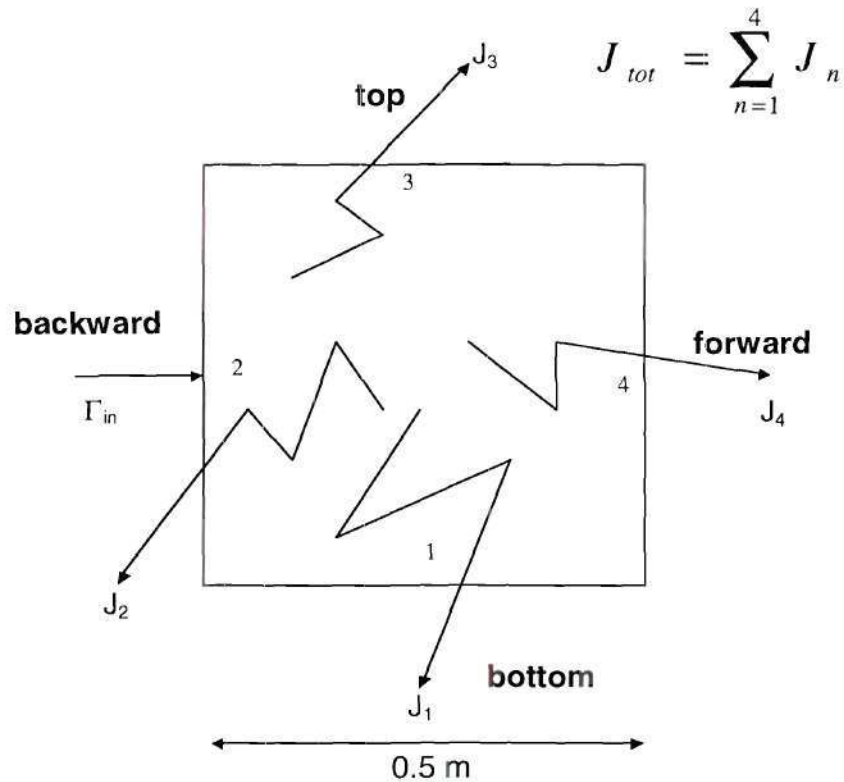
Figure 3.16. Computational model used to compute directional escape probability factor.

Table 3.8. Directional Escape Fractions in a Square Region with an Isotropic Plane Source Incident on the Left Surface

$c_i = 0.80$; V/S = 0.025				
mfp (m) $\rightarrow$	0.11	0.45	1.118	2.23
$J_{forward}/J_{total}$	0.5425	0.8009	0.8932	0.9357
$J_{backward}/J_{total}$	0.4575	0.1991	0.1068	0.0643
$\Lambda_{forward}/\Lambda_{backward}$	0.6279	0.8930	0.9595	0.9817

$c_i = 0.80$; V/S = 0.05				
mfp (m) $\rightarrow$	0.11	0.45	1.118	2.23
$J_{forward}/J_{total}$	0.3369	0.6934	0.8286	0.8932
$J_{backward}/J_{total}$	0.6631	0.3066	0.1714	0.1068
$\Lambda_{forward}/\Lambda_{backward}$	0.3688	0.7979	0.9187	0.9595

$c_i = 0.80$; V/S = 0.125				
mfp (m) $\rightarrow$	0.11	0.45	1.118	2.23
$J_{forward}/J_{total}$	0.0635	0.4825	0.6934	0.8009
$J_{backward}/J_{total}$	0.9365	0.5175	0.3066	0.1991
$\Lambda_{forward}/\Lambda_{backward}$	0.0629	0.5533	0.7979	0.8930

$c_i = 0.80$; V/S = 0.25				
mfp (m) $\rightarrow$	0.11	0.45	1.118	2.23
$J_{forward}/J_{total}$	0.0028	0.2614	0.5425	0.6934
$J_{backward}/J_{total}$	0.9972	0.7386	0.4575	0.3066
$\Lambda_{forward}/\Lambda_{backward}$	0.0027	0.2774	0.6279	0.7979

$c_i = 0.80$; V/S = 0.5				
mfp (m) $\rightarrow$	0.11	0.45	1.118	2.23
$J_{forward}/J_{total}$	---------	0.0635	0.3369	0.5425
$J_{backward}/J_{total}$	---------	0.9365	0.6631	0.4575
$\Lambda_{forward}/\Lambda_{backward}$	---------	0.0629	0.3688	0.6279

$$y_1 = \frac{0.999}{\left(1 + \left(\dfrac{x}{2.279}\right)^{1.337}\right)}$$

$$y_2 = \frac{0.979}{\left(1 + \left(\dfrac{x}{1.799}\right)^{1.212}\right)}$$

$$y_3 = -127.4\left(e^{-1.122(x+1.083)} - e^{-1.098(x+1.083)}\right)$$

$$y_4 = \frac{0.979}{\left(1 + e^{\frac{(x+1.145)}{1.434}}\right)}$$

$$y_5 = 8.296\left(e^{-0.739(x+1.473)} - e^{-1.043(x+1.473)}\right)$$

$$y_6 = \frac{2.326}{\left(1 + e^{\frac{(x+0.268)}{0.996}}\right)}$$
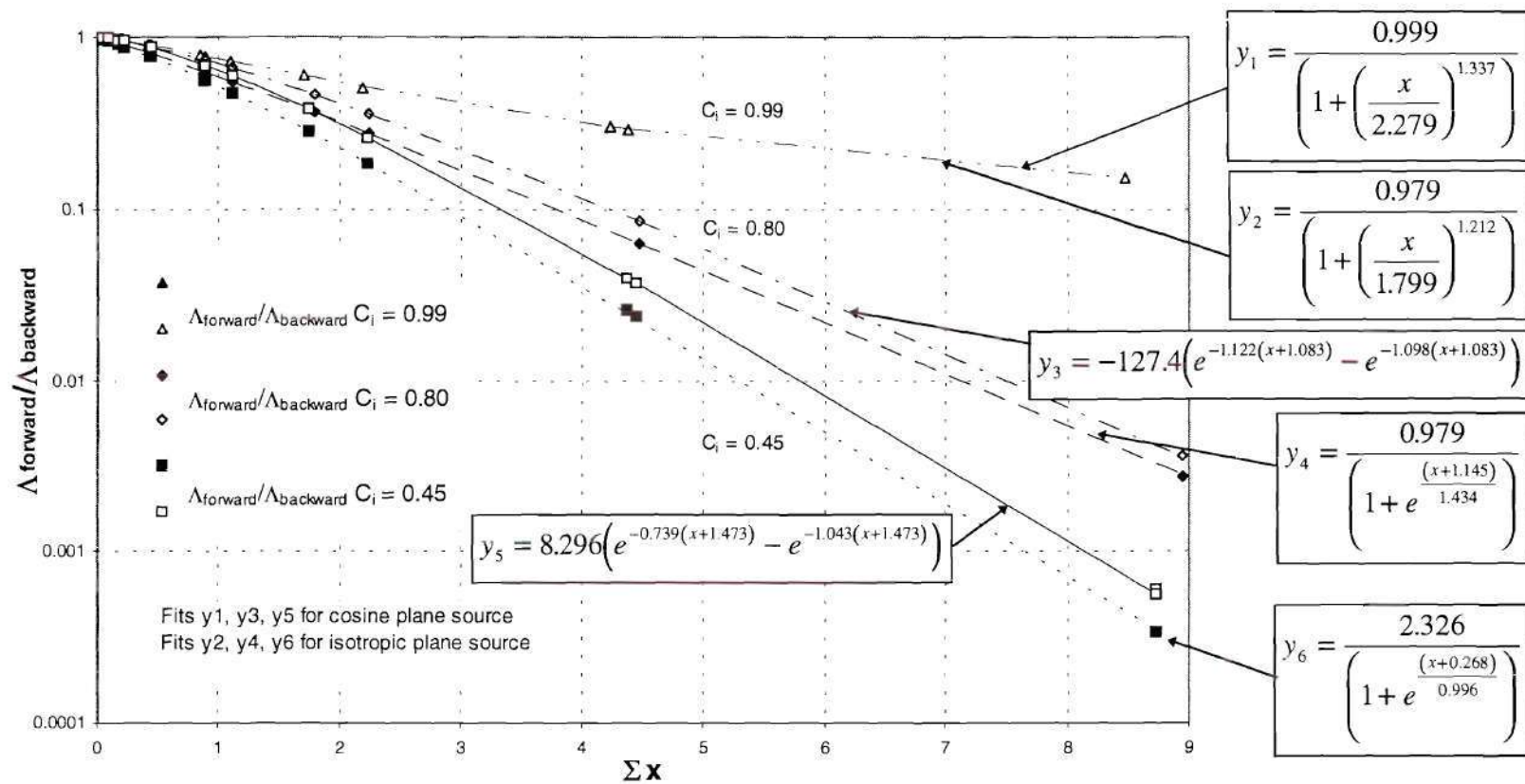
Figure 3.17. Directional escape probability factor (closed symbol: isotropic plane source, open symbol: cosine plane source).

71

3.6 Reflection from a Material Wall

The purpose of this section is to discuss the validity of the treatment of reflection from a material wall. The TEP based code, GTNEUT, assumes that reflection from a material wall is isotropic. On the other hand, both the MCNP4B and DEGAS codes are capable of reflecting particles from a "real" material wall (i.e., carbon, tungsten, etc.) with a cosine distribution. They also can model a "mirror" wall material with specular reflection characteristics. Thus, it seems appropriate to test the treatment of reflection since this condition can, under a number of circumstances, affect the angular distribution of particles in a particular problem.

The test was done on a square region with a uniform plasma background, such shown in figure 3.18. An incident flux of particles entered the left side of the square. Vacuum boundary conditions were imposed on the four surfaces of the square. An identical model was used in the Monte Carlo calculation.

Earlier it was discussed that the first collision distribution of an incident flux is predominantly towards the entering surface. Thus, the escape probability over the entering surface tends to be greater than the escape probability over the opposite surface. The TEP method assumes that there is no preferential direction for the collided escape probability. In fact, it assumes that the escape fraction across a given surface, Λ, is proportional to the fractional surface area.

In order to isolate the effect of the treatment of reflection, the directional escape probability, Λ, was adjusted in GTNEUT to match the values of the exiting uncollided as well as collided fluxes (at each of the four surfaces of the square) to the predicted Monte

Carlo results. Then, the vacuum boundary condition of the top surface was replaced with a reflective boundary condition. In the Monte Carlo simulation, the wall material "mirror" was used on the top surface. The purpose of this study is to compare the use of the specular reflection condition in Monte Carlo and the use of the isotropic reflection condition in GTNEUT, under a variety of conditions.

The comparison included both short and long mean free path regimes. The situation is illustrated in figure 3.18. The results of the comparison are shown in table 3.9. This shows the exiting current, J_i, at each of the surfaces of figure 3.18 as a function of mean free path. The table also shows the total exiting current, i.e., $J_{tot} = \sum_{n=1}^{4} J_n$. In the short mean free path regime, GTNEUT and Monte Carlo predicted essentially identical currents (i.e., collided, uncollided and total currents) exiting the box. In Monte Carlo a particle collision with the wall was treated as a specular reflection. Since the particle had a short mean free path, the next collision event occurred close to the wall. This created an isotropic distribution of particles near the wall which mimicked the isotropic reflection condition used by GTNEUT. This could explain the agreement between the two codes.

As the mean free path became equal to or greater than the characteristic dimension of the region (Δx), the reflected particle had its next collision farther away from the wall and perhaps outside of the box. Thus, the distribution of the reflected particles was no longer isotropized near the reflecting wall in the Monte Carlo calculation. In these long mean free path regimes, the isotropic reflection assumption used by GTNEUT led to significantly different results than the specular reflection model in the Monte Carlo code. This is clearly

shown by the results of table 3.9 for the cases of $\lambda = 0.45$ m and $\lambda = 1.11$ m. In these cases, GTNEUT agreed quite well the total current exiting the box; however, agreement in predictions of the separate collided, uncollided and total currents exiting a given surface was poor. These results exposed a limitation in the GTNEUT code to model effectively reflection from a material wall (assuming the correctness of the Monte Carlo reflection model). The isotropic reflection assumption in GTNEUT only agrees with Monte Carlo in regimes in which the characteristic dimension of the region is greater than the mean free path. In other words, there is agreement only if $\Delta x/\lambda > 1$.
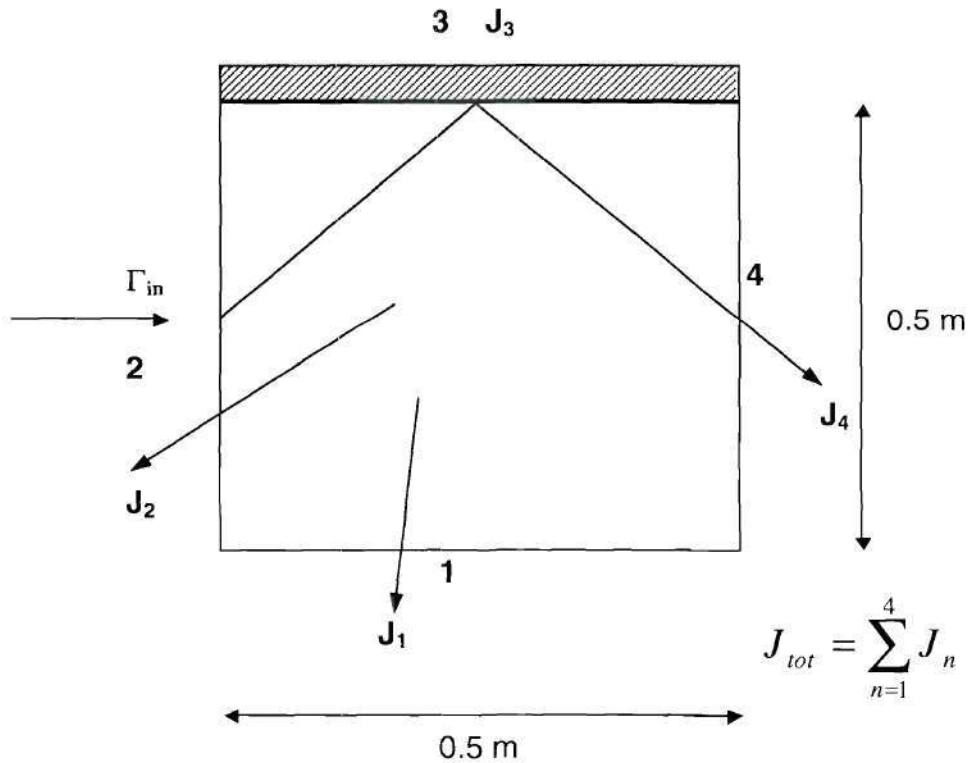
Figure 3.18. Two-dimensional reflection model.

Table 3.9. Current Balance in the Reflection Model

mfp (m) = 0.11						
	GTNEUT			**Monte Carlo**		
Current	**Total**	**Collided**	**Uncollided**	**Total**	**Collided**	**Uncollided**
J_1	0.1259	0.0783	0.0475	0.1200	0.0724	0.0475
J_2	0.3097	0.3038	0.0059	0.2990	0.2990	0.0000
J_3	0.0000	0.0000	0.0000	0.0000	0.0000	0.0000
J_4	0.0224	0.0142	0.0081	0.0231	0.0204	0.0027
J_{tot}	**0.4579**	**0.3963**	**0.0616**	**0.4421**	**0.3918**	**0.0503**

mfp (m) = 0.45						
	GTNEUT			**Monte Carlo**		
Current	**Total**	**Collided**	**Uncollided**	**Total**	**Collided**	**Uncollided**
J_1	0.2944	0.1208	0.1737	0.2857	0.1267	0.1590
J_2	0.2293	0.1902	0.0391	0.2050	0.2050	0.0000
J_3	0.0000	0.0000	0.0000	0.0000	0.0000	0.0000
J_4	0.2233	0.0822	0.1411	0.2518	0.1117	0.1401
J_{tot}	**0.7470**	**0.3931**	**0.3539**	**0.7425**	**0.4434**	**0.2991**

mfp (m) = 1.11						
	GTNEUT			**Monte Carlo**		
Current	**Total**	**Collided**	**Uncollided**	**Total**	**Collided**	**Uncollided**
J_1	0.3624	0.0790	0.2834	0.3478	0.0935	0.2543
J_2	0.1665	0.1032	0.0633	0.1165	0.1165	0.0000
J_3	0.0000	0.0000	0.0000	0.0000	0.0000	0.0000
J_4	0.3567	0.0613	0.2954	0.4206	0.0876	0.3330
J_{tot}	**0.8855**	**0.2435**	**0.6420**	**0.8849**	**0.2976**	**0.5873**

3.7 Conclusions

A number of calculations were performed to assess the accuracy and validity of approximations used in the implementation of the TEP method. The expression (2.24) used to calculate the first flight transmission probability in uniform and nonuniform regions produced results that were in excellent agreement with Monte Carlo.

Monte Carlo simulations performed on a number of geometries with different volume-to-surface ratios and different mean free paths revealed that the first flight escape probability depended on only a single parameter, namely $X = 4V/\lambda S$.

A new rational approximation ($n = 2.09$) generated by fitting the Monte Carlo results proved to be very accurate in the calculation of the first flight escape probability in a variety of geometries. The application of the new rational approximation in nonuniform mediums produced results that agreed well with those predicted by Monte Carlo.

It was demonstrated also that the error in the total escape probability in regions with uniform conditions was always less than the error in the first flight escape probability.

The study demonstrated that directional effects were of little importance in regions with nonuniform temperature distribution and a uniform source. However, the directionality error was significant in regions with a nonuniform density and a uniform source.

Contrary to the nonpreferential direction for the collided escape probability, the study demonstrated that the first collision source distribution of an incident partial current was anisotropic. Particles escaped across the incident surface at a much greater rate than they did across the opposite exiting surface. This directionality error was represented by a fit

which was created by the ratio of the forward to backward escape fractions.

Finally, Monte Carlo calculations indicated that the isotropic reflection assumption used by the TEP-based code GTNEUT was only valid in regions where $\Delta x/\lambda > 1$.

CHAPTER IV

TEST OF THE ICB METHODOLOGY IN A SLAB GEOMETRY

4.1 Introduction

The purpose of this chapter is to explore the validity of the basic transport assumptions of the ICB method. During the implementation of the ICB method it was assumed that: 1) the angular flux distribution at the interfaces is isotropic in each half space (i.e., double P_0 approximation); 2) a region can be characterized by a uniform mean free path; 3) charge-exchange and scattering are isotropic; and 4) the distribution of the collision rate due to scattering (once collided particles, twice collided particles, etc.) is also isotropic.

4.2 Isotropization Error in a Purely Ionizing Region [35, 36]

Embedded in the first assumption are the ideas that the uncollided and collided currents exiting a region have the same distribution, and that their combination gives rise to an isotropic angular flux distribution in the incident hemisphere as they enter successive regions.

With reference to figure 2.1, it can be shown [42] that in a purely absorbing medium the emerging current at a distance L from an isotropic plane source S at x = 0 is

$$J^+_{unc}(x = L) = \frac{S}{2} E_2(L\Sigma_{ti})$$

(4.1)

where E_2 represents the exponential integral of the 2nd order previously defined in equation 2.5.

78

Since $E_n(0) = 1$ then $J_{total}^+(0) = \dfrac{S}{2}$. Therefore, the first flight transmission probability is

given by

$$T_{0i} = \frac{J_{unc}^+(x=L)}{J_{total}^+(0)} = E_2(L\Sigma_{ti}) \qquad (4.2)$$

If the entire slab is to be treated as a single region, the transmission probability at the right boundary will be $T_0 = E_2(L\Sigma_{ti})$. However, if the slab of thickness L is subdivided into N equally spaced cells or subregions (i.e., $\Delta = L/N$), the transmission coefficient, as calculated by the ICB methodology, at a distance L from the source would be

$$\frac{J(L\Sigma_t)}{J_0} = E_2\left(\sum_{i=1}^{N}\Delta_i\Sigma_{ti}\right) \neq \prod_{i=1}^{N}E_2(\Delta_i\Sigma_{ti}) \qquad (4.3)$$

If the angular flux is isotropic at each interface, the contributions of the uncollided and collided components of the flux would be the same regardless of the number of interfaces and the distance traveled. This situation is depicted in figure 4.1-a. However, those particles coming from a region directly in front of the interface will have to travel a distance Δ. Those coming from a region far away from the interface will have to traverse a distance l which is proportional to $\Delta/\cos\theta$. Thus, their attenuation is greater than those coming a distance Δ away, mainly, $e^{-\Sigma\Delta/\cos\theta}$. Subsequently, at each new interface farther away from the source, the angular distribution function of the uncollided flux becomes more forward peaked. This situation is shown in figure 4.1-b. Therefore, for intermediate cells of a multiregion problem, the transmission probability depends on the degree of

79

anisotropy of the neutral distribution function $f(x, \mu)$ at the interfaces. It can be shown that for a distribution $f(x, \mu) \sim \mu^n$,

$$T_{0,k} = (n+2)E_{n+3}(\Delta_k \Sigma_{ki}) \quad \text{for } k = 2, \text{N} \text{ and } n = 0, 1, 2, \ldots \quad (4.4)$$

$T_{0,1}$ in the cell adjacent to the isotropic plane source is equal to $E_2(\Delta_1\Sigma_{t1})$. Yet the value for $T_{0,i}$ for intermediate cells (i.e., $T_{0,k}$ $k = 2$, N) can be calculated by using equation (4.4). For instance, if

$$f \sim \mu^{-1} \text{ (near a surface source)} \quad \Rightarrow \quad T_0 = E_2(L\Sigma_t)$$

$$f \sim \mu^0 \text{ (isotropic)} \quad \Rightarrow \quad T_0 = 2E_3(L\Sigma_t)$$

$$f \sim \mu \text{ (cosine)} \quad \Rightarrow \quad T_0 = 3E_4(L\Sigma_t)$$

Since the distribution function $f(x, \mu)$ becomes more forward peaked further away from the surface source, the transmission probability corresponding to higher values of n are expected to be more appropriate for intermediate cells.
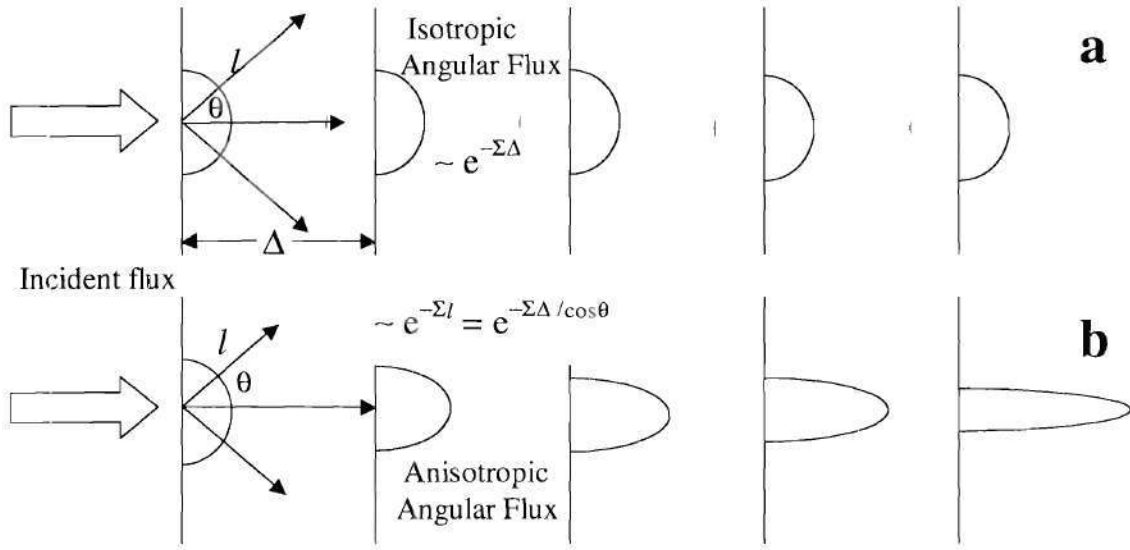
Figure 4.1. Isotropization effect in a multiregion slab.

This fact was demonstrated in a test with a simple slab with a totally ionizing medium with uniform plasma conditions. The slab had an isotropic plane source at the left boundary (x = 0), vacuum conditions on the right boundary, and an optical thickness (defined in equation 3.1) of 5. The test was done for a selective range of grid size over mean free path, $\Delta x/\lambda$, (0.094 – 4.7), and for three representative distribution functions (i.e., n = -1, 0, and 1). A Monte Carlo simulation was carried out with a similar slab, source, and plasma conditions. The results are shown in figures 4.2 - 4.4.

The results for $f \sim \mu^{-1}$ (which is the flux distribution near an isotropic plane source) are shown in figure 4.2. The transmission probability at each of the intermediate interfaces is given by $T_0 = E_2(\Sigma x)$. If the slab were treated as a single region ($\Delta x/\lambda$ = 4.7) the ICB result was in perfect agreement with Monte Carlo. However, when the slab was subdivided into 5 ($\Delta x/\lambda$ = 1), 10 ($\Delta x/\lambda$ = 0.5) or 50 ($\Delta x/\lambda$ = 0.09) cells, the isotropization

Transmission Probability: $T_0 = E_2(\Sigma x)$
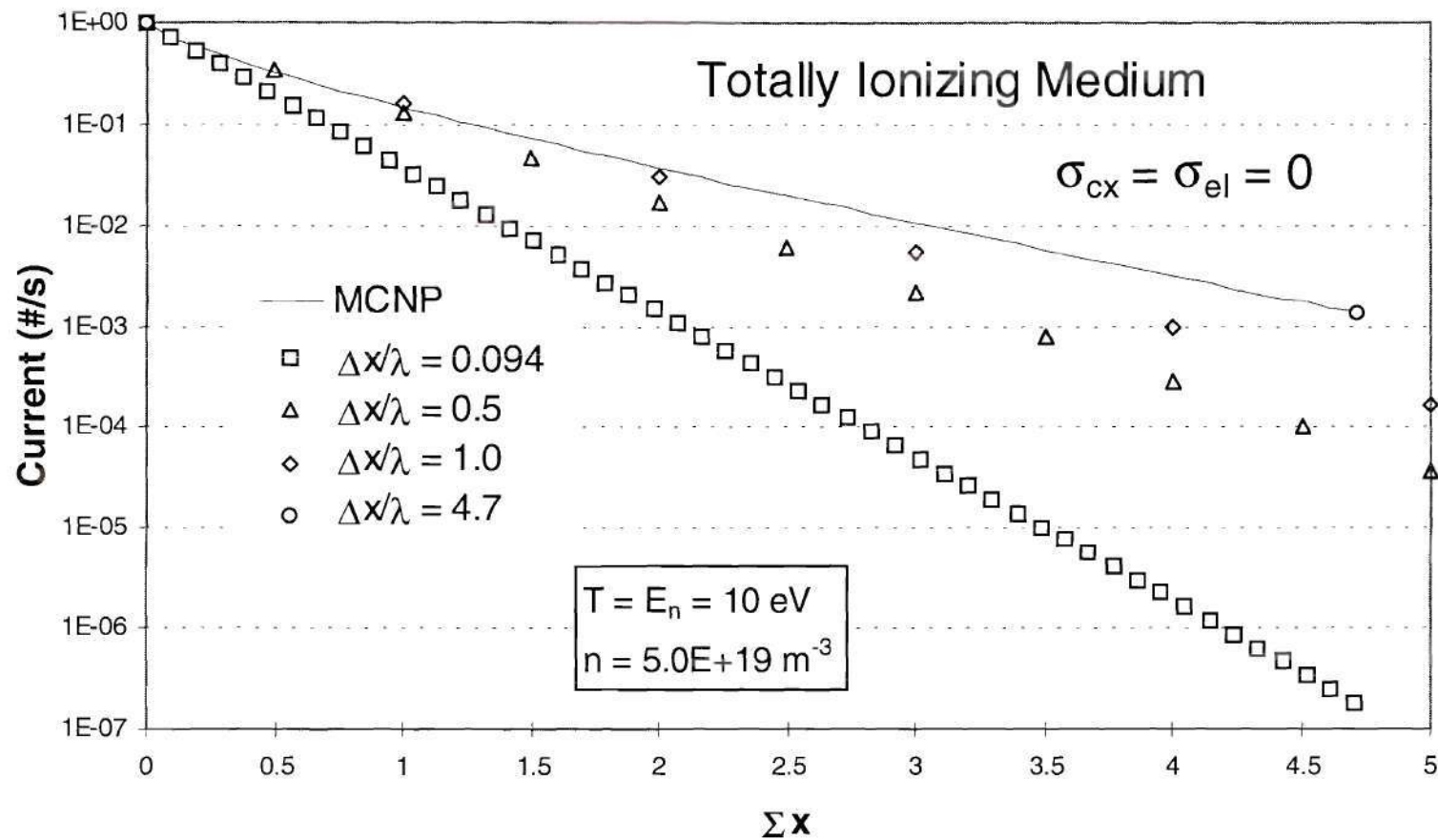
Figure 4.2. Penetration problem with transmission probability $T_0 = E_2(\Sigma x)$ in a totally ionizing medium.
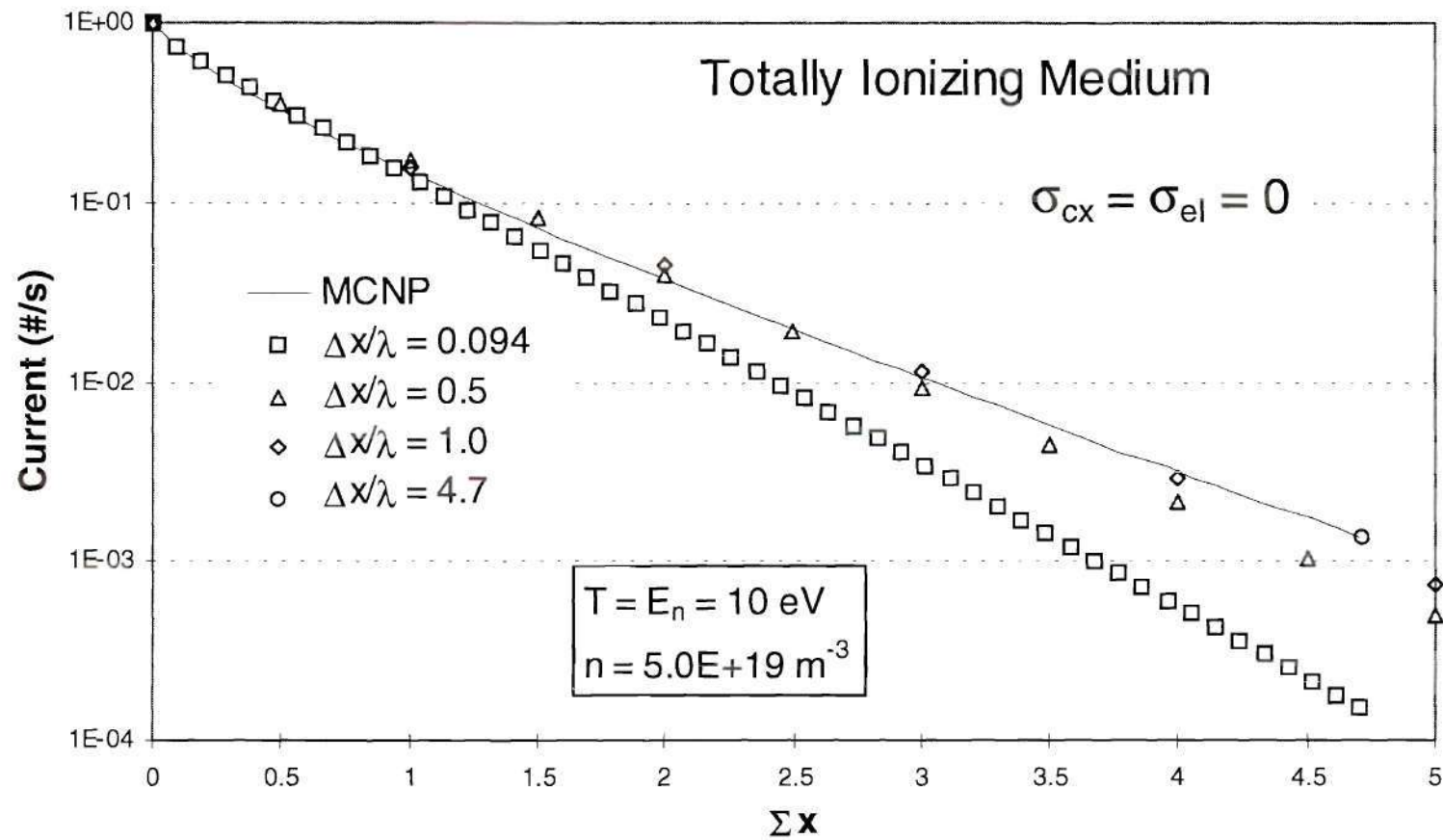
Figure 4.3. Penetration problem with transmission probability $T_0 = 2E_3(\Sigma x)$ in a totally ionizing medium.
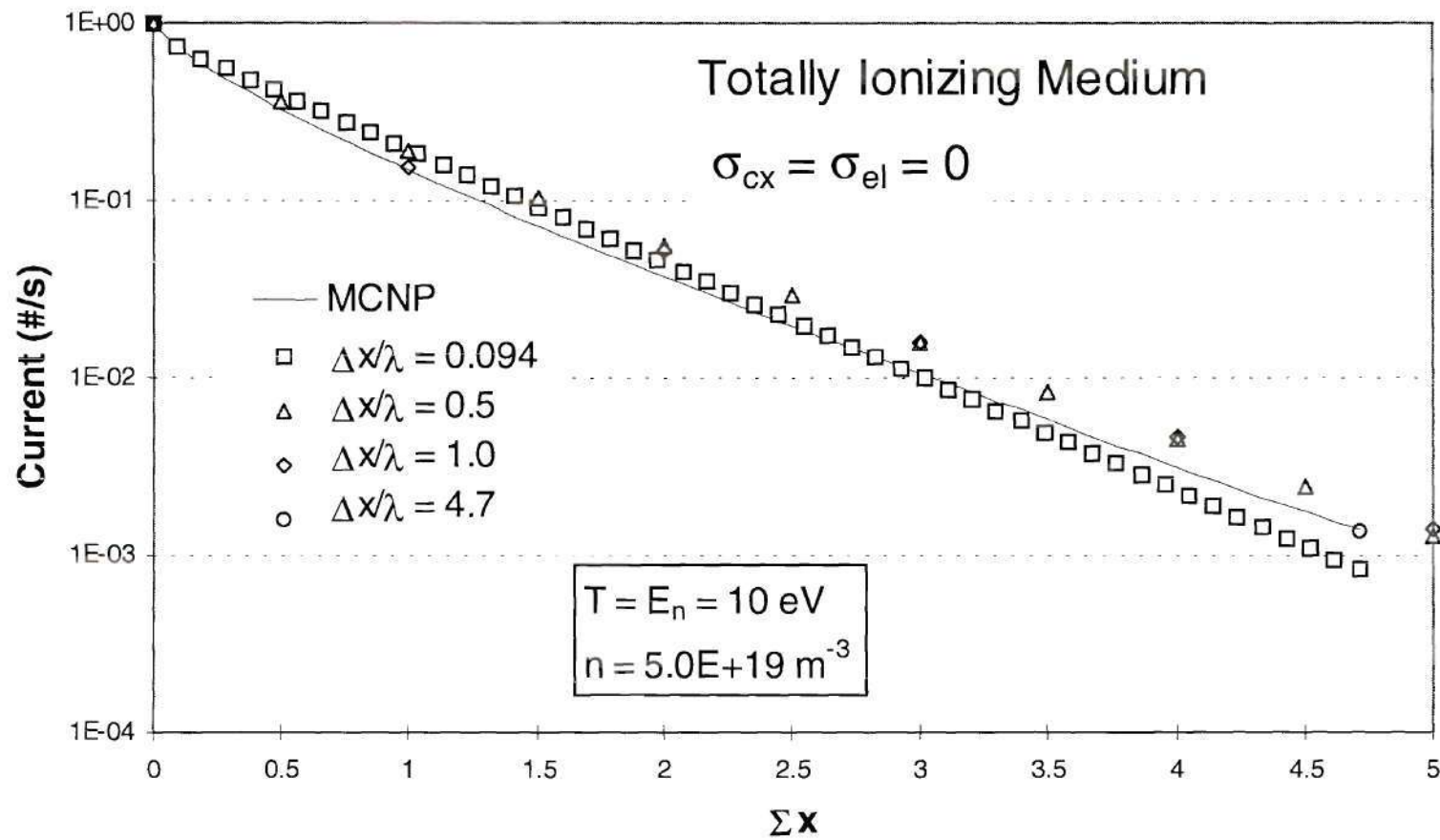
Figure 4.4. Penetration problem with transmission probability $T_0 = 3E_4(\Sigma x)$ in a totally ionizing medium.

assumption implicit in the transmission probabilities for each of the intervals generated a considerable amount of error. As the number of subdivisions increased, the isotropization error increased as well. This caused penetration in the slab to be underpredicted for practically all optical thicknesses. Note also that the degree of underprediction increased with the number of interfaces at which the isotropization assumption was made.

The results for $f \sim \mu^0$ (which corresponds to an isotropic flux distribution due to a cosine plane source) are shown in figure 4.3. The transmission probability at each of the intermediate interfaces is given by $T_0 = 2E_3(\Sigma x)$. In this particular case the distribution function becomes more forward peaked, thus reducing the isotropization error by a noticeable amount. The results for the Monte Carlo simulation were the same as in the previous problem. The isotropization error was small for all model problems with $\Delta x/\lambda \leq 1$ up to an optical thickness Σx of 1. However, for an optical thickness greater than 1, the isotropization error in the model problem with $\Delta x/\lambda = 0.094$ became dominant, and penetration was reduced considerably. The isotropization error for model problems with $\Delta x/\lambda = 1$ and $\Delta x/\lambda = 0.5$ became important for optical thicknesses Σx greater than 3. For an optical thickness Σx less than 3, the ICB code predicted currents were in good agreement with Monte Carlo. It is important to note that good agreement was obtained between the Monte Carlo and the ICB results for the model problem with $\Delta x/\lambda = 1$ up to an optical thickness Σx of 5.

Lastly, the results for $f \sim \mu^1$ (which is the equivalent to a cosine flux distribution at each interface) are shown in figure 4.4. The transmission probability at each of the intermediate

interfaces is given by $T_0 = 3E_4(\Sigma x)$. The predicted currents were in fairly good agreement with the predicted Monte Carlo results. The isotropization error was such that the penetration was overpredicted slightly for $\Delta x/\lambda = 1$ and for $\Delta x/\lambda = 0.5$. For $\Delta x/\lambda = 0.094$ the error was positive (overprediction) up to an optical thickness Σx of 2.5 and then it turned negative (underprediction).

4.3 Isotropization Error in a Medium with Charge-Exchange and Scattering [35, 36]

In a real plasma, the conditions are such that a pure ionizing medium is not very likely. In fact, the most likely situation is that charge-exchange and elastic scattering would account for 50% to 80% of the neutral interactions. Charge-exchange and elastic scattering have an isotropizing effect on the distribution of the uncollided fluxes. Thus, charge-exchange and elastic scattering would tend to reduce the underprediction of the first flight transmission in the forward direction that was investigated in the previous section.

The previous three calculations were repeated for $f \sim \mu^0$ and $f \sim \mu^1$, but now with a fraction of charge-exchange plus scattering, c_i equal to 0.8. The resulting currents can be seen in figures 4.5 and 4.6. The isotropizing effect of charge-exchange and scattering can be seen in figure 4.5. Once again, the transmission probability at each of the intermediate interfaces in the slab was calculated with $T_0 = 2E_3(\Sigma x)$. It was shown in chapter III that with charge-exchange and elastic scattering, the forward directed escape probability was overpredicted because of the effect of a distributed first collision source within each region. It is very important to note that when $\Delta x/\lambda = 1$, the isotropization and escape
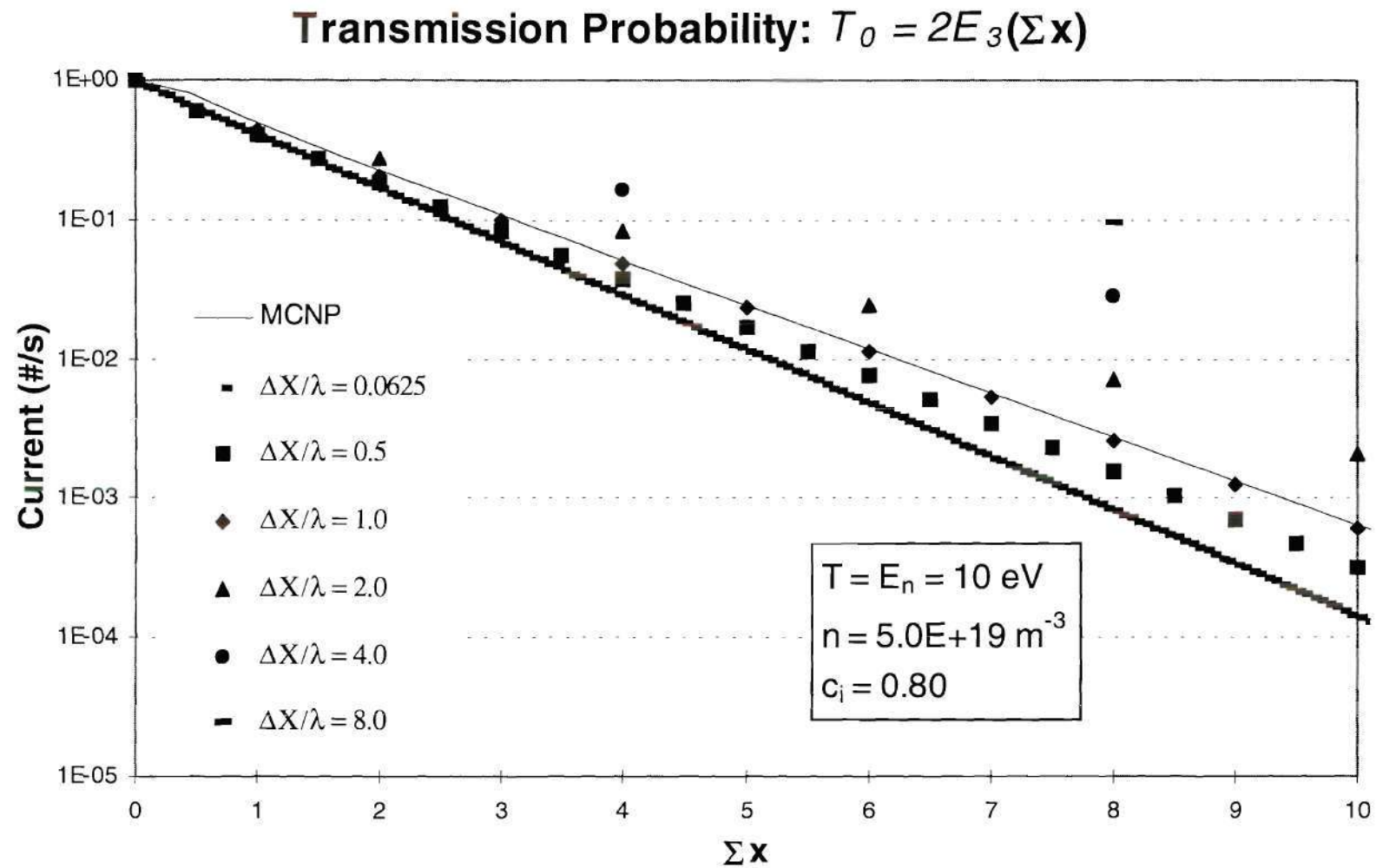
Figure 4.5. Penetration problem with transmission probability $T_0 = 2E_3(\Sigma x)$ and $c_i = 0.8$.
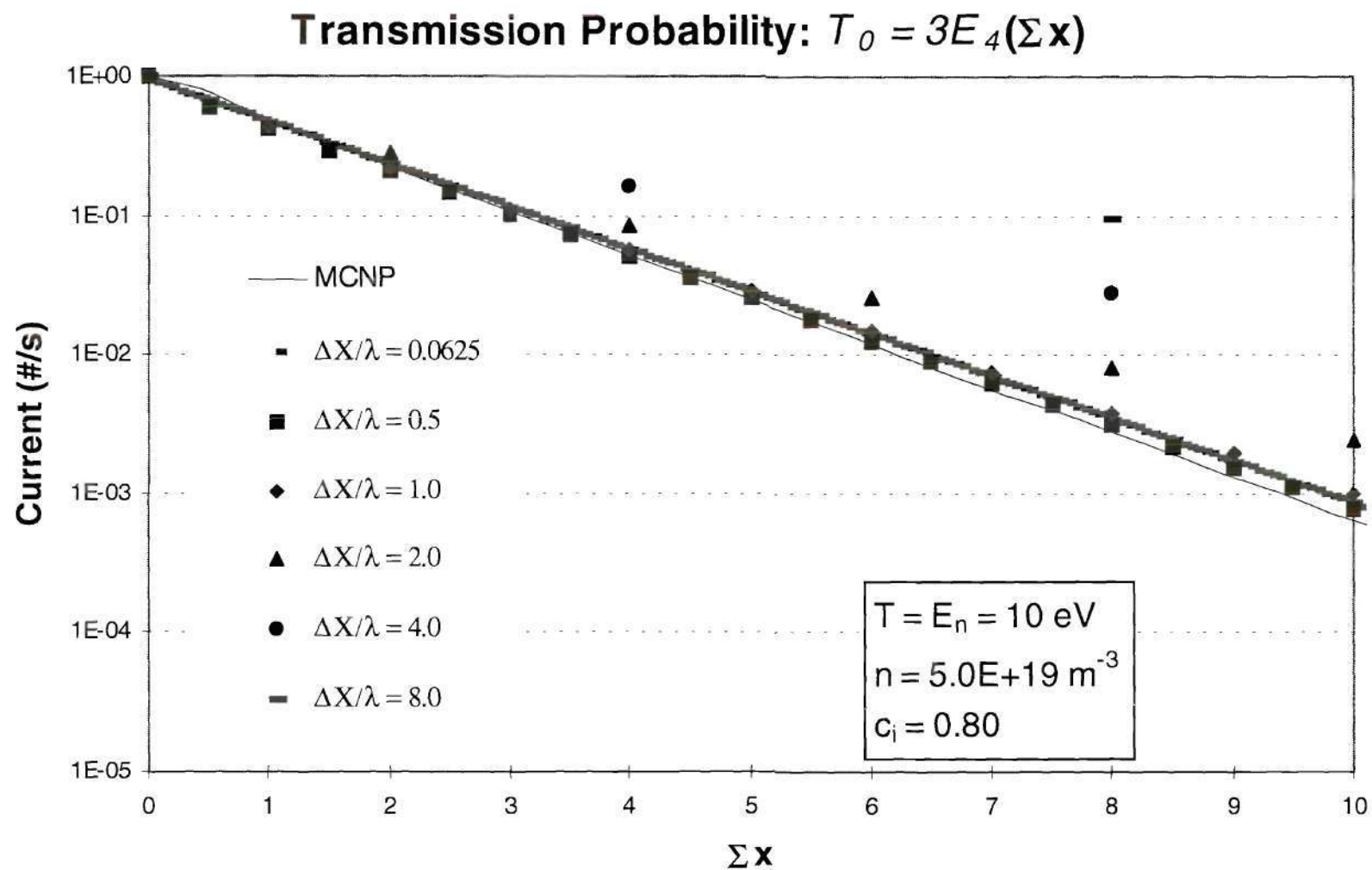
Figure 4.6. Penetration problem with transmission probability $T_0 = 3E_4(\Sigma x)$ and $c_i = 0.8$.

directionality errors appear to balance each other. In this instance, the predicted ICB currents were in excellent agreement with those predicted by Monte Carlo. When $\Delta x/\lambda < 1$, the isotropization error was dominant, causing penetration to be underpredicted. When $\Delta x/\lambda > 1$, the escape probability directionality error became quite dominant, causing the overprediction of penetration.

Figure 4.6 shows the isotropizing effect of charge-exchange and scattering on a problem where the transmission probability at each of the intermediate interfaces in the slab was calculated using $T_0 = 3E_4(\Sigma x)$, corresponding to the assumption of strong forward peaking of the flux distribution. Since the flux distribution is strongly peaked forward, the presence of charge-exchange and scattering had a modest effect on the isotropization of the uncollided fluxes for all model problems with $\Delta x/\lambda \leq 1$. This was evident from the results since the compensating of errors effect proved to be rather insensitive to the number of subdivisions in model problems with $\Delta x/\lambda \leq 1$. The results revealed that a very good agreement with Monte Carlo could be found when $\Delta x/\lambda = 0.5$. For $\Delta x/\lambda > 1$ the escape probability directionality error was very dominant relative to any isotropization error.

Since the effect of compensation of errors is a function of the amount of charge-exchange and elastic scattering found in the region, it was necessary to carry out a couple of calculations with $c_i = 0.45$. The new results are shown in figures 4.7 and 4.8. These confirmed that the isotropization and escape directionality errors tended to compensate almost exactly for $\Delta x/\lambda = 1$.

Figure 4.7. Penetration of an incident current in a slab with transmission probability $T_0 = 2E_3(\Sigma x)$ and $c_i = 0.45$.

Figure 4.8. Penetration of an incident current in a slab with transmission probability $T_0 = 3E_4(\Sigma x)$ and $c_i = 0.45$.

4.4 Compensating Errors In Penetration Problems [35,36]

With reference to figure 4.5, it is evident that charge-exchange and scattering isotropized the angular distribution function at each interface. These results clearly indicated that when the mean free path was greater than the dimension of the region ($\Delta x/\lambda < 1$) the isotropization error increased and became dominant. When $\Delta x/\lambda > 1$, the governing error was due to the directionality of the escape probability. A compensating balance was achieved when $\Delta x/\lambda = 1$.

The most likely way to correct for the anisotropy error is to use a higher order double P_n expansion of the angular flux distribution. In this manner, the method would be able to handle the increasing anisotropy of the distribution at successive interfaces. Unfortunately, this can become a very complex task with adverse effects on the computational economy of the method. The escape probability error can be handled and perhaps corrected completely by using a directional escape probability factor. This factor was introduced in chapter III. It is possible to redefine the reflection coefficient introduced in equation (2.2). Instead of an isotropic reflection, the new reflection coefficients would have a forward and backward component, namely

$$R_i^{f/b} \equiv \Lambda_{f/b}^i \frac{c_i P_{0i} \left[1 - 2E_3\left(\Delta_i \Sigma_{ti}\right)\right]}{1 - c_i\left(1 - P_{0i}\right)} \tag{4.5}$$

where

$$\Lambda_f^i \equiv \frac{1}{1 + \left(\Lambda_f/\Lambda_b\right)_i^{-1}} \quad , \quad \Lambda_b^i \equiv \frac{1}{1 + \left(\Lambda_f/\Lambda_b\right)_i} \tag{4.6}$$

92

These ratios (i.e., $\left(\Lambda_f \big/ \Lambda_b\right)_i$) are given in figure 3.17

Thus, the new transmission and reflection coefficients are $T_i = T_{oi} + R_i^f$ and $R_i = R_i^b$. The application of this directional escape probability factor to a problem with an isotropic plane source, a distribution $f \sim \mu^0$, for $c_i = 0.8$, and for $\Delta x/\lambda = 0.09 - 4.45$ is shown in figure 4.9. The uncorrected results are shown as closed symbols. The isotropization and escape directionality errors were present in all the uncorrected results. Once again, when $\Delta x/\lambda < 1$, the dominant error was due to the isotropization assumption, which caused penetration to be underpredicted. When $\Delta x/\lambda > 1$, the escape probability directionality error was the governing error in the problem, causing penetration to be overpredicted. When the escape directionality factor was applied, the second error was eliminated, leaving only the isotropization error. The underprediction of penetration is clearly evident. By suppressing the escape directionality error, all the results for $\Delta x/\lambda = 1$, 2.2, and 4.45 collapsed to a result (open symbols) that showed only the isotropization error. The corrected results did not have good agreement with Monte Carlo, but rather had selfconsistency.

4.5 Effective Transmission and Reflection Probabilities [35,36]

In the previous problem, the isotropization and escape probability directionality errors balanced each other for the uncorrected $\Delta x/\lambda = 1$ results (closed symbols). These results agreed quite well with the predicted Monte Carlo results. This fact was used to generate a
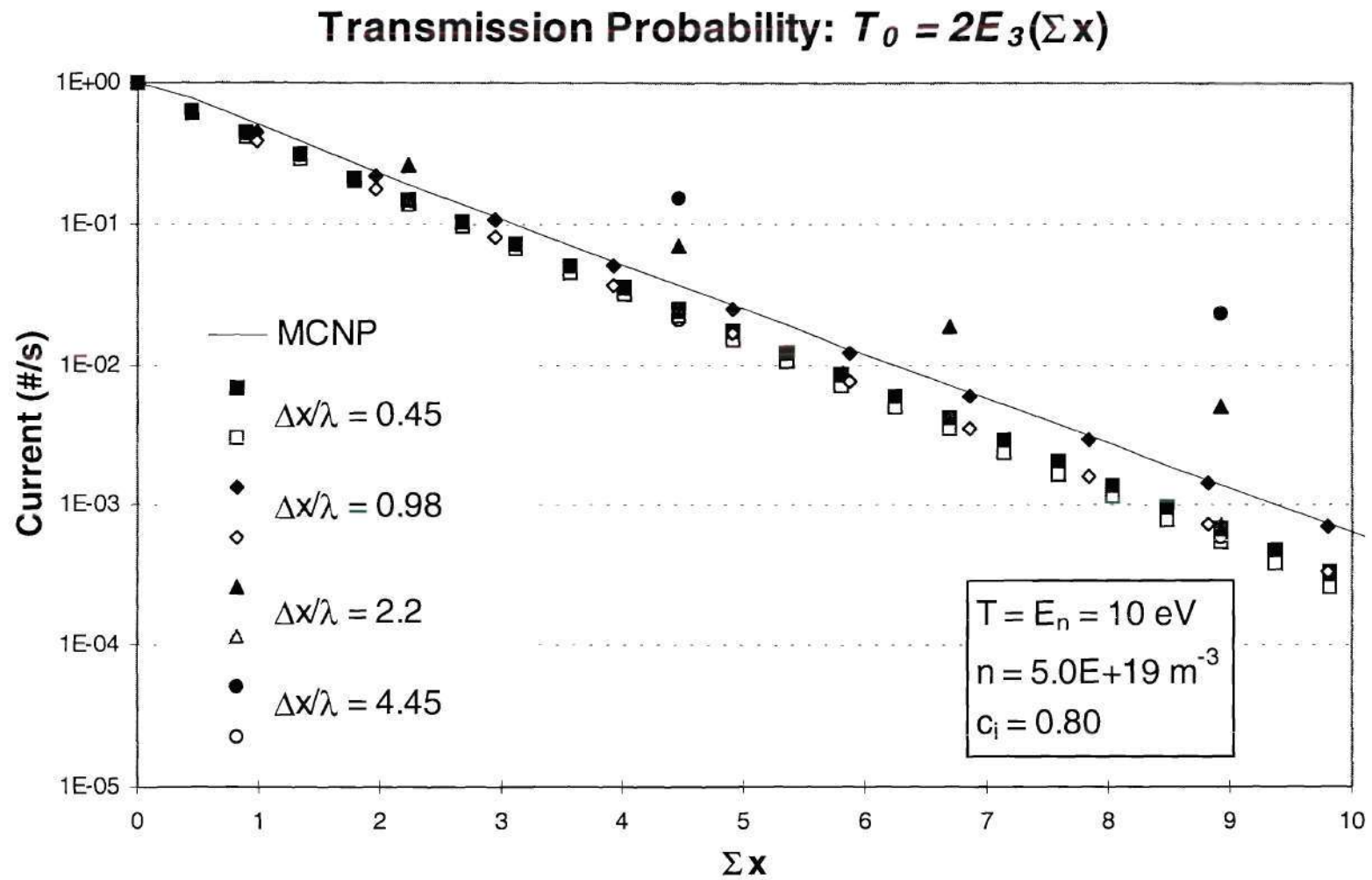
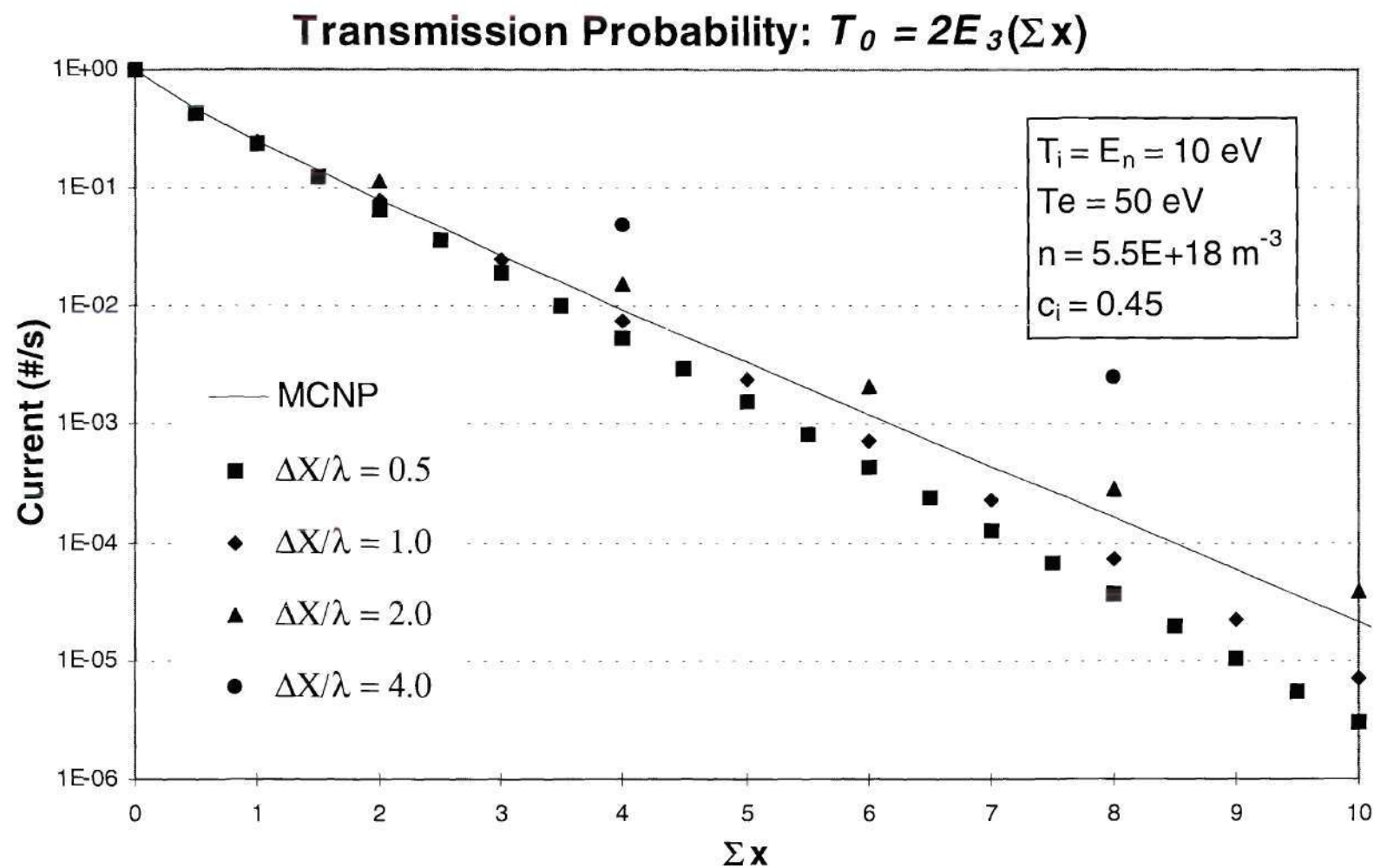Figure 4.9. Penetration of an incident current in a slab with transmission probability $T_0 = 2E_3(\Sigma x)$ and $c_i = 0.8$ (closed symbol uncorrected, open symbol corrected).

set of effective transmission and escape probabilities for regions in which $\Delta x/\lambda \neq 1$ (i.e., $\Delta x/\lambda = 1/3$, ½, 1, 2, 3, etc). This was accomplished by solving the matrix equation

$$k\left(\frac{\Delta}{\lambda} = n\right) = \left[k\left(\frac{\Delta}{\lambda} = 1\right)\right]^n \qquad (4.7)$$

This matrix k is the right hand side of equation (2.25). A few of these effective transmission and reflection coefficients are shown in table 4.1. The application of these effective coefficients was demonstrated by solving the same problem used in the previous section. The results are shown in figure 4.10. The closed symbols represent the uncorrected results. The open symbols represent the results obtained with the effective transmission and reflection probabilities. It is clear that by using coefficients $\Delta x/\lambda = 1$ as the basis of the matrix in equation (4.7), the net effect of both isotropization and escape probability directionality errors was minimized. The new results were in very good agreement with the results predicted by Monte Carlo. It is evident that the use of this approach showed results far superior than the use of an escape probability directionality factor alone. In this latter approach both errors were systematically reduced.

Figure 4.11 shows the results of the application of the effective coefficients to a problem with a cosine plane source, a distribution $f \sim \mu^0$, $c_i = 0.8$, and for $\Delta x/\lambda = 0.09 - 4.45$.

Table 4.1. Effective Transmission and Reflection Probabilities

Δ/λ	$\hat{T}_i$	$\hat{R}_i^b$
½	$\left[T_i \left(1 - \left(\dfrac{\frac{1}{2} c_i \hat{P}_i}{1 + T_i} \right)^2 \right) \right]^{\frac{1}{2}}$	$\dfrac{\frac{1}{2} c_i \hat{P}_i}{1 + T_i}$
1	T_i	$\frac{1}{2} c_i \hat{P}_i$
2	$\dfrac{T_i^{\,2}}{1 - \left(\frac{1}{2} c_i \hat{P}_i \right)^2}$	$\frac{1}{2} c_i \hat{P}_i \left[1 + \dfrac{T_i^{\,2}}{\left(1 - \left(\frac{1}{2} c_i \hat{P}_i \right)^2 \right)} \right]$
3	$\dfrac{T_i^{\,3}}{\left(1 - \left(\frac{1}{2} c_i \hat{P}_i \right)^2 \right)^2 - \left(\frac{1}{2} c_i \hat{P}^2_{\ i} \right) T_i^{\,2}}$	$\frac{1}{2} c_i \hat{P}_i \left[1 + \dfrac{T_i^{\,2} \left(1 - \left(\frac{1}{2} c_i \hat{P}_i \right)^2 \right) + T_i^{\,4}}{\left(1 - \left(\frac{1}{2} c_i \hat{P}_i \right)^2 \right)^2 - \left(\frac{1}{2} c_i \hat{P}_i \right)^2 T_i^{\,2}} \right]$

Where $\hat{P} = P\left(1 - T_{0i} \right)$
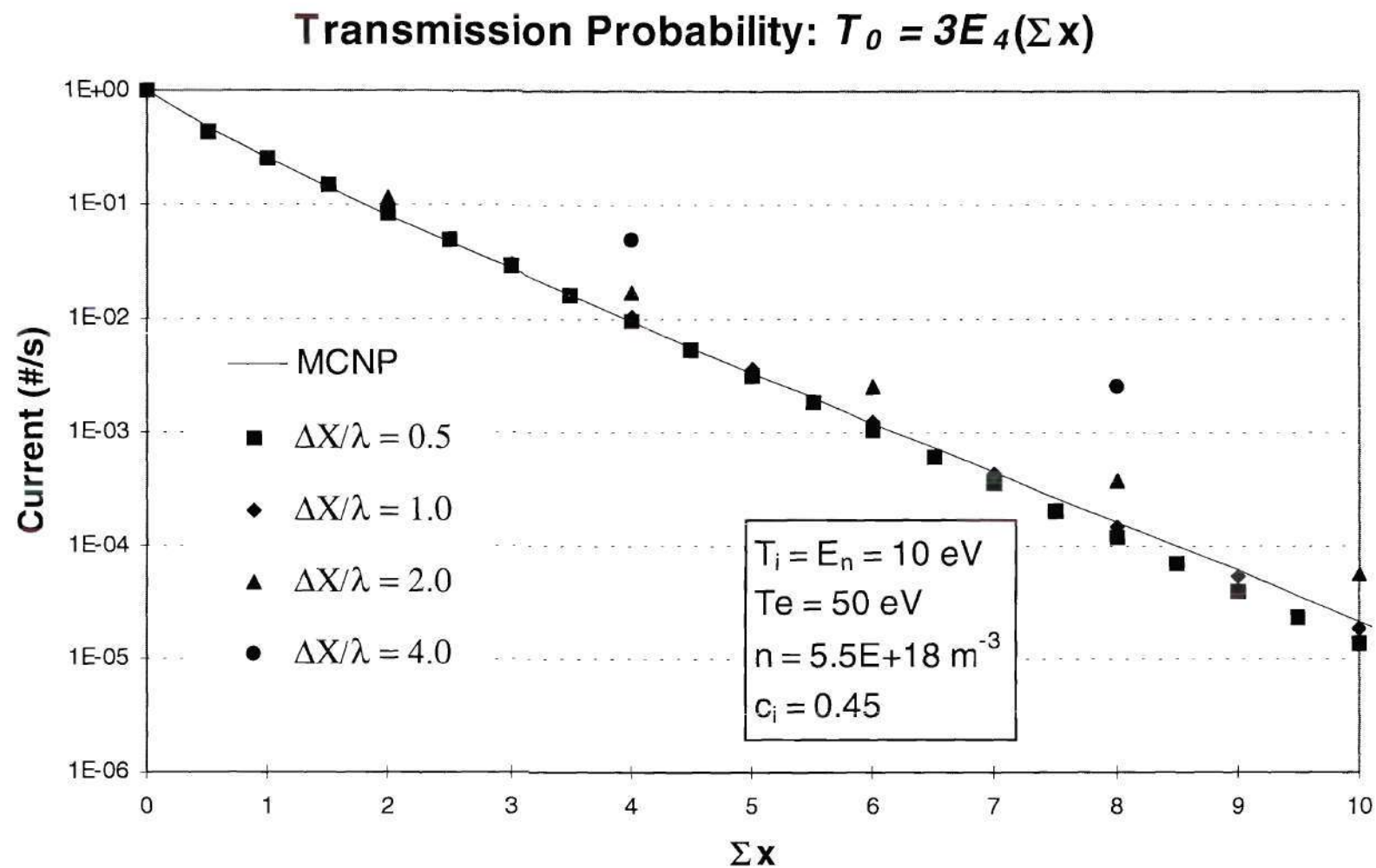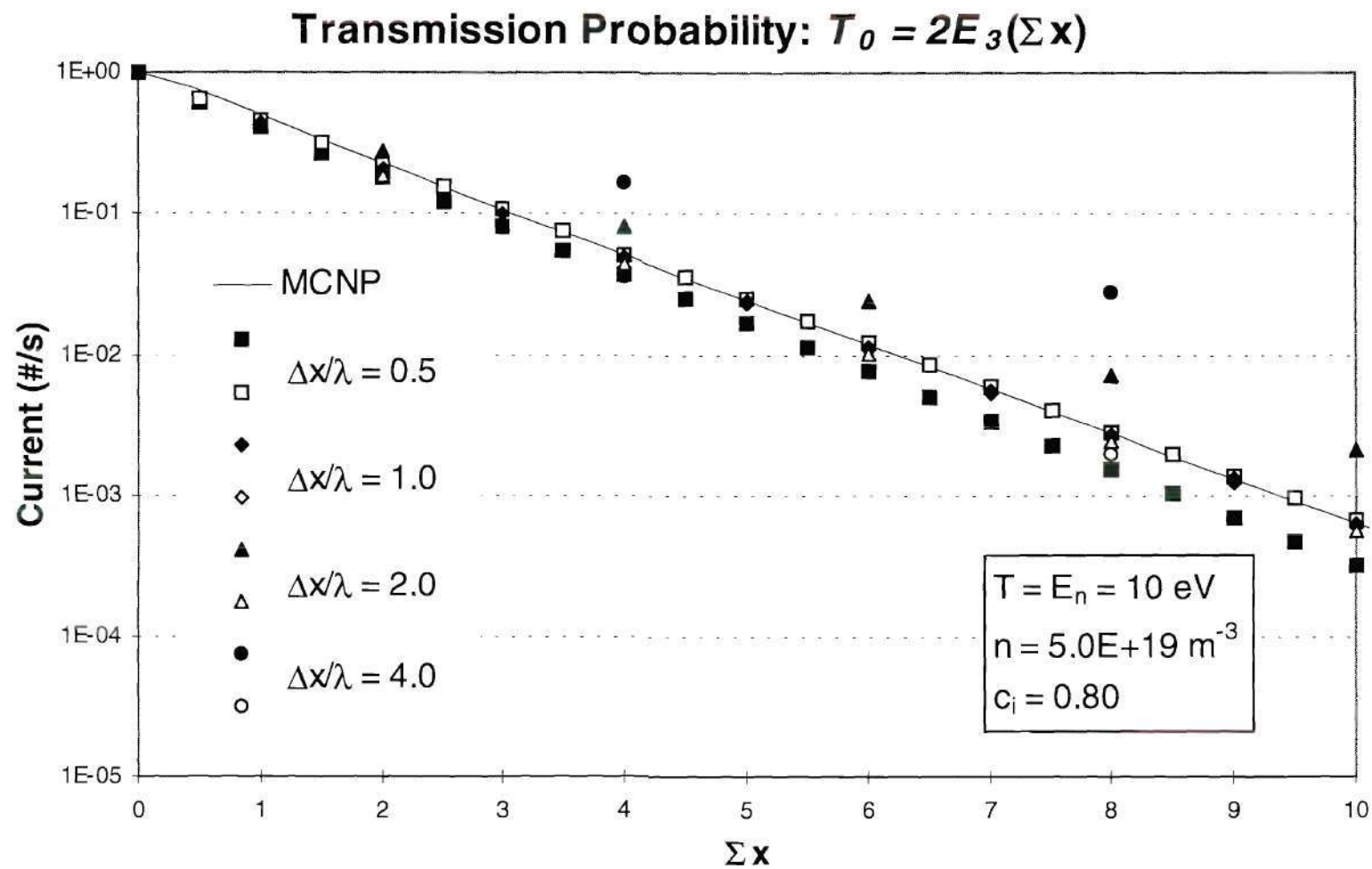
Figure 4.10. Penetration of an incident current in a slab with transmission probability $T_0 = 2E_3(\Sigma x)$ and $c_i = 0.8$ using effective transmission and reflection probabilities (closed symbol uncorrected, open symbol corrected).
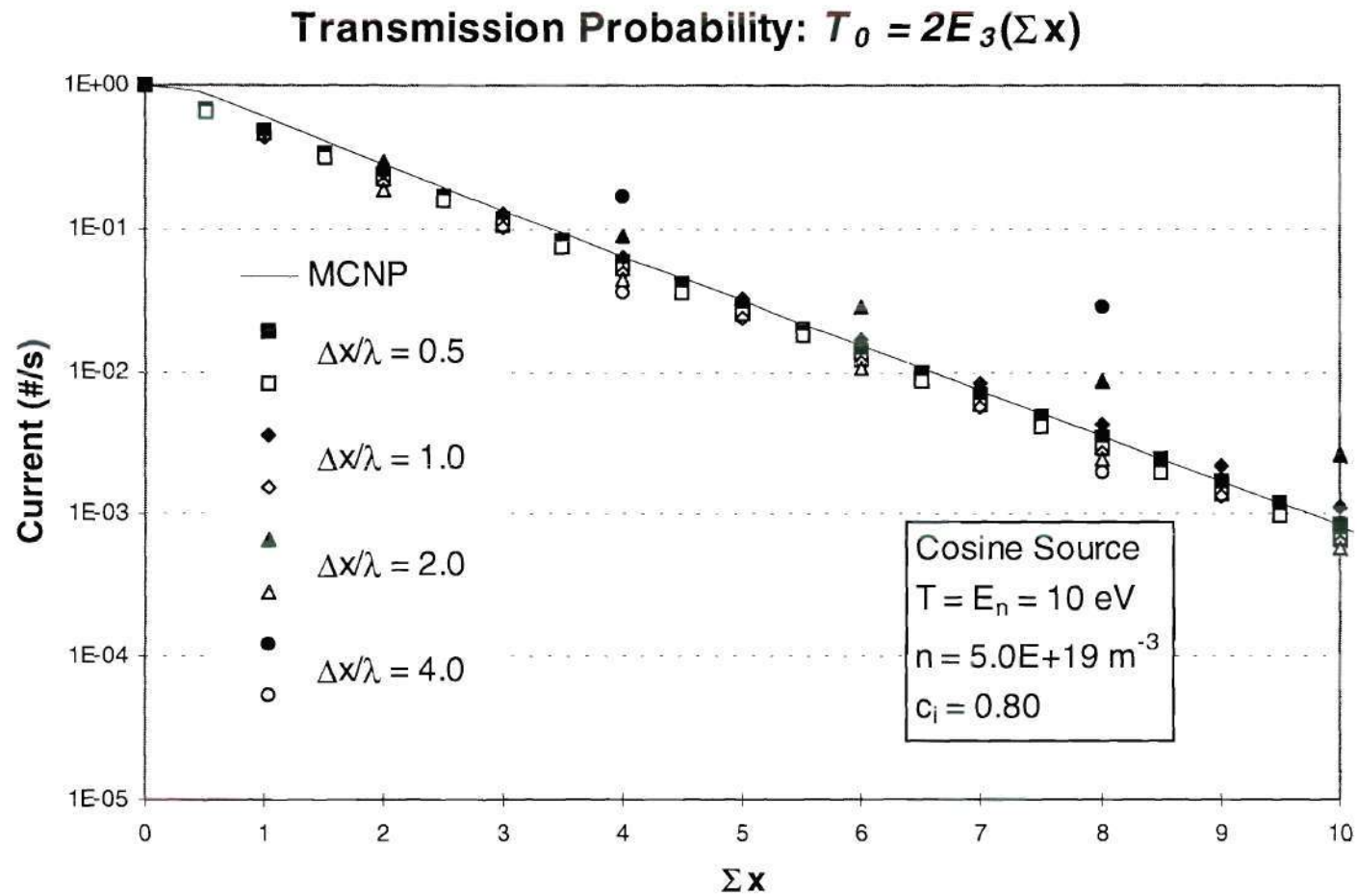
Figure 4.11. Penetration of an incident current (produced by a cosine source) in a slab with transmission probability $T_0 = 2E_3(\Sigma x)$ and $c_i = 0.8$ using effective transmission and reflection probabilities (closed symbol uncorrected, open symbol corrected).

4.6 Characterization of Nonuniform Regions [35, 36]

This section discusses the accuracy of using an average mean free path, λ_{av}, (based on an average plasma parameters) which characterizes a nonuniform medium, in the calculation of transmission probability T_0. In general

$$T_0 = (n+2)E_{n+3}(\alpha(\Delta))$$
$$\alpha(\Delta) = \int_0^\Delta \frac{dx}{\lambda(x)} \tag{4.8}$$

where $\alpha(\Delta)$ represents the optical thickness of the region [17]. It is clear that T_0 is a function of the optical thickness along the total path traveled. It is possible, at least in principle, to calculate the actual optical thickness of the region exactly. Unfortunately, this can become a computational-intensive task in nonuniform regions. Thus, it was computationally desirable to approximate $\alpha(\Delta)$ by means of an "average" mean free path, λ_{av}. The simplest way to accomplish this was by using a linear average, namely

$$\lambda_{av} = \lambda\left(\tfrac{x_1+x_2}{2}\right) \tag{4.9}$$

where x represents the quantity being averaged (i.e., temperature or density) and the subscripts 1 and 2 represent the boundaries of the region.

The expression (4.9) was evaluated using the above prescription for the λ_{av}. This calculation was done on a 50 cm thick slab region subject to two nonuniform situations. In the first case, the temperature was allowed to vary linearly while the density remained constant at 5×10^{18} m^{-3}. In the second case, the density was allowed to vary linearly while

the temperature remained fixed at 10 eVs. The evaluation was done for mediums with several optical thicknesses. Both situations are illustrated in figure 4.12.

The results of this study can be seen in table 4.2. For optically thick regions with a temperature range of 1 - 10 eVs, the error was about 10%. Over the same temperature range, but for an optically thin region, the error was not greater than 1.4%.

Table 4.2. $T_0 \equiv 2E_3(\Delta/\lambda_{av})$ for Slab with Linear Temperature Variation, Uniform Density

T (ev)	100 - 50	100 - 10	100 - 1	10 – 1
Optical Thickness	2.130	2.252	2.244	2.164
T_0 **exact**	0.0513	0.0441	0.0446	0.0492
T_0 (λ_{av})	0.0517	0.0429	0.0410	0.0543
Error %	0.78	2.72	8.07	**10.3**

T (ev)	100 - 50	100 - 10	100 - 1	10 – 1
Optical Thickness	0.213	0.225	0.224	0.216
T_0 **exact**	0.6891	0.6757	0.6765	0.6854
T_0 (λ_{av})	0.6898	0.6731	0.6692	0.6943
Error %	0.07	0.38	1.07	1.3

The results, shown in table 4.3, revealed that T_o could be predicted exactly in all problems with a nonuniform density distribution. This was due to the fact that $\lambda^{-1} \equiv \Sigma = n\sigma(T)$, but more importantly because the density was allowed to vary only linearly and also because the TEP-based code GTNEUT does not include density-dependent electron impact ionization cross section data.

100
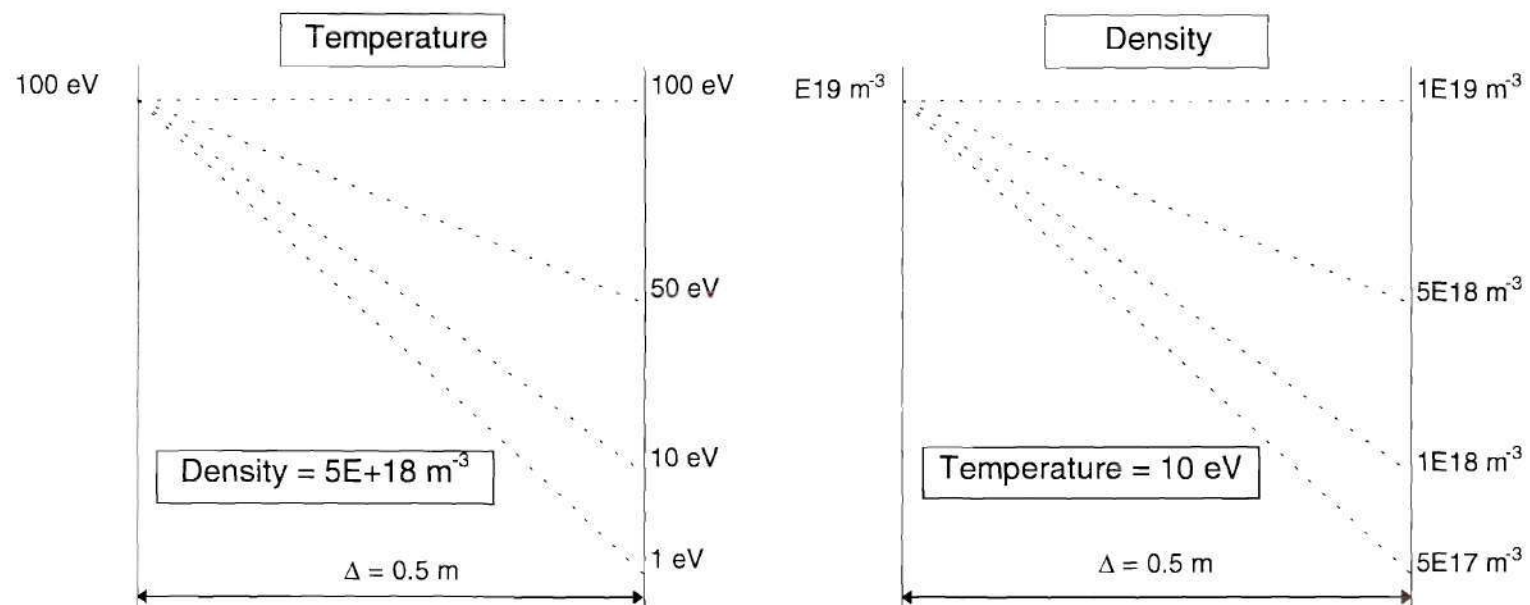
Figure 4.12. Temperature and density distributions for a nonuniform region model.

Table 4.3. $T_0 \equiv 2E_3(\Delta/\lambda_{av})$ for Slab with Linear Density Variation, Uniform Temperature

n (m^{-3})	1E19 -5E18	1E19 -1E18	1E19 –5E17
T_0 exact	0.011749	0.034224	0.039226
T_0 (λ_{av})	0.011749	0.034224	0.039226
Error %	0.0	0.0	0.0

Based on these results, the error that was introduced in calculating the uncollided fraction, T_0, of incident particles transmitted through a medium with a nonuniform temperature distribution was small enough to justify the use of an average mean free path. The same was valid for regions with a linear density distribution.

4.7 Neutral Energy Dependency

It is evident that both the transmission and escape probabilities depend on the mean free path of the particle.

$$\Sigma = \lambda^{-1} = \frac{n\langle \sigma v(T_n)\rangle}{v_n} = \frac{n\langle \sigma v(T_n)\rangle}{\sqrt{\frac{2T_n}{m}}} = \frac{n\langle \sigma v(T_n, T_i)\rangle}{\sqrt{\frac{2E_n}{m}}} \qquad (4.10)$$

It is important to keep in mind that the reaction rate $\langle \sigma v \rangle$ can also be a function of ion temperature, ion density, or electron density and that the mean free path is inversely proportional to the energy of the neutral. The original version of the TEP-based code, GTNEUT, assumed that the neutral energy remained fixed throughout the lifetime of the neutral. This assumption is valid in a medium where the neutral can travel undisturbed,

such as in a vacuum or in a medium with very little scattering. However, in a medium with strong scattering and/or charge-exchange, such as in front of a divertor plate, this assumption breaks down. The neutrals can either gain or lose energy through successive scattering or charge-exchange with energetic ions. A more realistic assumption might be that after a collision event, a neutral acquires some or all the energy of the ion. Another possibility might be that a neutral attains an average energy based on the local energy distribution of the ions in the region in question. Therefore, for a number of divertor conditions, the assumption that the neutral gains a Maxwellian energy distribution at the local ion temperature seems more plausible.

The previous sections in this chapter demonstrated that in model problems characterized by a directional flow of particles, transport was sensitive to isotropization and escape directionality effects. It was noted, however, that both effects tended to balance each other when $\Delta x/\lambda \approx 1$. It was observed, in this instance, that in uniform one-dimensional multiregion problems the TEP-based code GTNEUT and Monte Carlo agreed well. It was assumed in these problems that the neutrals had a Maxwellian energy distribution characterized by the local ion temperature of the region in question. Under these circumstances, energy effects were minor or not noticeable given the magnitude of the isotropization and escape directionality effects. Energy effects could be more noticeable in nonuniform multiregion problems, particularly in problems where $\Delta x/\lambda \approx 1$ (since both isotropization and escape directionality effects compensate for each other).

In order to evaluate the assumption that the neutrals acquire an energy corresponding to a Maxwellian at the local ion temperature, two nonuniform one-dimensional multiregion

103

problems were tested. Both models consisted of ten regions subjected to a linear temperature distribution and uniform density. Vacuum boundary conditions were imposed on the left and right surfaces of the models and a source of puffed neutrals with strength equal to 1 #/s was located on the left boundary. In the first model the temperature varied from 10 eV on the left boundary, to 100 eV on the right boundary. In the second model, it varied from 1 eV to 10 eV over the corresponding boundaries. The characteristic dimension Δx of each region was set equal to the mean free path of the neutral in the region, thus forcing the necessary condition for which isotropization and escape directionality effects are minimized (i.e., $\Delta x / \lambda = 1$). The charge-exchange and scattering fraction in the first model problem varied between 0.78, in the first region to 0.59 in the last region. In the second model, this varied from 1.0 in the region next to the source to 0.78 in the rightmost region. The first model is illustrated in figure 4.13. A similar arrangement was used in the second model.

In GTNEUT, the neutral puff had a Maxwellian energy distribution at the local ion temperature of the first region. In DEGAS, neutrals were also puffed and their energy also corresponded to a Maxwellian distribution at the ion temperature of the first region. While in GTNEUT the angular distribution of the puffed neutrals was isotropic, in DEGAS this was cosine distributed.

The GTNEUT calculation assumed that the neutrals going from region to region acquired a Maxwellian energy distribution at the local ion temperature of the region in question, i.e., $E_n = T_i$. DEGAS, on the other hand, calculated a continuous energy distribution.
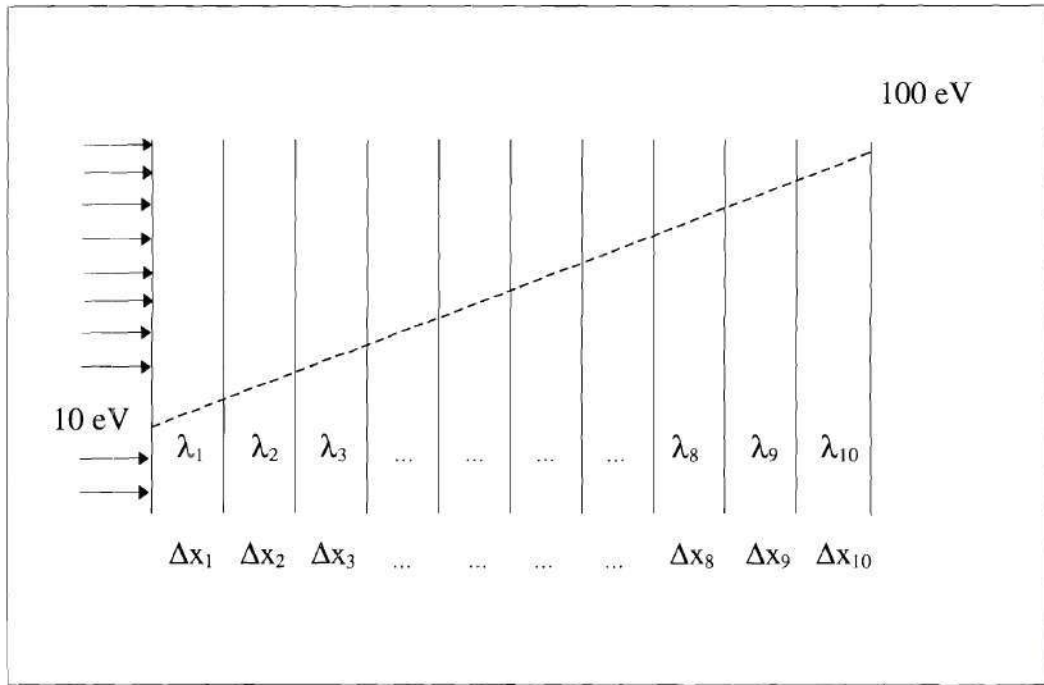
Figure 4.13. Temperature distribution and spatial arrangement for a nonuniform multiregion model.

The results of the GTNEUT and DEGAS predictions showing the ionization rate can be seen in figures 4.14 and 4.15. These figures also show the GTNEUT prediction for a neutral puff with fixed energy ($\times$ symbol). The predicted results of the GTNEUT and DEGAS codes for the local ion temperature model showed excellent agreement in both model problems. However, the results for the constant neutral energy model showed some larger discrepancies, particularly in deep penetration. With reference to equation 4.10, by assuming that the neutral energy is constant, the predicted neutral energy should underpredict the actual neutral energy (which should be approximately a Maxwellian at the local ion temperature). Furthermore, this assumption would cause the neutral velocity to be underpredicted in regions where there are large differences between the constant
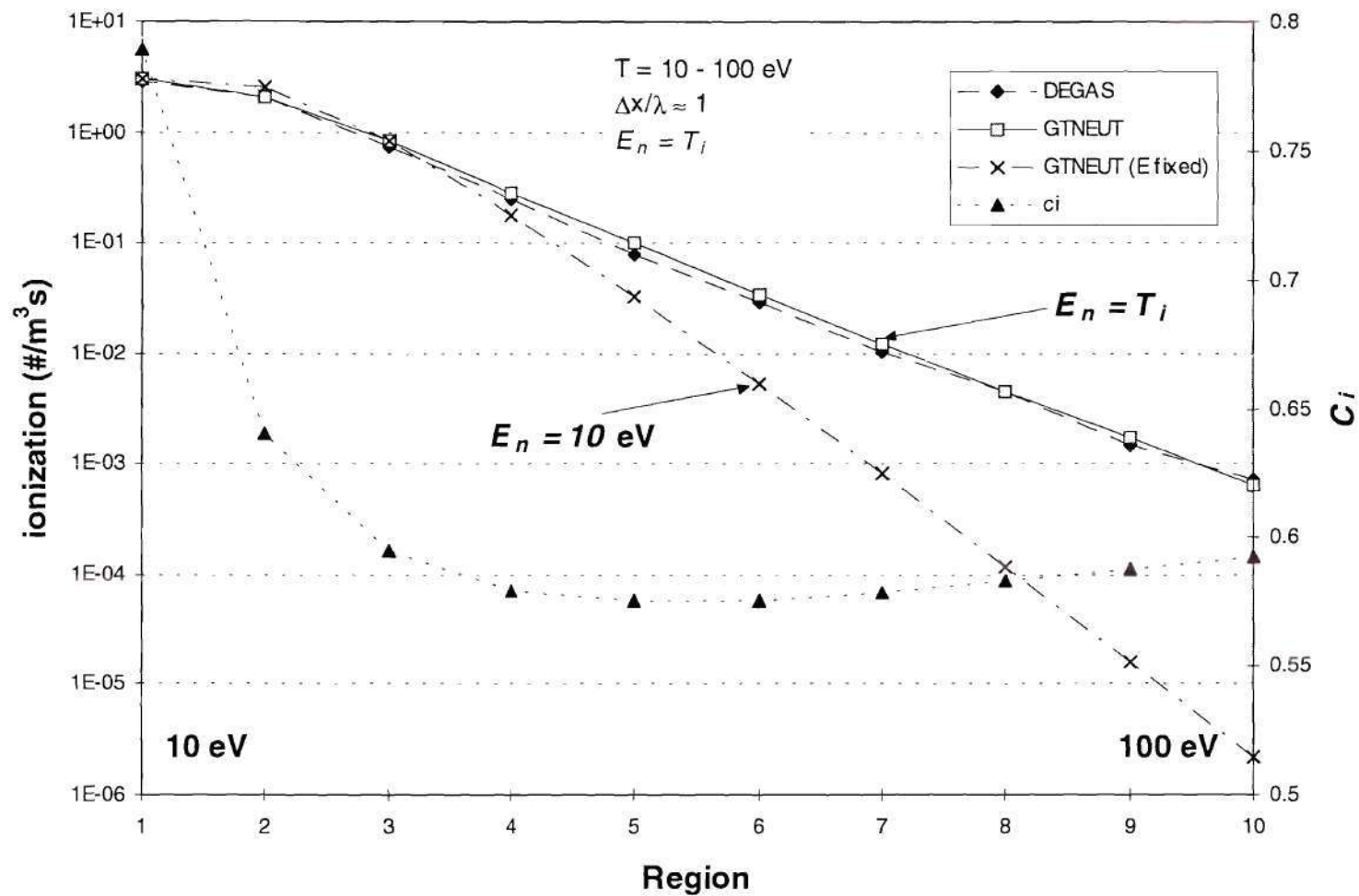
Figure 4.14. Ionization rate in a problem with linearly varying temperature. Neutral energy equal to the local ion temperature ($\square$), $E_n = T_i$. Fixed neutral energy ($\times$), $E_n = 10$ eV.
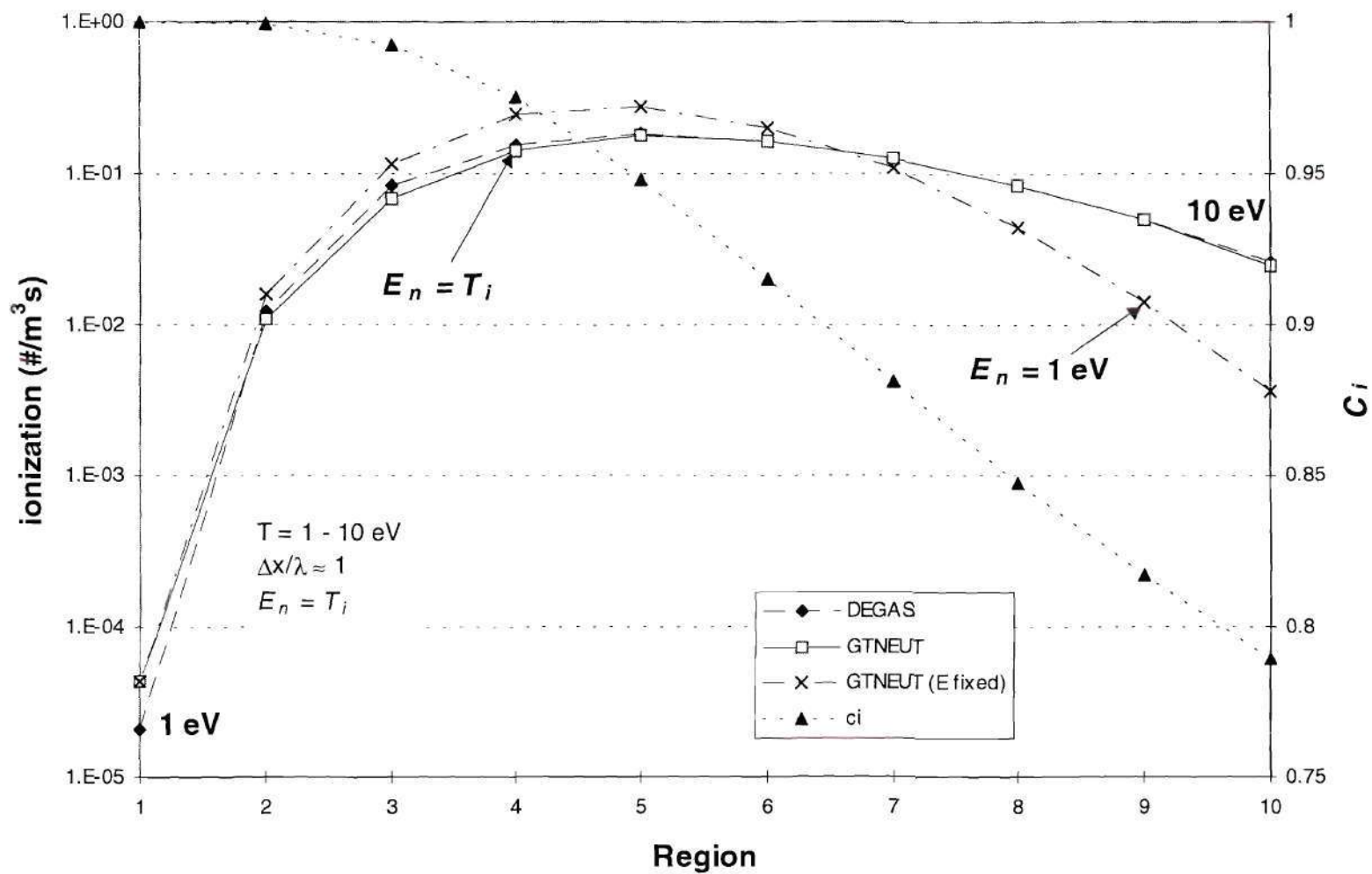
Figure 4.15. Ionization rate in a problem with linearly varying temperature. Neutral energy equal to the local ion temperature ($\square$), $E_n = T_i$. Fixed neutral energy ($\times$), $E_n = 1$ eV.

neutral energy and the local ion temperature. It should be clear that $\langle \sigma v \rangle_{ion}$ is not affected since it depends primarily on the electron temperature. However, the quantity that would be more affected by the constant energy model would be $\langle \sigma v \rangle_{cx}$ and $\langle \sigma v \rangle_{elas}$ since they depend on E_n and T_i. Thus, the constant neutral energy model would tend to underpredict $\langle \sigma v \rangle_{cx}$ and $\langle \sigma v \rangle_{elas}$. Since v_n and $\langle \sigma v \rangle_{cx}$ are underpredicted, the net results would be the overprediction of the mean free path (longer mean free path) which in turn would cause the underprediction of penetration. This effect is clearly visible in figure 4.14 and 4.15. The results of these two nonuniform one-dimensional model problems demonstrate that the assumption that the neutrals acquire a Maxwellian energy distribution with the local ion temperature is adequate and that it would not limit the accuracy of the calculation. They also suggest that a full treatment of the neutral energy dependence would not be necessary, although it could be very useful in more practical applications.

4.8 Conclusions

By assuming that the uncollided and collided components of the angular flux are isotropic at each interface, a considerable amount of error was introduced in the calculation of the penetration of the uncollided flux component. This error (underprediction of penetration) became progressively larger wherever $\Delta x / \lambda < 1$.

The study indicated that by assuming that the spatial distribution of the collision rate due to scattering is uniform, an escape directionality error was introduced. This error was manifested in the failure to account for the predominant escape of particles back across the

incident surface. Subsequently, this error caused an overprediction of penetration wherever $\Delta x/\lambda > 1$.

The Monte Carlo and GTNEUT comparison indicated that the isotropization and escape probability directionality errors tended to balance almost exactly in regions where $\Delta x/\lambda = 1$.

It was demonstrated that the directional error could be eliminated by making use of an escape directionality factor (shown in figure 3.17) which was a function of $\Delta x/\lambda$ and c_i. A more effective way to correct the isotropization and escape directionality errors relied on the fact that both errors compensated for each other when $\Delta x/\lambda = 1$. This served as the basis for defining a new set of effective transmission and reflection probabilities.

The accuracy of using a mean free path calculated at the average plasma parameters to characterize a nonuniform region was demonstrated. A simple linear average of the form $\lambda_{av} = \lambda(x_1 + x_2)/2$ generated an error of 10% or less in regions with temperature distributions typically found in edge plasmas.

Finally, the results of nonuniform multiregion problems indicated that the energy of the neutrals can be described adequately by a Maxwellian energy distribution with the local ion temperature.

CHAPTER V

TRANSPORT IN 2D MULTIREGION PROBLEMS

5.1 Introduction

In chapter III, the various assumptions involved in the calculation of the transmission and escape probabilities were discussed, and the errors to be expected in the calculation of transport within and across a single region were evaluated. In chapter IV, the cumulative effect of these various assumptions on multiregion calculations were evaluated for one-dimensional geometry. The purpose of this chapter is to evaluate the cumulative effect of the various assumptions in two-dimensional model problems.

5.2 Transport in a Uniform Nine Region Model

The purpose of this section is to explore the transmission and escape probabilities approximations in a two-dimensional multiregion setting. The main objective was to determine how good the approximations were in model problems that are sensitive to these aspects of the calculation. The model used was a square region composed of nine identical cells. The characteristic dimension of each cell was $\Delta x = 0.30$ m. The model had uniform plasma conditions and vacuum or reflective boundary conditions on the four surfaces of the box. An incident flux of particles entered the right surface of the sixth cell. The same cell arrangement and plasma parameters were used to run the Monte Carlo and GTNEUT simulations. The cell arrangement is illustrated in figure 5.1.

110
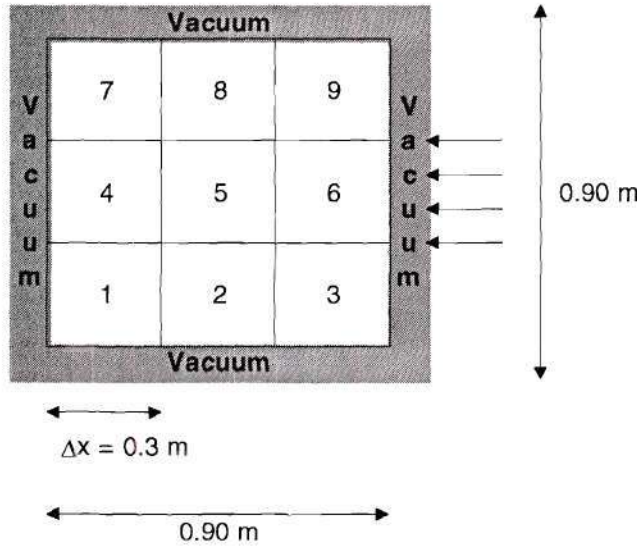
Figure 5.1. Nine uniform regions model.

There were three regimes of particular interest: $\Delta x/\lambda > 1$, $\Delta x/\lambda < 1$, and $\Delta x/\lambda \approx 1$. As stated earlier, the TEP method assumes that there is an isotropic angular distribution at each of the interfaces. Furthermore, it assumes that for a uniformly distributed first collision source, the directional escape probability Λ_{ij} is proportional to the surface area of each cell (in the case of the square, Λ_{ij} for each of the surfaces is equal to 0.25). It was found in the one-dimensional model problems discussed in chapter IV that 1) the isotropization assumption introduced an underprediction of penetration error which increased with increasing mean free path in the region, and that 2) the assumption of Λ_{ij} proportional to the surface area introduced an overprediction of penetration error which increased with decreasing mean free path in the region, for problems with an incident surface flux on one of the boundaries. Both

111

errors were found to increase with the number of interfaces (regions) in the problem. These assumptions are illustrated schematically in figure 5.2
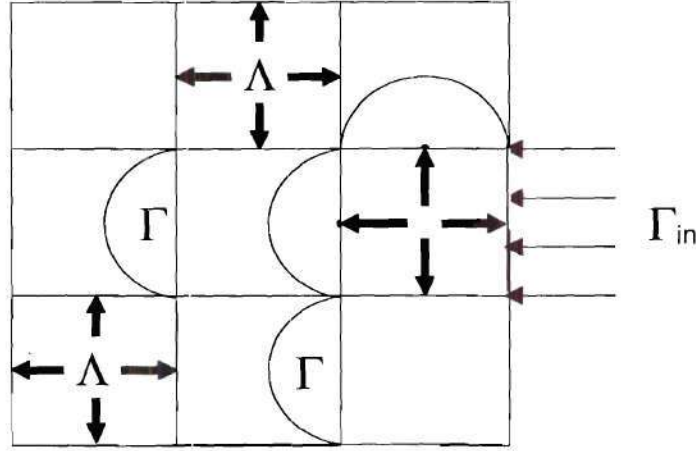
Figure 5.2. Assumptions made by the TEP method.

In the first case considered, the temperature was fixed at 10 eV, and the density at 1×10^{19} m^{-3}. The fraction of charge-exchange/elastic scattering in this problem was $c_i = 0.8$. The mean free path of the neutral was $\lambda = 0.112$ m., which was smaller than the characteristic dimension of each cell (i.e., $\Delta x/\lambda = 2.7$). For $\Delta x/\lambda \gg 1$, the directional escape probability error should be dominant over the isotropization error, resulting in a net overprediction of penetration. The first collision source distribution was peaked towards the entering surface. This caused the true escape probability over the entering surface to be greater than the escape probability over the opposite surface (between regions 6 and 5). The escape directionality error (due to the assumption that $\Lambda = 0.25$ for all surfaces) caused the overprediction of particles emerging from the opposite surface of region 6 into region 5. In other words, penetration was

112

overpredicted. Thus, the particle ionization rate predicted by GTNEUT was expected to be greater than that predicted by Monte Carlo in the cells further away from the source (i.e., cells 1, 4, 7, 2, 5, 8), and indeed it was. With reference to figure 5.3, the results for cell 6 were in excellent agreement with Monte Carlo because the total escape probability (i.e., total number of particles leaving the cell) was the same for both GTNEUT and Monte Carlo. The results in cells 3 and 9 were also in good agreement because the directional escape probability from region 6 across the lateral surfaces into regions 3 and 9 was not sensitive to the distribution of the first collision source rate.

Recalling from chapter III that GTNEUT assumes an isotropic distribution of wall reflected neutrals and that DEGAS uses a specular reflection condition (for the "mirror" material option), but that when $\Delta x/\lambda \gg 1$ the specularly reflected particles are isotropized near the point of reflection by scattering and charge-exchange, the use of reflecting boundary conditions was not expected to introduce any false differences between the GTNEUT and DEGAS calculations.

The vacuum boundary conditions were replaced with a reflective condition on the top, bottom, and right surfaces, and the calculations were repeated. As shown in figure 5.4, the differences between the GTNEUT and DEGAS calculations were similar to those with vacuum boundary conditions and arose primarily from the directional escape probability error in GTNEUT.

Figure 5.3. Ionization rate density for nine regions model with $\Delta x/\lambda = 2.7$, vacuum boundary conditions, and $c_i = 0.8$.

Figure 5.4. Ionization rate density for nine regions model with $\Delta x/\lambda = 2.7$, reflective boundary conditions, and $c_i = 0.8$.

115

In the second case, the ion density was equal to 1×10^{18} m^{-3}. The temperature and the amount of charge-exchange/elastic scattering were identical to those in the first case. The mean free path of the neutrals was $\lambda = 1.12$ m. so that $\Delta x/\lambda = 0.26 \ll 1$. When the characteristic dimension of the region was smaller than the mean free path of the particle, the uncollided fluxes became more forward-peaked while traversing the region, thus introducing an increasing isotropization error at each new interface. This isotropization error underpredicts penetration and would be expected to dominate the directional escape probability error for $\Delta x/\lambda \ll 1$. This would cause the ionization rate predicted by GTNEUT to be less than that predicted by Monte Carlo in the cells away from the source (i.e., cells 1, 2, 4, 5, 7, 8). This result can be observed in figure 5.5. It is also noteworthy that the results in cells 3, 6, and 9 were in excellent agreement with Monte Carlo. The reason for this is the same as in the first case (i.e., correct total escape from cell 6 and fractional escape from cell 6 into cells 3 and 9).

Replacing the vacuum boundary condition on the top and bottom with a specular reflective condition generally increases the right-to-left penetration of incident particles in the DEGAS calculation, whereas the isotropic reflective condition used in GTNEUT has no tendency to bias the penetration. The reflective condition on the right and lateral side boundaries would tend to increase the number of neutrals in the problem relative to the case with vacuum boundary conditions. The effect of the reflective boundary conditions can be seen by comparing the ionization rates in regions 1, 4, and 7 between figures 5.5 (vacuum) and 5.6 (reflective).

116

Figure 5.5. Ionization rate density for nine regions model with $\Delta x/\lambda = 0.26$, vacuum boundary conditions, and $c_i = 0.8$.

Figure 5.6. Ionization rate density for nine regions model with $\Delta x/\lambda = 0.26$, reflective boundary conditions, and $c_i = 0.8$.

In the third case, the ion density was equal to 3.7×10^{18} m^{-3}. The temperature and the amount of charge-exchange and scattering were identical to those in the first case. The mean free path of the neutrals was $\lambda = 0.30$ m. When the mean free path was equal to the characteristic dimension of the region (i.e., $\Delta x/\lambda = 1$), the isotropization and directional escape probabilities errors tended to balance each other. Thus, a good agreement was to be expected. This agreement can be seen clearly in figure 5.7.

Substituting the vacuum conditions on the top, bottom, and right surfaces with a reflective surface would be expected to cause DEGAS to predict more penetration than GTNEUT because of the specular reflection in DEGAS; however, comparison of figures 5.8 and 5.7 indicates that this effect is very small for $\Delta x/\lambda = 1$. It is interesting to note that cells 3 and 9 had two wall segments bordering them. This explains the higher ionization rate predicted by GTNEUT than by DEGAS, since the contribution from the isotropic reflection from the walls was greater than in Monte Carlo.

Similar effects were observed in a problem with a characteristic $\Delta x/\lambda = 1$, but with a $c_i = 0.6$. Figures 5.9 and 5.10 illustrate this point. Once again, the effects of the isotropic reflection condition, present in GTNEUT, were clearly observed in two of the corner cells (i.e., cells 3 and 9) shown in figure 5.10. The contribution from the wall segments around these cells was greater than any other cell.
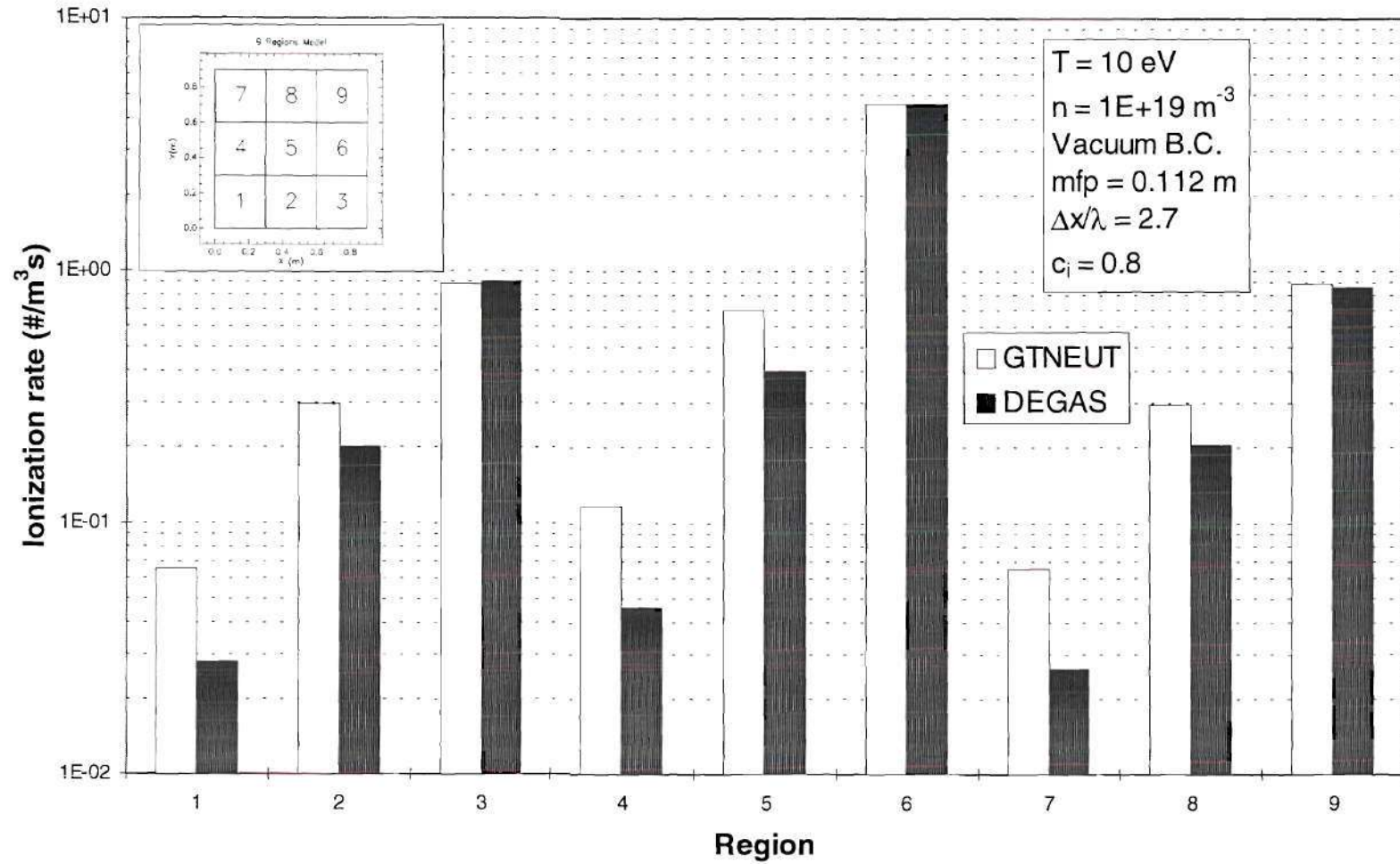
Figure 5.7. Ionization rate density for nine regions model with $\Delta x/\lambda = 1.0$, vacuum boundary conditions, and $c_i = 0.8$.
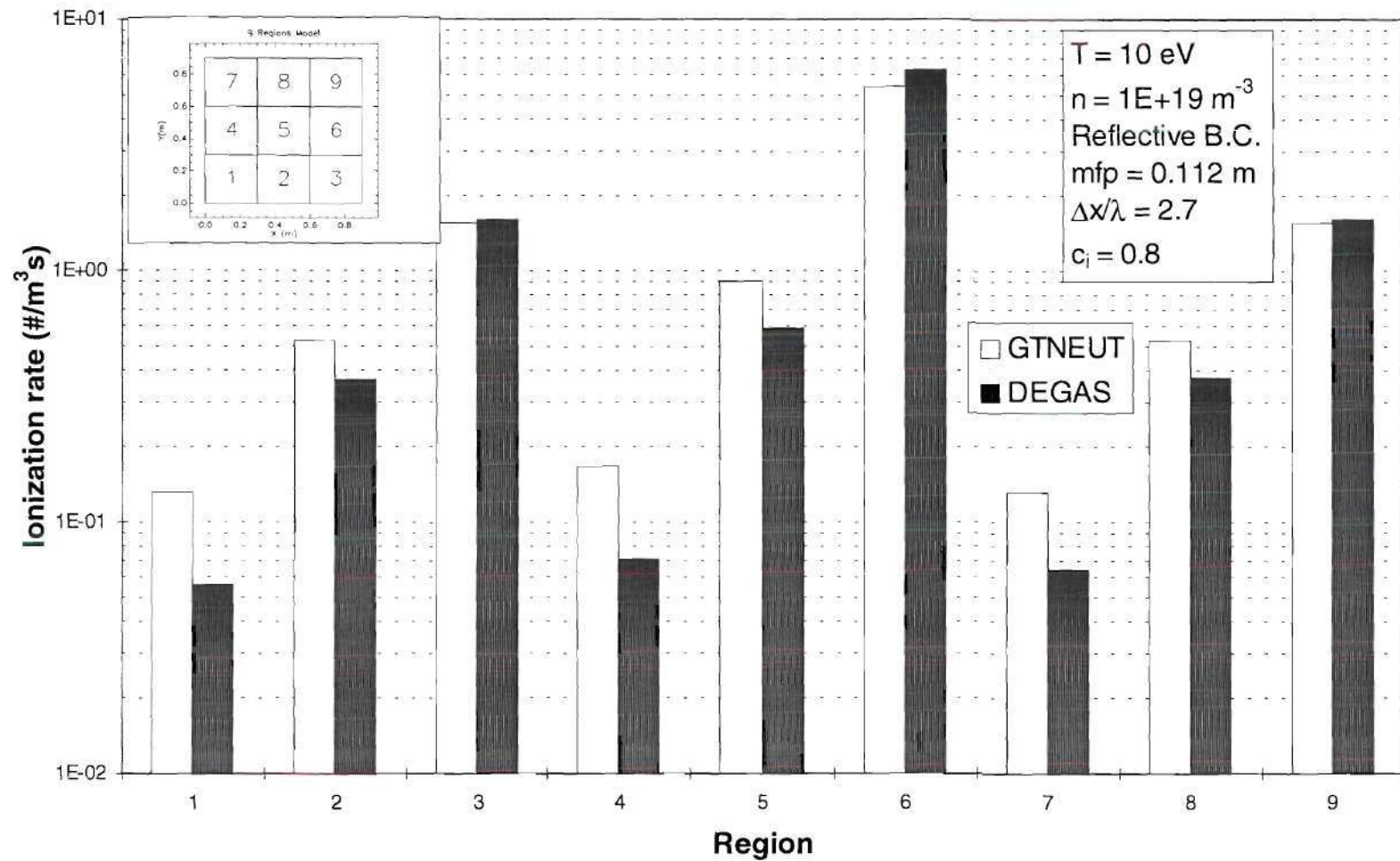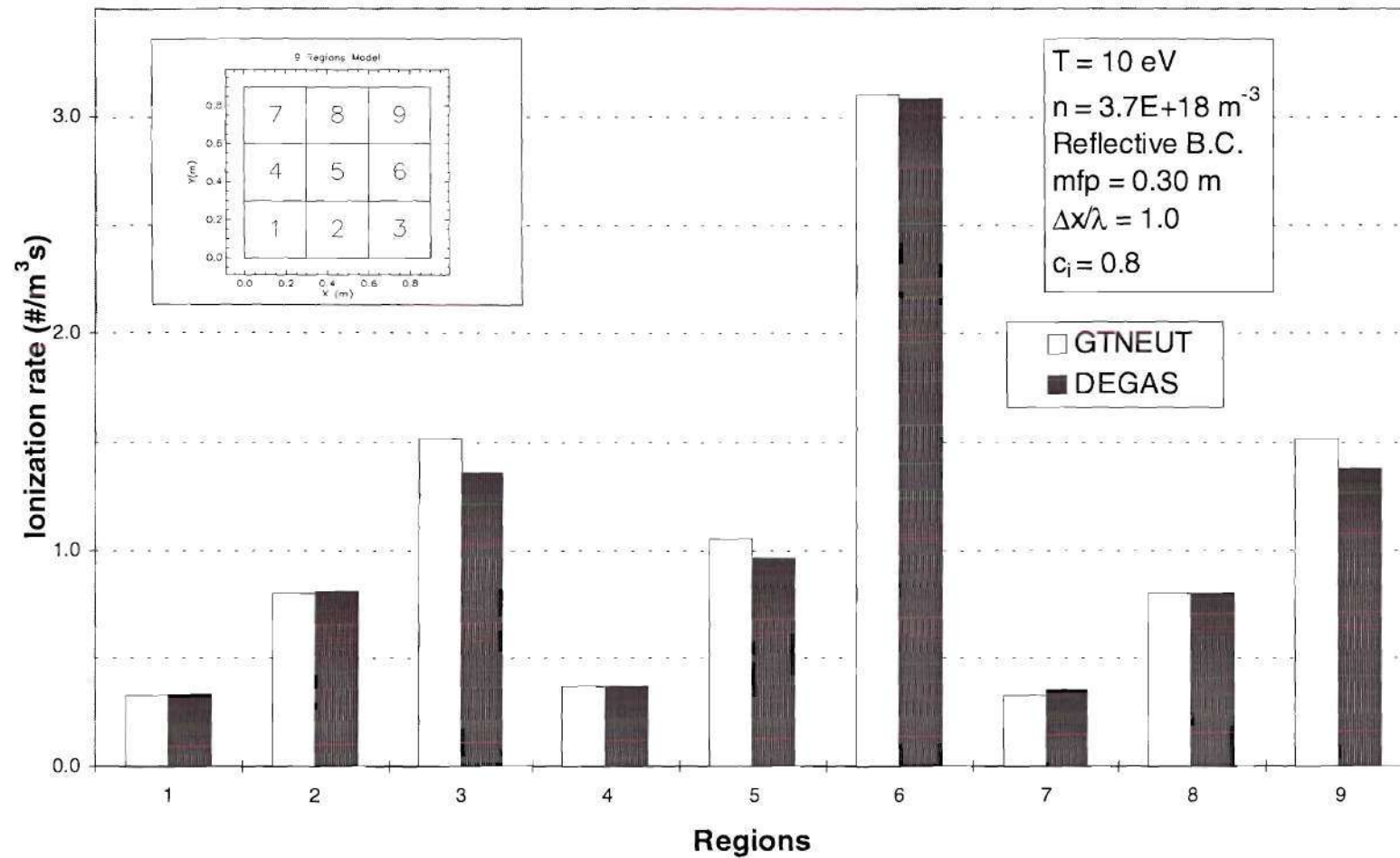
Figure 5.8. Ionization rate density for nine regions model with $\Delta x/\lambda = 1.0$, reflective boundary conditions, and $c_i = 0.8$.

121
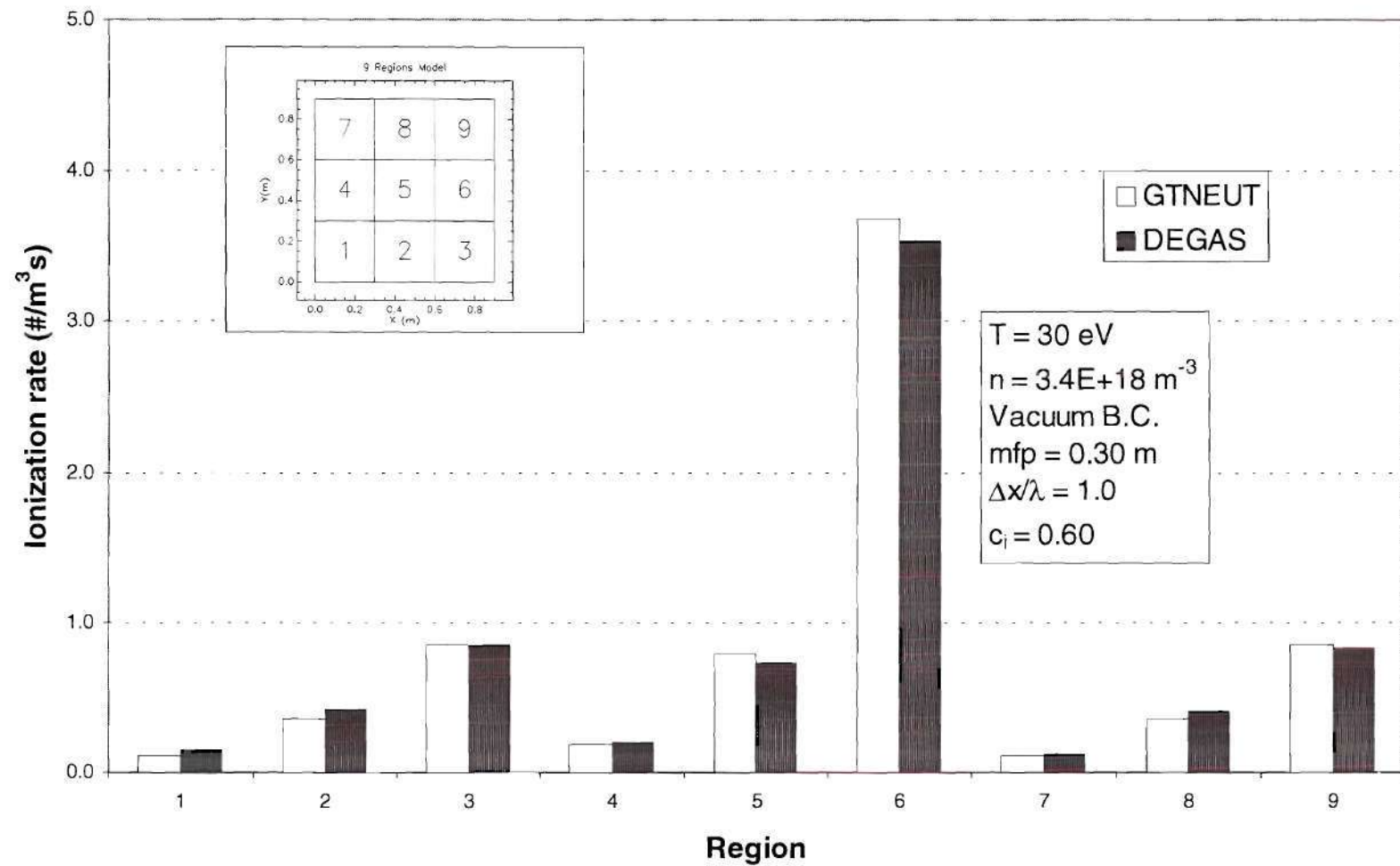
Figure 5.9. Ionization rate density for nine regions model with $\Delta x/\lambda = 1.0$, vacuum boundary conditions, and $c_i = 0.6$.

122
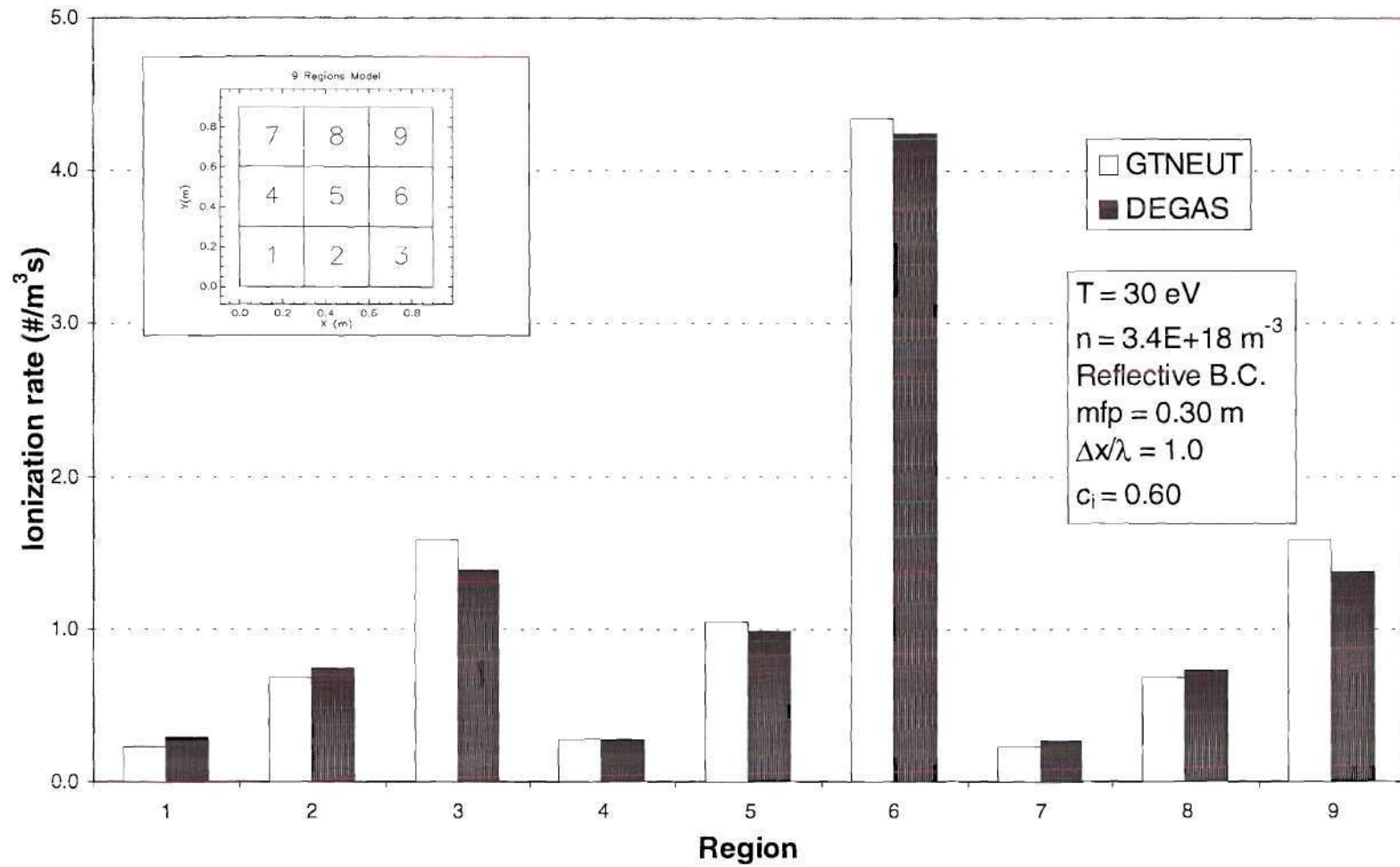
Figure 5.10. Ionization rate density for nine regions model with $\Delta x/\lambda = 1.0$, reflective boundary conditions, and $c_i = 0.6$.

5.3 Transport in a Uniform Thirty Six Region Model

Since the isotropization and directional escape probability errors tended to compensate for each other in the previous series of model problems when $\Delta x/\lambda = 1$, it was necessary to determine if this was indeed the case for all values of Δx. Thus, a new model problem consisting of 36 cells in a squared grid was prepared by dividing each of the cells in the previous model problem into four equal square cells. Each new square cell had a characteristic dimension of $\Delta x = 0.15$ m. The boundary and plasma conditions used in this new model were similar to the conditions used in the first model. A flux of particles was emitted on the right surface of cells 18 and 24. An identical model was prepared to run the Monte Carlo simulation. The arrangement can be seen in figure 5.11.
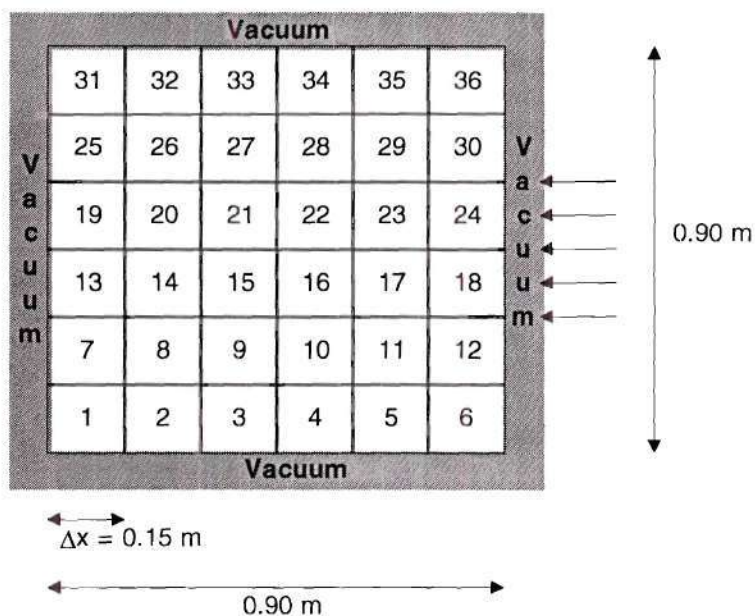
Figure 5.11. Thirty six uniform regions model.

The results for the cases of interest are shown in figures 5.12 - 5.14. It is clear that results shown in figures 5.12 and 5.13 exhibit differences between the GTNEUT and DEGAS calculations that are similar to those found in the 9-region model, for $\Delta x/\lambda > 1$ and for $\Delta x/\lambda < 1$. However, for $\Delta x/\lambda = 1$ shown in figure 5.14, the almost exact compensation of the isotropization and directional escape probability errors found in the 9-region model was not found in the 36-region model of the same spatial domain. The results in cells 12, 18, 24, and 30 were expected since there would be little error caused by the fractional escape probability across a lateral surface. However, the significant underprediction of the ionization rates in the left part of the domain (i.e., regions 1, 7, 13, 19, 25, 31, 2, 8, 14, 20, 26, 32) indicated that GTNEUT was underpredicting penetration of the flux incident on the right surface, which implied that the isotropization (underprediction) error was dominant over the directional escape probability (overprediction) error. The results of cells 6, 12, 18, 24, 30, and 36 were not unexpected since in these cells the governing error was due to escape directionality.

The good agreement expected for the case $\Delta x/\lambda = 1$, shown in figure 5.14, did not materialize. GTNEUT underpredicted penetration. A possible explanation for the disagreement could be that the model was formulated with twice the number of interfaces in the direction of penetration than in the previous model. Thus, the value of $\Delta x/\lambda$ at which exact compensation is found between the isotropization and directional escape probability error depends on the number of regions into which the
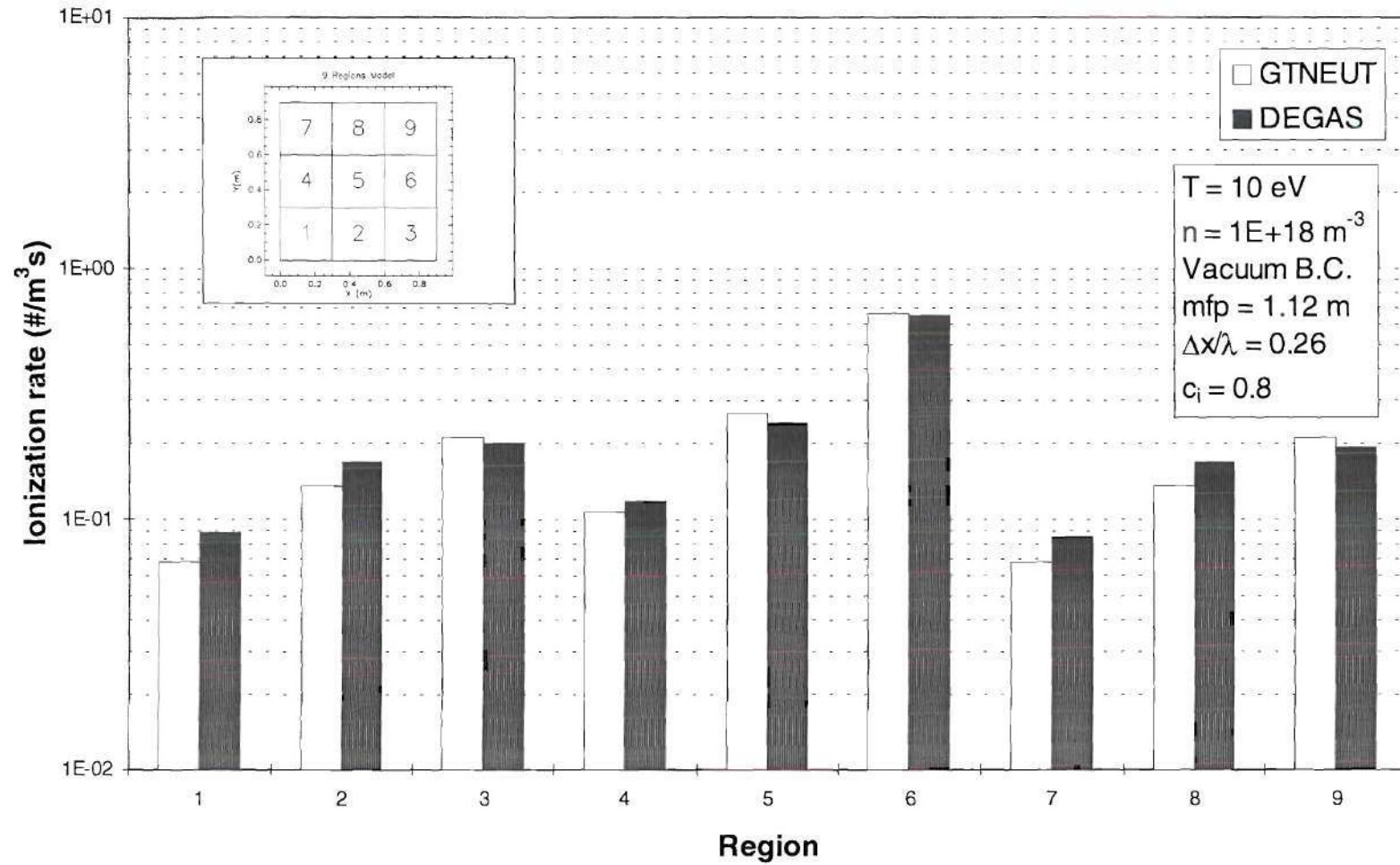
125
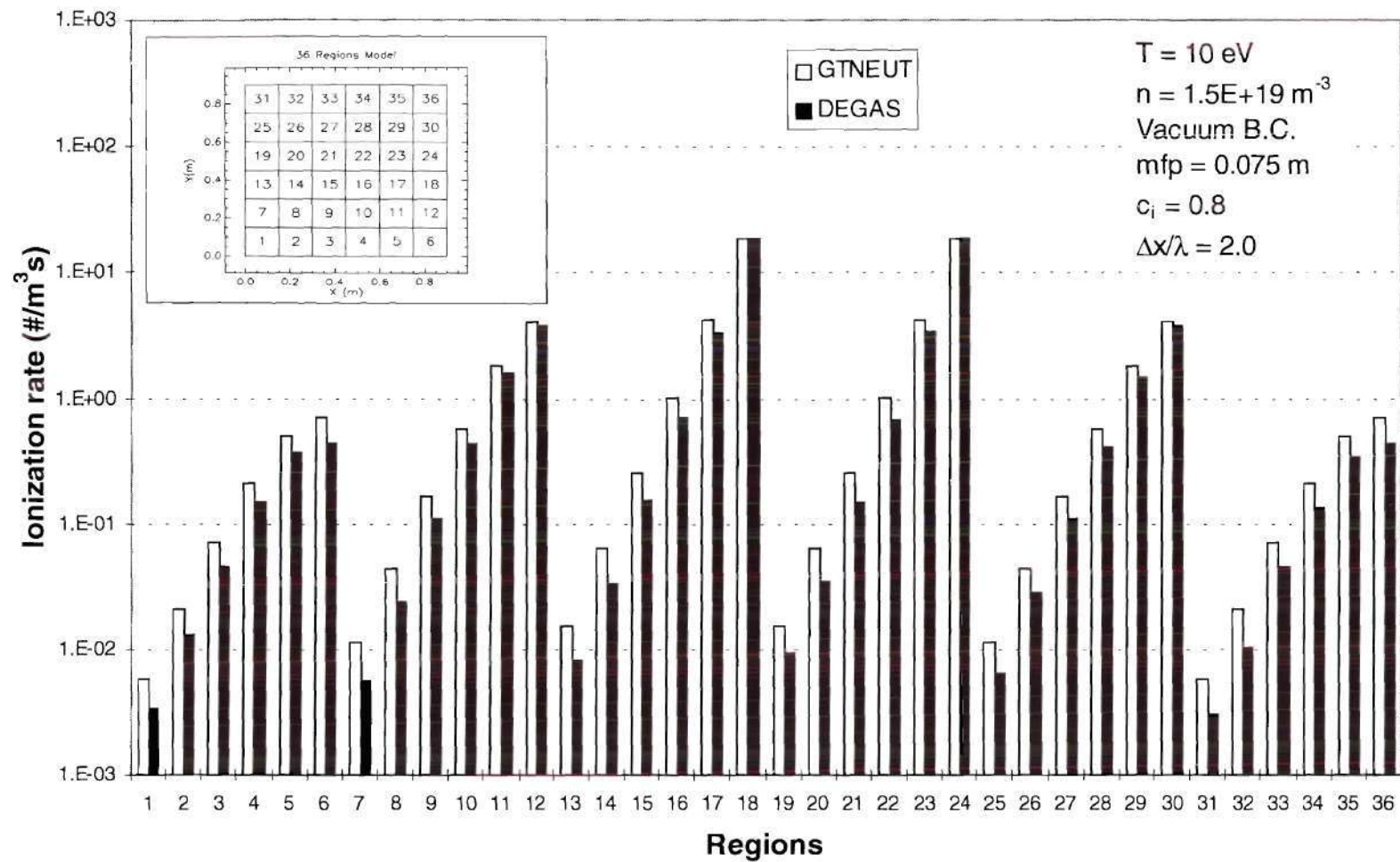
Figure 5.12. Ionization rate density for thirty six regions model with $\Delta x/\lambda = 2.0$, vacuum boundary conditions, and $c_i = 0.8$.
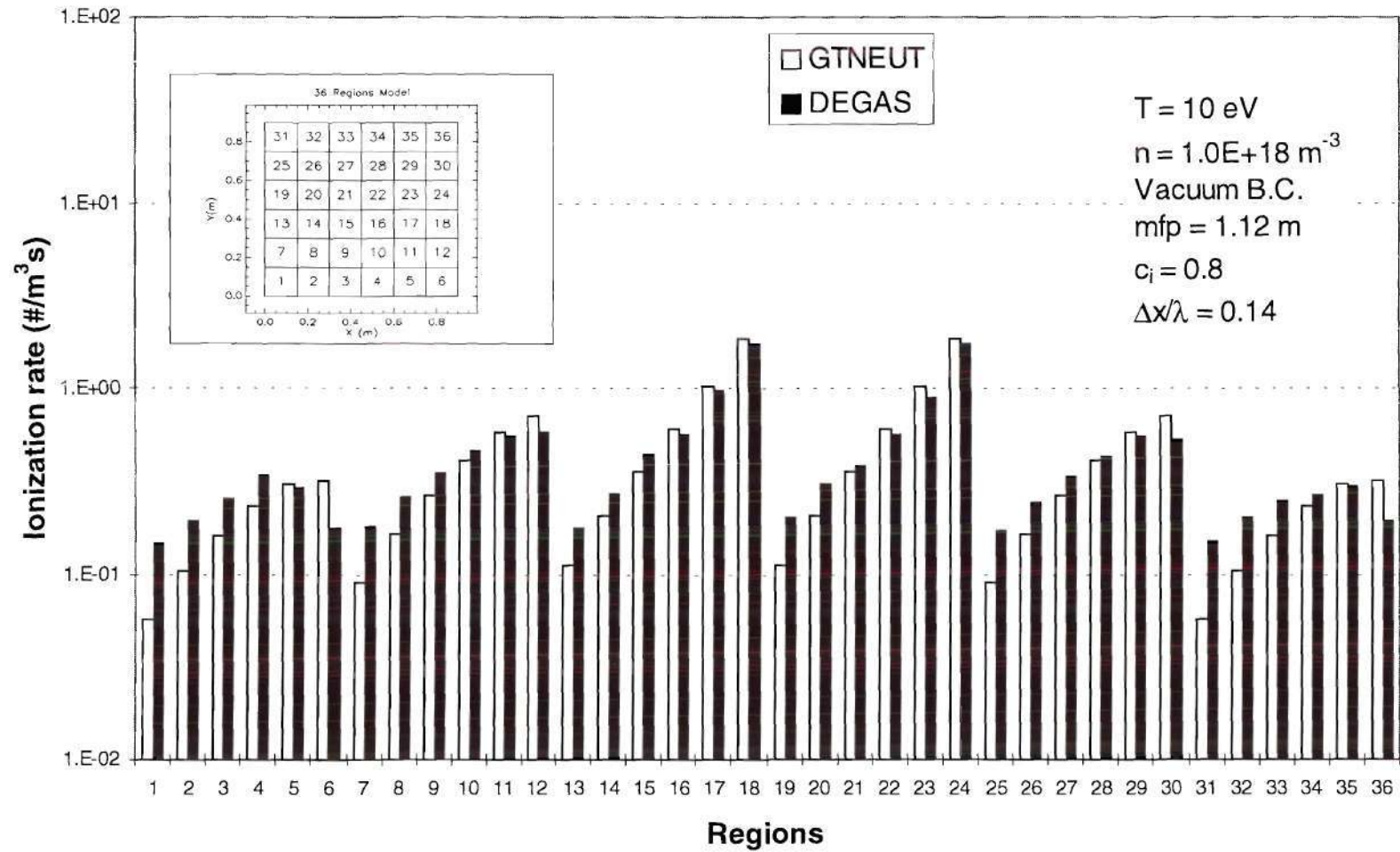
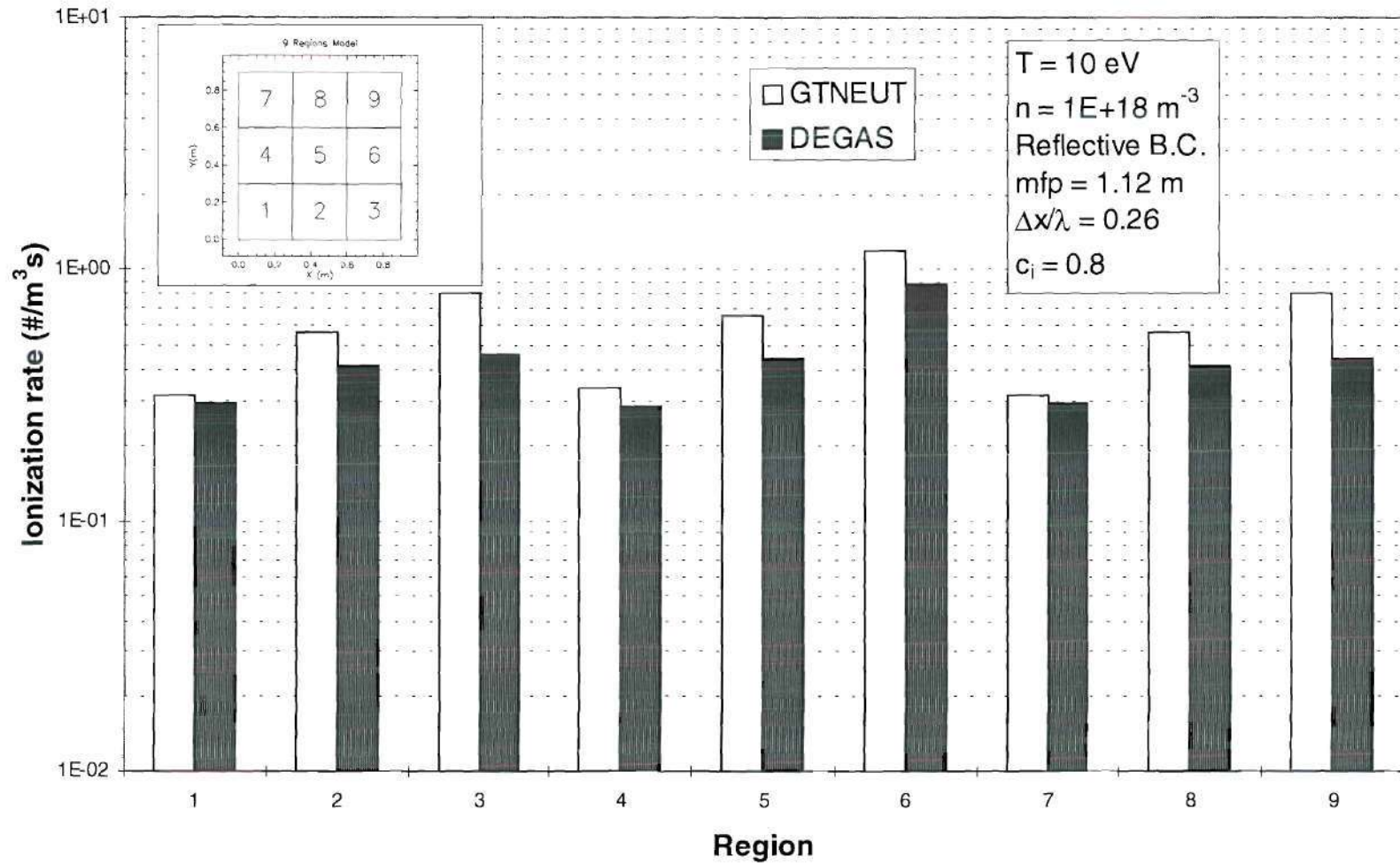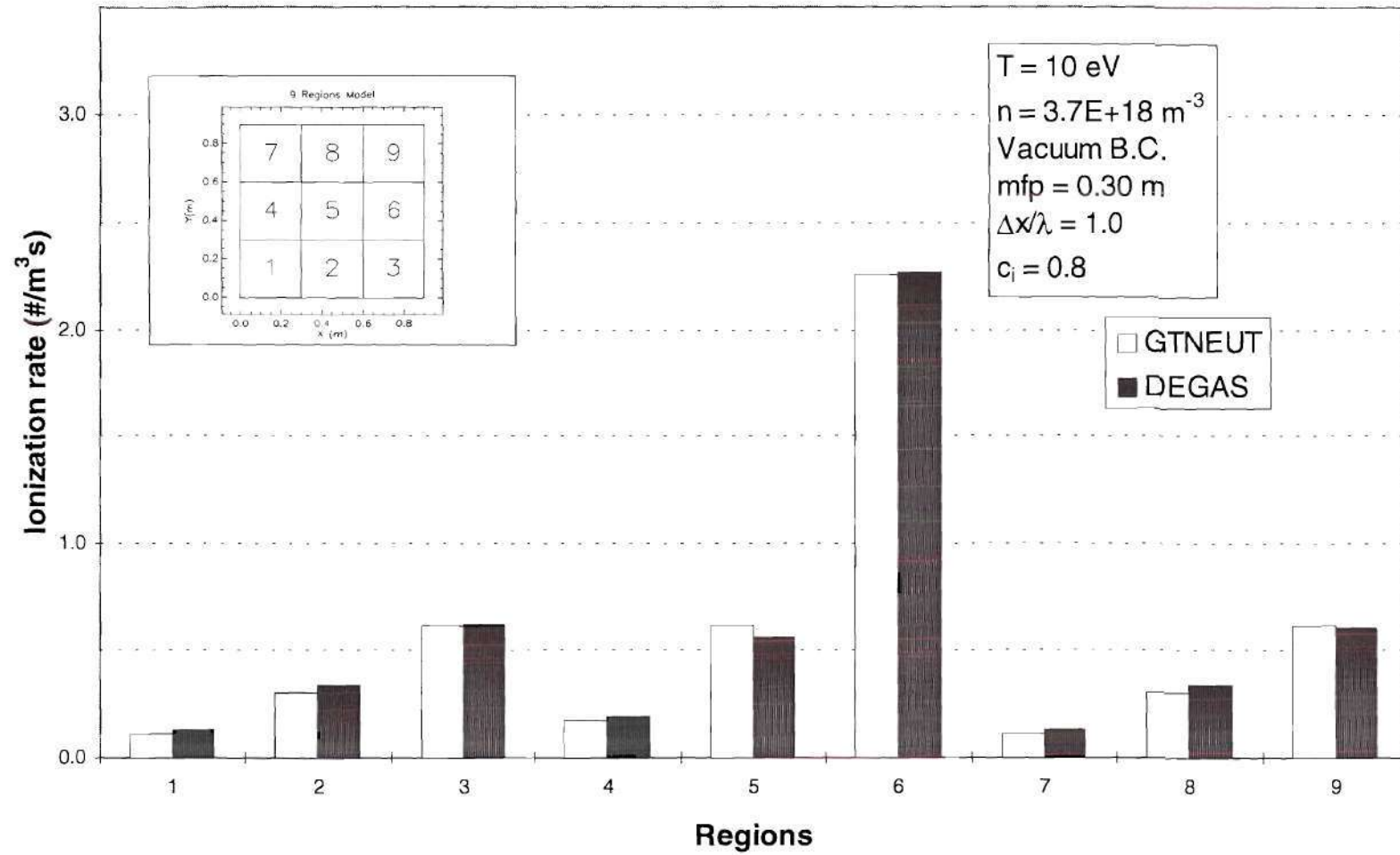Figure 5.13. Ionization rate density for thirty six regions model with $\Delta x/\lambda = 0.14$, vacuum boundary conditions, and $c_i = 0.8$.
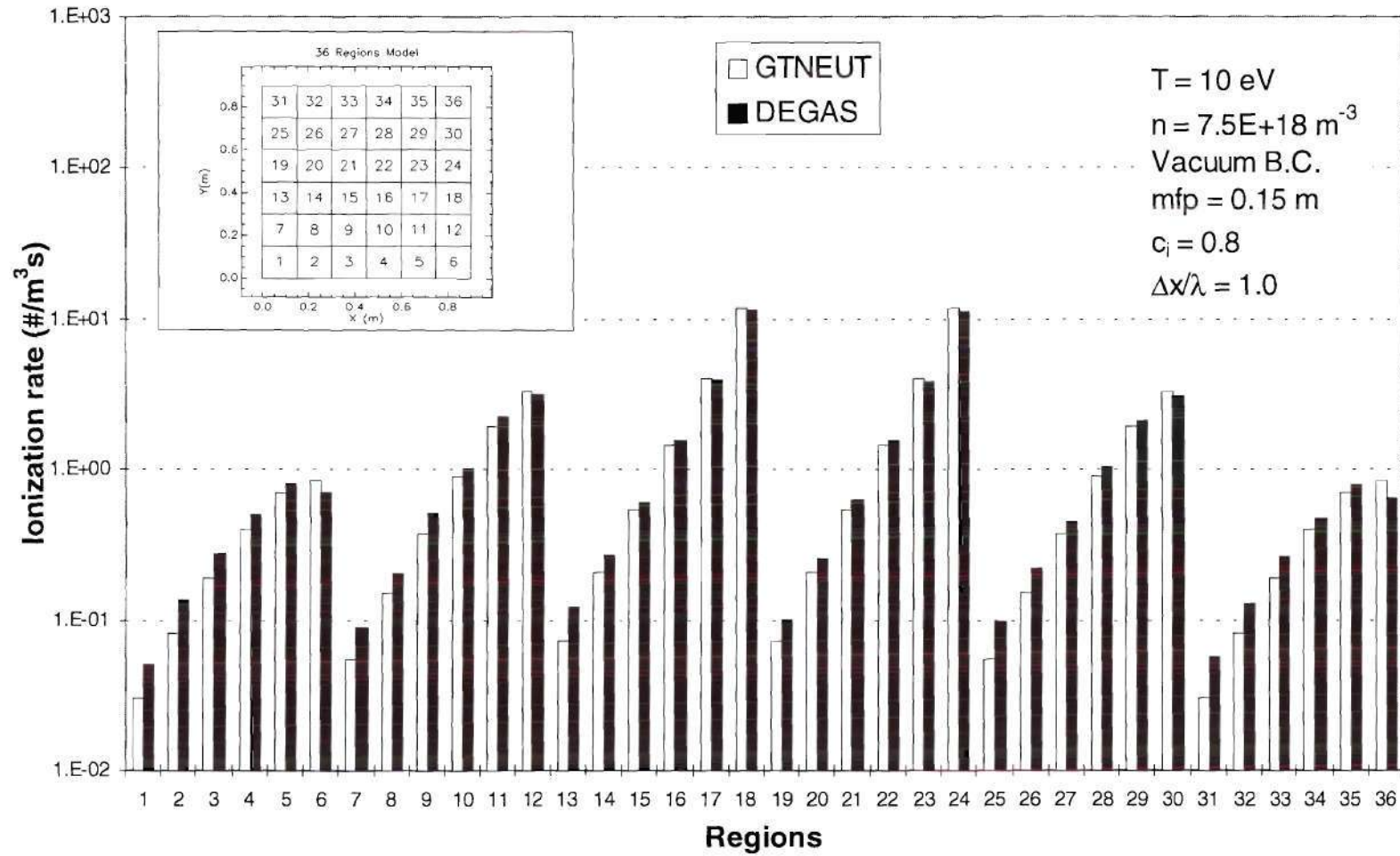
Figure 5.14. Ionization rate density for thirty six regions model with $\Delta x/\lambda = 1.0$, vacuum boundary conditions, and $c_i = 0.8$.

computational domain is divided (i.e., the number of interfaces at which the errors are made). It can be inferred from these results that the value $\Delta x/\lambda$, at which compensation of errors occurs, generally decreases with the number of interfaces in the direction of penetration.

5.4 Transport in a Uniform Multiregion Slab with Internal Sources

In the previous sections the presence of an incident surface flux induced the onset of isotropization and escape directionality errors. In this section the original TEP assumptions were tested in a multiregion model with internal sources and in the absence of an incident flux. The slab model consisted of 50 regions or cells, each of which was 1 cm thick and 50 cm high. The uniform plasma condition was set by fixing the temperature at 10 eV. Each region in the slab had a uniform volumetric internal source of strength equal to 0.5 #/s. The charge-exchange/elastic scattering fraction, c_i in this problem, was 0.8. Vacuum boundary conditions were imposed on every surface of the slab. The Monte Carlo (DEGAS and MCNP4B) simulations had identical cell arrangements and plasma parameters, and were run with 100,000 histories. Figure 5.15 depicts the multiregion slab model.

A problem like this could very well represent the conditions in the divertor region in which recombination and molecular dissociation could constitute an internal source of neutrals.

129
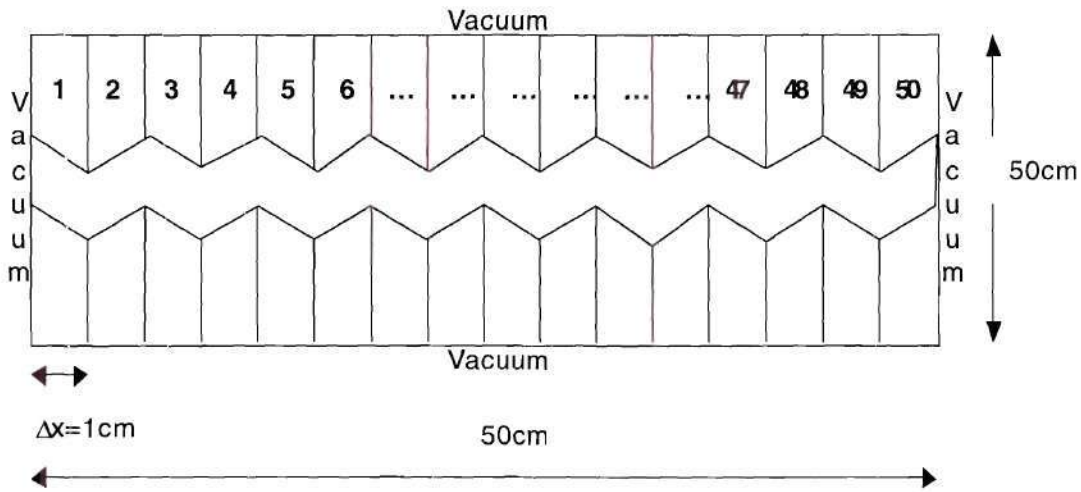
Figure 5.15 Multiregion slab model.

The results in chapters III, IV, and those from the previous sections of this chapter indicate that the isotropization and escape directionality errors are specifically associated with penetration. Thus, these errors would always be present in problems in which there is a strong directional flow of particles. However, it is unknown if the isotropization and escape directionality errors would be present (and if they were present to what degree) in problem models without strong directional flow effects. The main objective of this section was to determine if these errors were present in problems without an incident flux of particles. Furthermore, this section also tried to demonstrate how well the assumptions of the transmission and escape probability method will hold in both long and short mean free path regimes in problem models with internal sources.

To understand this aspect of neutral transport, a selective range of region thickness over mean free path ratios, $\Delta x/\lambda$, varying from 0.01 to 10 was used. The predicted

130

results for the volumetric ionization rate obtained with GTNEUT and with the Monte Carlo codes DEGAS and MCNP4B, for the different ratios of $\Delta x/\lambda$, are shown in figure 5.16 – 5.21. In the short mean free path regime ($\Delta x/\lambda = 10$) shown in figure 5.16, charge-exchange and scattering were the most dominant effects. In these simulations, the Monte Carlo and GTNEUT codes yielded comparable results. It is noteworthy that in this regime, diffusion theory would also be able to predict similar results.

In reference to the TEP method, it seems clear that the neutral flux distribution going from one region to the next is quite isotropic. This is due to the isotropization effect that charge-exchange and elastic scattering have on the outgoing fluxes. Thus, two of the basic assumptions of the TEP method --that the incident neutral flux is isotropic over the inward hemisphere and that the neutral flux is uniformly distributed over the surface— are well justified in this model problem.

Based on the results of the problem with an incident flux, it was expected that for $\Delta x/\lambda = 10$, the directional escape probability error would be the dominant transport effect. However, no such effect was observed.

In all the long mean free path regimes tested, the results predicted by GTNEUT were in good agreement with those predicted by Monte Carlo. It was expected that for all regimes with $\Delta x/\lambda < 1$, the isotropization error would be dominant, causing the underprediction of penetration. However the results shown in figure 5.18 – 5.21 did not show any larger discrepancies with Monte Carlo. The results indicated that both

131
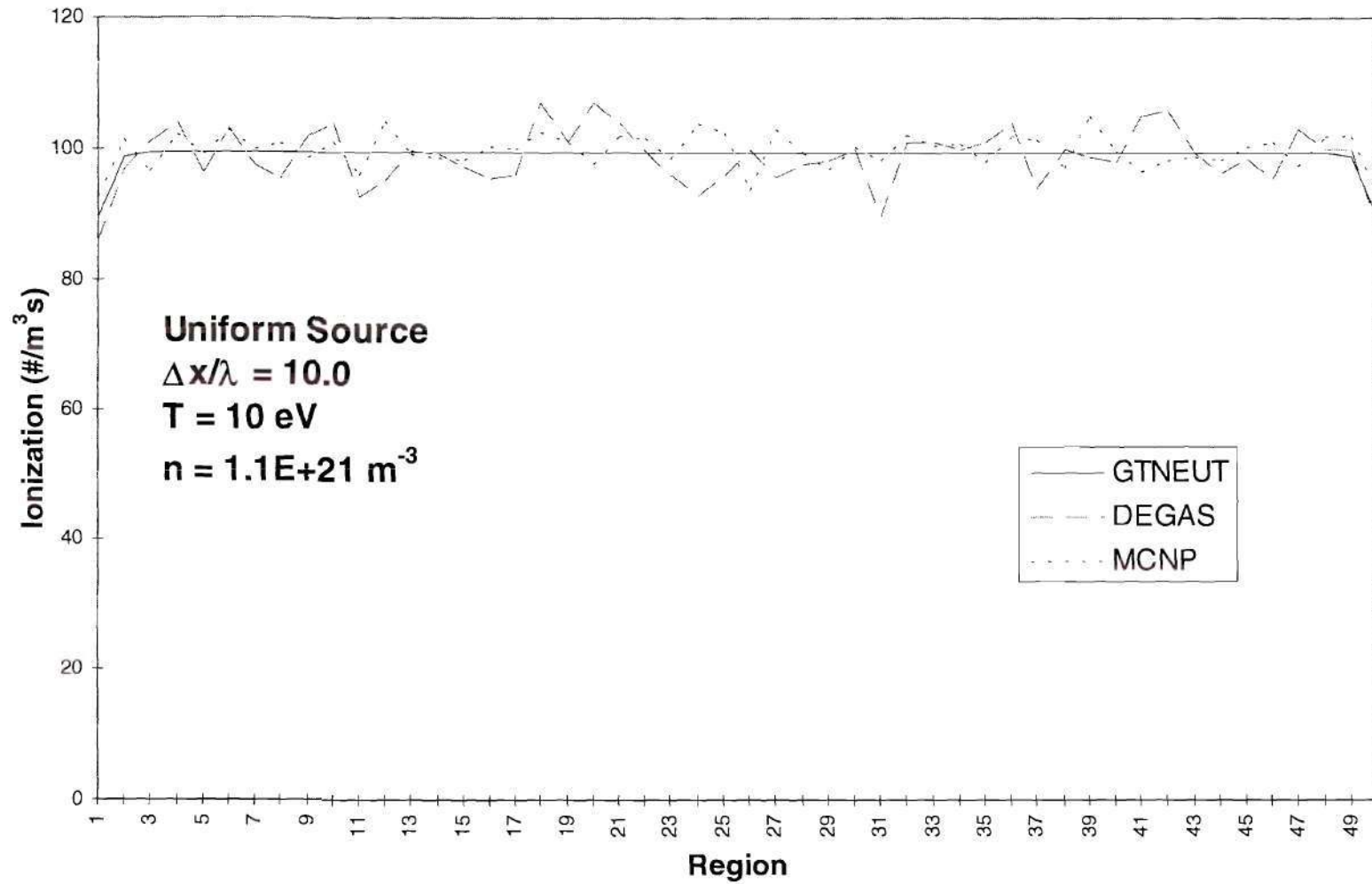
Figure 5.16. Ionization rate density for slab with a uniform source, $\Delta x/\lambda = 10$, and $c_i = 0.8$.
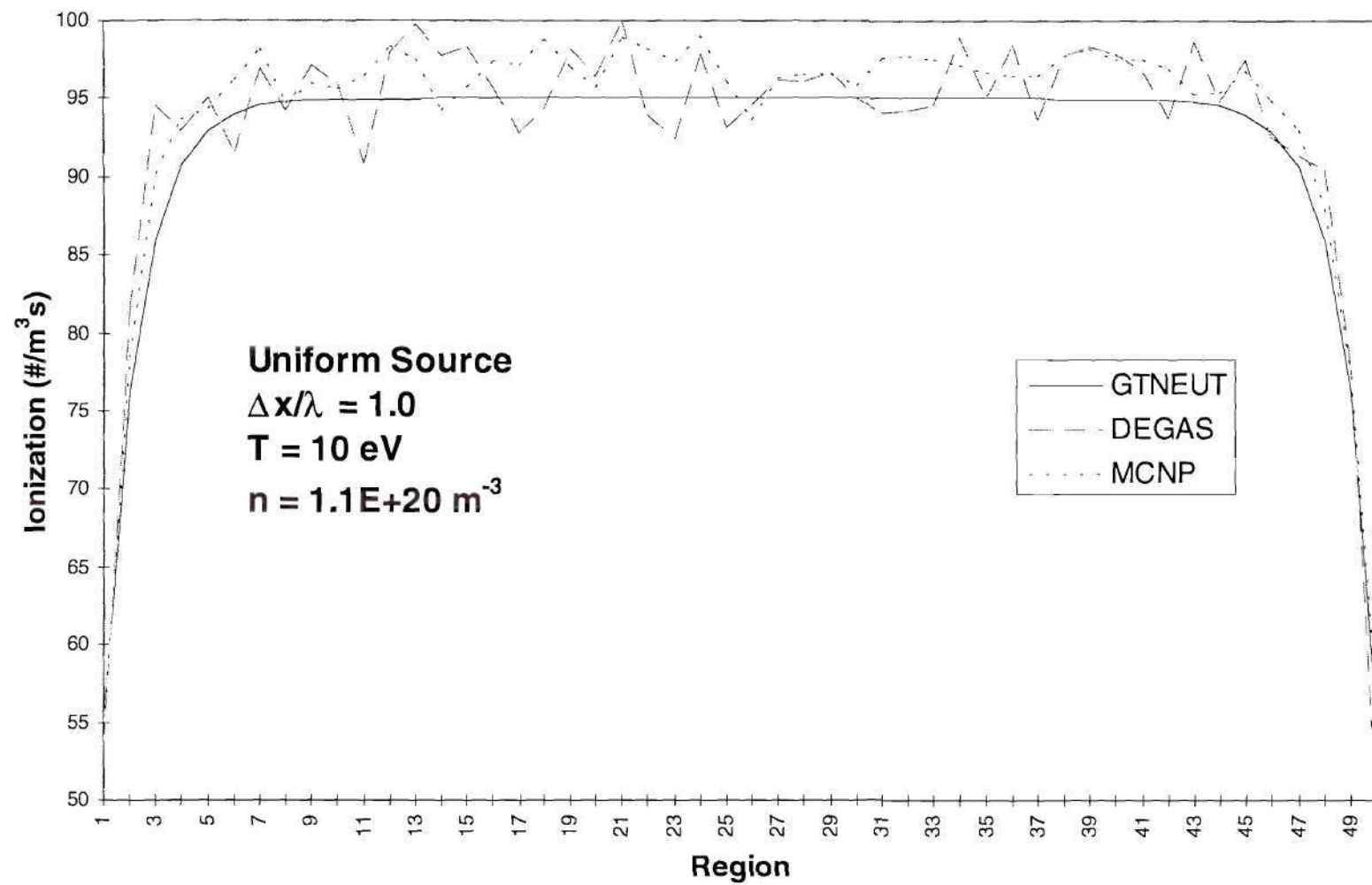
Figure 5.17. Ionization rate density for slab with a uniform source, $\Delta x/\lambda = 1$, and $c_i = 0.8$.
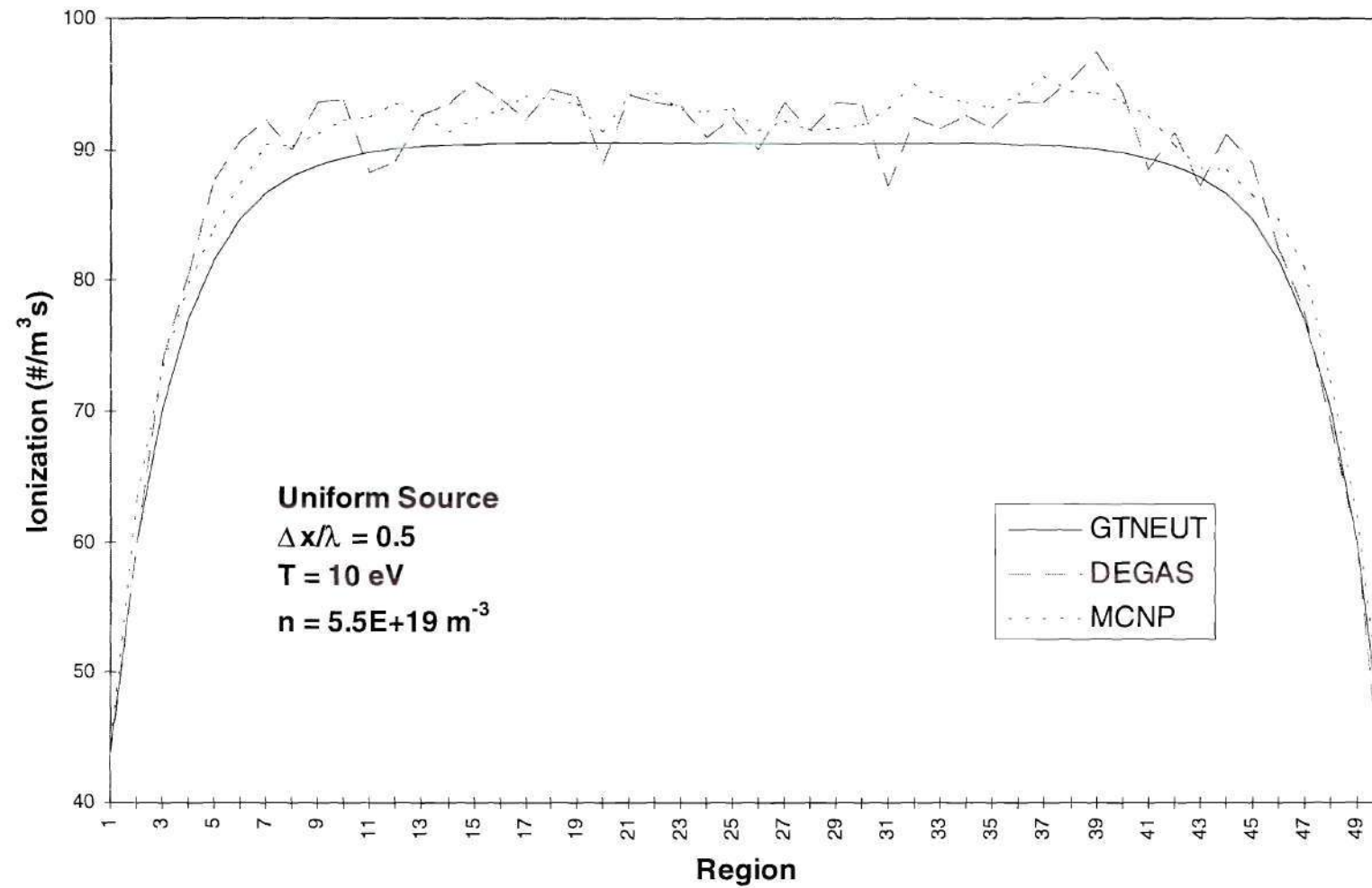
Figure 5.18. Ionization rate density for slab with a uniform source, $\Delta x/\lambda = 0.5$, and $c_i = 0.8$.
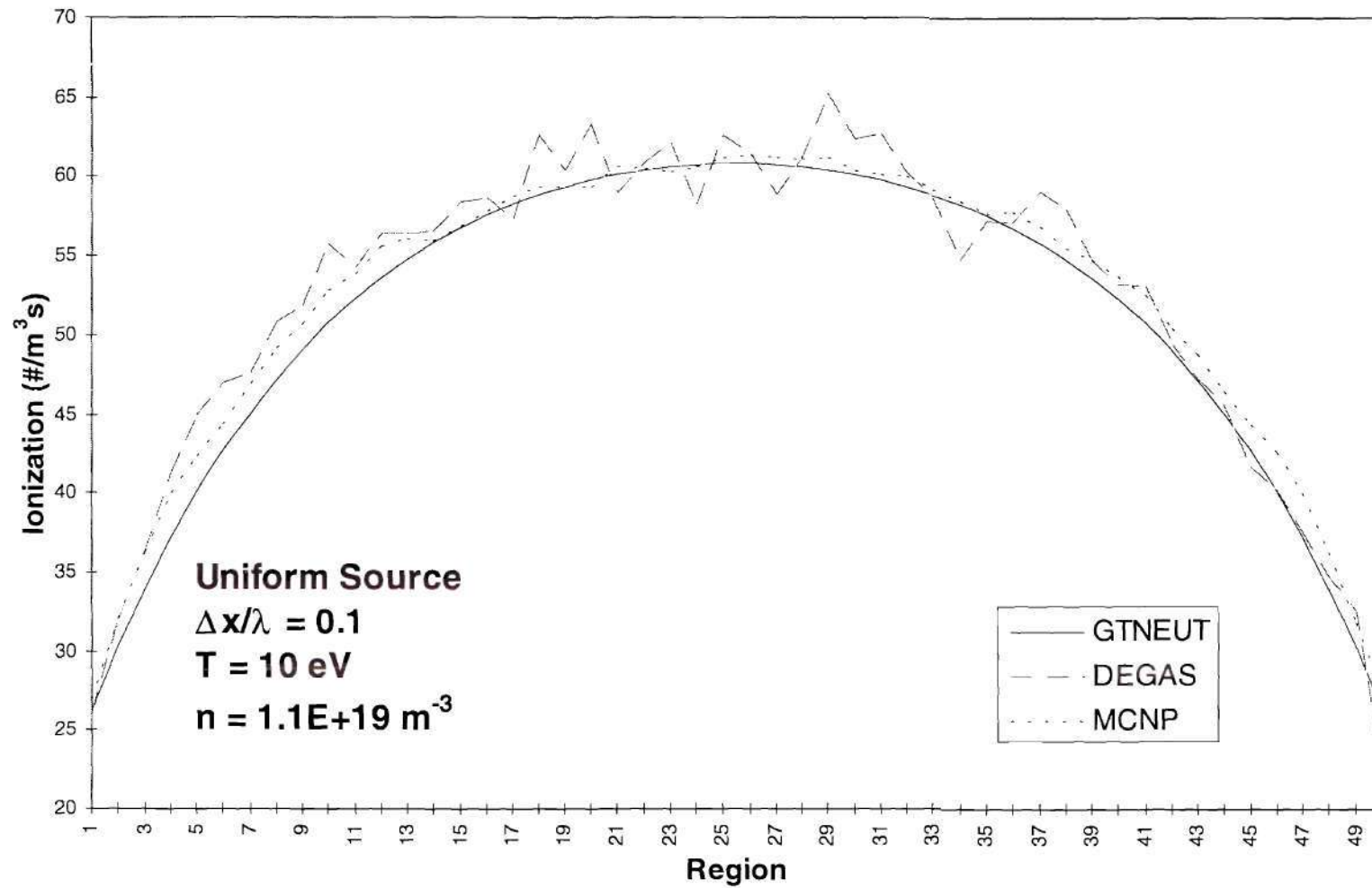
Figure 5.19. Ionization rate density for slab with a uniform source, $\Delta x / \lambda = 0.1$, and $c_i = 0.8$.
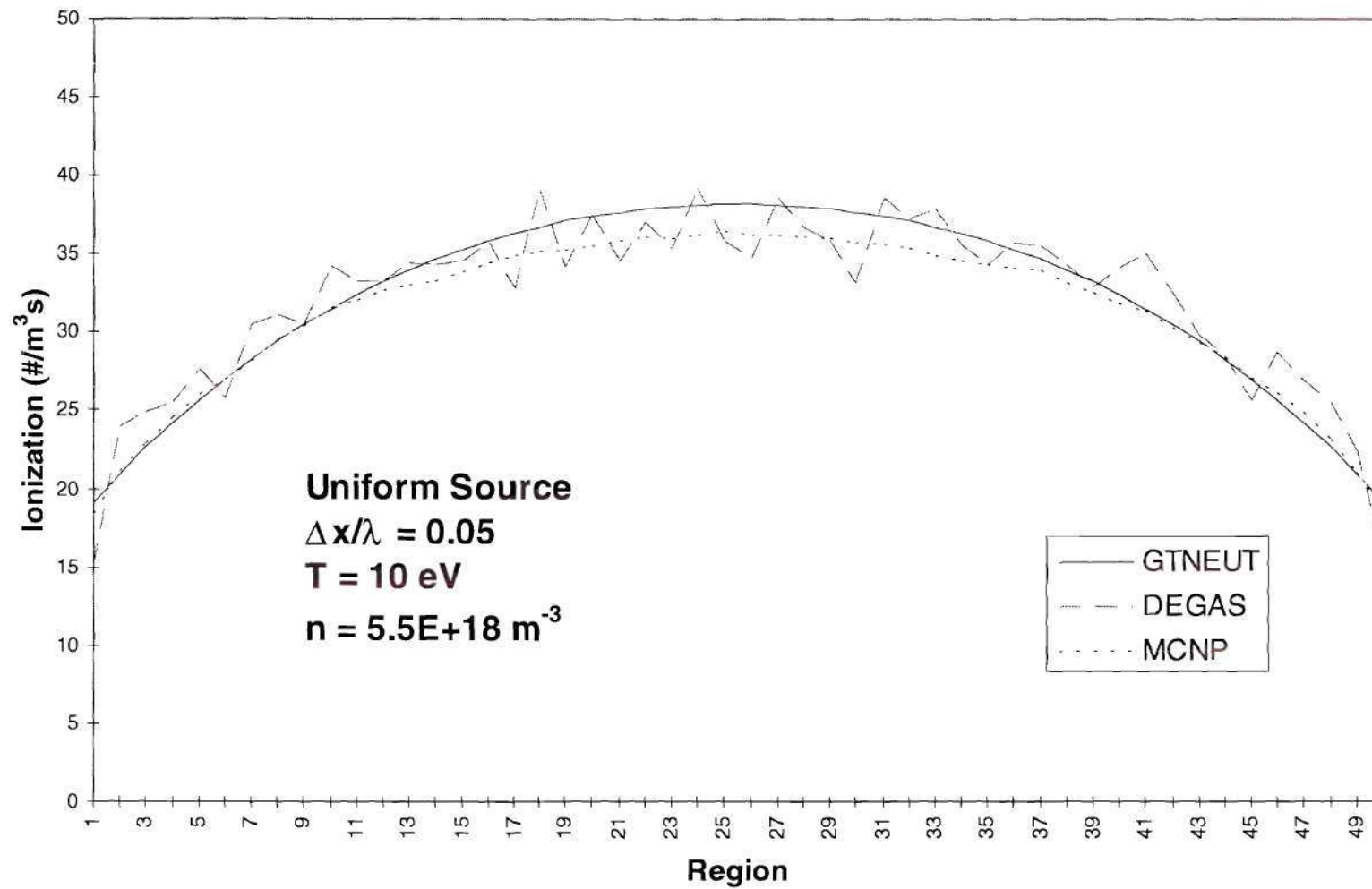
Figure 5.20. Ionization rate density for slab with a uniform source, $\Delta x/\lambda = 0.05$, and $c_i = 0.8$.
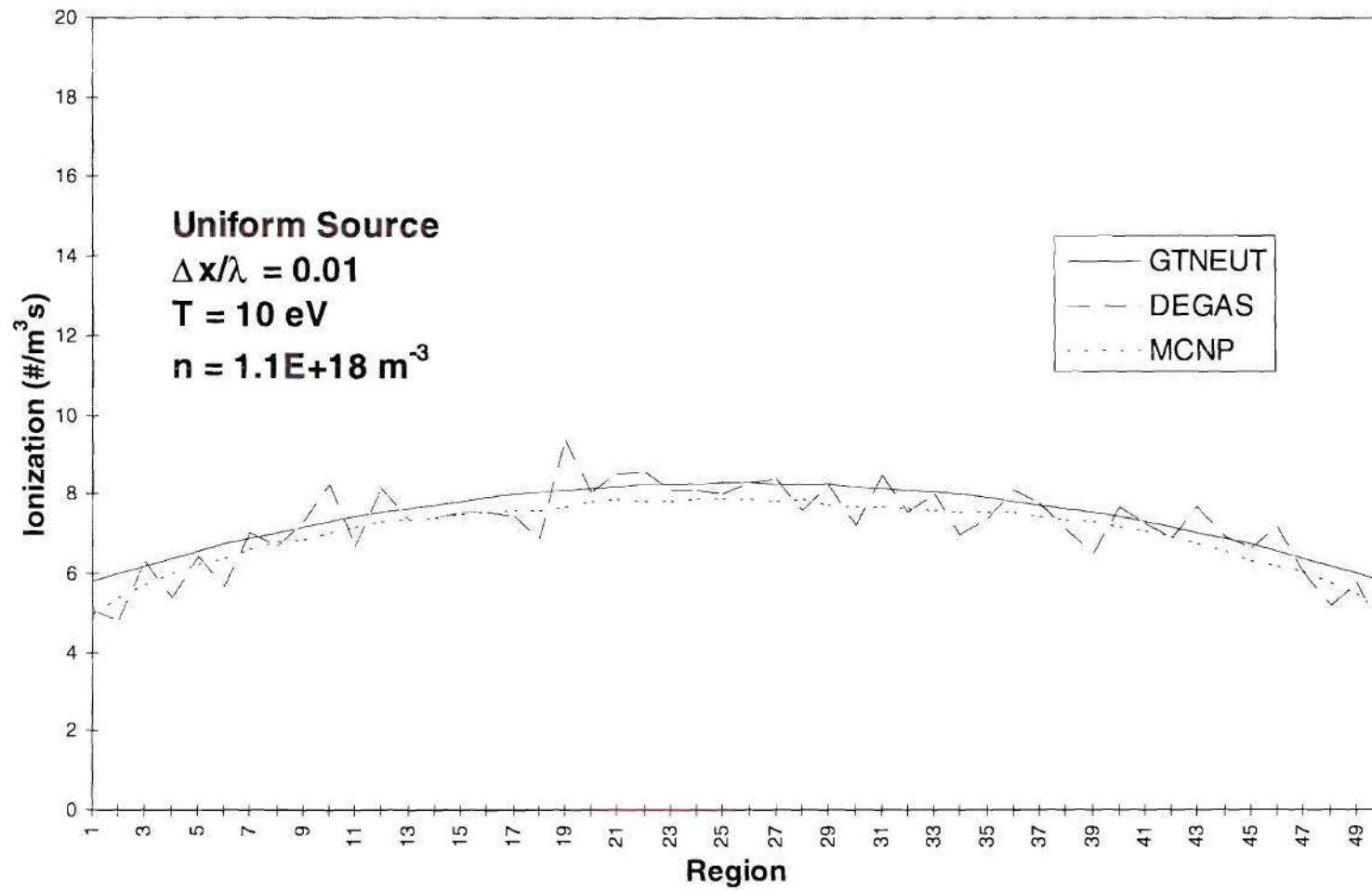
Figure 5.21. Ionization rate density for slab with a uniform source, $\Delta x/\lambda = 0.01$, and $c_i = 0.8$.

137

isotropization and escape directionality were not present in problems with a uniform internal source. The results also indicate that in these kind of problems (problem models with internal sources) the TEP method is applicable for all regions with $\Delta x/\lambda$ greater than 0.01.

5.5 Conclusions

The results observed in the two-dimensional multiregion problems were similar to those observed in the one-dimensional configurations. The presence of a surface flux induced the onset of isotropization and escape directionality errors. It was confirmed that the isotropization assumption introduced an error that caused underprediction of penetration with increasing mean free paths in the region (i.e., $\Delta x/\lambda < 1$). The assumption that the directional escape probability, Λ_{ij}, was proportional to the surface area introduced an overprediction of penetration in regions away from the source when the characteristic dimension of the region was greater than the mean free path (i.e., $\Delta x/\lambda > 1$).

It was also noted that in two-dimensional multiregion problems, the total escape probability was in very good agreement with Monte Carlo in the region adjacent to the surface source, and that the directional escape probability across lateral surfaces was not sensitive to the distribution of the first collision source.

The results indicated that the isotropization and directional escape probability errors tended to balance each other, independent of the fraction of charge-exchange and scattering when $\Delta x/\lambda = 1$. This observation could be useful in the preparation of two-dimensional multiregion models when the plasma conditions are well known. However,

these errors did not balance each other exactly when the original computational domain was subdivided further (i.e., going from a nine region problem to a thirty six region problem). This last result indicated that the value of $\Delta x/\lambda$ at which the exact compensation could be found depended on the number of interfaces into which the computational domain was divided.

Finally, the results confirmed that in the absence of a directional flow of particles (i.e., no surface sources) the escape directionality and isotropization errors were nonexistent, and that in such conditions and with problem models with internal sources the TEP method is applicable in all regions with $\Delta x/\lambda > 0.01$.

CHAPTER VI

COMPARISON OF THE TEP/MONTE CARLO CALCULATIONS
FOR REALISTIC SOL/DIVERTOR MODELS

6.1 Introduction

The results of simple model problem calculations intended to isolate and test the basic transport treatment in the TEP/ICB method were discussed in the previous chapters. The results, for both the treatment of internal sources and for incident neutral fluxes, were generally in good agreement with those obtained with DEGAS and MCNP4B; and where disagreement was found the cause was identified and sometimes corrections factors were developed.

Since the most likely application of the GTNEUT code will be to model the transport of neutrals in a diverted tokamak, it was appropriate to consider a few cases for more realistic diverted plasmas. A quantitative understanding of the neutral fluxes is not only fundamental in analyzing recycling divertors, but also an essential component in the calculation of particle and heat fluxes to the divertor plate. This section presents the comparisons of the GTNEUT and DEGAS codes for three diverted plasma models. The plasma models selected for this purpose were for the General Atomics Doublet III-D (DIII-D) and the Massachusetts Institute of Technology's *Alto Campo Torus* (Alcator C-Mod) fusion experiments and the International Thermonuclear Experimental Reactor engineering design activities (ITER-EDA).

6.2 DIII-D Model

Located in San Diego, California, the General Atomics DIII-D is the nations largest, best diagnosed and most versatile fusion experiment at the present time [53]. This third generation tokamak has done extensive work on particle exhaust, density limit and magnetic divertor configurations. These experiments have provided a wealth of data that the scientific community has used as benchmarks to improve the understanding of plasmas. Thus, a neutral particle transport simulation of this fusion experiment would be a representative test of the ability of the TEP method to calculate neutral densities in present tokamak experiments.

A neutral transport simulation with a full scale DIII-D geometry was performed. The representative geometry of the plasma, scrape-off layer (SOL), divertor, and plenum regions are shown in figure 6.1. The DIII-D geometric model was represented in GTNEUT with 48 cells [54]. The low density regions near the wall were represented by the cells with odd numbers between 1 and 41. The SOL region was represented by the cells labeled with even numbers between 2 and 42. The inner divertor plate was represented by the wall segment 52. Particles were recycled in front of the inner divertor plate in cell 2. The wall segment 75 represented the outer divertor plate. The corresponding recycling cell was 43. The private flux region was represented by cells 44 through 48. Table 6.1 summarizes the location of different regions of interest for the DIII-D model. The background plasma temperatures and densities that were selected were representative of DIII-D plasma conditions. These are summarized in table 6.2.
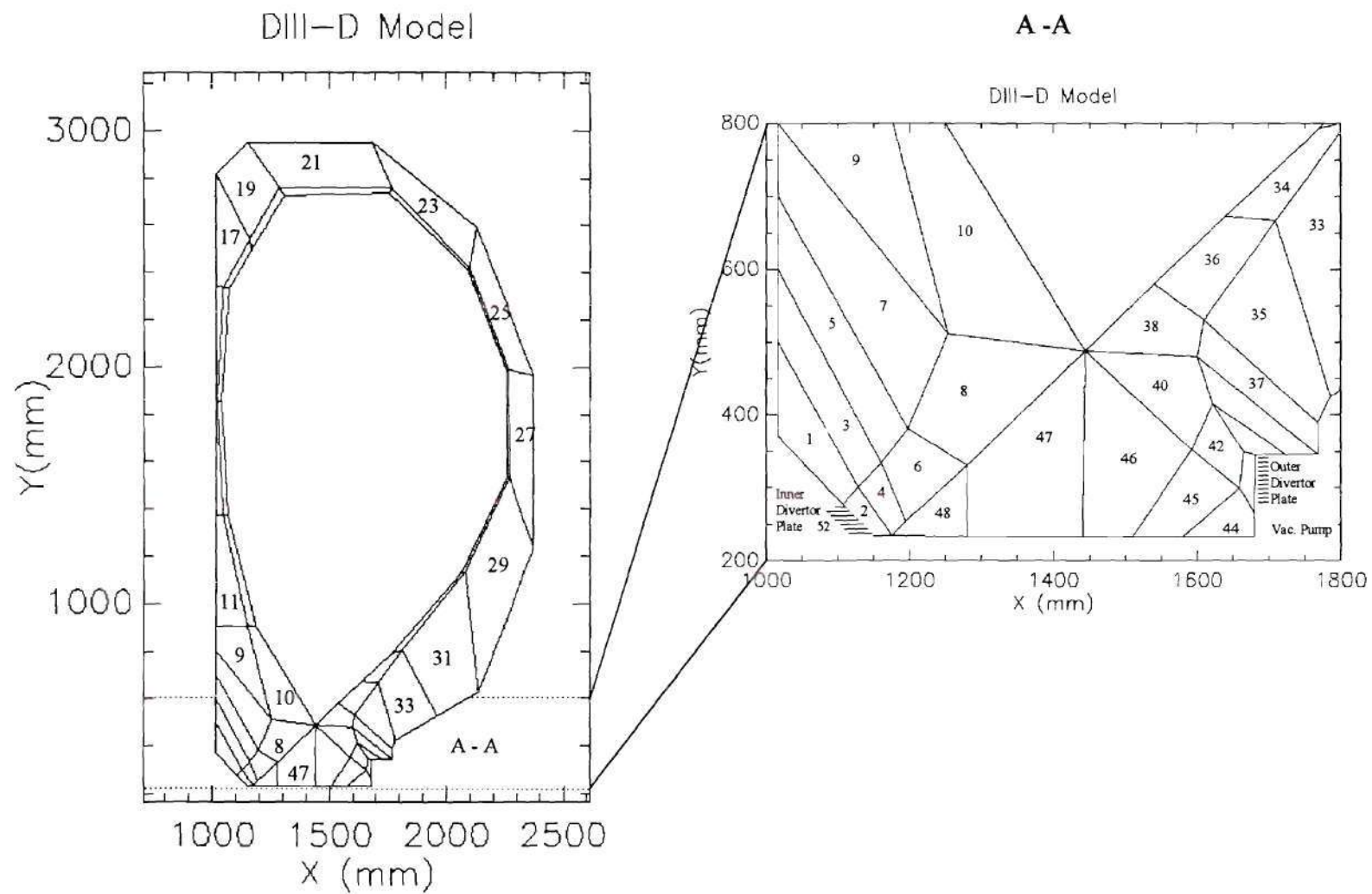
Figure 6.1. Neutral atom transport model for the DIII-D plasma.

142

The ion flux incident upon both the inner and outer divertor plates was equal to 2.2×10^{22} s^{-1}. The ion flux was reflected as neutrals atoms with a Maxwellian energy distribution characterized by the ion temperature just in front of the divertor plate and then transported into the corresponding adjacent cells, i.e., cells 2 and 43. The GTNEUT calculation assumed that the neutrals reflected from the divertor plate, those reflected from the wall, and those neutrals transported into a given region (acquired via charge-exchange and scattering) a Maxwellian energy distribution with the local ion temperature of the region in question.

Table 6.1. Cell Assignments for the DIII-D Model

Location	Cells	Wall Segments
Wall-vacuum	odd numbers 1 - 41	52 - 81
SOL	even numbers 2 - 42	-
Outer Divertor	43	75
Inner Divertor	2	52
Pump - Vacuum	44 – 48	76 - 82

Table 6.2. Temperature and Density Assignments for the DIII-D Model

Cells	Temperature (eV)	Density (#/m^3)
Central Plasma	200	1.0×10^{20}
Cells (odd numbers) 1 – 41	10	5.0×10^{18}
Cells (even numbers) 8 – 40	100	1.0×10^{19}
Cells 2, 43	10	1.0×10^{20}
Cells 4, 6, 42	50	5.0×10^{19}
Cells 44 -- 48	10	5.0×10^{18}

The wall segments were assigned a reflection coefficient equal to 1.0 and a pumping fraction of 0.0. The wall segment 76 represented the location of the opening of the pumping duct. Here the assigned values for the reflection coefficient and pumping fraction were 0.0 and 1.0 respectively.

For comparison, a benchmark DEGAS simulation was carried out with the same cell arrangements and plasma parameters. In the GTNEUT calculation ions were reflected isotropically, whereas in the Monte Carlo calculation they were specularly reflected ("mirror" wall boundary condition). It was demonstrated in section 3.6 of chapter III that specular reflection was adequate in regions with short mean free path since the next collision would occur close to the wall, thus creating an isotropic distribution of particles that would mimic the reflection condition used by GTNEUT. The recycling of the incident ion flux was approximated by a puff of neutrals with an energy corresponding to a Maxwellian with the local ion temperature of the region in front of the divertor plates (i.e., regions 2 and 43). DEGAS calculates the neutral energy distribution in all regions.

144

6.2.1 Analysis of the Results

The results of the GTNEUT and DEGAS simulations showing the ionization rate distribution and neutral particle density are shown in figures 6.2 and 6.3. With reference to figure 6.3, the results of GTNEUT and DEGAS agreed quite well in the vicinity of the recycling source in the divertor region and reasonably well in the lower part of the model where the neutral density was significant. For example, the GTNEUT and DEGAS compression ratios at the X-point, n_{DIV}/n_{Xpt}, which were on the order of 10^2, were in excellent agreement; but above the midplane, where the compression ratio was greater than 10^3, the disagreement between the GTNEUT and DEGAS predictions were an order of magnitude different.

The DEGAS calculation was carried out with 500,000 histories, and the error bars were less than 1% for regions 1-10 (in or near the inner divertor region) and for regions 37-48 (in or near the outer divertor region). The error bars fluctuated from 12% to 40% in regions located between the midplane and the upper stagnation point, i.e., regions 14-27. In these regions GTNEUT showed a neutral attenuation relative to the neutral density at the divertor plate on the order of 10^5 at the midplane and 10^8 at the upper stagnation point. The corresponding DEGAS attenuation was 10^4 and 10^6, respectively. There were large discrepancies between the results of the two codes in regions 12-36. These can be explained, in part, by the DEGAS statistics in those regions. Larger differences began to be observed in regions 11 and 37 where the results for the ionization rate and neutral density differed by a factor of approximately two. It is believed that these were due to the

145
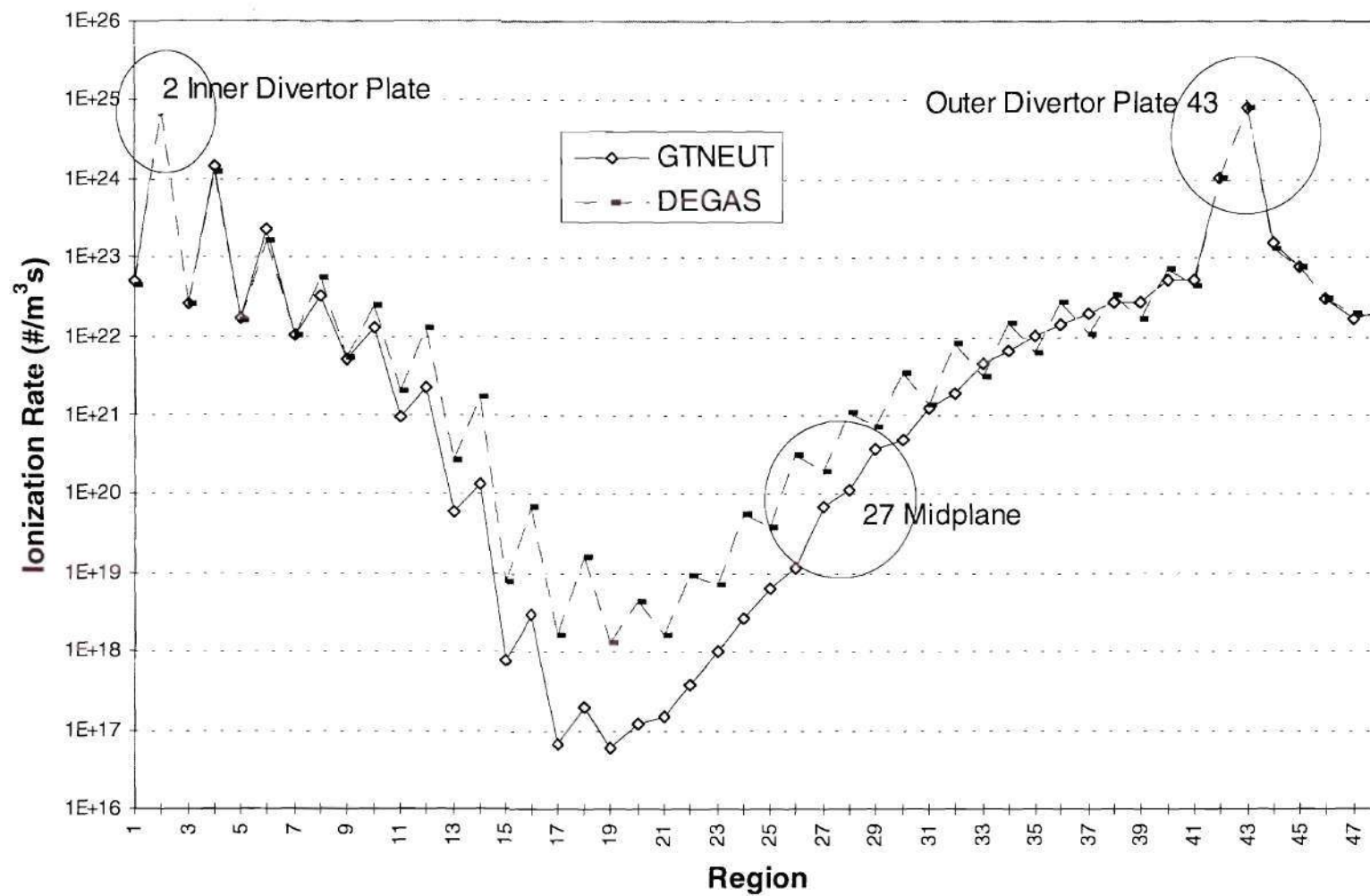
Figure 6.2. Ionization rate density for the DIII-D model.
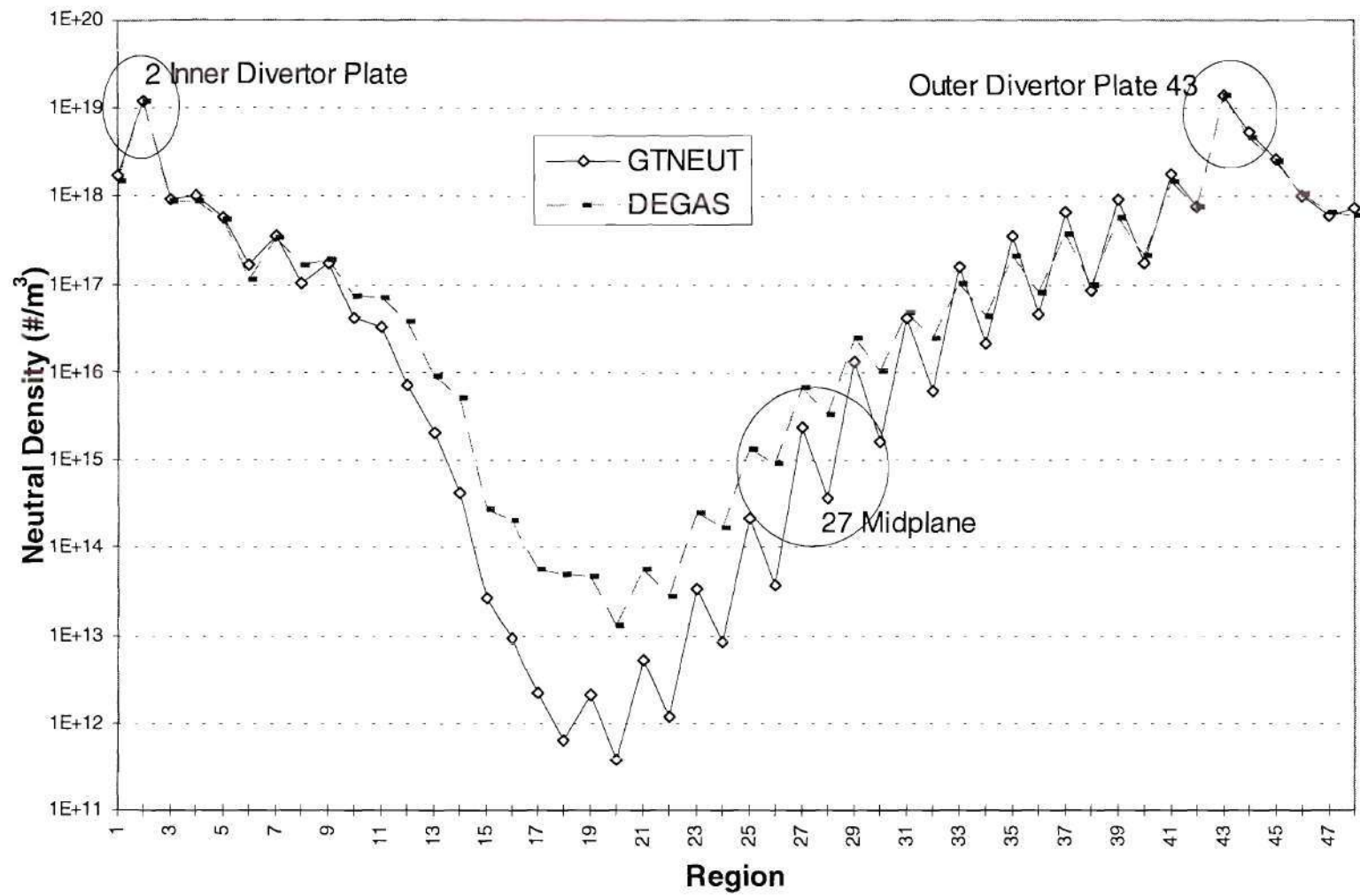
Figure 6.3. Neutral particle density for the DIII-D model.

difference in the treatment of the reflective boundary conditions at the wall and edge-core interface in the two codes. In general, the agreement between the two codes was good in all regions where the neutral density did not attenuate more than 10^3-10^4 with respect to the divertor plate (i.e., regions 1-12, 36-48).

The simulations were done on a Cray J90. The time required to carry out the GTNEUT calculation was 18 cpu seconds, while the time needed by DEGAS to run 500,000 histories was 12,784 cpu seconds.

6.3 C-Mod Model

MIT's Alcator C-Mod fusion experiment is well known for its compact size and high field environment. It can produce the density and the confinement necessary for a useful fusion reaction. As a result, Alcator experiments have performed at levels rivaling the largest fusion experiments in the world [55].

A realistic neutral transport simulation with a full scale Alcator C-Mod geometry was carried out. The main goal in solving this problem was to find the neutral particle density and the ionization rate distribution everywhere within the regions of interest, in particular near the divertor plates. The representative geometry of the plasma, SOL, divertor, and plenum regions are shown in figure 6.4. The C-Mod-like model was represented with 70 GTNEUT cells. The low density regions near the wall were represented by the cells with odd numbers between 1 and 55. The SOL region was represented by the cells labeled with even numbers between 2 and 62. The inner divertor plate was represented by the wall

148

Figure 6.4. Neutral atom transport model for CMOD plasma.

149

segments 74 through 78. Particles were recycled in front of the inner divertor plate in cells 1, 2, 3, and 5. Wall segments 104 through 109 represented the outer divertor plate. The corresponding recycling cells were 57, 59, 61, 63, and 64. The private flux region was represented by cells 65 through 70. Table 6.3 summarizes the location of different regions of interest. The background plasma temperatures and densities that were used in the GTNEUT model were taken from a recent UKAEA report [7], and are summarized in table 6.4 and in figure 6.5.

Table 6.3. Cell Assignments for the CMOD Model

Location	Cells	Wall Segments
Wall-vacuum	odd numbers 1 - 55	74 - 108
SOL	even numbers 2 - 62	-
Outer Divertor	57, 59, 61, 63, 64	104 -109
Inner Divertor	1, 2, 3, 5	74 - 78
Pump - Vacuum	65 - 70	110 - 118
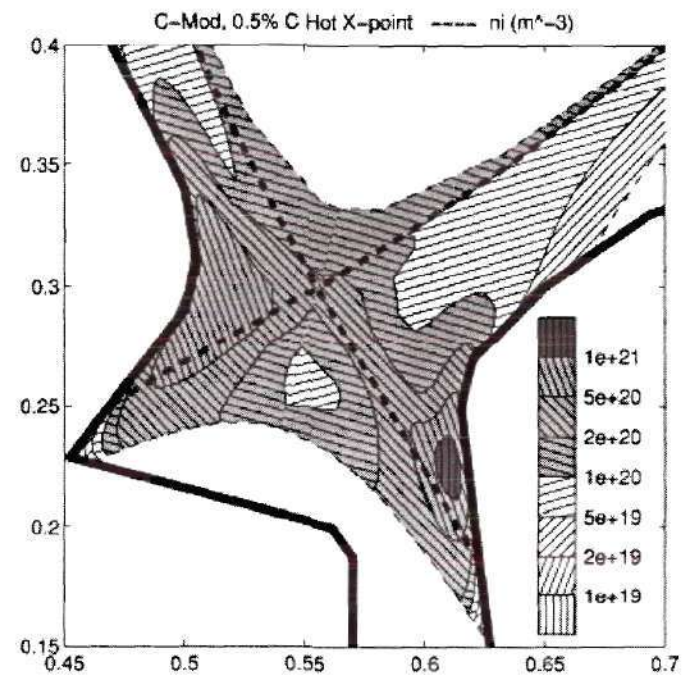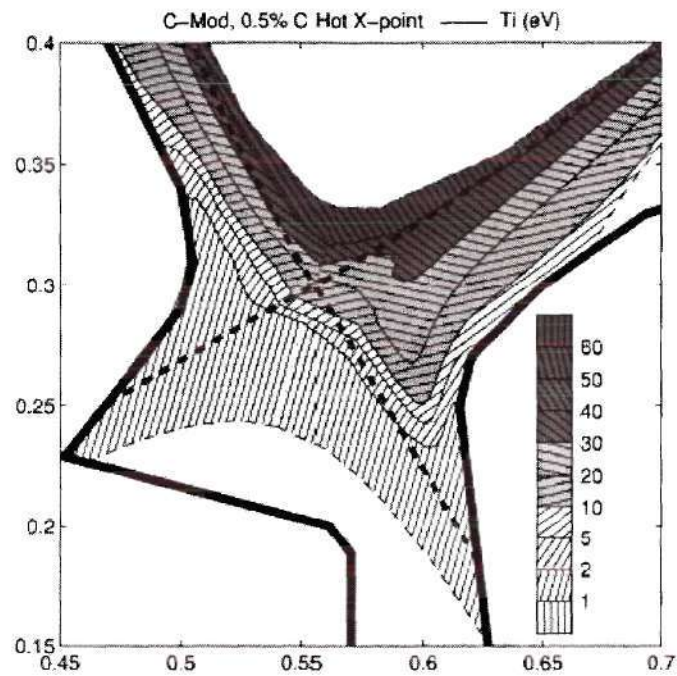
Figure 6.5. Ion temperature and ion density distributions in Alcator C-Mod, from reference 7.

Table 6.4. Temperature and Density Assignments for the CMOD Model

Cells	Temperature (eV)	Density (#/m³)
Central Plasma	100	1.5×10^{20}
Cells (odd numbers) 7 - 55	15	2.5×10^{19}
Cells (even numbers) 8 - 56	35	7.5×10^{19}
Cells 1, 2, 3, 5	1.5 - 7.5	$2.0 - 7.5 \times 10^{20}$
Cells 4, 6, 8	3.5	$0.7 - 5.0 \times 10^{20}$
Cells 57, 59, 61, 63, 64	1.5	$1.1 - 8.75 \times 10^{20}$
Cells 58, 60, 62	3.5 - 5.0	$1.1 - 2.5 \times 10^{20}$
Cells 65 - 70	1.5	$1.0 - 5.0 \times x10^{20}$

The ion flux (also taken from the UKAEA report) incident upon the inner and outer divertor plates varied from 8.5×10^{22} to 1.8×10^{23} s^{-1}, and 4.1×10^{22} to 2.4×10^{23} s^{-1} respectively. The ion flux was reflected from the divertor plates and entered the corresponding adjacent cells, i.e., cells 1, 2, 3, 5, 57, 59, 61, 63, 64. The GTNEUT calculation assumed that the neutrals reflected from the divertor plate, walls, and those neutrals going from region to region acquired a Maxwellian energy distribution with the local ion temperature of the region in question. The DEGAS calculation, on the other hand, calculates a continuous neutral energy distribution.

The wall segments were assigned a reflection coefficient equal to 1.0 and a pumping fraction of 0.0. The wall segment 111 represented the location of the opening of the pumping ducts. Here the assigned values for the reflection coefficient and pumping fraction were 0.0 and 0.5 respectively. Identical cell arrangements and plasma parameters

152

were used to run a DEGAS simulation. Ions, in the GTNEUT calculation, were reflected as neutrals with an isotropic distribution. The DEGAS calculation, on the other hand, treated the collision with the wall as a specular reflection ("mirror" option). Specular reflection generates an isotropic distribution of particles near the wall only in regions with short mean free path. Thus, this condition was similar to the assumption used by GTNEUT. The recycling of the incident ion flux, in Monte Carlo, was approximated by a puff of neutrals with an energy corresponding to a Maxwellian with the local ion temperature of the region in front of the divertor plates (i.e., regions 1, 2, 3, 5, 57, 59, 61, 63, and 64).

6.3.1 Analysis of the Results

The results of the GTNEUT and DEGAS simulations showing the volumetric ionization rate and the neutral particle density can be seen in figures 6.6 and 6.7. With reference to figure 6.7, the predicted results of the GTNEUT and DEGAS codes agreed fairly well. Both codes predicted similar X-point, n_{DIV}/n_{Xpt}, and midplane, n_{DIV}/n_{Mid}, compression ratios. GTNEUT predicted n_{DIV}/n_{Xpt} and n_{DIV}/n_{Mid} compression ratios of 6.0×10^2 and 2.2×10^8 respectively. DEGAS predicted an X-point compression ratio equal to 1.4×10^4 and a midplane compression ratio equal to 1.74×10^7. The DEGAS calculation was carried out with 400,000 histories, and the error bars were less than 1% for regions 1-5 (in or near the inner divertor region) and for regions 60-70 (in or near the outer divertor and private flux region). The error bars were less than 10% for regions 6-14 near the inner divertor plate and for regions 50-59 near the outer divertor plate. The error bars

153
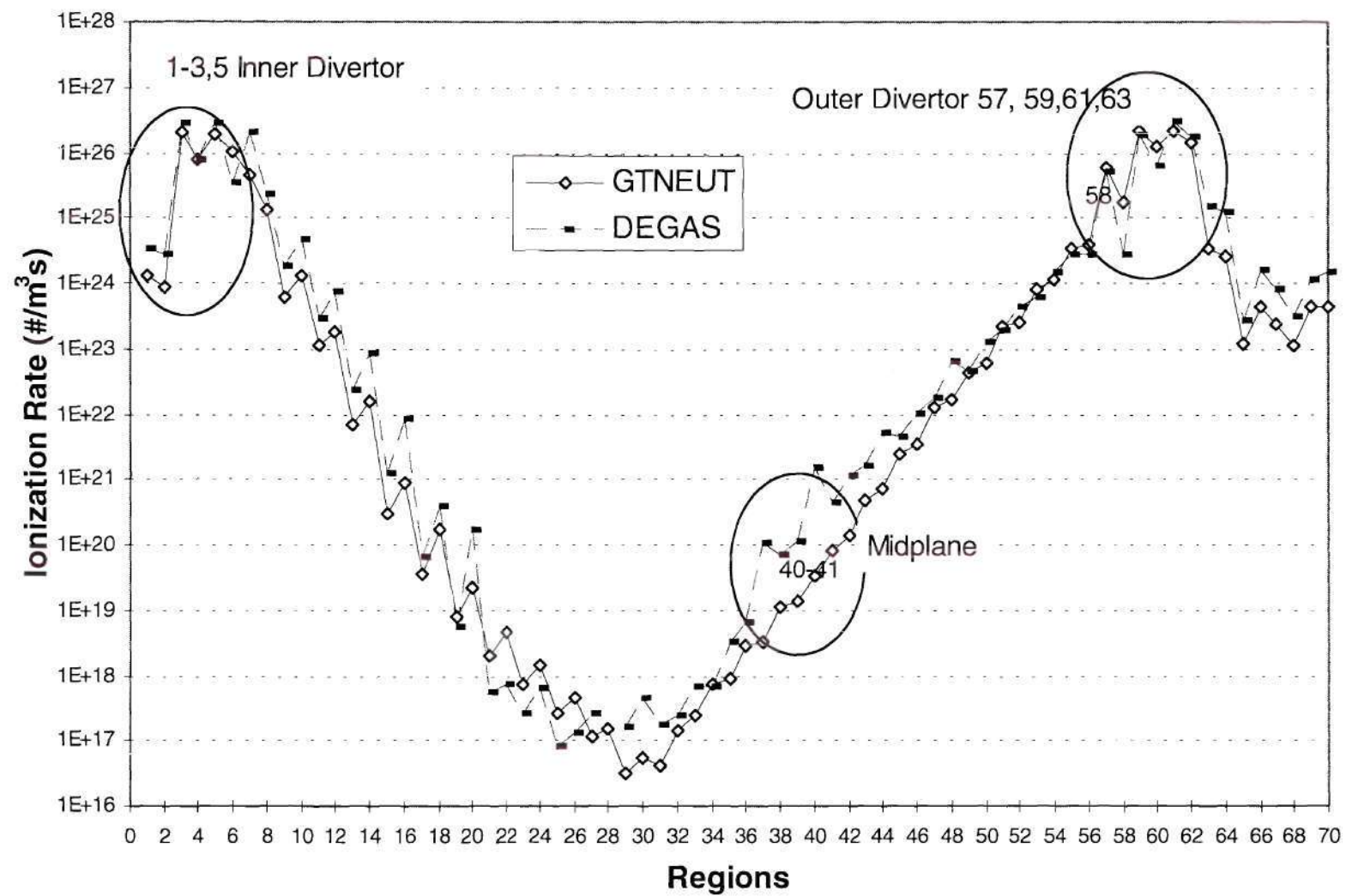
Figure 6.6. Ionization rate density for the CMOD model.
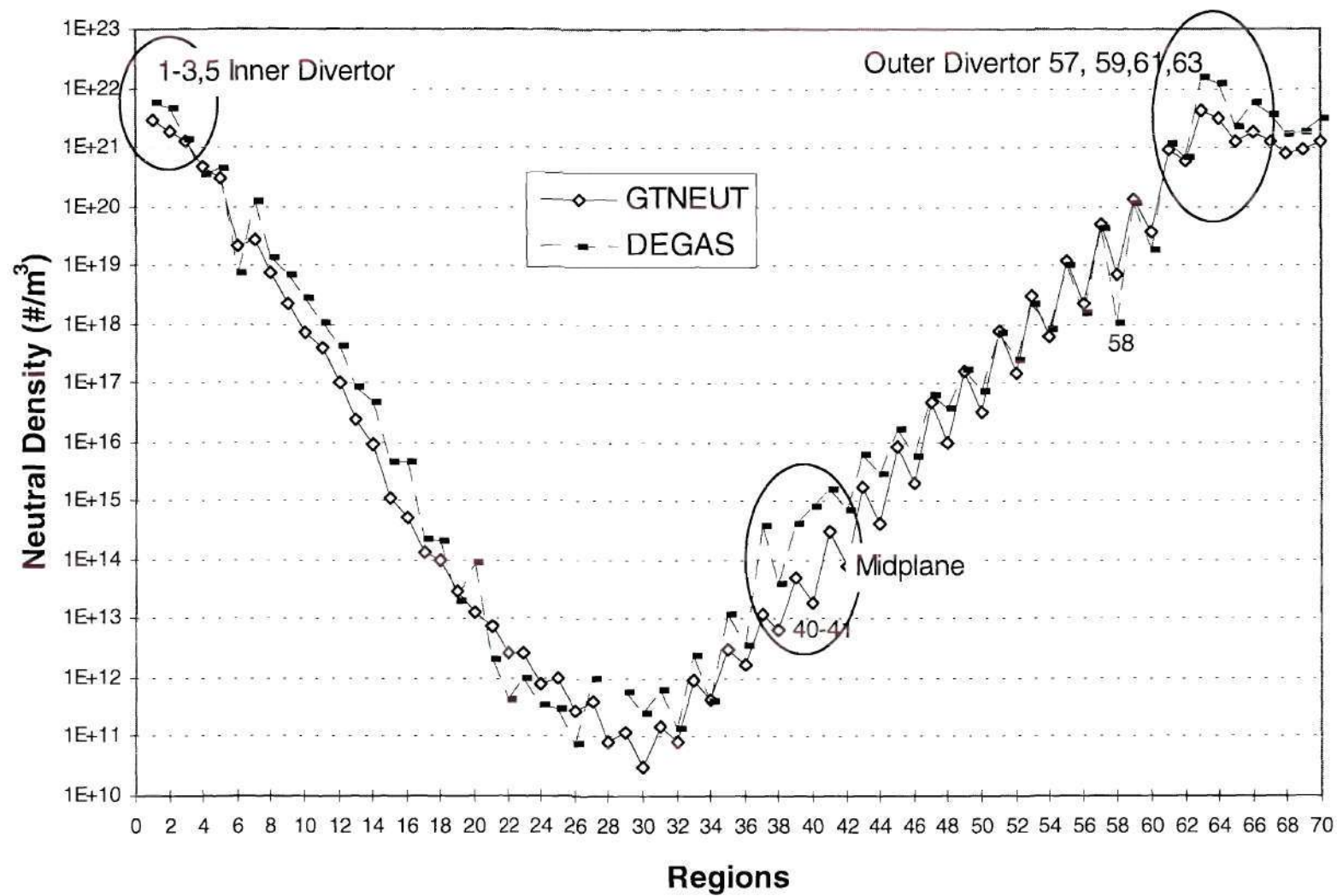
Figure 6.7. Neutral particle density for the CMOD model.

fluctuated from 18% to 100% between regions 15-46. These regions were located around the midplane and upper stagnation point of the C-Mod model. There were large discrepancies between the results of the two codes in regions around the X-point, namely, regions 6, 7, 58, and 60. In these regions the ionization rate and neutral density differed by a factor of 2-4 and 2-7 respectively. There were also large differences between the results of the two codes in the private flux region (i.e., regions 65-70). In these regions the ionization rate and neutral density varied by a factor of 2-4. Since statistics in DEGAS were rather poor in all regions in and above the midplane, it would be premature to draw a conclusion about the results in this general location. For instance, the value for the midplane compression ratio (1.74×10^7) predicted by DEGAS was questionable.

On the other hand, the discrepancies in regions 1, 2, 6, 7, 63, 64-70 could be attributed to the differences in reaction cross sections at low temperatures (1.5 eV - 7.0 eV). Those errors in regions 6, 7, 58, and 60 were more likely to be caused by the different treatment of reflection between the two codes (the mean free path varied from 3 to 10 cm). However, other possible reasons for the disagreement in the regions near the divertor plates, X-point and private flux region could be the inadequate treatment of the isotropic and escape probabilities errors in GTNEUT, and the assumption employed by GTNEUT that the energy of the neutral is given by a Maxwellian with the local ion temperature. In general, the agreement between the two codes was fair in all regions where the neutral density was not attenuated more than 10^3-10^4 with respect to the divertor plate (i.e., regions 1-10, 58-70).

The simulations were done on a Cray J90. The time required to carry out the GTNEUT calculation was 35 cpu seconds while the time needed by DEGAS to run 400,000 histories was 70,542 cpu seconds.

6.4 ITER Model

The International Thermonuclear Experimental Reactor, ITER, is the product of a summit level initiative that took place in 1985. Today, the ITER program involves the collaborative efforts of three of the four major fusion programs in the world (European Community, Japan, and Russia). The main objective of this "next generation tokamak experiment" is to demonstrate the scientific and technological feasibility of fusion energy for peaceful purposes [56].

The ITER model used in the neutral transport calculations presented here corresponds to the now finished Engineering Design Activities (EDA) phase. The representative geometry of the outer half of the ITER-EDA plasma, SOL, divertor, and plenum regions are shown in figure 6.8. The divertor configuration modeled here corresponded to the vertical target option whose cross section and isometric views are shown in figure 6.9 [57]. The ITER-EDA model was represented with 29 GTNEUT cells. The low density regions near the wall were represented by the cells with odd numbers between 1 and 23. The SOL region was represented by the cells labeled with even numbers between 2 and 26. The wall segment 46 represented the outer divertor plate. The corresponding recycling cell is 25. The private flux region and pump were represented by cell 29. The dome area

157
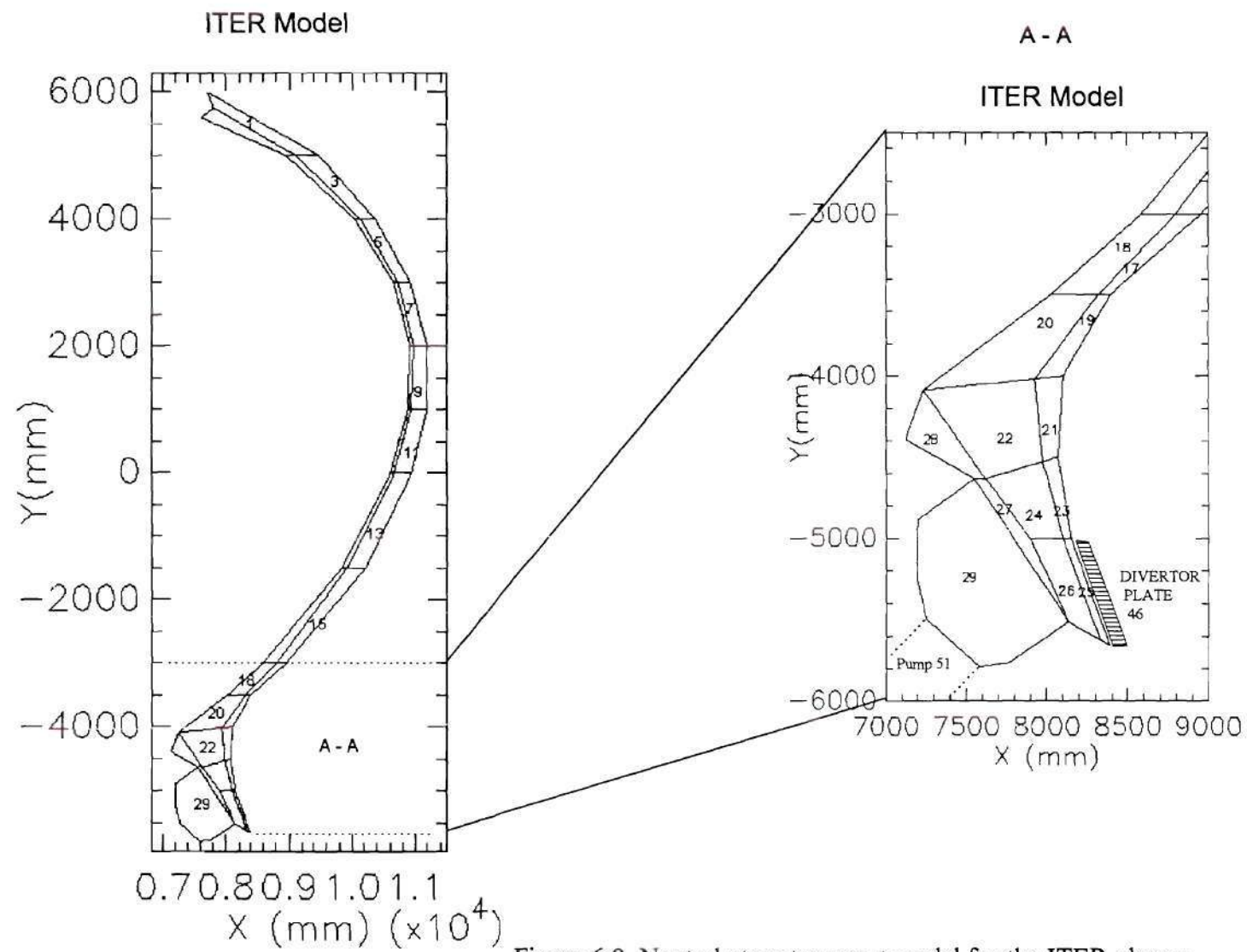
Figure 6.8. Neutral atom transport model for the ITER plasma.
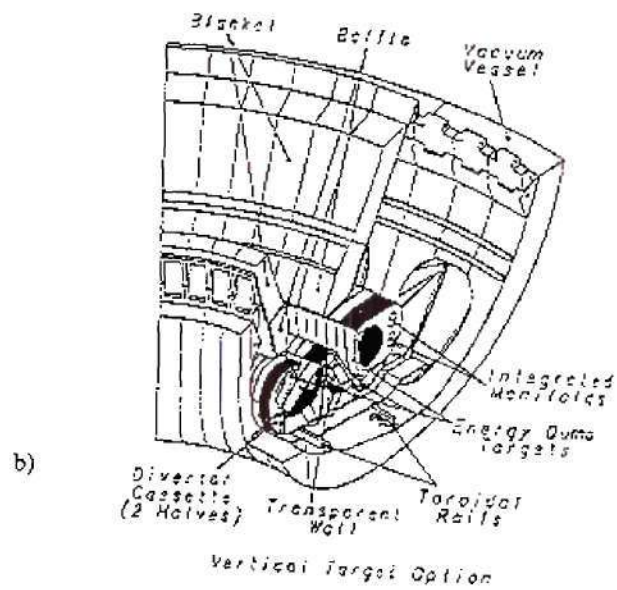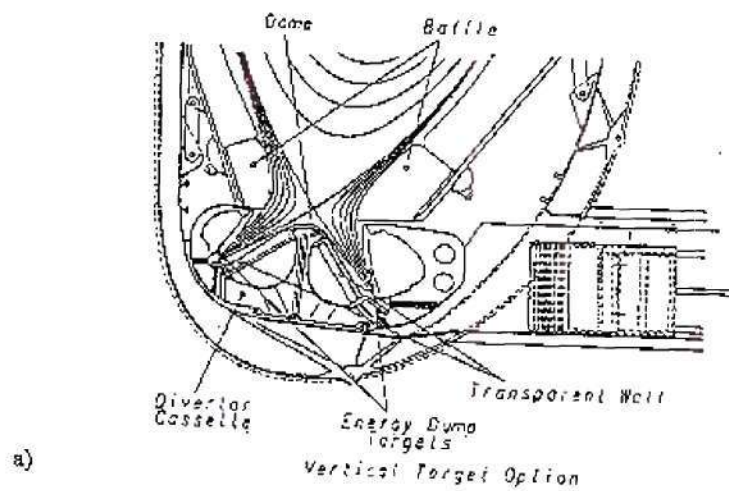
Figure 6.9. Vertical target option for the divertor configuration in ITER-EDA; a) cross section, b) isometric view. From reference 57.

159

was represented by cell 28. Table 6.5 summarizes the location of different regions of interest. *The background plasma temperatures and densities that were used in GTNEUT cells are summarized in table 6.6.*

Table 6.5. Cell Assignments for the ITER Model

Location	Cells	Wall Segments
Wall-vacuum	1, 3, 5, 7, 9, 11, 13, 15, 17, 19, 21, 23	-
Pseudo SOL	22, 24, 26	-
SOL	2, 4, 6, 8, 10, 12, 14, 16, 18, 20	-
Divertor	25	46
Pump - Vacuum	29	51
Dome	28	55

Table 6.6. Temperature and Density Assignments for the ITER Model

Cells	Temperature (eV)	Density (#/m^3)
Central Plasma	500	1.3×10^{20}
Cells 1, 3, 5, 7, 9, 11, 13, 15, 17, 19, 21, 23	50	1.0×10^{15}
Cells 2, 4, 6, 8, 10, 12, 14, 16, 18, 20	160	1.3×10^{20}
Cells 22, 24, 26	85	7.1×10^{20}
Cells 25	10	1.3×10^{21}
Cells 27, 28, 29	50	1.0×10^{15}

The total ion flux incident upon the divertor plate was taken to be equal to 1.71×10^{24} s^{-1}. The ion flux was reflected from the divertor plate and entered the

160

corresponding adjacent cell, i.e., cell 25. The GTNEUT calculation assumed that the neutrals reflected from the divertor plate, walls, and those neutrals going from region to region acquired a temperature/energy corresponding to a Maxwellian with the local ion temperature of the region in question. The Monte Carlo simulation assumed a continuous energy distribution of neutrals.

The wall segments were assigned a reflection coefficient equal to 1.0 and a pumping fraction of 0.0. The wall segment 51 represented the location of the opening of the pumping duct. Here the reflections coefficient and pumping fraction were 0.0 and 0.5 respectively. Identical geometry and plasma parameters were used to run a DEGAS simulation. The Monte Carlo calculation treated the ion collisions with the wall as a specular reflection ("mirror" wall boundary condition option). GTNEUT assumed that the particles were reflected isotropically. The treatment of reflection in DEGAS was proven satisfactory only in regions with short mean free paths. In this regime neutrals isotropize near the wall, thus approximating the isotropic distribution used by GTNEUT. The recycling of the incident ion flux was approximated by a puff of neutrals with an energy corresponding to a Maxwellian with local ion temperature of the region in front of the divertor plate (i.e., region 25).

6.4.1 Analysis of the Results

The predicted results of the GTNEUT calculation along with the predicted results of the DEGAS simulation for the ionization rate distribution and neutral particle density can be seen in figures 6.10 and 6.11. It is evident from these figures that both codes predicted

161
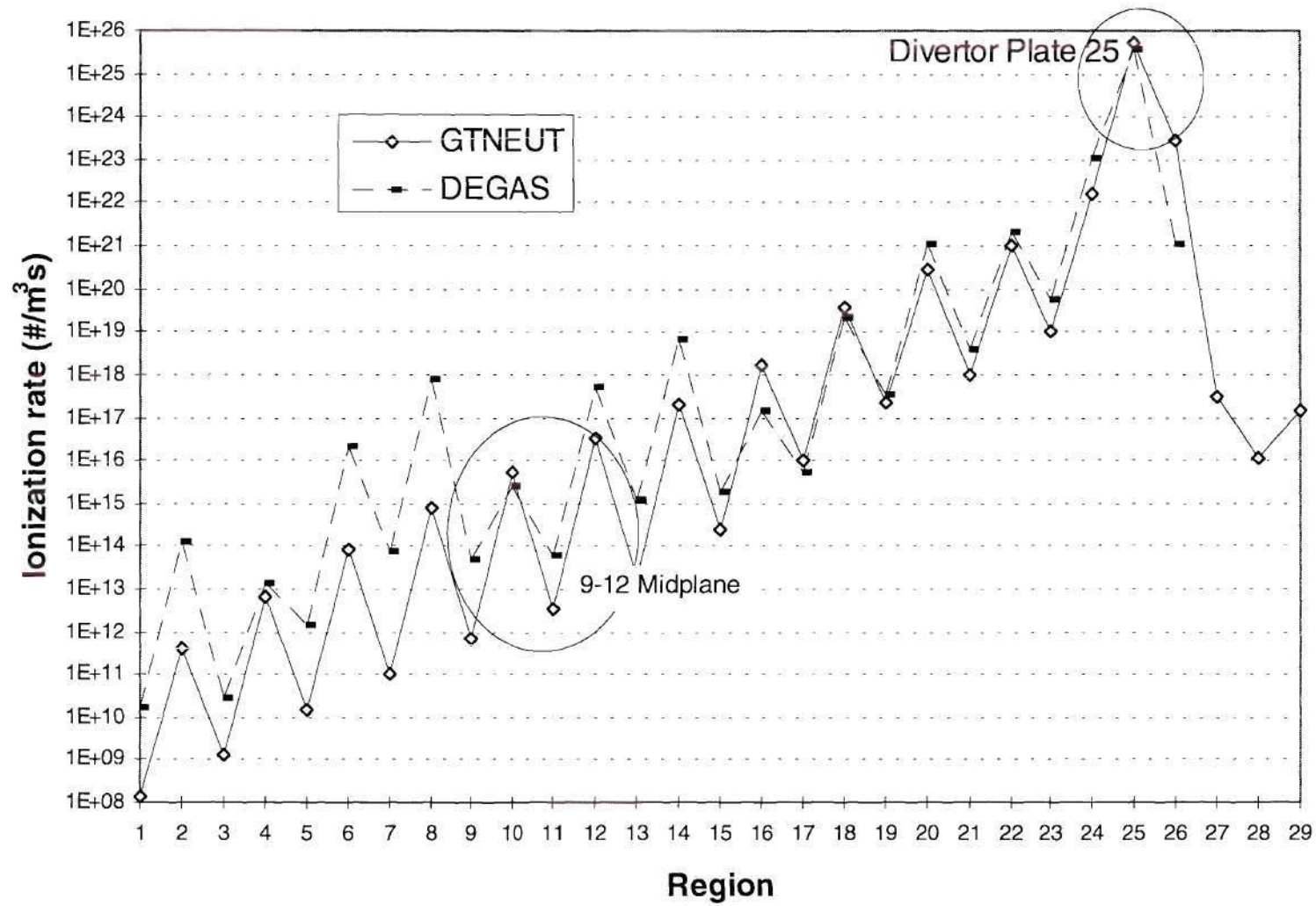
Figure 6.10. Ionization rate density for the ITER-EDA model.

162
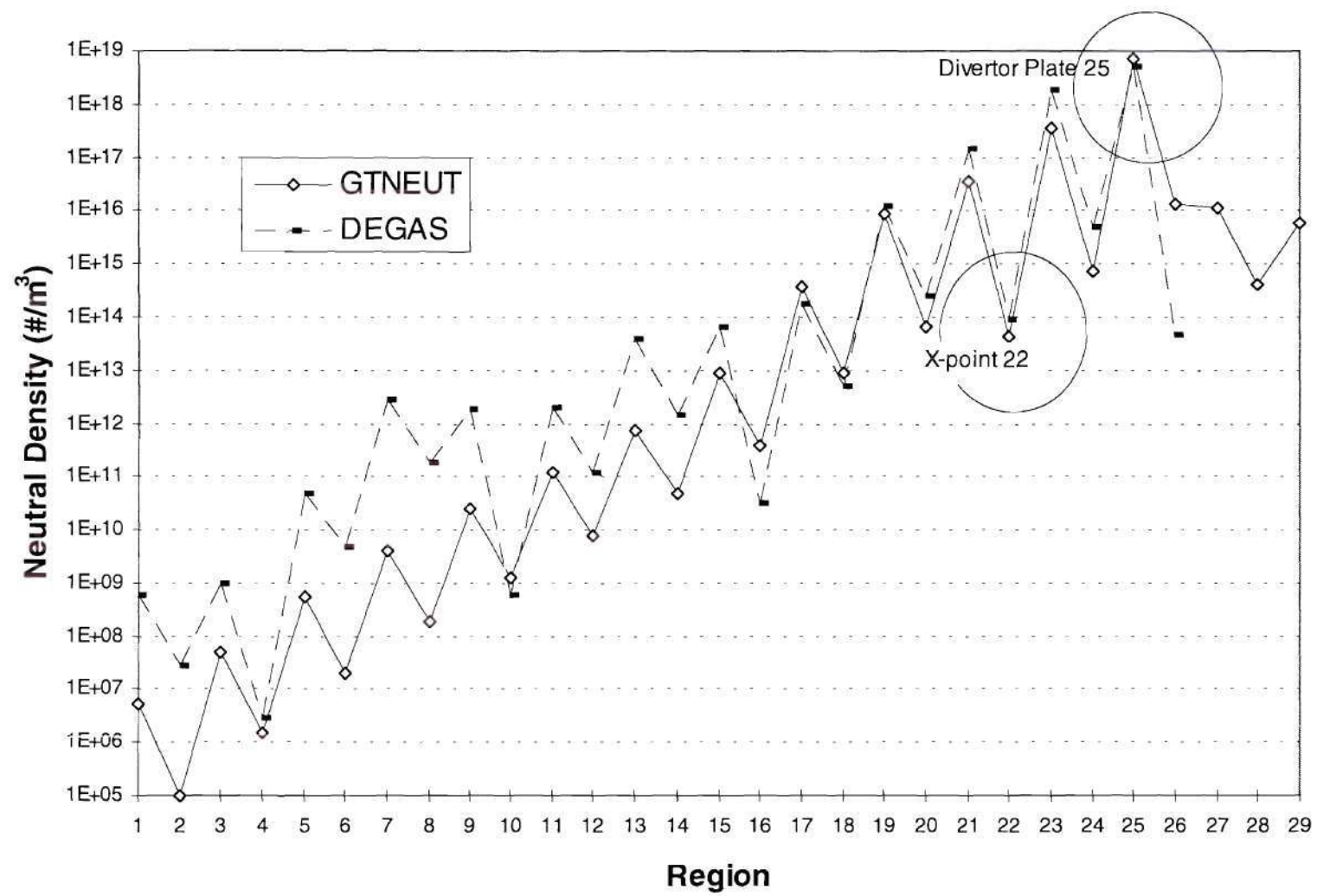
Figure 6.11. Neutral particle density for the ITER-EDA model.

accurately the ionization rate and neutral density in the recycling region, i.e. cell 25. The results were in excellent agreement; they only differed by a factor of 0.74. For the most part, the agreement between the two codes was fairly good in all regions where the neutral density was not attenuated more than 10^3-10^4 with respect to the divertor plate (i.e., regions 22-25). However, the predictions of both codes showed some discrepancies.

It is clear, from figure 6.11, that the neutral density was largest near the divertor plate and decreased rapidly towards the cells surrounding the plasma core. DEGAS failed to produce meaningful results in regions near the mid-plane and stagnation point (i.e., regions 1-16). The error bars in these regions were greater that 50%. This explained the poor DEGAS results in those cells. GTNEUT predicted a compression ratio equal to 1.6×10^5 at the X-point and 2.95×10^8 at the midplane. DEGAS predicted an X-point ratio equal to 0.6×10^5 and a midplane ratio of 2.9×10^6. However, due to the large uncertainty in the midplane region ($\pm$ 90 %), the midplane compression ratio predicted by DEGAS was questionable.

In the cells just above the divertor, GTNEUT consistently underpredicted DEGAS in calculating the ionization rate and neutral density. There were large discrepancies between the results of the two codes in regions 23, 24 and 26. These could not be explained by the poor DEGAS statistics since the error bars (for example in regions 23 and 24) were less than 5%. The error in region 26 was about 23%. It is believed that specular reflection in the DEGAS calculation was projecting the fluxes up the divertor throat. Region 23 was a vacuum; here the mean free path was about 1000 m. Under these conditions and

164

regardless of the direction in which the neutral traveled, $\Delta x/\lambda < 1$. This meant that the isotropization error decreased (i.e., fluxes were less forward peaked) causing an underprediction of penetration. However, since the mean free path was so long, the treatment of reflection in GTNEUT was no longer isotropic. In fact, the uncollided fluxes became highly peaked, causing particles to be transported to other regions. DEGAS did not yield results in regions 27 through 29. This was attributed to the extremely low electron/ion densities used to characterize these regions. Another possible reason for the disagreement in the regions near the divertor plates and X-point was the assumption used by GTNEUT that the energy of the neutral is given by a Maxwellian with the local ion temperature.

Both simulations were performed on a Cray J90. The time required to carry out the GTNEUT calculation was 10 cpu seconds while the time needed by DEGAS to run 100,000 histories was 2,984 cpu seconds.

6.5 Conclusions

The results of neutral transport calculations with full scale diverted tokamak models were very encouraging. The TEP-based code, GTNEUT, was able to predict both ionization rate and neutral particle densities everywhere in the models. DEGAS, on the other hand, had problems scoring in regions far away from the divertor plates. The results were in excellent agreement with those predicted by Monte Carlo in close proximity to the recycling region and divertor plates. There were some noticeable differences between the predicted results of both codes in regions located a distance away from the divertor plates,

165

in particular near the X-points and midplanes. These were attributed to the treatment of reflection and the compensating isotropization and escape directionality errors in GTNEUT. In addition, GTNEUT was able to carry out the transport calculations in geometrically complex models at a fraction of the computer time required by Monte Carlo.

CHAPTER VII

COMPARISON WITH DIII-D NEUTRAL MEASUREMENTS

7.1 DIII-D Neutral Experiment

The purpose of this chapter is to compare the neutral density, as predicted by the TEP-based code, GTNEUT, with both a recent measurement of the neutral density near the X-point in the DIII-D tokamak and a plasma fluid/Monte Carlo neutrals calculation.

A new method to measure the neutral density around the X-point region was developed recently [58]. It consisted of measuring the D_α light emission in the lower divertor by means of a tangentially-viewing charge injection device (CID) video camera (TTV). The image obtained was later used to generate a poloidal D_α light distribution. The electron temperature and density were measured at the divertor Thomson scattering location shown in figure 7.1.
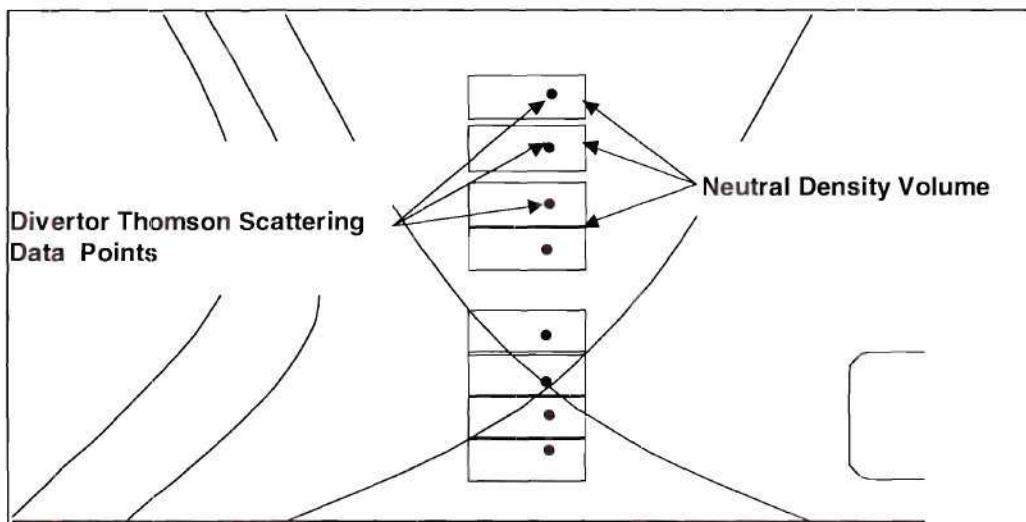
Figure 7.1 Location of divertor Thomson scattering data points (•), and tangential TV intensity data sampling areas (rectangles), taken from reference 58.

The neutral density was then calculated by using the relation

$$I_{D_\alpha} = n_e n_0 \langle \sigma(T_e, n_e) v_e \rangle_{exc} \tag{7.1}$$

where the quantities I_{D_α}, n_e, and $\langle \sigma(T_e, n_e) v_e \rangle_{exc}$ represent the intensity of the TTV, the electron density measured by the Divertor Thomson Scattering (DTS), and the electron excitation rate coefficient respectively. During the process of taking the measurement, the location of the X-point was adjusted and held in place for 0.5 seconds. Three time slices were taken of shot #96740, namely, t = 2250 ms, t = 3750 ms, and t = 4250 ms. The corresponding X-point heights above the divertor floor for these three time slices were 13.8 cm, 10.0 cm, and 6.9 cm, respectively. The measurement taken at t = 2250 ms provided the most data, as well as the best data.

A two-dimensional model based on an iterated solution of a plasma fluid (B2.5) and Monte Carlo (DEGAS) neutrals codes was used by Colchin et al. to predict the experimental measurements [58]. The geometry for the two-dimensional GTNEUT model was based on this DEGAS model (which used the background plasma solution from B2.5). In the GTNEUT calculation, it was assumed that neutrals acquired an energy corresponding to a Maxwellian with the local ion temperature of the regions in question. DEGAS, on the other hand, calculated a continuous energy distribution in each region. The geometric model consisted of 190 regions, chosen to represent as accurately as possible the location of the divertor plate, the X-point, SOL, and plasma core. The model is depicted in figure 7.2. The X-point was located at 13.8 cm above the divertor floor. The

168

DIII-D Model
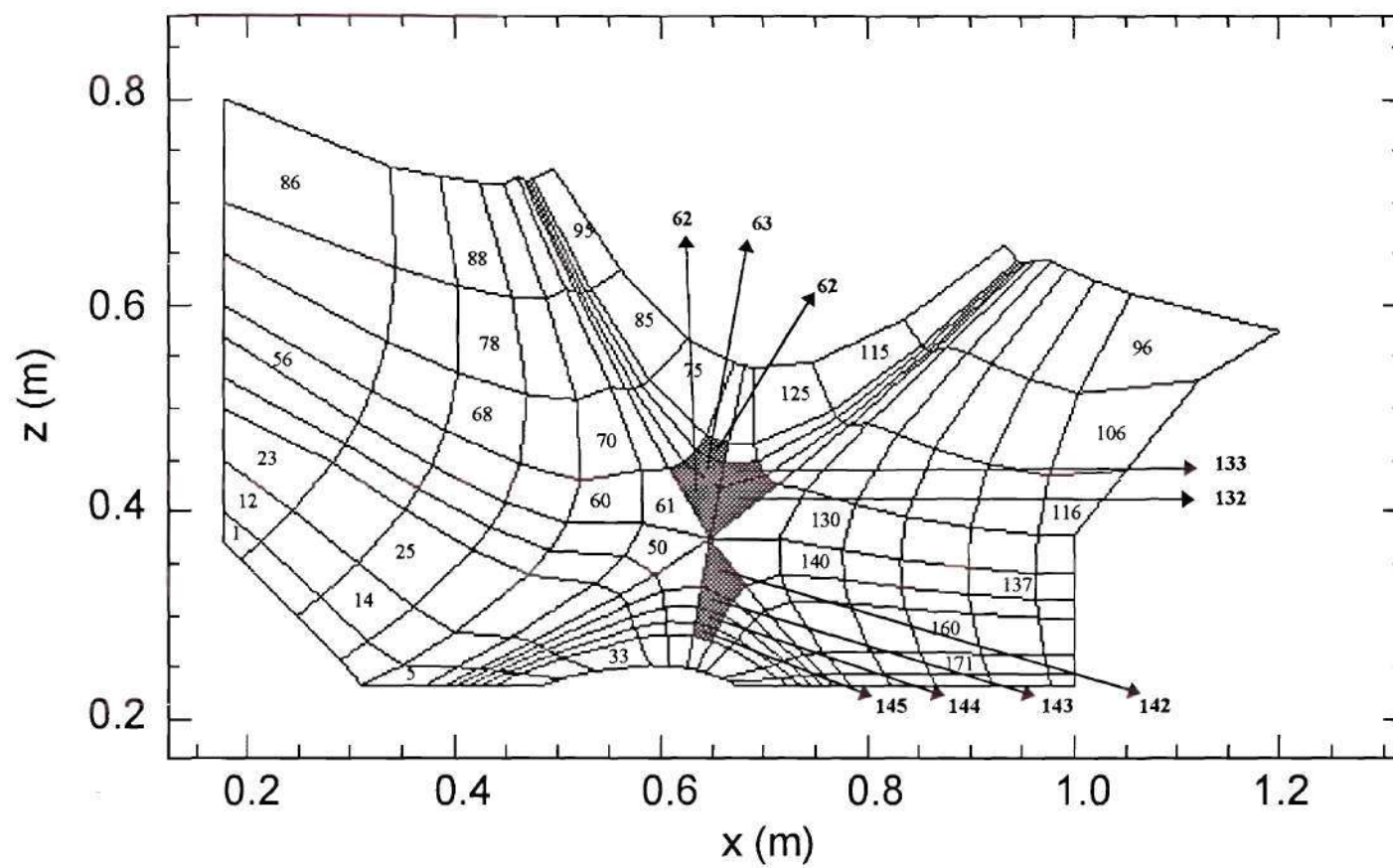
Figure 7.2. Neutral atom transport model for the DIII-D plasma experiment.

regions representing the location at which the measurements were taken are summarized in table 7.1 and shown in figure 7.2. The plasma background temperature, density, and source were also taken from DEGAS. The results predicted by GTNEUT, along with the predicted results obtained with DEGAS and the experimental measurements [58], are shown in figure 7.3.

Table 7.1. Location of the Regions in the GTNEUT Model Corresponding to the Height Above the Divertor Floor at Which Measurements Were Taken

Height above the floor (cm)	Cell
5.2	145
6.5	144
8.6	143
11.3	142
17.4	(62 + 132)/2
20.8	(63 + 133)/2
22.8	64

The results obtained with the DEGAS model showed very good agreement with the measured neutral density above the X-point in the core plasma. The results were not as good for those regions below the X-point. The discrepancies between the DEGAS model and the experiment were attributed [58] to two factors: 1) the fluid code's inaccurate representation of the plasma parameters in the region below the X-point, and 2) the neglect of the molecular contribution to the total intensity of the D_α light emission in
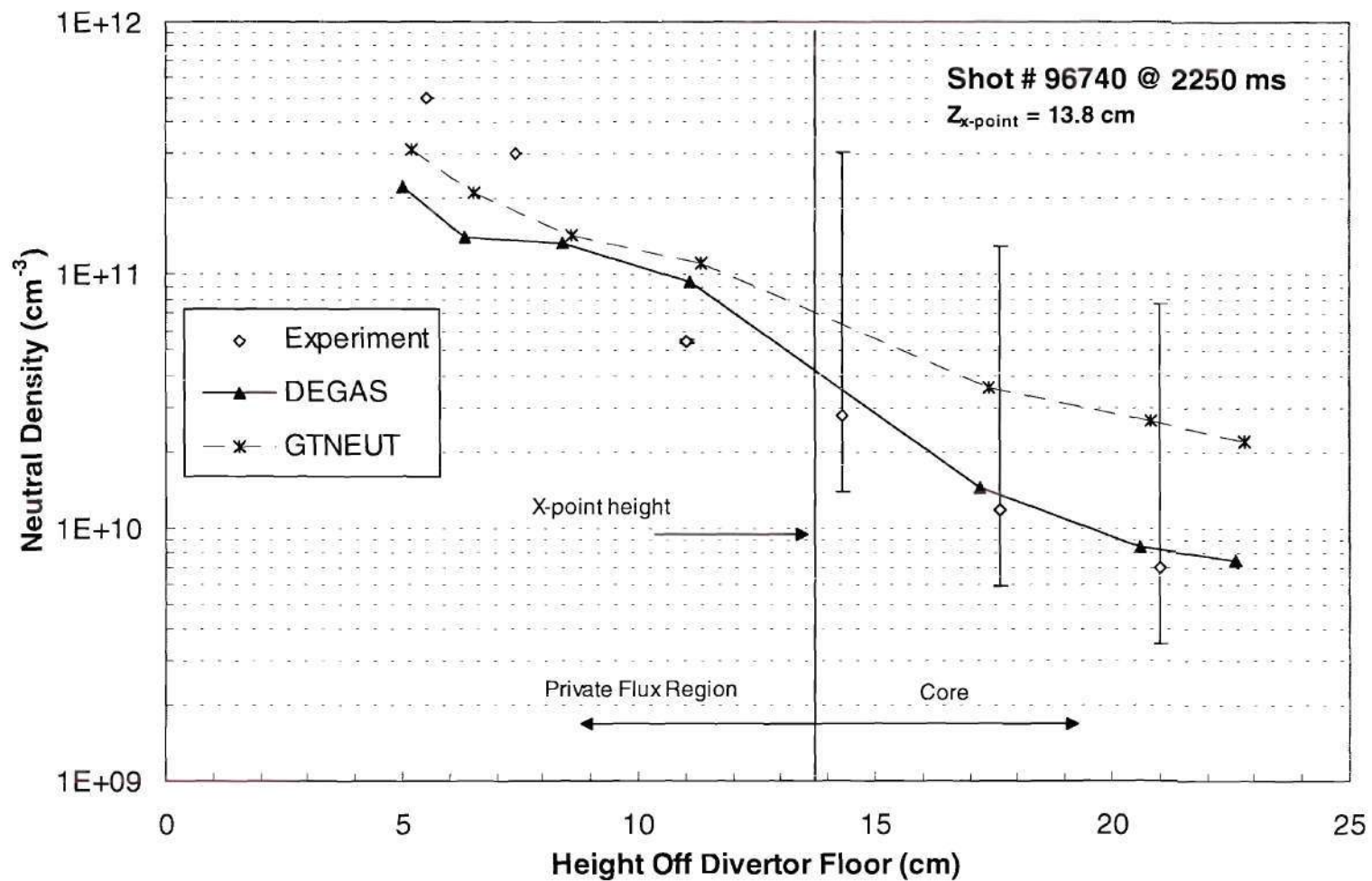
Figure 7.3. Neutral density as a function of height above the divertor floor (molecular effects and density-dependent ionization rates included in DEGAS, but not in GTNEUT).

evaluating the measured neutral density (equation 7.1 did not include molecular contributions to the D_α light emission). Molecular effects should be important in regions close to the divertor plate at low temperatures (2-3 eV). They should be relatively unimportant inside the core, given the fact that very few molecules are present. The GTNEUT calculation, which did not include molecular effects, agreed with the experiment to within the error bars. However, for regions above the X-point, the GTNEUT code overpredicted both the experimental measurements and the predicted DEGAS values by at least a factor of two.

7.2 Monte Carlo and GTNEUT Modeling Differences

With reference to figure 7.3, GTNEUT obtained somewhat better agreement with the experiment in the private flux region than DEGAS because both GTNEUT and the interpretation of the experimental data neglected molecular effects, whereas molecular effects were included in the DEGAS calculation.

However, in the core region above the X-point, where molecular effects are unimportant, there was a factor of at least two difference between the DEGAS simulation and the GTNEUT calculation. At least seven possible explanations could account for these discrepancies: 1) different treatment of geometry in DEGAS and in GTNEUT, 2) different treatment of molecular and ionization rate effects in DEGAS and in GTNEUT, 3) different treatment of the wall boundary condition in DEGAS and GTNEUT, 4) different treatment of particle recycling in DEGAS and GTNEUT, 5) inadequate treatment of the directional escape probability, Λ, in GTNEUT, 6) inaccurate description of the flux distributions at

172

the interfaces in GTNEUT, and 7) the assumption in GTNEUT that the neutral energy distribution is a Maxwellian with the local ion temperature.

The first four explanations could be considered nontransport differences and could be explained by the differences with which Monte Carlo and GTNEUT modeled the experiment. To understand these differences, a number of simulations were performed with DEGAS to determine the degree of importance of each of these effects.

7.2.1 Geometrical Differences

GTNEUT modeled the experiment using a cylindrical geometry. DEGAS, on the other hand, explicitly treated a toroidal configuration. Thus, it seemed necessary to study the sensitivity of the DEGAS simulation to geometric effects. Two DEGAS runs were made. Both runs were done with identical plasma parameters, differing only in the geometric setup. The results of the cylindrical Monte Carlo simulation were divided by $2\pi R$ (where R corresponds to the radius at which the measurements took place) to obtain toroidally equivalent results. The predictions shown in figure 7.4 indicate that geometric effects in DEGAS are not important. Thus, it is doubtful that a geometric difference could account for the differences seen between the Monte Carlo and GTNEUT predictions in figure 7.3

7.2.2 Molecular and Cross Section Differences

The data for the reaction rates used by the GTNEUT code did not include molecular effects. These data also assumed that the electron impact ionization rate, $<\sigma v>_{ion}$, was independent of density. Since DEGAS treated molecular effects and density-dependent $<\sigma v>_{ion}$, it seemed necessary to study the sensitivity of the DEGAS simulation to both of

173
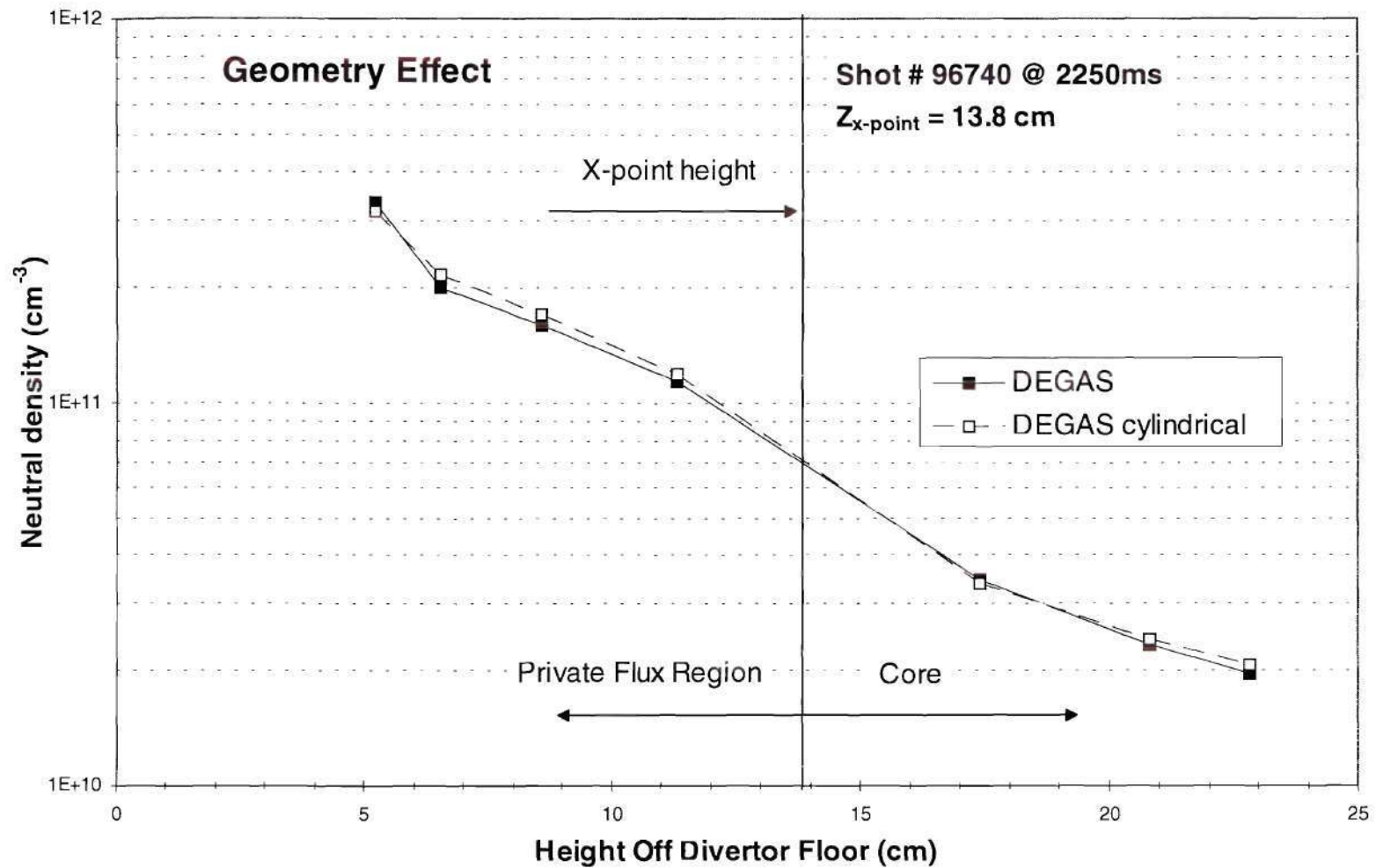
Figure 7.4. DEGAS geometry effect. Toroidal geometry (■) versus cylindrical geometry (□).

174

these assumptions in order to evaluate their effect on the direct comparison of the GTNEUT and DEGAS transport calculations shown in figure 7.2. Thus, two additional DEGAS runs were made. In the first run, the Monte Carlo simulation was performed without molecular effects, but with the electron impact ionization rate $<\sigma v>_{ion}$ dependent on density. In the second run, the Monte Carlo simulation was carried out without molecular effects, and with no ionization dependence on density. The error bars for these two new Monte Carlo simulations (for 100,000 histories) were less than 4% both in the private flux region below the X-point and in the core plasma.

The results shown in figure 7.5 compare the two new DEGAS calculations with the Monte Carlo predictions that included molecular and density-dependent $<\sigma v>_{ion}$ and the experiment. Comparison of the two calculations (■ and □), which differed only by the treatment of the density dependence of $<\sigma v>_{ion}$, indicated that this is a relatively small effect, albeit one which contributes to the differences between the GTNEUT and DEGAS calculation shown in figure 7.3. Comparison of the two calculations (▲ and ■) which differed only by the treatment of molecular effects indicated that the treatment of molecules is quite important, particularly in the private flux region below the X-point. Ignoring molecular effects can increase the neutral density by a factor of between 1.5 - 4.0 in the private flux region. The treatment of molecular effects clearly makes a large contribution to the difference in the DEGAS and GTNEUT calculations of the neutral density in the private flux region shown in figure 7.3.

175
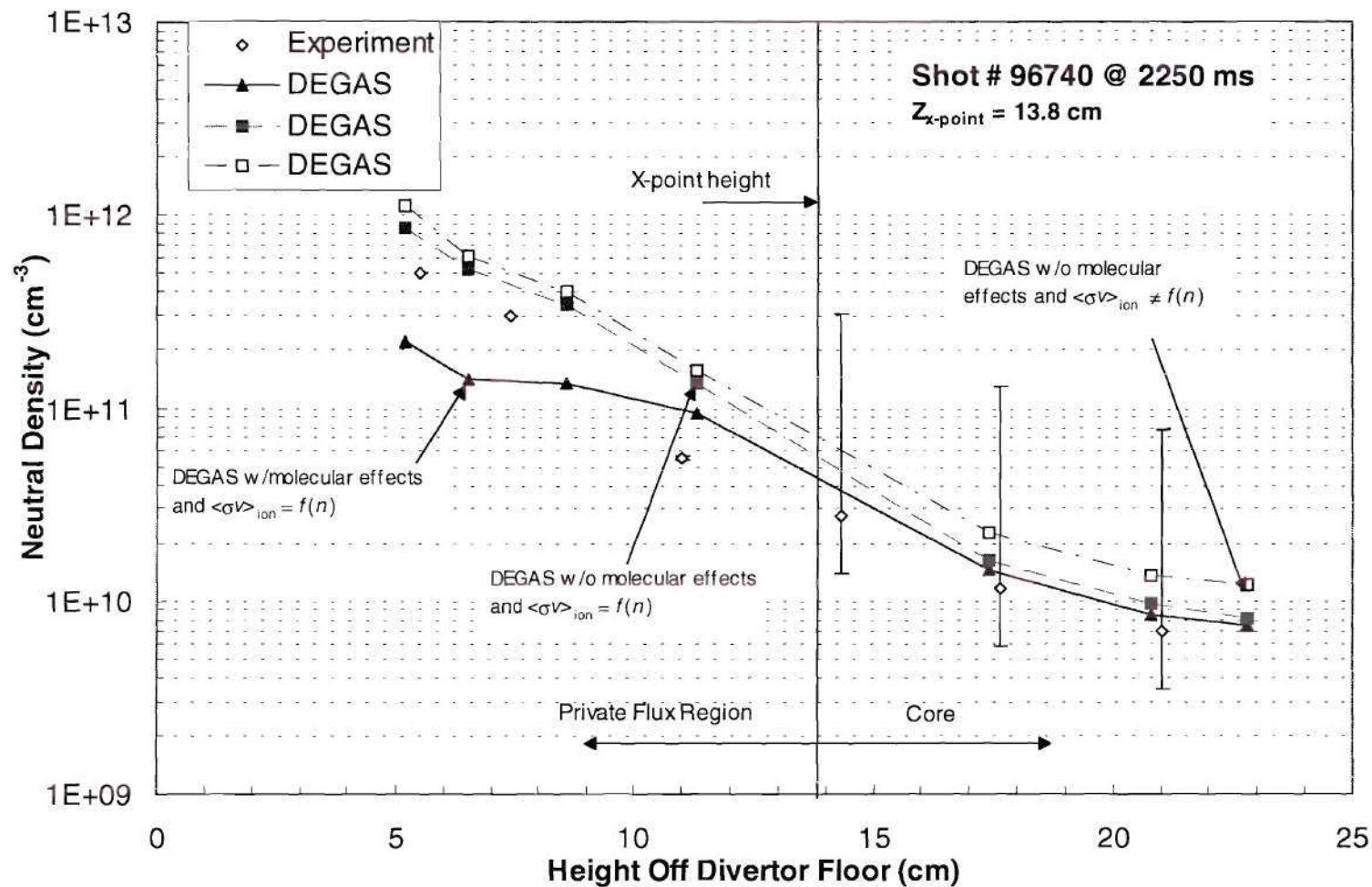
Figure 7.5. Neutral density as a function of height above the divertor floor.
Sensitivity study to molecular and cross section effects.

These results indicate that the difference between the Monte Carlo and GTNEUT predictions in figure 7.3 could be due in large part to differences in the treatment of molecular and cross section effects in the two calculations.

The three calculations all agreed with the experiment to within the error bars. However, the calculations which ignored molecular effects were generally in better agreement with the experiment, which also ignored molecular effects in defining the measured neutral density, in the private flux region below the X-point.

7.2.3 Wall Boundary Condition Differences

GTNEUT assumes that reflection from the walls is isotropic. The mean free path in practically all regions near the wall was about 1 meter. Thus, an isotropic treatment of the reflected fluxes from the walls could lead to inaccurate flux distributions. In DEGAS, reflection is a function of wall material and of the energy of the incident ions. Furthermore, particles are reflected with a cosine distribution, and the reflection coefficient depends on the material being used. The material used in the original DEGAS simulations was "carbon." Thus, the Monte Carlo treatment of particles reflected from a carbon wall is different than that used by GTNEUT. In order to understand the effect of this difference on the angular distribution of the reflected particles (cosine in DEGAS, isotropic in GTNEUT) two DEGAS simulations were performed. Both simulations were done in toroidal geometry and with the same plasma conditions (no molecules and $<\sigma v>_{ion} \neq f(n)$) and differed only in the wall boundary condition. In the first simulation the wall material was "carbon." In the second it was "mirror," which has specular reflective properties. The

second material option was shown to approximate in regions with short mean free paths, the isotropic reflection condition used by the GTNEUT code (since particles would isotropize near the wall). (See section 3.6 in chapter III). The Monte Carlo predictions, shown in figure 7.6, indicate that the angular distribution of the reflected particles is very important in the private flux region. The results for the simulation with a "carbon" (■) wall differed with the "mirror" (○) wall by a factor of 2 to 5 below the X-point in the private flux region. The difference between the two simulations in the core plasma is unimportant. It seems probable that the choice of wall material could contribute to the difference seen in the private flux region between the Monte Carlo and the GTNEUT predictions in figure 7.3. Since this effect seems to be on the same order as the molecular and cross section effects, it is difficult to determine which one is more important.

7.2.4 Recycling Particle Source Representation Differences

Another potentially important difference between GTNEUT and DEGAS is the treatment of recycling particles. DEGAS recycles D^+ into D^0 using an elaborate physics module. The current version of GTNEUT, on the other hand, does not have a recycling model. In GTNEUT, particles enter the "computational space" by means of a particle puff or as the isotropic reflection of an ion flux incident on the divertor plate. Since DEGAS is capable of simulating the injection of neutral particles using a Maxwellian puff, it seemed necessary to study the sensitivity of the results to these two different representations of particle sources. Two additional DEGAS simulations were performed. Both simulations were done in toroidal geometry and with the same plasma conditions (with molecules and

178
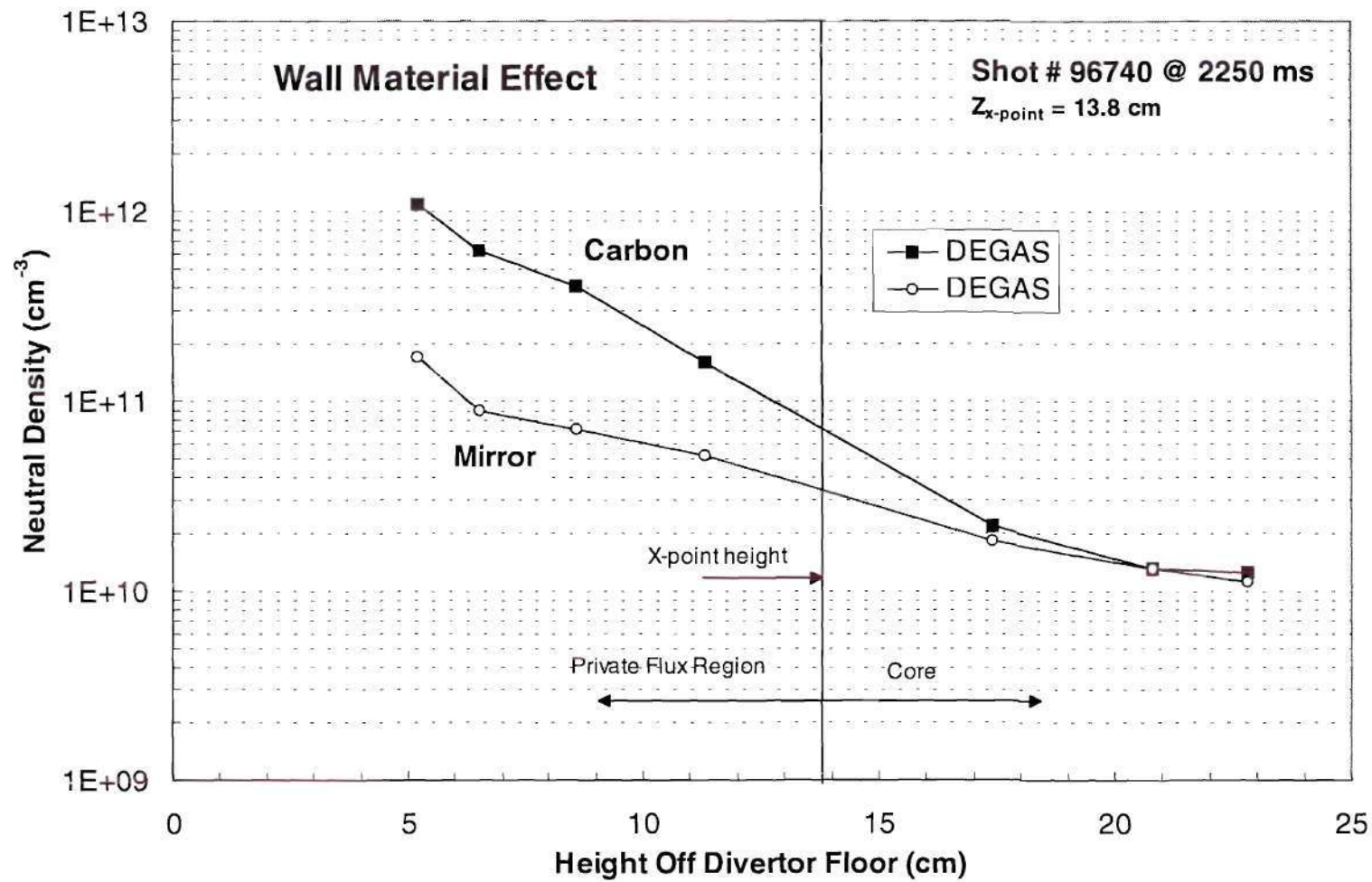
Figure 7.6. DEGAS wall material effect. Carbon wall (■) versus mirror wall (○).

$<\sigma v>_{ion} = f(n))$ and with "carbon" as the wall material. The simulations differed only in the manner in which the particles entered the computational space (i.e., a neutral puff or ions recycling from the plate). The recycling module in DEGAS selected an ion energy E_i from a Maxwellian at the local ion temperature of the region in front of the divertor plate and incident energy was then increased by the sheath acceleration, $3T_e$. The incident ion was either reflected with an energy $E_i + 3T_e$ and a probability R or reemitted as a molecule with an energy $E_{desorption}$ and probability $(1 - R)$. This may be written

$$E_n = R(E_{Maxw}(T_i) + 3T_e) + (1 - R)E_{desorption} \qquad (7.2)$$

The reflection coefficient, R, for the wall material is a function of the ion's incident energy and angle, and $E_{desorption}$ is the energy of desorption of the atom or molecule (usually a Maxwellian at the wall temperature). It is evident that the average energy of the recycled neutrals is the sum of two Maxwellians.

In the puff model in DEGAS, the initial energy of the neutral puff was calculated by taking a volume averaged temperature (of ions and electrons) of all regions directly in front of the divertor plate. In essence, the energy of the neutral puff was a Maxwellian $f(E_n) = f_{Max}(T_n)$ at $T_n = \langle T_i \rangle$. GTNEUT also assumed that the energy of the neutral puff was a Maxwellian at the local ion temperature of the regions in front of the divertor plate.

It is important to mention that the angular distribution of the entering neutrals in both the puff and the recycling source options was cosine distributed. In GTNEUT the angular distribution of the entering neutrals is isotropically distributed.

180

The results shown in figure 7.7 show that the source of particles used did not affect the neutral density distribution in the private flux region. However, in the region inside the plasma core, a small difference was observed. The neutral density distribution for the puffed neutrals was about 1.5 times greater than that of the recycled neutrals. Similar results were observed for a simulation done without molecules.

These results indicate that the choice of the particle source representation could contribute to the difference seen between the Monte Carlo and GTNEUT predictions in the core plasma in figure 7.3. However, the particle source differences are not as important as the atomic/molecular effects and wall boundary condition. Thus, it is unlikely that the choice of recycling particle source representation can account for discrepancies observed in figure 7.3 both above and below the X-point.

7.3 Monte Carlo and GTNEUT Benchmark

The results from the previous sections suggested that nontransport differences in the modeling of the experiment by DEGAS and GTNEUT could account, at least in part, for the differences observed between DEGAS and GTNEUT in figure 7.3. Thus, it seemed necessary to carry out a final comparison between the two codes to determine the extent of the nontransport differences. For this purpose, a "benchmark" DEGAS model was constructed which modeled the atomic/molecular physics and recycling treatments used in GTNEUT as closely as possible.

This benchmark was done using the representative experimental model with cylindrical geometry, "mirror" wall material, no molecules, and density independent ionization rate.
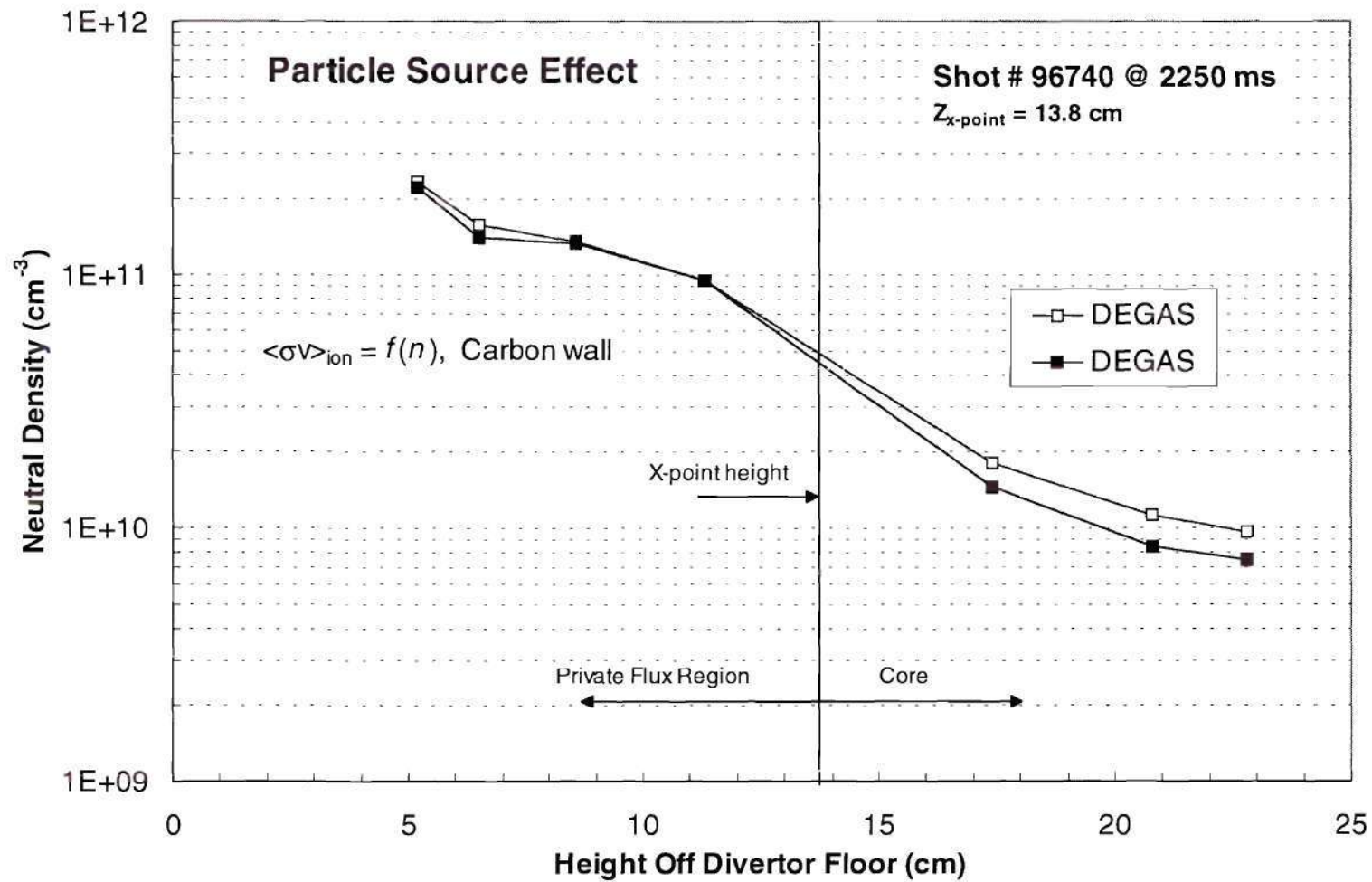
Figure 7.7. DEGAS particle source effect. Recycling (■) versus puffing (□). Carbon wall and density dependent ionization.

The "mirror" option was necessary since in regions with short mean free path, the reflected neutrals isotropize near the wall creating an isotropic particle distribution similar to the isotropic reflection condition used by GTNEUT.

The particle source used in the Monte Carlo simulation was a neutral puff with a Maxwellian energy distribution characterized by the volume averaged ion temperature of the regions in front of the divertor. Similar energy distribution was assumed by GTNEUT. The results of this final comparison are shown in figure 7.8. Figure 7.8 also shows the original DEGAS calculation (which includes molecules and density dependent ionization) and the experimental measurements. The agreement between GTNEUT and the new DEGAS predictions was remarkably good both below and above the X-point. It is important to mention that these new results also agreed with the experiment within the error bars.

The results strongly suggest that nontransport differences in the modeling could account for most of the differences observed between the GTNEUT and the original DEGAS calculation shown in figure 7.3.

7.4 GTNEUT Recycling Model

The previous section demonstrated that if the different nontransport effects were eliminated, the Monte Carlo and GTNEUT predictions were in very good agreement. Furthermore, these calculations agreed within the experimental error bars.

It was found that the nontransport differences that affected the Monte Carlo predictions the most were: 1) the presence of molecules, 2) the wall boundary condition
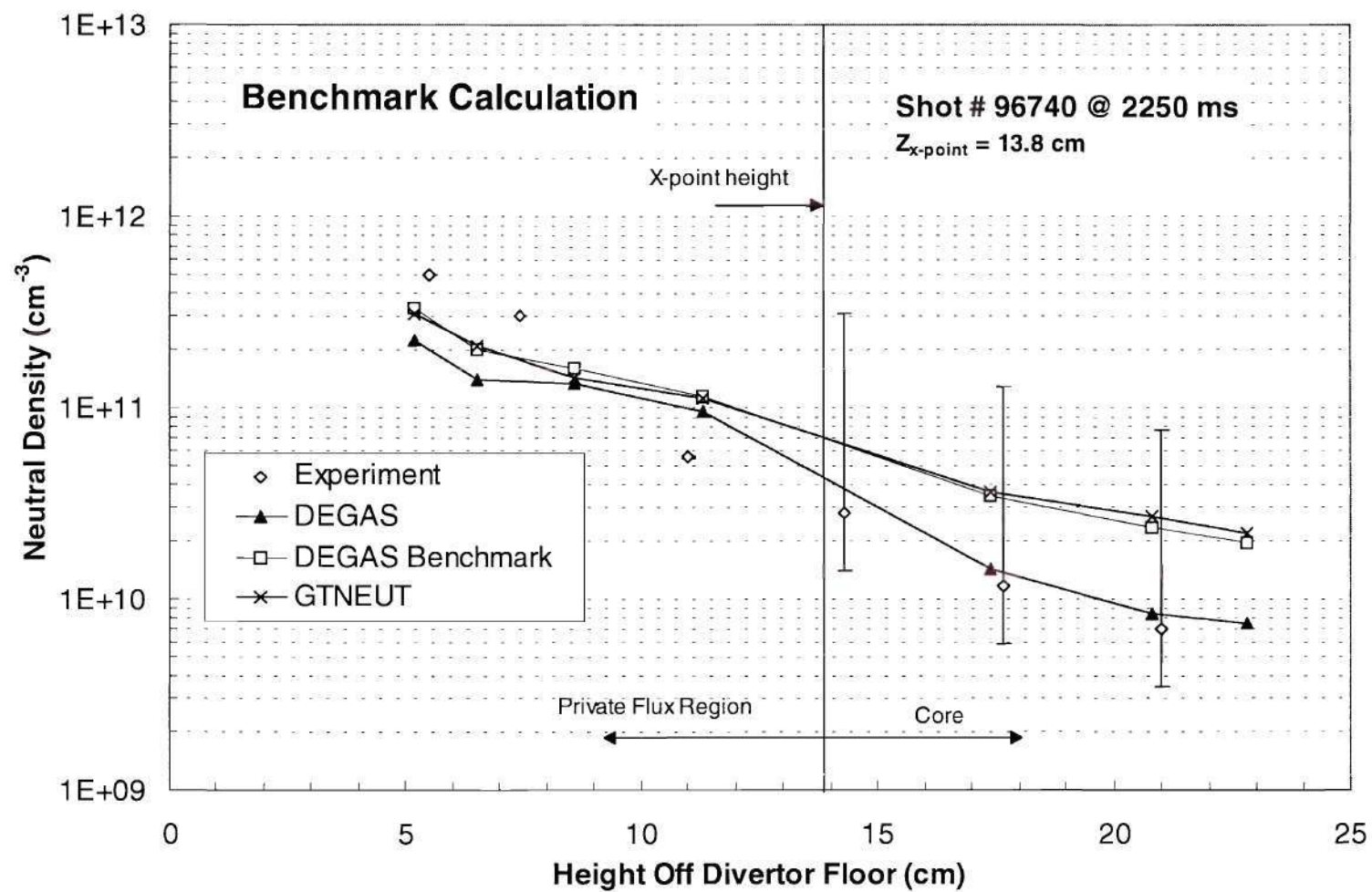
Figure 7.8. Benchmark calculation. DEGAS (□) and GTNEUT (×) with gas puffing, mirror wall, and no molecules.

(which affected the angular distribution of the reflected neutrals), and 3) to a lesser extent cross section effects.

In an effort to improve the agreement between GTNEUT and Monte Carlo and the experiment, this section introduces a simple particle recycling model for GTNEUT. The model assumed that a portion of the incident ions would be reflected from a carbon surface as neutrals with the incident energy. The reflection coefficients for the carbon surface were based on the reflection coefficient for monoenergetic particles that Thomas et al. compiled [23, 59, 60]. The incident energy of the ions was increased by $3T_e$, the sheath acceleration. The model also assumed that another fraction of the ions would be reemitted as molecules to be immediately dissociated into D^+ and D^0. The mean energy of the dissociated fractions was equal to 4.3 eV. Thus, the energy of the recycled neutral is similar to the one used by DEGAS, namely

$$E_n = R\left(T_{i,Maxw} + 3T_e\right) + \left(1 - R\right)4.3 \qquad (8.3)$$

These neutrals were recycled as an isotropic source. The predictions of GTNEUT with the recycling model are shown, along with the original GTNEUT results, the Monte Carlo predictions and the experimental measurements in figure 7.9. The recycling model actually resulted in a slightly poorer agreement with DEGAS and the experiment (by about a factor of two) in the plasma core above the X-point.
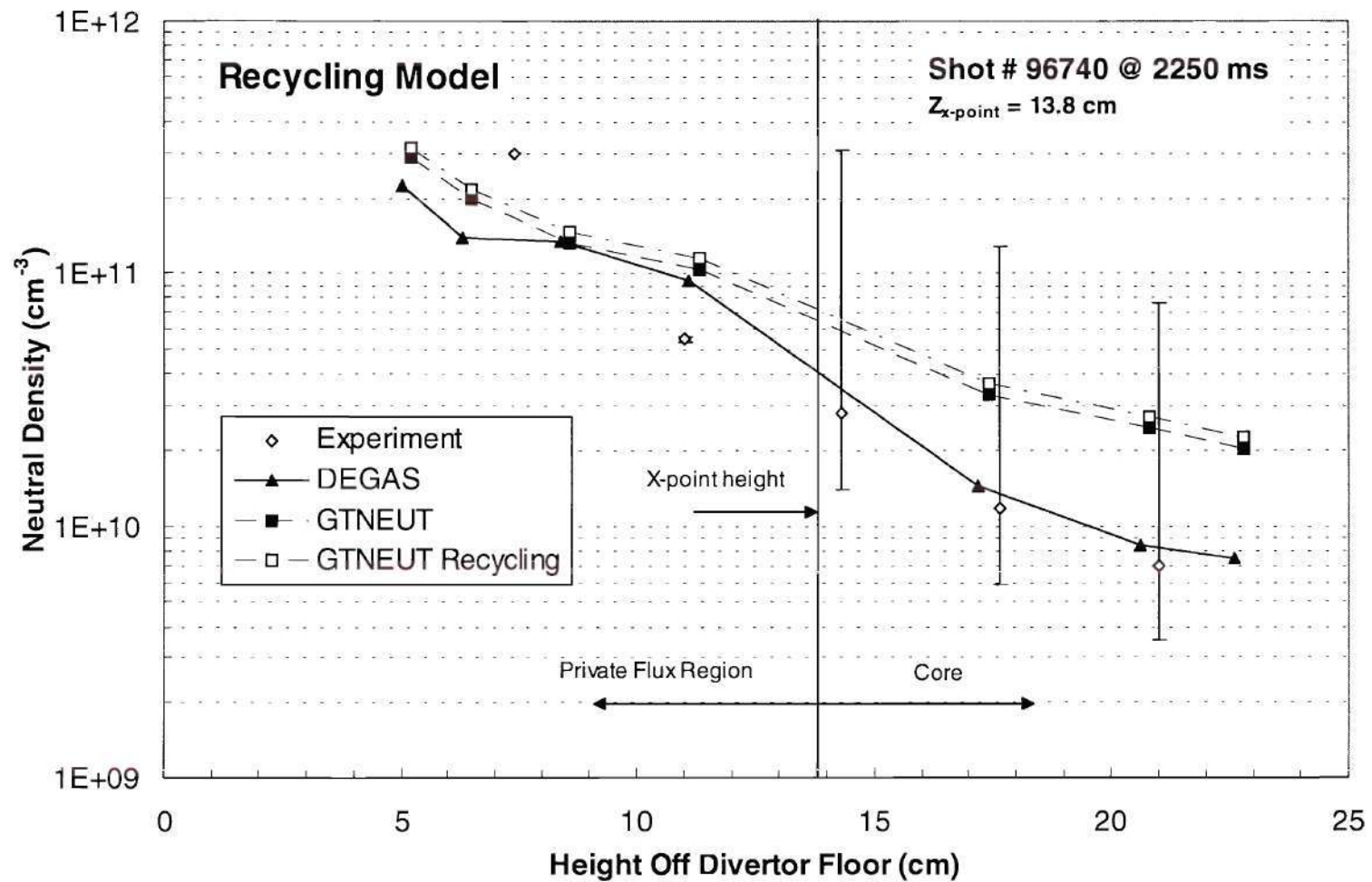
Figure 7.9. GTNEUT recycling model. GTNEUT without recycling (■) versus GTNEUT with recycling (□). Mirror wall, no molecules and gas puffing in GTNEUT. Experiment and DEGAS predictions also shown.

Based on this study and the results obtained in the previous sections, it can be inferred that in GTNEUT the treatment of the angular distribution of the reflected neutrals is more important than a correct treatment of the energy of recycling neutrals.

7.5 Conclusion

The GTNEUT calculation agreed with the measured neutral density to within the error bars. The discrepancies observed between GTNEUT and DEGAS in figure 7.3 were attributed for the most part to nontransport differences. When the experimental conditions were simulated without taking molecular and cross section effects into account, the GTNEUT and DEGAS results were both in very good agreement with the experimental results, which were interpreted without accounting for molecular effects (see figure 7.5). The approximately factor-of-two difference in the GTNEUT and DEGAS results observed in figure 7.3 could be attributed primarily to the different treatment of molecules and wall boundary conditions (which affect the angular distribution of the reflected neutrals) and to a lesser extent to cross section differences between the two codes.

CHAPTER VIII

CONCLUSIONS

8.1 Conclusions

This thesis has investigated the validity of the basic transport methodology of the transmission and escape probabilities (TEP) and interface current balance (ICB) methods, and of the assumptions made in their practical implementations. The accuracy of a number of approximations made in the implementation of the methodology were evaluated by comparing them with Monte Carlo. Furthermore, this work compared the TEP-based code GTNEUT with Monte Carlo calculations for various diverted tokamak plasma models and with recent experimental results for neutral density in the DIII-D fusion experiment.

The detailed evaluation of the transport assumptions of the one-dimensional interface current balance and of the two-dimensional transmission and escape probabilities methods revealed the following findings:

1. The first flight escape probability, P_0, depends on a single parameter, namely X ($X = 4V/\lambda S$). The parametric dependence was demonstrated by the Monte Carlo evaluation of P_0 on a number of geometric regions with different volume-to-surface ratios and with uniform properties.

2. A new rational approximation, $P_0 = \dfrac{1}{X}\left(1 - \left(1 + \dfrac{X}{n}\right)^{-n}\right)$ with $n = 2.09$ provides an alternative approach to avoid the time penalty associated with the exact calculation of the first flight escape probability as defined by equation 2.27. This Sauer-like rational

188

approximation was superior to those suggested by Wigner ($n = 1$) and Sauer ($n = 4.58$) over an intermediate range of X. The P_0 predicted by the new rational approximation was within 5% of the one predicted by Monte Carlo for all geometries tested except cylindrical, for which Sauer's approximation was superior.

3. First flight transmission, T_0, and escape probabilities, P_0, in regions characterized by linear nonuniformaties can be calculated by using a mean free path, λ_{av}, based on a linear average of the nonuniform quantity (i.e., temperature and/or density). Calculation of T_0 and P_0 in nonuniform regions with different optical thicknesses produced results that were within 5% of those predicted by Monte Carlo.

4. The presence of a directional flow of particles, such as recycling from the divertor plate, creates a nonuniform first collision source distribution in a region which leads to preferential escape back across the incident surface. Neglect of this escape directionality in the present implementation of the methodology caused the overprediction of penetration, which increased as $\Delta x/\lambda > 1$.

5. A significant error was introduced in the calculation of the penetration of the uncollided component of the angular flux in problems with a strong directional flow of particles. This error arose from the assumption that the angular flux was isotropic at successive interfaces. This isotropization error caused an underprediction of penetration which increased as $\Delta x/\lambda < 1$.

189

6. In problems with a directional flow of particles, when $\Delta x/\lambda \cong 1$ the isotropization and escape directionality errors tend to balance each other almost exactly. In this instance, Monte Carlo and ICB predictions were in very good agreement.

The directionality error could be eliminated by making use of an escape directionality correction factor (see figure 3.17). However, a more effective and systematic way to correct both the isotropization and escape directionality errors is by defining effective transmission and reflection coefficients for an arbitrary $\Delta x/\lambda$ to match the results that would be obtained if the problem was subdivided into regions with $\Delta x/\lambda = 1$.

7. The isotropic reflection assumption used by the TEP-based code GTNEUT only agrees with Monte Carlo calculations using specular reflection in regimes in which the characteristic dimension of the region was greater than the mean free path of the neutral, so that the specular reflected Monte Carlo neutrals were effectively isotropized near the wall. This assumption is only valid when $\Delta x/\lambda > 1$.

8. The energy of the neutrals is adequately described by a Maxwellian distribution with the local ion temperature. This was demonstrated in uniform and nonuniform one-dimensional multiregion problems, and corroborated in two-dimensional diverted tokamak models.

9. The TEP-based code, GTNEUT, is able to predict, at a fraction of the computer time required by Monte Carlo, both ionization rate and neutral particle densities in all regions in full scale diverted tokamak models (DIII-D, CMOD, and ITER-EDA). However, some models present some noticeable differences in regions located near the X-points and

midplanes. These can be attributed to the inadequate treatment of the isotropization and escape directionality errors, as well as to the inadequate reflection condition in GTNEUT.

10. A GTNEUT calculation agreed with a recent measurement of the neutral density near the X-point in the DIII-D tokamak to within the experimental error bars. A detailed comparison of the neutral density, as predicted by the GTNEUT and DEGAS codes presents some discrepancies attributed for the most part to nontransport differences between physical models in the two codes. These discrepancies arise primarily because of the different treatment of molecules and wall boundary conditions (which affect the angular distribution of the reflected neutrals). When these differences are removed, a very good agreement between the two codes is achieved.

8.2 Recommendations

This work has identified two potentially major deficiencies in the present implementation of the TEP/ICB methodology. These deficiencies are both associated with strong directional flow away from a source. The first deficiency is an isotropization error introduced by assuming that the collided and uncollided components of the angular flux have an isotropic angular distribution within the forward hemisphere regardless of the number of interfaces the computational domain might have. The second deficiency is an escape directionality error introduced by the assumption that the first collision source rate distribution within a region is uniform. Therefore, the calculation of penetration of neutrals due to a plane source located on a bounding surface of a multiregion problem has a combination of these two errors. The isotropization error causes underprediction of penetration and the escape

191

directionality error causes overprediction of penetration. The study demonstrated, by comparison with Monte Carlo, that when the characteristic dimension of a region is greater than the mean free path (i.e., $\Delta x/\lambda > 1$), the escape directionality error is dominant. In contrast, when the characteristic dimension of a region is less than the mean free path (i.e., $\Delta x/\lambda < 1$), the isotropization error dominates. It was also shown that when the characteristic dimension of a region equals the mean free path (i.e., $\Delta x/\lambda = 1$), the two errors tend to compensate almost exactly.

The escape directionality error can be eliminated by using an escape directionality factor. Unfortunately, since this factor is a function of both mean free path and the charge-exchange/scattering fraction, a substantial amount of work would be necessary to prepare such a correction factor for practical application.

A more convenient way to eliminate these errors is to use a set of effective transmission and reflection coefficients. It was shown, at least in one dimension, that this approach reduces the net effect of both isotropization and escape directionality errors. The computational algorithm is manageable for integer values of $\Delta x/\lambda$; for fractional values the task can be very difficult, but is still possible.

The present implementation of the TEP/ICB methodology makes the assumption that the incident current is isotropically distributed in angle over the inward half-space, for the purpose of calculating uncollided transmission probabilities. The flux is assumed to be isotropic in both the forward and backward directional hemisphere. However, the probability for a direction in the forward hemisphere is different than the probability for the

192

symmetric direction in the backward hemisphere. This derivation corresponds to a double P_0 expansion. Since the isotropization error underpredicts the uncollided component of the angular flux, a higher order double P_n expansion could correct this problem. This subject has been studied extensively in heterogeneous reactor transport calculations. Most of the work done has focused on a double "P_1 expansion about an arbitrary direction" [61, 62]. It has been demonstrated by a number of authors that this approach improves the accuracy of results in multicell problems [39, 61-68]. Therefore, extension of the methodology to a higher order double P_n expansion is recommended.

Another major recommendation is to develop a first collision source correction to allow the calculation of directional escape probabilities.

In closing, the TEP/ICB method has proven, after considerable testing, to be capable of handling neutral transport calculations in complex diverted plasma configurations. In spite of the identified potential deficiencies, the method was shown to compare quite favorably with Monte Carlo and the experiment in practical calculations of fusion experiments. The method is robust and versatile, capable of treating accurately and at a fraction of the computation time, regions with long and short mean free paths. Thus, the method has the qualities for performing routine realistic neutral calculations in the edge plasma and divertor region of fusion plasmas that no other method has.

REFERENCES

1. J. Wesson, *Tokamaks*, Second Ed., Oxford University Press, Inc., New York, 17 (1997).

2. M. Tendler, and D. Heifetz, "Neutral Particle Kinetics in Fusion Devices," *Fusion Technology*, **11**, 289 (1987).

3. R. D. M. Garcia, G. C. Pomraning and C. E. Siewert, "On the Transport of Neutral Hydrogen Atoms in a Hydrogen Plasma," *Plasma Physics*, **24**, 903 (1982).

4. J. Hackmann, Y. C. Kim, E. K. Souw, and J. Uhlenbusch, " Investigation of Neutral Particle Behavior Between Plasma and Wall Including Wall interactions," *Plasma Physics*, **20**, 309 (1978).

5. D. Heifetz, D. Post, M. Petravic, J. Weisheit, and G. Bateman, "A Monte Carlo Model of Neutral-Particle Transport in Diverted Plasmas," *J. Computational Physics*, **46**, 309 (1982).

6. B. Lehnert, "On Particle Transport in Toroidal Plasmas," *Plasma Phys. and Control. Fusion*, **26**, 1237 (1984).

7. P. Helander, F. Wising, P. J. Catto and R. D. Hazeltine, "Ion Transport in a Partially Ionized Impure Edge Plasma," *Phys. Plasmas*, **4**, 12 (1997).

8. P. C. Stangeby and G. M. McCracken, "Plasma Boundary Phenomena in Tokamaks", *Nuclear Fusion*, **30**, 1225 (1990).

9. A. Niemczwski, I. H. Hutchinson, B. LaBombard, B. Lipschultz, and G. M. McCraken, "Neutral Particle Dynamics in the Alcator C-Mod Tokamak," *Nuclear Fusion*, **37**, 151 (1997).

10. K. Tsuchiya, H. Takenaga, T. Fukuda, Y. Kamada, S. Ishida, M. Sato, T. Takizuka, and JT-60 Team. "Effect of edge neutrals on the condition of the H-mode transition in JT-60U," *Plasma Phys. and Control. Fusion*, **38**, 1295 (1996).

11. W. M. Stacey, M. A. Mahdavi, R. Maingi, and T. W. Petrie, "Multi-faceted symmetric radiation from the edge formation in DIII-D high-confinement mode discharges with continuous gas puffing," *Phys. Plasmas*, **6**, 3941 (1999).

194

12. K. Janev, M. F. A. Harrison, and H. W. Drawin, "Atomic and Molecular Database for Fusion Plasma Edge Studies," *Nuclear Fusion*, **29**, 109 (1989).

13. H. A. Claasen and H. Gerhauser, "Introduction to Plasma Edge Physics," *Fusion Technology*, **25**, 225 (1994).

14. G. M. McCraken and P. E. Stott, "Plasma-Surface Interactions in Tokamaks," CLM-P573, 1979.

15. R. V. Meghreblian and D. K. Holmes, *Reactor Analysis,* McGraw-Hill, New York 366, 1960.

16. H. Greenspan, C. N. Kelber, and D. Okrent, *Computing Methods in Reactor Physics*, Gordon & Breach, New York, 271 (1968).

17. E. E. Lewis and W. F. Miller Jr., *Computational Methods of Neutron Transport*, John Wiley & Sons, New York, 1984.

18. A. F. Henry, *Nuclear Reactor Analysis, 4th* printing, MIT Press, 333 (1975).

19. G. I. Bell and S. Glasstone, *Nuclear Reactor Theory*, Van Nostrand Reinhold, New York, 1970.

20. B. Davison, *Neutron Transport Theory*, Oxford University Press, London, 1957.

21. M. M. R. Williams, *Mathematical Methods in Particle Transport Theory*, The Butterworth Group, London, 1971.

22. J. J. Duderstadt, W. R. Martin, *Transport Theory*, Wiley-Interscience, New York 1979.

23. W. M. Stacey, E. W. Thomas, and T. M. Evans, "Data and Extended Diffusion Theories for Neutral Particle Transport in Tokamak Divertors," *Phys. Plasmas*, **2**, 3740 (1995).

24. M. Z. Hasan, R. W. Conn, and G. C. Pomraning, "Application of Diffusion Theory to Neutral Atom Transport in Fusion Plasmas," *Nuclear Fusion*, **27**, 117 (1987).

25. E. L. Vold, A. K. Prinja, F. Najmabadi, R. W. Conn, "The Neutral Diffusion Approximation in a Consistent Tokamak Edge Plasma-Neutral Computation," *J. Nucl. Mat.*, **570**, 176 (1990).

26. E. Greenspan, "Calculation of the Transport of Neutral Atoms in Highly Ionized Plasmas Using Neutron Transport Methods," *Nuclear Fusion* **14**, 771 (1974).

27. J. G. Gilligan, S. L. Gralnick, W. G. Price, Jr., and T. Kammash, "Multigroup Calculations of Low-Energy Neutral Transport in Tokamak Plasmas," *Nuclear Fusion*, **18**, 63 (1978).

28. J. H. Marable and E. M. Oblow, "The Application of Neutron Transport Codes to the Transport of Neutrals in Plasmas," *Nucl. Sci. & Engr.*, **61**, 90 (1976).

29. E. Cupini, A. De Matteis, and Simonini, "Nimbus - Monte Carlo Simulation of Neutral Particle Transport in Fusion Devices," NET report Nr. 9, April 1983.

30. L. L. Carter and E. D. Cashwell, *Particle Transport Simulation with the Monte Carlo Method.* LANL 1975.

31. A. B. Chilton, J. K. Shultis, and R. E. Faw, *Principles of Radiation Shielding*, Prentice-Hall, New Jersey 1984.

32. W. M. Stacey Jr. and J. Mandrekas, "A Transmission/Escape Probability Model for Neutral Particle Transport in the Outer Regions of a Diverted Tokamak," *Nuclear Fusion*, **34**, 1385 (1994).

33. K. Audenaerde, G. A. Emmert, and M. Gordinier, "SPUDNUT: A transport code for neutral atoms in plasmas," *J. Comp. Phys.* **34**, 268 (1980).

34. W. M. Stacey Jr., "An Interface Current Balance Formulation of Neutral Atom Transport Theory in Plasmas," *Phys. Plasmas*, **4**, 179 (1997).

35. W. M. Stacey, J. Mandrekas, R. Rubilar, "TEP/ICB Method for Neutral Particle Transport," accepted for publication in *Contrib. Plasma Phys.*

36. W. M. Stacey, J. Mandrekas, R. Rubilar, "Interface Current Integral Transport Methods for the Calculation of Neutral Atom Transport in the Edge Region of Fusion Plasmas," accepted for publication in *J. Transp. Theory & Stat. Phys.*

37. J. Stepanek and M. Segev, "Surface Current Double-Heterogeneous Multilayer Multicell Methodology," *Nucl. Sci. Eng.*, **108**, 215 (1991).

38. G. Marleau, A. Hebert, "Interface Current Method for Cluster Geometry," *Nucl. Sci. Eng.*, **92**, 240 (1986).

39. Z. Chunlei, X. Zhongsheng, and Y. Banghua, "Two-Dimensional Calculation of Neutron Flux and Power Distribution in the Fuel Assembly of a Light Water Reactor," *Nucl. Sci. Eng.*, **100**, 260 (1988).

40. J. J. Stamm'ler, M. J. Abbate, "Methods of Steady-State Reactor Physics in Nuclear Design," Academic Press, London, 1983.

41. W. M. Stacey, *Nuclear Reactor Physics*, Wiley-Interscience, New York, 2001.

42. K. M. Case, F. de Hoffman, and G. Placzek, "Introduction to the Theory of Neutron Diffusion, Vol I," Los Alamos Scientific Laboratory report (1953).

43. W. G. Bickley and J. Nayler, "A Short Table of the Functions $Ki_n(x)$ from n = 1 to n = 16," *Phil. Mag. Series 7*, **20**, 343 (1935).

44. F. G. Lehter, "Some Observations on the Numerical Computation of the Cylindrical-Exponential Integral $D_n(x)$," *J. Quant. Spectrosc. Radiat. Transfer*, **43**, 187 (1990).

45. A. G. Gibbs, "Time-Dependent Escape Probabilities and Chord Distribution Functions," *Nucl. Sci. Eng.*, **99**, 365 (1988).

46. E. P. Wigner, E. Creutz, H. Jupnik, and T. Snyder, "Resonance Absorption of Neutrons by Spheres," *J. Appl. Phys.*, **26**, 260 (1955).

47. A. Sauer, "Approximate Escape Probabilities," *Nucl. Sci. Eng.*, **16**, 260 (1963).

48. H. P. Raghav, "Polynomial Expression for the Neutron Escape Probability from an Absorbing Body," *Nucl. Sci. Eng.*, **73**, 302 (1980).

49. Y. A. Chao, M. B. Yarbrough, and A. S. Martinez, "Approximations to Neutron Escape Probability and Dancoff Correction," *Nucl. Sci. Eng.*, **78**, 89 (1981).

50. H. P. Raghav, "Polynomial Expressions for the Neutron Escape Probability," *Nucl. Sci. Eng.*, **78**, 91 (1981).

51. Y. A. Chao, Reply to "Polynomial Expression for the Neutron Escape Probability from an Absorbing Body," *Nucl. Sci. Eng.*, **73**, 304 (1980).

52. MCNP - A General Monte Carlo N-Particle Transport Code. Version 4B, 1997.

53. General Atomics DIII-D National Fusion Facility, http://Fusion.gat.com/diii-d/

54. M. E. Rensick, personal communication.

55. Alcator C-Mod - Leading the quest for fusion power. http://alcpc1.psfc.mit.edu/cmod/

56. ITER, The International Thermonuclear Experimental Reactor. http://www.iter.org

57. G. Janischitz, K. Borrass, G. Federici, Y. Igitkhanov, A. Kukushkin, H. D. Patcher, G. W. Patcher, and M. Sugihara, "The ITER Divertor Concept," *J. Nuclear Materials*, **220-222**, 73 (1995).

58. R. J. Colchin, R. Maingi, M. E. Fenstermacher, T. N. Carlstrom, R. C. Isler, L. W. Owen, and R. J. Groebner, "Measurement of Neutral Density near the X Point in the DIII-D Tokamak," *Nuclear Fusion*, **40**, 175 (2000).

59. E. W. Thomas, R. K. Janev, and J. Smith, *Particle Reflection from Surfaces- A Recommended Data Base* (International Atomic Energy Agency, Vienna, 1994), International Atomic Energy Agency Report IDC(NDS)-249.

60. E. W. Thomas, R. K. Janev, and J. Smith, "Scaling of Particle Reflection Coefficients," *J. Nucl. Instrum. Methods B*, **69**, 427 (1992).

61. M. M. Anderson and H. C. Honeck, "An Interface Current Technique for Two-Dimensional Cell Calculations," Proc. Conf. Mathematical Models and Computational Techniques for Analysis of Nuclear Systems, Ann Arbor, Michigan, April 9-11, 1973, CONF-730414, I, 53, U.S. Atomic energy Commission (1973).

62. R. Sanchez, "Approximate Solutions of the Two-Dimensional Integral Transport Equation by Collision Probability Methods," *Nucl. Sci. Eng.*, **64**, 384 (1977).

63. F. Wasastjerna, "An Application of the Transmission Probability Method to the Calculation of Neutron Flux Distributions in Hexagonal Geometry," *Nucl. Sci. Eng.*, **72**, 9 (1979).

64. P. D. Krishnani, "An Evaluation of Approximate Methods For Calculating Anisotropic Flux Escape and Transmission Probabilities For Cylindrical Annular Regions," *Ann. Nucl. Energy*, **10**, 285 (1985).

65. R. Sanchez, "A Transport Multicell Method for Two-Dimensional Lattices of Hexagonal Cells," *Nucl. Sci. Eng.*, **92**, 247 (1986).

66. P. Mohanakrishnan, "Choice of Angular Current Approximations for Solving Neutron Transport Problems in 2-D by Interface Current Approach," *Ann. Nucl. Energy*, **9**, 261 (1982).

67. H. Haggblom and A. Ahlin, "Transmission Probability Method of Integral Neutron Transport Calculation for Two-Dimensional Rectangular Cells," *Nucl. Sci. Eng.*, **56**, 411 (1975).

68. J. M. Sicilian and M. M. Anderson, "Mean-Chord-Length Approximations in the Interface-Currents Formulation of the Collision-Probabilities Techniques," *Nucl. Sci. Eng.*, **57**, 78 (1975).

Vita

Roberto Rubilar Briones was born in Santiago, Chile in 1965. He earned his primary education in the public school system in Santiago. He received a Bachelor in Physics from Brigham Young University in 1992. As an undergraduate he became involved in fusion and decided to pursue a Ph. D. in Nuclear Engineering with emphasis in plasma physics. He was accepted to the Georgia Institute of Technology Doctoral Program in this discipline in 1993. While pursuing this degree, Roberto received the degree Master of Science with emphasis in fusion and fission in 1995, and the degree Master of Science in Health Physics in 1997. He completed the degree Doctor of Philosophy in Nuclear and Radiological Engineering from the Georgia Institute of Technology in 2000.